

**IMPROVED INERTIAL NAVIGATION SYSTEM
USING ALL-ACCELEROMETERS**

BY

YAZAN MOHAMMAD AL-RAWASHDEH

A Thesis Presented to the
DEANSHIP OF GRADUATE STUDIES

KING FAHD UNIVERSITY OF PETROLEUM & MINERALS

DHAHRAN, SAUDI ARABIA

In Partial Fulfillment of the
Requirements for the Degree of

MASTER OF SCIENCE

In

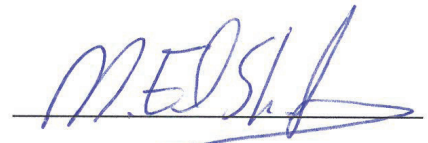
SYSTEM ENGINEERING DEPARTMENT

MAY 2014

KING FAHD UNIVERSITY OF PETROLEUM & MINERALS
DHAHRAN- 31261, SAUDI ARABIA

DEANSHIP OF GRADUATE STUDIES

This thesis, written by **YAZAN MOHAMMAD AL-RAWASHDEH** under the direction his thesis advisor and approved by his thesis committee, has been presented and accepted by the Dean of Graduate Studies, in partial fulfillment of the requirements for the degree of **MASTER OF SCIENCE IN SYSTEMS ENGINEERING**.



Dr. MOUSTAFA ELSHAFEI
(Advisor)



Dr. FOUAD AL-SUNNI
Department Chairman



Dr. SAMI ELFERIK
(Member)



Dr. SALAM A. ZUMMO
Dean of Graduate Studies



Dr. MUHAMMAD FAIZAN
(Member)

19/5/14
Date



© YAZAN MOHAMMAD AL-RAWASHDEH

2014

TO MY FATHER AND MOTHER

WITH LOVE

ACKNOWLEDGMENTS

I would like to thank the Ministry of Higher Education in the Kingdom of Saudi Arabia for supporting me during my M.Sc. level. I also would like to thank King Fahd University of Petroleum and Minerals, KFUPM Dhahran-Saudi Arabia, for providing the best academic and social environments I ever have. Never forget my thesis advisor, Prof. Moustafa Elshafei, for being like a father with his endless patience, support and guidance all the time. Great thanks go as well for my thesis committee members for their valuable comments and suggestions which helped in forming my thesis in its current form.

Yazan M. Al-Rawashdeh

TABLE OF CONTENTS

ACKNOWLEDGMENTS	V
TABLE OF CONTENTS	VI
LIST OF TABLES	XI
LIST OF FIGURES	XII
LIST OF ABBREVIATIONS	XXIV
ABSTRACT	XXVIII
ABSTRACT ARABIC	XXIX
CHAPTER 1 INTRODUCTION	1
CHAPTER 2 AIR VEHICLES NAVIGATION	7
2.1 Frames of Reference used in Navigation	8
2.2 Inertial Navigation Systems	10
2.2.1 Gimbaled (Stabilized platform)	10
2.2.2 Strapdown INS	12
2.3 Flight Navigation Frames Transformations	14
2.3.1 Transformation between Body (b) and vehicle-Carried (nv) frames	14
2.3.2 Transformation between local (n) and vehicle-carried NED (nv) frames	16
2.3.3 Relation between vehicle-Carried (nv) and Geodetic (g) frames	16
2.4 Flight Dynamics Equation	18
2.5 Summary	20
CHAPTER 3 LITERATURE REVIEW	22

3.1	Thesis background	22
3.2	INS Aided Systems	23
3.3	Calibration	25
3.4	Errors	26
3.5	Faults	27
3.6	Build INS	28
3.7	Dead Reckoning	29
3.8	Center of Gravity Change	29
3.9	ALL-Accelerometers Method	30
3.10	Alignment	34
3.11	Numerical Methods	37
3.12	Performance	38
3.13	Simulation	39
3.14	Testing	39
3.15	Data Fusion	40
3.16	Implementation	41
3.17	INS Mechanization	42
3.18	Patents	42
CHAPTER 4 SIMULATING RIGID BODY DYNAMICS		43
4.1	Rigid Body Dynamics equations	43
4.2	Simulating Rigid Body Dynamics using SimMechanics	45
4.2.1	Machine Environment Block	45
4.2.2	Six-DOF Mechanical Joint Block	46
4.2.3	Weld Mechanical Joint Block	46
4.2.4	Rigid Body Block	47

4.2.5	Body Actuator Block	47
4.2.6	Body Sensor Block	48
4.3	Modeling a Tri-axis linear accelerometer using SimMechanics	49
4.3.1	Accelerometer model	49
CHAPTER 5 ALL-ACCELEROMETERS BASED IMU		53
5.1	Mathematical Derivation.....	55
5.1.1	Estimation of Angular Velocities and Accelerations.....	56
5.1.2	Estimation of CoG position and inertial acceleration	60
5.2	Simulating All-accelerometers Based IMU.....	65
5.2.1	Simulating All-accelerometers Based IMU with 12-accelerometers	68
5.2.2	Simulating All-accelerometers Based IMU with 18 accelerometers	71
5.3	Summary	73
CHAPTER 6 FILTER DESIGN		75
6.1	Literature Review	75
6.2	Filter Design	79
6.2.1	Models used in Filter Design.....	85
6.2.2	Simulation Results of System 4 with different Measurement Models Using EKF	91
6.2.3	Simulation Results of System 6 with different Measurement Models Using EKF	101
6.2.4	Observability Check using different Measurement Models	109
6.2.5	Simulation Results of System 6 with different Measurement Models Using UKF.....	114
6.2.6	Comparison between EKF and UKF.....	120
6.2.7	Is a non-linear Filter really needed?.....	122
6.3	Summary	125
CHAPTER 7 GRAVITY COMPENSATION.....		127

7.1	Problem Formulation	131
7.2	Simulating the Gravity Gradient	144
7.2.1	Simulating Gravity Gradient using EGG	148
7.2.2	Simulating Gravity Gradient using SimMechanics/Simulink.....	151
7.2.3	Gravity Compensation Implementation.....	153
7.3	Summary	154
CHAPTER 8 SYSTEM IDENTIFICATION.....		155
8.1	System models used in Identification problem.....	155
8.2	Recursive Identification methods used.....	163
8.3	Simulation Results.....	165
8.4	Selecting an Identification Method and a Model.....	175
8.4.1	Competitive QR-Decomposition based WRLS Identification Scheme	176
8.4.2	QR-Decomposition based WRLS Bank and Maximum Likelihood Estimation Identification Scheme.....	178
8.4.3	Geometric Optimization with linear constraints and MLE Identification Scheme.....	186
8.4.4	Modified Geometric Optimization with linear constraints Identification Scheme.....	186
8.5	Minimum Angular Motion Needed for CoG Position Determination	187
8.6	Summary	191
CHAPTER 9 COMPLETE PICTURE.....		194
9.1	The Proposed IMU Structure	195
9.1.1	Identification Model #3 with gravity effect included	200
9.1.2	Solving the Attitude Problem.....	202
9.2	Simulation Results.....	203
9.2.1	Explaining the simulation procedures.....	204
9.2.2	Solving the navigation problem using UKF and QR-D based WRLS.....	204

9.2.3	Solving the navigation problem using EKF and QR-D based WRLS	208
9.2.4	Solving the navigation problem using KF and QR-D based WRLS	209
9.3	Hardware Implementation	211
CHAPTER 10 FUTURE WORK.....		215
REFERENCES.....		219
VITAE.....		231

LIST OF TABLES

Table 1: Simulation Schedule	68
Table 2: IMU Kinematics Equations for Systems 1 and 2.....	81
Table 3: IMU Kinematics Equations for Systems 3 and 4.....	81
Table 4: IMU Kinematics Equations for Systems 5 and 6.....	82
Table 5: IMU Kinematics Equations for Systems 4 when ($L \gg \mu$).....	84
Table 6: Discrete Version of System 4	86
Table 7: Discrete Version of System 6	86
Table 8: 1-D Measurement Model for System 4.	88
Table 9: 2-D Measurement Model for System 4.	88
Table 10: 3-D Measurement Model for System 4.	89
Table 11: 1-D Measurement Model for System 6.	89
Table 12: 2-D Measurement Model for System 6.	90
Table 13: 3-D Measurement Model for System 6.	90
Table 14: Measurement Matrix for Systems 4 and 6, linearized version.	90
Table 15: Maximum Percentage Error of the estimated angular velocity obtained using different Filters	126
Table 16: Various Models used in Identification parameters.	160
Table 17: System Identification MPE for CoG position Estimation	174
Table 18: Angular Motion plan To Identify CoG position.....	188

LIST OF FIGURES

Figure 1	: Frames of Reference used in navigation. ^[10]	9
Figure 2	: Gimbaled INS schematic diagram. ^[11]	11
Figure 3	: Stable platform (Gimbal) inertial navigation algorithm. ^[12]	12
Figure 4	: A typical strapdown INS. ^[13]	13
Figure 5	: Strapdown inertial navigation unit block diagram. ^[14]	13
Figure 6	: Strapdown inertial navigation algorithm. ^[15]	13
Figure 7	: Block diagram and the ideal features of the proposed IMU.....	21
Figure 8	: References spectrum related to INS.....	22
Figure 9	: Inertial and non-inertial frames.....	44
Figure 10	: Machine Environment Block with gravity as a Simulink signal.....	46
Figure 11	: Six-DOF Mechanical Joint Block.....	46
Figure 12	: Weld Mechanical Joint Block.....	47
Figure 13	: Body Block.....	47
Figure 14	: Body Actuator Block.....	48
Figure 15	: Body Sensor Block.....	48
Figure 16	: Available measurements in a Body Sensor Block.....	48
Figure 17	: Tri-axis model used in the thesis, where measurements are provided with respect to: (Ae) Inertial, and (Ab) Body frames.....	50
Figure 18	: Simulation setup used to test the tri-axis accelerometer model.....	50
Figure 19	: Accelerometer measurements relative to: (a) world (b) body coordinate systems when located at CoG (c) same as (b) but when shifted 2 meters in the X-direction from CoG.....	51
Figure 20	: Two Rings approach based on the proposed IMU.....	55
Figure 21	: F-15 jet fighter with three-Ring configuration. ^[18]	65

Figure 22	: Two Rings approach based on the proposed IMU using 18-accelerometer/Ring version.....	65
Figure 23	: Composite rigid body SimMechanics Machine.....	67
Figure 24	: SimMechanics visualization of the composite rigid body given in the example.....	67
Figure 25	: (a) Applied Moment (N.m), (b) Force (N) profiles used in the simulation.....	67
Figure 26	: Composite Object CoG Position (m) relative to the Geometric Center (0, 0, 0).....	68
Figure 27	: Estimation error of the position of the composite body CoG (m) using 12-accelerometer IMU version in Two-Rings Configuration.	69
Figure 28	: Estimation error of the acceleration of the composite body (m/sec ²) using 12-accelerometer IMU version in Two-Rings Configuration.....	69
Figure 29	: Estimation error of the angular velocity of the composite body (rad/sec) using 12-accelerometer IMU version in Two-Rings Configuration.....	70
Figure 30	: Estimation error of the angular acceleration of the composite body (rad/sec ²) in the range of 10 ⁻⁹ using 12-accelerometer IMU version in Two-Rings Configuration.....	70
Figure 31	: Estimation error of the position of the composite body CoG (m) using second modified version in Two-Rings Configuration.....	71
Figure 32	: Estimation error of the acceleration of the composite body (m/sec ²) using second modified version in Two-Rings Configuration.....	71
Figure 33	: Estimation error of the angular velocity of the composite body (rad/sec) using second modified version in Two-Rings Configuration.....	72
Figure 34	: Estimation error of the angular acceleration of the composite body (rad/sec ²) using second modified version in Two-Rings Configuration.....	72
Figure 35	: The usage of Filters within the proposed IMU.....	80

Figure 36	: Extended Kalman Filter Layout. ^[80]	87
Figure 37	: Simulink Model Used to Test System 4 with Different Measurement Models.....	91
Figure 38	: Composite Body Angular Velocity about X-axis (rad/sec) using 12-accelerometer/Ring in Two-Ring Configuration.....	92
Figure 39	: Composite Body Angular Velocity about Y-axis (rad/sec) using 12-accelerometer/Ring in Two-Ring Configuration.....	92
Figure 40	: Composite Body Angular Velocity about Z-axis (rad/sec) using 12-accelerometer/Ring in Two-Ring Configuration.....	92
Figure 41	: Composite Body Angular Velocity about Z-axis (rad/sec) using 12-accelerometer/Ring in Two-Ring Configuration, a close view.	93
Figure 42	: Composite Body Angular Velocity about X-axis (rad/sec) using 12-accelerometer/Ring in Two-Ring Configuration, L = 1m, with 1-D measurement model.....	95
Figure 43	: Composite Body Angular Velocity about Y-axis (rad/sec) using 12-accelerometer/Ring in Two-Ring Configuration, L = 1m, with 1-D measurement model.....	96
Figure 44	: Composite Body Angular Velocity about Z-axis (rad/sec) using 12-accelerometer/Ring in Two-Ring Configuration, L = 1m, with 1-D measurement model.....	96
Figure 45	: Composite Body Angular Velocity about X-axis (rad/sec) using 12-accelerometer/Ring in Two-Ring Configuration, L = 100m, with 1-D measurement model.....	97
Figure 46	: Composite Body Angular Velocity about Y-axis (rad/sec) using 12-accelerometer/Ring in Two-Ring Configuration, L = 100m, with 1-D measurement model.....	97
Figure 47	: Composite Body Angular Velocity about Z-axis (rad/sec) using 12-accelerometer/Ring in Two-Ring Configuration, L = 100m, with 1-D measurement model.....	98
Figure 48	: Composite Body Angular Velocity about X-axis (rad/sec) using 12-accelerometer/Ring in Two-Ring Configuration, L = 1m, with 2-D measurement model.....	98

Figure 49	: Composite Body Angular Velocity about Y-axis (rad/sec) using 12-accelerometer/Ring in Two-Ring Configuration, L = 1m, with 2-D measurement model.....	99
Figure 50	: Composite Body Angular Velocity about Z-axis (rad/sec) using 12-accelerometer/Ring in Two-Ring Configuration, L = 1m, with 2-D measurement model.....	99
Figure 51	: Composite Body Angular Velocity about X-axis (rad/sec) using 12-accelerometer/Ring in Two-Ring Configuration, L = 1m, with 3-D measurement model.....	100
Figure 52	: Composite Body Angular Velocity about Y-axis (rad/sec) using 12-accelerometer/Ring in Two-Ring Configuration, L = 1m, with 3-D measurement model.....	100
Figure 53	: Composite Body Angular Velocity about Z-axis (rad/sec) using 12-accelerometer/Ring in Two-Ring Configuration, L = 1m, with 3-D measurement model.....	101
Figure 54	: Simulink Model Used to Test System 6 with Different Measurement Models.....	102
Figure 55	: Composite Body Angular Velocity about X-axis (rad/sec) using 18-accelerometer/Ring in Two-Ring Configuration, L = 1m, with 1-D measurement model.....	102
Figure 56	: Composite Body Angular Velocity about Y-axis (rad/sec) using 18-accelerometer/Ring in Two-Ring Configuration, L = 1m, with 1-D measurement model.....	103
Figure 57	: Composite Body Angular Velocity about Z-axis (rad/sec) using 18-accelerometer/Ring in Two-Ring Configuration, L = 1m, with 1-D measurement model.....	103
Figure 58	: Composite Body Angular Velocity about X-axis (rad/sec) using 18-accelerometer/Ring in Two-Ring Configuration, L = 1m, with 2-D measurement model.....	104
Figure 59	: Composite Body Angular Velocity about Y-axis (rad/sec) using 18-accelerometer/Ring in Two-Ring Configuration, L = 1m, with 2-D measurement model.....	104
Figure 60	: Composite Body Angular Velocity about Z-axis (rad/sec) using	

	18-accelerometer/Ring in Two-Ring Configuration, L = 1m, with 2-D measurement model.....	105
Figure 61	: Composite Body Angular Velocity about X-axis (rad/sec) using 18-accelerometer/Ring in Two-Ring Configuration, L = 1m, with 3-D measurement model.....	105
Figure 62	: Composite Body Angular Velocity about Y-axis (rad/sec) using 18-accelerometer/Ring in Two-Ring Configuration, L = 1m, with 3-D measurement model.....	106
Figure 63	: Composite Body Angular Velocity about Z-axis (rad/sec) using 18-accelerometer/Ring in Two-Ring Configuration, L = 1m, with 3-D measurement model.....	106
Figure 64	: Composite Body Angular Velocity about X-axis (rad/sec) using 18-accelerometer/Ring in Two-Ring Configuration, L = 1m, with 1-D measurement model, and Sign ambiguity algorithm.....	108
Figure 65	: Composite Body Angular Velocity about Y-axis (rad/sec) using 18-accelerometer/Ring in Two-Ring Configuration, L = 1m, with 1-D measurement model, and Sign ambiguity algorithm.....	108
Figure 66	: Composite Body Angular Velocity about Z-axis (rad/sec) using 18-accelerometer/Ring in Two-Ring Configuration, L = 1m, with 1-D measurement model, and Sign ambiguity algorithm.....	109
Figure 67	: UKF layout. ^[87]	115
Figure 68	: Composite Body Angular Velocity about X-axis (rad/sec) using 18-accelerometer/Ring in Two-Ring Configuration, with 1-D measurement model, and Sign ambiguity algorithm with UKF.....	116
Figure 69	: Composite Body Angular Velocity about Y-axis (rad/sec) using 18-accelerometer/Ring in Two-Ring Configuration, with 1-D measurement model, and Sign ambiguity algorithm with UKF.....	116
Figure 70	: Composite Body Angular Velocity about Z-axis (rad/sec) using 18-accelerometer/Ring in Two-Ring Configuration, with 1-D measurement model, and Sign ambiguity algorithm with UKF.....	117
Figure 71	: Composite Body Angular Velocity about X-axis (rad/sec) using 18-accelerometer/Ring in Two-Ring Configuration, with 3-D measurement model, and Sign ambiguity algorithm with UKF.....	117

Figure 72	: Composite Body Angular Velocity about Y-axis (rad/sec) using 18-accelerometer/Ring in Two-Ring Configuration, with 3-D measurement model, and Sign ambiguity algorithm with UKF.....	118
Figure 73	: Composite Body Angular Velocity about Y-axis (rad/sec) using 18-accelerometer/Ring in Two-Ring Configuration, with 3-D measurement model, and Sign ambiguity algorithm with UKF, close view.....	118
Figure 74	: Composite Body Angular Velocity about Z-axis (rad/sec) using 18-accelerometer/Ring in Two-Ring Configuration, with 3-D measurement model, and Sign ambiguity algorithm with UKF.....	119
Figure 75	: Composite Body Angular Velocity about X-axis (rad/sec) using 18-accelerometer/Ring in Two-Ring Configuration, with 3-D measurement model, and Without Sign ambiguity algorithm with UKF.....	119
Figure 76	: Composite Body Angular Velocity about Y-axis (rad/sec) using 18-accelerometer/Ring in Two-Ring Configuration, with 3-D measurement model, and Without Sign ambiguity algorithm with UKF.....	120
Figure 77	: Composite Body Angular Velocity about Z-axis (rad/sec) using 18-accelerometer/Ring in Two-Ring Configuration, with 3-D measurement model, and Without Sign ambiguity algorithm with UKF.....	120
Figure 78	: Composite Body Angular Velocity about X-axis (rad/sec) using 18-accelerometer/Ring in Two-Ring Configuration, with Standard Kalman Filter and without noise.....	123
Figure 79	: Composite Body Angular Velocity about Y-axis (rad/sec) using 18-accelerometer/Ring in Two-Ring Configuration, with Standard Kalman Filter and without noise.....	124
Figure 80	: Composite Body Angular Velocity about X-axis (rad/sec) using 18-accelerometer/Ring in Two-Ring Configuration, with Standard Kalman Filter and without noise.....	124
Figure 81	: Composite Body Angular Velocities (rad/sec) using 18-accelerometer/Ring in Two-Ring Configuration, with Standard Kalman Filter and with noise.....	125

Figure 82	:	Rings Arrangement within a rigid body.....	139
Figure 83	:	Nomenclature and location of the 6 accelerometers of the GOCE Gradiometer in the Gradiometer Reference Frame (GRF) and with all Accelerometer Reference Frame (ARF) ^[132]	145
Figure 84	:	Electrostatic Gravity Gradiometer (EGG) ^[133]	146
Figure 85	:	Major Reference Frames for Gradiometry ^[132]	147
Figure 86	:	GOCE spacecraft ^[131]	147
Figure 87	:	Γ_{xx} gravity gradient component.....	148
Figure 88	:	Γ_{yy} gravity gradient component.....	149
Figure 89	:	Γ_{zz} gravity gradient component.....	149
Figure 90	:	Γ_{xy} gravity gradient component.....	149
Figure 91	:	Γ_{xz} gravity gradient component.....	150
Figure 92	:	Γ_{yz} gravity gradient component in order of 10^4	150
Figure 93	:	Simulink model used to simulate the gravity gradient.....	151
Figure 94	:	Γ_{xx} simulated gravity gradient component.....	151
Figure 95	:	Γ_{yy} simulated gravity gradient component.....	151
Figure 96	:	Γ_{zz} simulated gravity gradient component.....	152
Figure 97	:	Γ_{xy} simulated gravity gradient component.....	152
Figure 98	:	Γ_{xz} simulated gravity gradient component.....	152
Figure 99	:	Γ_{yz} simulated gravity gradient component.....	152
Figure 100	:	G_x gravity component.....	153
Figure 101	:	G_y gravity component.....	153
Figure 102	:	G_z gravity component.....	153
Figure 103	:	Body position (m).....	154
Figure 104	:	Simulink Model used in Parameter Identification.....	163

Figure 105 :	Estimated CoG Position using Standard RLS and Model #1.....	166
Figure 106 :	Estimated Vehicle Inertial Acceleration using Standard RLS and Model #1.....	166
Figure 107 :	Estimated CoG Position using Standard RLS and Model #2.....	166
Figure 108 :	Estimated Vehicle Inertial Acceleration using Standard RLS and Model #2.....	167
Figure 109 :	Estimated CoG Position using Standard RLS and Model #3.....	167
Figure 110 :	Estimated Vehicle Inertial Acceleration using Standard RLS and Model #3.....	167
Figure 111 :	Estimated CoG Position using Standard RLS and Model #4.....	168
Figure 112 :	Estimated Vehicle Inertial Acceleration using Standard RLS and Model #8.....	168
Figure 113 :	Estimated CoG Position using Weighted RLS and Model #1.....	169
Figure 114 :	Estimated Vehicle Inertial Acceleration using Weighted RLS and Model #1.....	169
Figure 115 :	Estimated CoG Position using Weighted RLS and Model #2.....	169
Figure 116 :	Estimated Vehicle Inertial Acceleration using Weighted RLS and Model #2.....	170
Figure 117 :	Estimated CoG Position using Weighted RLS and Model #3.....	170
Figure 118 :	Estimated Vehicle Inertial Acceleration using Weighted RLS and Model #3.....	170
Figure 119 :	Estimated CoG Position using Weighted RLS and Model #4.....	171
Figure 120 :	Estimated Vehicle Inertial Acceleration using Weighted RLS and Model #8.....	171
Figure 121 :	Estimated CoG Position using NLMS and Model #1.....	172
Figure 122 :	Estimated Vehicle Inertial Acceleration using NLMS and Model #1.....	172
Figure 123 :	Estimated CoG Position using NLMS and Model #2.....	172

Figure 124 :	Estimated Vehicle Inertial Acceleration using NLMS and Model #2.....	173
Figure 125 :	Estimated CoG Position using NLMS and Model #3.....	173
Figure 126 :	Estimated Vehicle Inertial Acceleration using NLMS and Model #3.....	173
Figure 127 :	Estimated CoG Position using NLMS and Model #4.....	174
Figure 128 :	Estimated Vehicle Inertial Acceleration using NLMS and Model #8.....	174
Figure 129 :	Estimated CoG Position using QR-D base WRLS and Model #3...	176
Figure 130 :	Estimated Vehicle Inertial Acceleration using QR-D based WRLS and Model #3.....	176
Figure 131 :	Estimated CoG Position using Competitive QR-D base WRLS and Model #3.....	177
Figure 132 :	Estimated Vehicle Inertial Acceleration using Competitive QR-D based WRLS and Model #3.....	177
Figure 133 :	Simulink Blocks representing the Competitive QR-D based WRLS Identification Scheme.....	178
Figure 134 :	Schematic Diagram illustrating the principle of QR-D based WRLS Bank Identification Scheme.....	179
Figure 135 :	QR-Decomposition based WRLS Bank and Maximum Likelihood Estimation Identification Scheme Implemented locally within the proposed IMU in open/closed loop configuration.....	184
Figure 136 :	Global implementation of the MLE in open/closed loop configuration assuming ideal sensor network.....	184
Figure 137 :	Estimated CoG Position using QR-D based WRLS Bank and MLE in local open loop configuration.....	185
Figure 138 :	Estimated Vehicle Acceleration using QR-D based WRLS Bank and MLE in local open loop configuration.....	185
Figure 139 :	CoG Position Variance, in order of $1e^{-9}$	185
Figure 140 :	Block diagram of the Modified Geometric Optimization with	

	linear constraints Identification Scheme.....	187
Figure 141 :	Estimated CoG Position when only angular motion about X-axis is present.....	189
Figure 142 :	Estimated Inertial acceleration when only angular motion about X-Axis is present.....	189
Figure 143 :	Estimated CoG Position when only angular motion about Y-axis is present.....	190
Figure 144 :	Estimated Inertial acceleration when only angular motion about Y-Axis is present.....	190
Figure 145 :	Estimated CoG Position when only angular motion about Z-axis is present.....	190
Figure 146 :	Estimated Inertial acceleration when only angular motion about Z-Axis is present.....	191
Figure 147 :	The recent version of the proposed IMU.....	195
Figure 148 :	Actual accelerometers' configuration (Ring) along with Suggested units for future work.....	196
Figure 149 :	A look inside the Simulated Ring.....	196
Figure 150 :	Core units in the proposed IMU.....	197
Figure 151 :	Attitude Finding unit along with IMU Performance Unit suggested for future work.....	198
Figure 152 :	Units used to estimate inertial data and acceleration due to gravity.	199
Figure 153 :	Blocks reserved for future expansion responsible of finding the mass and inertia of the vehicle.....	199
Figure 154 :	Block reserved for optimal smoothers suggested for future work....	200
Figure 155 :	Flow diagram of the proposed IMU showing INS Mechanization procedure.....	201
Figure 156 :	Estimating acceleration due to gravity using the proposed IMU according to [42].....	202
Figure 157 :	Simulink model used to facilitate simulating the complete IMU.....	203

Figure 158 :	Composite Body Attitude used to check the performance of the proposed IMU.....	205
Figure 159 :	Composite Body Inertial Acceleration, after subtracting the gravity contribution, obtained using the proposed IMU utilizing UKF with 1-D Measurement model.....	205
Figure 160 :	Composite Body Inertial Velocity obtained using the proposed IMU utilizing UKF with 1-D Measurement model.....	205
Figure 161 :	Composite Body Inertial Position obtained using the proposed IMU utilizing UKF with 1-D Measurement model.....	206
Figure 162 :	Composite Body position obtained using the proposed IMU utilizing UKF with 1-D Measurement model.....	206
Figure 163 :	Composite Body Inertial Acceleration, after subtracting the gravity contribution, obtained using the proposed IMU utilizing UKF with 3-D Measurement model.....	207
Figure 164 :	Composite Body Inertial Velocity obtained using the proposed IMU utilizing UKF with 3-D Measurement model.....	207
Figure 165 :	Composite Body Inertial Position obtained using the proposed IMU utilizing UKF with 3-D Measurement model.....	207
Figure 166 :	Composite Body position obtained using the proposed IMU utilizing UKF with 3-D Measurement model.....	208
Figure 167 :	Composite Body Inertial Acceleration, after subtracting the gravity contribution, obtained using the proposed IMU utilizing EKF with 1-D Measurement model.....	208
Figure 168 :	Composite Body Inertial Velocity obtained using the proposed IMU utilizing EKF with 1-D Measurement model.....	208
Figure 169 :	Composite Body Inertial Position obtained using the proposed IMU utilizing EKF with 1-D Measurement model.....	209
Figure 170 :	Composite Body position obtained using the proposed IMU utilizing EKF with 1-D Measurement model.....	209
Figure 171 :	Composite Body Inertial Acceleration, after subtracting the gravity contribution, obtained using the proposed IMU utilizing KF.....	209

Figure 172 :	Composite Body Inertial Velocity obtained using the proposed IMU utilizing KF.....	210
Figure 173 :	Composite Body Inertial Position obtained using the proposed IMU utilizing KF.....	210
Figure 174 :	Composite Body position obtained using the proposed IMU utilizing KF.....	210
Figure 175 :	Gravity Estimation using the proposed IMU.....	211
Figure 176 :	HL20 Example Simulink Model.....	216

LIST OF ABBREVIATIONS

AEM	:	Around-Earth Model
AGV	:	Automatic Guided Vehicle
ARW	:	Angular Random Walk
ATEKF	:	Adaptive Two-stage EKF
CA	:	Carrier Aircraft
CoG	:	Center of Gravity
DCM	:	Direction Cosine Matrix
DDF2	:	2 nd Order Divided Difference Filter
DoF	:	Degrees of Freedom
DSP	:	Digital Signal Processing
DWPA	:	Discrete Wiener Process Acceleration
ECEF	:	Earth Centered Earth Fixed
EKF	:	Extended KF
ESA	:	European Space Agency
FAA	:	Federal Aviation Administration

FDI : Faults Detection and Isolation

FDIR : Faults Detection, Isolation, and Recovery

FEM : Flat-Earth Model

FOS : Fast Orthogonal Search

FPGA : Field Programmable Gate Array

GINS : Gimbal INS

GPS : Global Positioning System

HRG : Hemispherical Resonator gyro

IMU : Inertial Measurement Unit

INS : Inertial Navigation System

IVCR : Instantaneous Velocity Center of rotation

KF : Kalman Filter

LAD : Least Absolute deviation

LDTV : Linear Discrete Time Variant

LMI : Linear Matrix Inequality

MACH : Dimensionless quantity representing the ratio of speed of an object moving through a fluid and the local speed of sound. Named after Ernst

Mach.

- MEMS : Micro-Electro-Mechanical Systems
- MLE : Maximum Likelihood Estimation
- MUKF : Marginalized UKF
- NED : North East Down
- PCI : Parallel Cascade Identification
- PD : Proportional Derivative
- RFDF : Robust Fault-Detection Filter
- RISS : Reduced Inertia Sensor System
- RKF : Robust KF
- RLS : Recursive Least Squares
- SCSM : Subtractive Composite Simpson Method
- SINS : Strapdown INS
- STL : STereoLithography file format
- TA : Transfer Alignment
- UAV : Unmanned Aerial Vehicle
- UKF : Unscented KF

WGS 84 : World Geodetic System 1984

WRLS : Weighted RLS

ABSTRACT

Full Name : [YAZAN MOHAMMAD SULIMAN AL-RAWASHDEH]
Thesis Title : [IMPROVED NAVIGATION SYSTEM USING ALL-ACCELEROMETERS]
Major Field : [SYSTEMS AND CONTROL ENGINEERING]
Date of Degree : [MAY 2014]

Changing position of Center of Gravity (CoG) for an aerial vehicle is a challenging part in navigation and control of such vehicles. In this thesis, the work done to improve all-accelerometers based inertial navigation systems is presented. A novel approach using such setup is explored, analyzed, and extended based on an issued patent. The thesis provided improved method for estimating the position of CoG, so that control rules can be updated accordingly to achieve better trim conditions for the air vehicle. The accelerometers' readings were used to find the angular velocity/acceleration using Kalman Filter (KF), Extended KF (EKF) and Unscented KF (UKF). The angular velocity was then used to extract the vehicle's attitude. Standard Recursive Least Squares (RLS), Normalized Least Mean Squares (NLMS) and Weighted RLS (WRLS) Identification techniques were investigated and used in estimating the position of CoG. A gravity compensation technique was implemented to correct the acceleration readings. Along with the angular velocity/acceleration and vehicle's attitude, the corrected accelerometers' measurements were used to find the inertial information of the vehicle and its CoG position under the influence of varying gravity effect using an identification scheme.

ملخص الرسالة

الاسم الكامل: يزن محمد سليمان الرواشدة

عنوان الرسالة: نظام ملاحه متطور بالإعتماد على حساسات التسارع الخطي

التخصص: هندسة النظم و التحكم

تاريخ الدرجة العلمية: أيار 2014

ان تغير مركز الثقل يعد تحديا كبيرا امام التحكم و الملاحة للمركبات الطائرة. في هذه الرسالة, يتم تقديم العمل الذي اسهم في تطوير نظام الملاحة المعتمد على حساس التسارع الخطي بشكل رئيس. لقد تم التوصل إلى حل فريد باستخدام هذا الحساس اعتمادا على براءة اختراع حيث تم تطوير و تحليل النتائج المقترحة فيها. إن هدف هذه الرسالة هو زيادة دقة تحديد مركز الثقل بحيث يتسنى تحديث أنظمة التحكم تبعا لذلك مما يساعد في تحسين استقرار المركبة. لقد تم استخدام قراءات حساسات التسارع الخطي في ايجاد السرعة و التسارع الدورانيين باستخدام KF, EKF, UKF. تم بعد ذلك استخدام السرعة الدورانية في ايجاد وضعية المركبة. كما تم التحقق من RLS, WRLS, NMLS في ايجاد مركز الثقل. كما تم استخدام طريقة لتقليل أثر الجاذبية الارضية على قراءة الحساس المستخدمة. الى جانب استخدام السرعة و التسارع الدورانيين فقد تم استخدام وضعية المركبة و قراءات حساسات التسارع الخطي المعدلة في ايجاد معلومات الملاحة و مركز الثقل تحت تأثير الجاذبية الأرضية المتغيرة باستخدام طريقة System Identification.

CHAPTER 1

INTRODUCTION

Dynamic equations of an aircraft vehicle are normally derived under the assumption of known and stationary Center of Gravity (CoG). Variations in loads due to picking up/dropping off loads or consuming fuel will result in a change in both the vehicle's mass and position of CoG. This immigration in the position of CoG will introduce dynamic couplings to the flight dynamics [1]. This dynamic coupling will appear in the angular as well as the linear accelerations and in the lateral and longitudinal motions [2]. According to FAA [3], a CoG limits envelope is determined for each craft, in which a safe and good flight conditions can be maintained even under CoG position changes. Different approaches to estimate the position of CoG have been reported in literature, for example in [2] an adaptive weighted data fusion based on optimal weight distribution principle, and an identification technique based on neural network were utilized to improve the effectiveness of such estimation. In [1], the change in CoG position was modeled to describe its effect on an aircraft under heavy load airdrop. While in [4], both static and dynamic measurements were used to estimate the position of CoG of a helicopter on ground and in-flight respectively. The dynamic approach of [4] depends on finding the modal frequencies by solving an eigenvalue problem where any change in a certain modal frequency will be an indication of a CoG position change which can be determined through monitoring that particular frequency. Changing position of CoG in helicopters

was also the main concern of [5], in which an estimation algorithm, based on Extended Kalman Filter (EKF), consists of a rigid body aircraft motion feedback and an internal model of the helicopter was presented. This estimation algorithm was successful in estimating the CoG position within 1 second and its weight within 10 seconds provided that sufficient motion is present to ensure the observability of the parameters. Also, different ways of finding CoG position and the moment of inertia of a spacecraft on the ground were reported in [6].

In this thesis, a new approach to estimate the CoG position based on an All-accelerometers Inertial Measurement Unit (IMU) as proposed in [7] is evaluated and improved.

Having an estimate of CoG position, it then can be transferred to a vehicle management system, such as Active Center of Gravity, that could transfer fuel among the fuel tanks to adjust the position of CoG as required during flight [2], or to update the control approach. In [8], different controllers, namely linear PD, feedback linearization, and adaptive controllers, were tested in controlling a Quadrotor subjected to various disturbances including the change in CoG position where the first two controllers failed to achieve the desired responses.

It is obvious that the change in the position of CoG greatly affects the behavior of air vehicles during maneuvering or disturbances. It sometimes may lead to instability, which will endanger the safety of lives onboard or at least the asset itself in the case of unmanned aerial vehicles (UAV). It is true that adaptive, and robust control schemes can handle such cases in a very good way, but still there is a need to estimate the position of

CoG which will be reflected as more fuel saving and increased maneuverability if the vehicle still controllable. The previous claim depends for sure on the quality of the estimation by which the position of CoG is provided.

For aerial vehicles, measuring the attitude, velocity, and acceleration are one of the important measurements a measuring suite must provide. Although it is true that different types of sensors may be used to measure the same quantity, it is the design requirements that make a certain type favored over others. For attitude measurements, inclinometers and gyroscopes are the first choices most the time. For velocity one may use the accelerometer and integrates its measurements with respect to time to retrieve the velocity provided that the initial velocity is known. Different sensors may be used to measure directly or indirectly the same physical quantity and it is the responsibility of the designer to choose among the available alternatives the best one that meets the requirements.

It is the main focus of this thesis to show how the usage of only linear accelerometers can be possible to retrieve the vehicle's dynamics, hence the name All-accelerometers. It should be noted that it is not intended here, by any means, to set up a comparison between different types of sensors that can be used in navigation. The feasibility of using a certain type of accelerometers in this thesis depends on the precision it can provide as will be stated in Chapter 9.

In general, Inertial Measurement Units (IMUs) are used in aerial vehicles to retrieve the vehicle dynamics, so the better this IMU is, the better the measurement it can provide. As will be shown later in chapter three, most IMUs consist of a number of gyros,

accelerometers, inclinometers, magnetometers that may vary according to the application. The IMU unit is one block within the Inertial Navigation System (INS) that is actually used in navigation, and the fact is clear again: the better the IMU is, the better the INS will be.

In All-accelerometer based IMUs, the only used sensors are linear accelerometers. The accelerometers' measurements are affected by the gravity effect. So in this thesis, the usage of only linear accelerometers to build an IMU that is capable of compensating for varying gravity acceleration without external aids, providing the kinematics of CoG, and providing redundancy on both the elements level and the IMU level is presented.

The previous objectives were formulated in an identification scheme, where the inertial acceleration, CoG kinematics, and acceleration due to gravity are to be determined. Such a problem formulation has not been reported in literature up to the point this thesis has been written as far as the author is aware of.

This thesis is organized as follows:

Chapter two will put forward some important terminology that is used in this work. In addition, Frames used in navigation and the transformation among them will be presented. Finally, the chapter will conclude by providing the dynamics equations that can be used in conjunction with the thesis's results in control design applications.

Chapter three provides a survey of some efforts done so far in the area this thesis is involved in, namely: CoG position estimation, Gravity compensation, and All-accelerometers INS.

Chapter four opens the door in front of the reader to meet the set of dynamic equations used to describe the motion of a rigid body in 3D space, based on the rigid body dynamics theory. In addition, it exposes the usage of SimMechanics library in this work.

Chapter five presents the first main block in this thesis, namely: the development of an IMU based on all-accelerometers method without introducing the gravity effect into the scene, and only an estimation of the position of the CoG along with the vehicle inertial acceleration are shown.

Chapter six will add another piece into the scene, which is the design of different filters which can be used within the proposed IMU to retrieve a better estimation of the vehicle dynamics.

In Chapter seven, the extension of the previous formulation to include gravity effect will be presented. The identification problem formulation presents the estimation of CoG Kinematics, Gravity Compensation, and the Inertial Acceleration of the vehicle is also shown.

Chapter eight will handle the identification problem formulated in Chapter seven in more detail. Different techniques are used and the results are compared to each other.

In Chapter nine, different parts building up the thesis body are brought together and simulation results show the performance of the proposed IMU.

Finally, Chapter ten will propose future extensions for the current achievements and will state some conclusions.

The main objectives of this thesis are listed next:

- 1- Investigate a suitable filter technique to estimate vehicle's angular velocities from All-accelerometers measurements.
- 2- Compensating for the gravity effect which was ignored in [7] and the following will be investigated:
 - a. Gravity compensation without knowing the Center of Gravity (CoG) position.
 - b. Gravity compensation with knowing the Center of Gravity (CoG) position.
- 3- Use different system identification methods to improve the estimation of the position of the Center of Gravity (CoG).
- 4- Investigate the relation between the CoG position and Gravity compensation in an Identification scheme.

CHAPTER 2

AIR VEHICLES NAVIGATION

Navigation can be defined as the ability to move an object between two points provided the information about its acceleration, orientation and time are available. There are basic types of navigation that one may encounter, namely: Pilotage, Dead Reckoning, Celestial, Radio, Radar, and finally Satellite navigation. It is worth noting that these types can be combined to enhance the performance of a particular type.

Inertial navigation is a dead reckoning type of navigation system that computes its position based on inertial motion sensors, i.e. gyroscopes and accelerometers. Once the initial position is provided, the system keeps tracking it through the usage of available inertial measurements. The Inertial Navigation System (INS) is immune against weather changes and it does not depend on external aids in its operation as a basic mean, rather it can be considered as self-contained, so that it cannot be jammed or detected. The most serious problem it has is that its performance may deteriorate with time because of accumulation of errors caused by bias instability and drifts, or due to the numerical technique used to retrieve some variables from their time derivatives [9]. Inertial navigation systems must therefore be frequently corrected using values from some other types of navigation systems.

The main advantages of the Inertial Navigation systems is the fact of being self-contained, undetectable, and immune against signal jamming and unavailability of GPS

information. It is off course evident that other methods still have attractiveness and advantages acting side by side to their disadvantages, but it is for sure not intended in this thesis to make a comparison between different types and techniques available for navigation systems. One may imagine the possibility of having a navigation system that is completely autonomous and still have the ability to fuse data from outside sources to enhance its performance, to justify the importance of such types.

It is clear that for locating an object, a reference is needed which can be inertial “Fixed” or non-inertial “Moving” frame. So, it is a must to describe the frames of reference commonly used in flight navigation and the relations between them.

2.1 Frames of Reference used in Navigation

The main types of frames of reference used in navigation, control, guidance may differ according to the type of object or vehicle being dealt with and the assumptions made too. In some cases, the number of frames used may vary as well, so it is preferable to restrict the context on those types mainly used in air vehicles. The main frames used in flight navigation are the following [10]:

1. The geodetic coordinate system.

The geodetic coordinate system is used in GPS-based navigation. This coordinate system characterizes a coordinate point near the earth’s surface in terms of longitude, latitude, and height (or altitude) denoted by λ , ϕ , and h respectively.

2. The Earth-Centered Earth-Fixed (ECEF) coordinate system denoted by $(O_c X_c Y_c Z_c)$.

3. The local North-East-Down (NED) coordinate system denoted by $(O_n X_n Y_n Z_n)$.

4. The vehicle-carried NED coordinate system denoted by $(O_{nv}X_{nv}Y_{nv}Z_{nv})$

5. The body coordinates system denoted by $(O_bX_bY_bZ_b)$.

It is worth mentioning that the last type is considered to be a non-inertial frame in which the work to be done in this thesis is based upon. It should be clear how the well-defined transformations will serve in moving the analysis from one frame to another especially when it comes to the stage of making the data available for flight dynamic modeling and automatic flight control which are based on both the body and vehicle-carried NED frames.

Figure 1, shows the different frames mainly used in flight navigation and the relationship between them. These frames are described in more detail in Literature, such as [10].

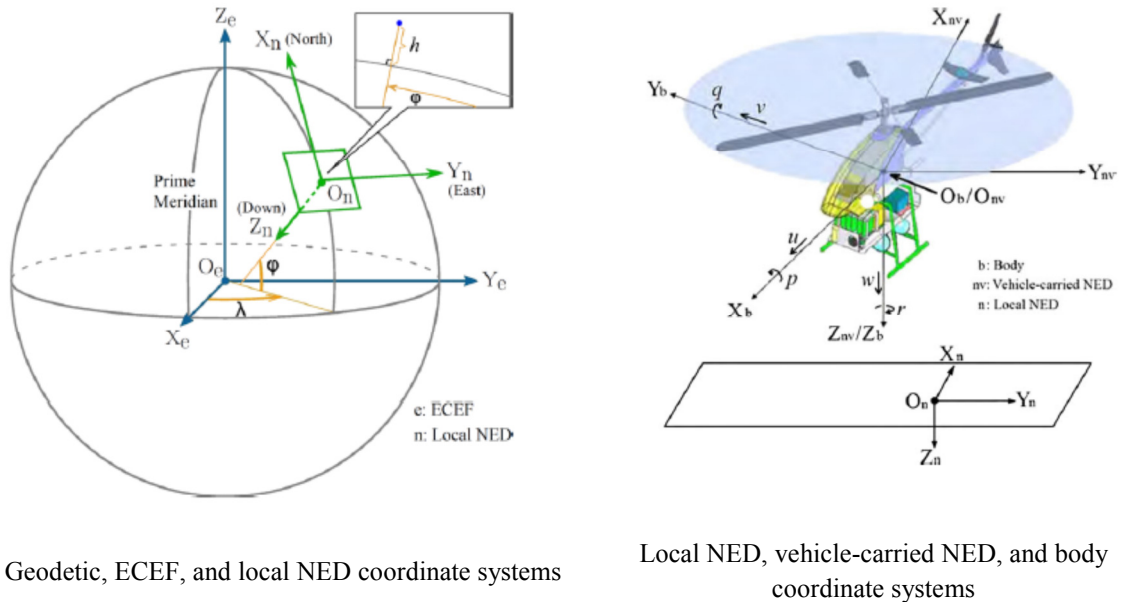


Figure 1: Frames of Reference used in navigation.^[10]

Now, Inertial Navigation Systems are presented in more detail.

2.2 Inertial Navigation Systems

An Inertial navigation System (INS) is a device that uses inertial sensors, i.e. accelerometers and gyroscopes, to continuously estimate the position, velocity, and angular (attitude) rate of the vehicle in which it is installed.

An INS contains the following:

- Dedicated electronics.
- An Inertial Measurement Unit (IMU).
- Navigation computer unit.

A number of gyroscopes and accelerometers are contained in an IMU and they are fastened to a common frame to keep the same relative orientation between them.

The body rotational motion, with respect to inertial reference frame, can be measured using gyroscopes or by a number of linear accelerometers.

There are two types of INS, namely: Gimbaled, and Strapdown.

2.2.1 Gimbaled (Stabilized platform)

This is the main type of INS devices. In such systems, the sensors are fixed to a stabilized platform to isolate them from the vehicle rotational motion. Application need very accurate navigation data are still using this type of INS.

At least three gimbals, as shown in Figure 2, are required to isolate the sensors from the vehicle's rotational motion in 3D space, typically labeled roll, pitch, and yaw (Azimuth)

axes. A mechanism, consists of gimbals and torque servos, is used to cancel out the rotation of stable platform on which the inertial sensors are mounted.

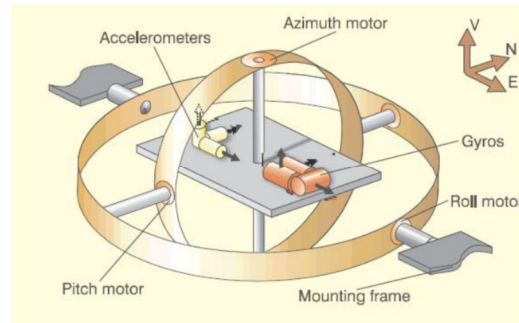


Figure 2: Gimballed INS schematic diagram. ^[11]

The basic principle for stabilized platform is the cancellation of relative orientation with respect to the inertial frame. This approach will serve a lot in reducing the mathematics involved and will allow simpler calculations to be implemented than the Strapdown type. A sensitive angle measuring device is connected to each gimbal and it senses the change in angular position with respect to the stabilized position, i.e. parallel to the inertial frame, and this change is sent to a dedicated control loop that actuates the servo motors responsible of controlling the position of each gimbal. This approach is highly sophisticated and can be considered more accurate than the strapdown approach, so it is still used in many vehicles requiring high navigation accuracy such as ships. The main problem associated with such type, is the possibility of being locked about one axis so no motion about that axis will be measured and a reset process must take place. Other issues to be considered are its high cost and tedious maintainability that requires close attention to its structure and components especially the mechanical ones so an alternative does exist. The INS mechanization of the gimballed type is shown in Figure 3.

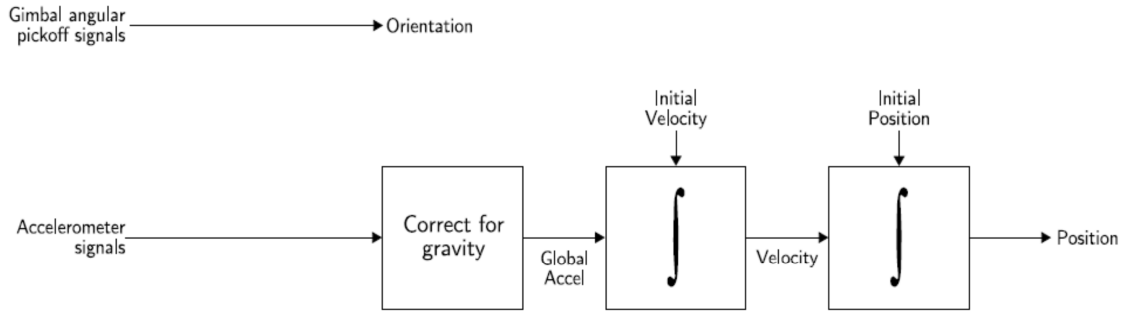


Figure 3: Stable platform (Gimbal) inertial navigation algorithm. ^[12]

2.2.2 Strapdown INS

In order to avoid the mechanical problem associated with Gimbaled type INS, a Strapdown type INS was put forward in which the inertial sensors are rigidly fixed on/in the vehicle frame. Several points must be considered before dealing with such type, such as the mathematics involved, which can be taken care of due the availability of sophisticated Digital Signal Processing (DSP) devices, and the errors associated with MEMS devices that may deteriorates the whole system during flight as time passes. So a compromise will be involved when considering such type of INS at least in the current years since huge advancement is taking place in MEMS industry, that may take it to better level than they are at the moment. During the course of the thesis, extra care will be taken regarding the usage of the linear-accelerometers-based strap down INS in a configuration called: All-accelerometers in which only accelerometers are used and hence the name. It is worth mentioning that this method does not force the usage of MEMS accelerometers, rather it would be only a choice to reduced cost with acceptable accuracy to facilitate the usage of such techniques in small-sized vehicles. Further investigation about the effect of using different types of accelerometers may be a subject by itself

which is beyond the scope of this thesis. A typical strapdown INS fitted in a plane is shown in Figure 4 along with the standard notation ascribed to it by Aerospace community. A block diagram for strapdown INS is also shown in Figure 5, and the INS mechanization of this type is shown in Figure 6.

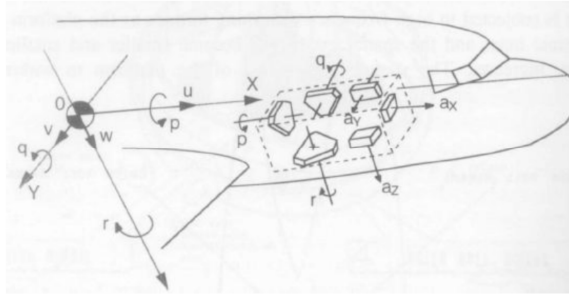


Figure 4: A typical strapdown INS. ^[13]

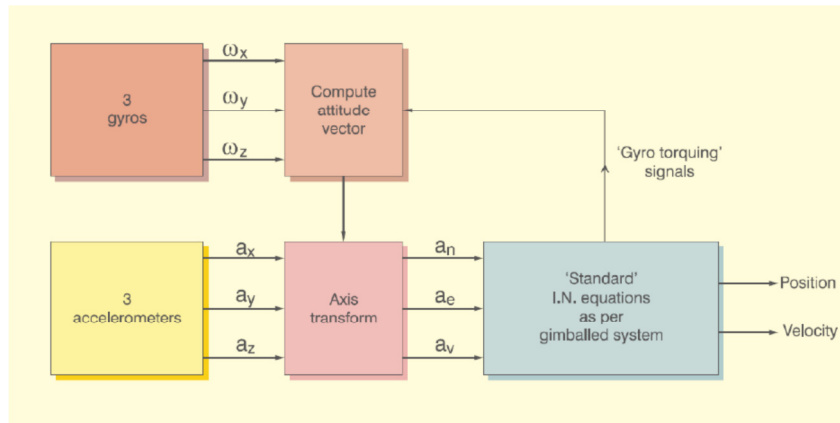


Figure 5: Strapdown inertial navigation unit block diagram. ^[14]

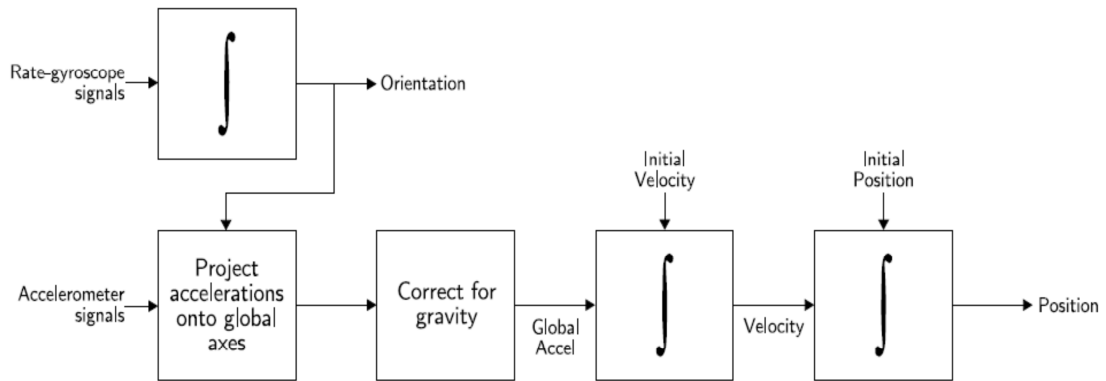


Figure 6: Strapdown inertial navigation algorithm. ^[15]

The following section contains the basic mathematics relating the body frame with the vehicle carried NED frame, the vehicle carried NED frame with local NED frame, and also the relation between the inertial frame and the vehicle carried NED frame. The first and second relations can be further used as an intermediate transformation between the vehicle body frame and the ECEF frame, which then can be transformed into the geodetic frame of reference if the navigation problem is to be solved with respect to it.

In this thesis, only the results obtained in the vehicle body frame will be presented although the complete picture of how the proposed IMU can be used to solve the navigation problem is shown in Chapter 9. Solving the navigation problem in more detail through the integration of the method proposed here can be an extension to the current work as can be found in Chapter 10.

2.3 Flight Navigation Frames Transformations

In this section, some of the important flight navigation transformations will be presented briefly. These relations can be used to facilitate projecting the INS measurements onto different frames and solving the navigation problem.

2.3.1 Transformation between Body (b) and vehicle-Carried (nv) frames

Automatic flight control and the modeling of flight dynamics rely heavily upon this transformation. The translational (1-4) and rotational (5-6) Kinematics relations between these frames respectively are given as follows [10]:

$$\vec{V}_b = \mathbf{R}_{b/nv} \vec{V}_{nv} = \mathbf{R}_{b/nv} \begin{pmatrix} u_{nv} \\ v_{nv} \\ w_{nv} \end{pmatrix} \quad (1)$$

$$\vec{a}_b = \mathbf{R}_{b/nv} \vec{a}_{nv} = \mathbf{R}_{b/nv} \begin{pmatrix} \dot{u}_{nv} \\ \dot{v}_{nv} \\ \dot{w}_{nv} \end{pmatrix} \quad (2)$$

$$\vec{a}_{mea,b} = \mathbf{R}_{b/nv} \vec{a}_{mea,nv} = \mathbf{R}_{b/nv} \begin{pmatrix} a_{mx,nv} \\ a_{my,nv} \\ a_{mz,nv} \end{pmatrix} \quad (3)$$

$$\mathbf{R}_{b/nv} = \begin{bmatrix} c_\theta c_\psi & c_\theta s_\psi & -s_\theta \\ s_\phi s_\theta c_\psi - c_\phi s_\psi & s_\phi s_\theta s_\psi + c_\phi c_\psi & s_\phi c_\theta \\ c_\phi s_\theta c_\psi + s_\phi s_\psi & c_\phi s_\theta s_\psi - s_\phi c_\psi & c_\phi c_\theta \end{bmatrix} \quad (4)$$

$$\begin{pmatrix} p \\ q \\ r \end{pmatrix} = \mathbf{S} \begin{pmatrix} \dot{\phi} \\ \dot{\theta} \\ \dot{\psi} \end{pmatrix} \quad (5)$$

$$\mathbf{S} = \begin{bmatrix} 1 & 0 & -s_\theta \\ 0 & c_\phi & s_\phi c_\theta \\ 0 & -s_\phi & c_\phi c_\theta \end{bmatrix} \quad (6)$$

Where, ($c_{_}$) and ($s_{_}$) denote $\cos(_)$ and $\sin(_)$ respectively, and ($a_{mea,nv}$) is the projection of proper acceleration ($a_{mea,b}$), see (18), measured in the body frame, denoted by subscript b, onto the vehicle-carried NED frame, denoted by subscript nv. The linear acceleration and velocity are denoted using (\vec{a}) and (\vec{V}) respectively. ($[\dot{\phi}, \dot{\theta}, \dot{\psi}]^T$) is the Euler angles rates in vehicle-carried frame, and ($[p, q, r]^T$) is the angular rates in body frame. ($\mathbf{R}_{b/nv}$) and (\mathbf{S}) are transformation matrices. As shown in Figure 6, the previous transformation is essential for Strapdown INS measurements to be projected onto the correct frame in which the navigation problem is to be solved. Before that, the gravity should be compensated for to provide the true kinematic accelerations of the vehicle.

It is obvious that, in all-accelerometers method, the angular velocity estimation is provided through the usage of the available accelerometers' measurements, which are

affected by gravity, to solve nonlinear equations. So and in this case, the gravity compensation must be done before even projecting the measurements onto other frames. This compensation will be the subject of Chapter seven. However, it will be clear that the gravity effect will not affect the estimation of the angular velocity and acceleration and hence it will not affect the vehicle's attitude as well.

2.3.2 Transformation between local (n) and vehicle-carried NED (nv) frames

Under the assumption of aligned local and vehicle-carried NED frames, the transformation between them will be identity, i.e. the kinematics relations for both the translational and rotational motion will be given as follows [10]:

$$\vec{V}_n = \mathbf{R}_{n/nv} \vec{V}_{nv} \quad (7)$$

$$\vec{a}_n = \mathbf{R}_{n/nv} \vec{a}_{nv} \quad (8)$$

$$\mathbf{R}_{n/nv} = \begin{bmatrix} 1 & 0 & 0 \\ 0 & 1 & 0 \\ 0 & 0 & 1 \end{bmatrix} \quad (9)$$

$$\begin{pmatrix} p \\ q \\ r \end{pmatrix} = \mathbf{S} \begin{pmatrix} \dot{\phi} \\ \dot{\theta} \\ \dot{\psi} \end{pmatrix} \quad (10)$$

$$\mathbf{S} = \begin{bmatrix} 1 & 0 & 0 \\ 0 & 1 & 0 \\ 0 & 0 & 1 \end{bmatrix} \quad (11)$$

2.3.3 Relation between vehicle-Carried (nv) and Geodetic (g) frames

In this section, the relation between vehicle-carried and geodetic frames is presented. These equations are essential when considering the GPS-All-Accelerometer aided INS.

Specifically, the relation between the geodetic position derivative and the vehicle-carried velocity which is given as follows, neglecting the earth self-rotation [10]:

$$\dot{\lambda} = \frac{v_{nv}}{(N_E + h)\cos\varphi} \quad (12)$$

$$\dot{\varphi} = \frac{u_{nv}}{M_E + h} \quad (13)$$

$$\dot{h} = -w_{nv} \quad (14)$$

$$\dot{u}_{nv} = -\frac{v_{nv}^2 \sin\varphi}{(N_E + h)\cos\varphi} + \frac{u_{nv}w_{nv}}{M_E + h} + a_{mx,nv} \quad (15)$$

$$\dot{v}_{nv} = \frac{u_{nv}v_{nv}\sin\varphi}{(N_E + h)\cos\varphi} + \frac{v_{nv}w_{nv}}{N_E + h} + a_{my,nv} \quad (16)$$

$$\dot{w}_{nv} = -\frac{v_{nv}^2}{N_E + h} - \frac{u_{nv}^2}{M_E + h} + g + a_{mz,nv} \quad (17)$$

$$a_{mea,nv} = \begin{pmatrix} a_{mx,nv} \\ a_{my,nv} \\ a_{mz,nv} \end{pmatrix} \quad (18)$$

$$P_g = \begin{pmatrix} \lambda \\ \varphi \\ h \end{pmatrix} \quad (19)$$

$$M_E = \frac{R_{Ea}(1 - e^2)}{(1 - e^2 \sin^2 \varphi)^{3/2}} \quad (20)$$

$$N_E = \frac{R_{Ea}}{\sqrt{1 - e^2 \sin^2 \varphi}} \quad (21)$$

$$e = 0.08181919 \quad (22)$$

$$R_{Ea} = 6,378,137.0 \text{ meter} \quad (23)$$

Where, (g) is the acceleration due to gravity, and (P_g) is a point in the geodetic system represented by longitude (λ) , latitude (φ) , and height (altitude: h). According to WGS 84, (M_E) and (N_E) are the meridian and the prime vertical radii of curvature respectively. (e) is the first eccentricity.

2.4 Flight Dynamics Equation

In [16], the flight dynamic equations of motion for a rigid body were derived referenced to an arbitrary point (\mathbf{A}) not necessarily its center of mass. They explicitly include the change in the position of center of mass (equivalent to center of gravity in a uniform gravitational field), so that its effect can be reflected onto the control law of the flight dynamics. This change is estimated by the proposed IMU. The equations are given as follows [16]:

$$\begin{aligned} \sum \vec{F}_x = m(\dot{U}_A + \Omega_y W_A - \Omega_z V_A - (\Omega_y^2 + \Omega_z^2)\Delta x_b + (\Omega_x \Omega_y - \dot{\Omega}_z)\Delta y_b \\ + (\Omega_x \Omega_z + \dot{\Omega}_y)\Delta z_b + g \sin \theta) \end{aligned} \quad (24)$$

$$\begin{aligned} \sum \vec{F}_y = m(\dot{V}_A + \Omega_z U_A - \Omega_x W_A + (\Omega_x \Omega_y + \dot{\Omega}_z)\Delta x_b - (\Omega_x^2 + \Omega_z^2)\Delta y_b \\ + (\Omega_y \Omega_z - \dot{\Omega}_x)\Delta z_b - g \cos \theta \sin \phi) \end{aligned} \quad (25)$$

$$\begin{aligned} \sum \vec{F}_z = m(\dot{W}_A + \Omega_x V_A - \Omega_y U_A + (\Omega_x \Omega_z - \dot{\Omega}_y)\Delta x_b + (\Omega_y \Omega_z + \dot{\Omega}_x)\Delta y_b \\ - (\Omega_x^2 + \Omega_y^2)\Delta z_b - g \cos \theta \cos \phi) \end{aligned} \quad (26)$$

$$\begin{aligned}
\sum M_{Ax} &= I_{xx}\dot{\Omega}_x - I_{xy}\dot{\Omega}_y - I_{xz}\dot{\Omega}_z + I_{xy}\Omega_x\Omega_z - I_{xz}\Omega_x\Omega_y + (I_{zz} - I_{yy})\Omega_y\Omega_z \\
&\quad + (\Omega_z^2 - \Omega_y^2)I_{yz} \\
&\quad + m \left((\Omega_x V_A - \Omega_y U_A + \dot{W}_A - g \cos \theta \cos \phi) \Delta y_b \right. \\
&\quad \left. + (\Omega_x W_A - \Omega_z U_A - \dot{V}_A + g \cos \theta \sin \phi) \Delta z_b \right)
\end{aligned} \tag{27}$$

$$\begin{aligned}
\sum M_{Ay} &= -I_{xy}\dot{\Omega}_x + I_{yy}\dot{\Omega}_y - I_{yz}\dot{\Omega}_z + I_{yz}\Omega_x\Omega_y - I_{xy}\Omega_y\Omega_z + (I_{xx} - I_{zz})\Omega_x\Omega_z \\
&\quad + (\Omega_x^2 - \Omega_z^2)I_{xz} \\
&\quad + m \left((\Omega_y U_A - \Omega_x V_A - \dot{W}_A + g \cos \theta \cos \phi) \Delta x_b \right. \\
&\quad \left. + (\Omega_y W_A - \Omega_z V_A + \dot{U}_A + g \sin \theta) \Delta z_b \right)
\end{aligned} \tag{28}$$

$$\begin{aligned}
\sum M_{Az} &= -I_{xz}\dot{\Omega}_x - I_{yz}\dot{\Omega}_y + I_{zz}\dot{\Omega}_z + I_{xz}\Omega_y\Omega_z - I_{yz}\Omega_x\Omega_z + (I_{yy} - I_{xx})\Omega_x\Omega_y \\
&\quad + (\Omega_y^2 - \Omega_x^2)I_{xy} \\
&\quad + m \left((\Omega_z U_A - \Omega_x W_A + \dot{V}_A - g \cos \theta \sin \phi) \Delta x_b \right. \\
&\quad \left. + (\Omega_z V_A - \Omega_y W_A - \dot{U}_A - g \sin \theta) \Delta y_b \right)
\end{aligned} \tag{29}$$

Where, $(\Delta p = [\Delta x_b, \Delta y_b, \Delta z_b]^T)$ is the change in the position of CoG (\vec{P}_c) in the body frame, (F) and (M) denote the force and moment respectively. (I) and (m) denotes the inertia matrix and the mass of the object respectively. $(\vec{\theta} = [\phi, \theta, \psi]^T)$ is the Euler angles, $(\vec{\Omega} = [\Omega_x, \Omega_y, \Omega_z]^T)$ denotes the angular velocity of the object, $(\dot{\vec{\Omega}} = [\dot{\Omega}_x, \dot{\Omega}_y, \dot{\Omega}_z]^T)$ denotes its angular acceleration, and finally $(\vec{v}_A = [U_A, V_A, W_A]^T)$

represents its linear velocity. Equations (24-26) can be given in a compact form as follows:

$$\sum \vec{F}_A = m(\dot{\vec{v}}_A + \vec{\Omega} \times \vec{v}_A) + \dot{\vec{\Omega}} \times m\Delta p + \vec{\Omega} \times (\vec{\Omega} \times m\Delta p) + \vec{W} \quad (30)$$

$$\text{Where, } \vec{W} = [\sin\theta, -\cos\theta\sin\phi, -\cos\theta\cos\phi]^T g$$

Also, Equations (27-29) can be given in a compact form as follows:

$$\sum \vec{M}_A = I\dot{\vec{\Omega}} + \vec{\Omega} \times I\vec{\Omega} + m\Delta p \times \dot{\vec{v}}_A + m\vec{\Omega} \times (\Delta p \times \vec{v}_A) + m\vec{v}_A \times (\vec{\Omega} \times \Delta p) - \Delta p \times \vec{W} \quad (31)$$

$$\text{Where, } I = \begin{bmatrix} I_{xx} & -I_{xy} & -I_{xz} \\ -I_{yx} & I_{yy} & -I_{yz} \\ -I_{zx} & -I_{zy} & I_{zz} \end{bmatrix}$$

Equations (24-29) provide the starting point when the mass and Inertia of the vehicle are to be found as will be stated in Chapter 9.

2.5 Summary

This chapter presented the needed mathematical relations between the flight navigation frames mainly used in aerospace applications and also presented the kinematics and dynamics of an air vehicle which can be used once this work is extended, see Chapter 9.

The block diagram shown in Figure 7 shows how the proposed IMU may fit within a complete aeronautic system, where $(\vec{L} = [\vec{p}_c, \vec{v}_c, \vec{a}_c]^T)$ denotes the kinematics of CoG, $(\vec{a}_A = \dot{\vec{v}}_A)$ is the linear acceleration of the vehicle at point (A), and finally any vector with subscript denoted by (v/c) resembles that this vehicle's dynamical variable was obtained when taking the CoG as the reference, and if it is subscripted by (v/A) it indicates that

point (A) is the reference. This IMU apparently provides more useful information than the traditional IMUs, and it should be kept in mind that it is the responsibility of the INS system to handle the needed transformations among those variables to provide them in the right frame.

The previous description of the proposed IMU was only the first thought once this thesis was started. In Chapter 9, it will become clearer that the proposed IMU reach the stage where it can be considered a complete INS by itself.

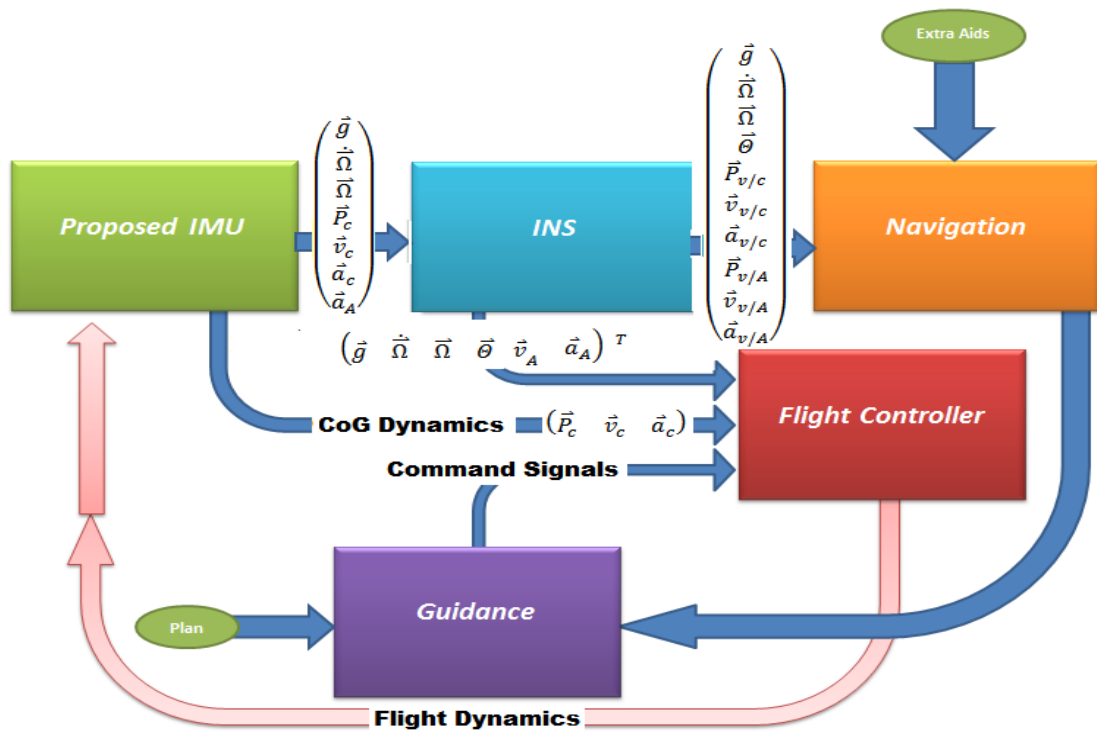


Figure 7: Block diagram and the ideal features of the proposed IMU.

CHAPTER 3

LITERATURE REVIEW

In this chapter, the work done in investigating the field of this thesis and the work previously reported in literature is presented. It was organized into categories under each one of them the related references are included. It is true that some of those references may include topics from other's categories, so that they were organized according to the main point of interest each one has. Figure 8 shows the spectrum of the selected references over years.

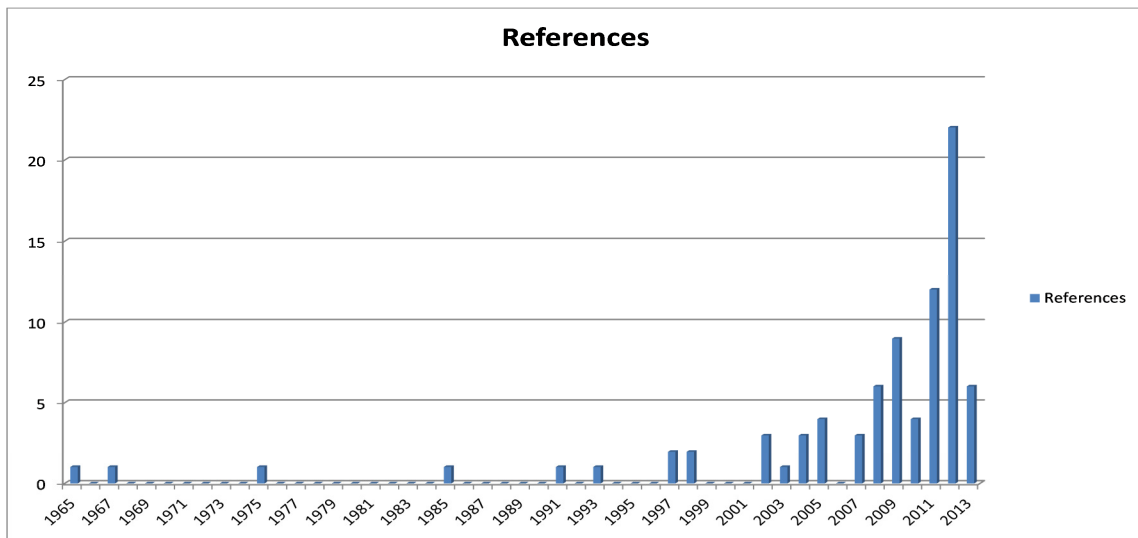


Figure 8: References spectrum related to INS.

3.1 Thesis background

The following, contains the main part of the literature review done during the preparation phase for this thesis, which was intended to establish a deep understanding of all-

accelerometers based IMUs and the problems associated with it. Although not all the references are directly related to the objectives of this thesis, they still of value since they may form a starting point for future work and the extension of the proposed method so that further improvement will be involved when considering the problems found in literature. While in progress, new references in certain topics were added and they are referred to in the appropriate places.

3.2 INS Aided Systems

In many applications, it is not sufficient to depend only on the Inertial Navigation System (INS) for a long period of time; because it is subjected to drift that propagate with time. So, it is usually aided with other navigation sensors that may vary in number and type according to the application of concern.

In [17], the limitations found in the Kalman Filter (KF) and smoothing techniques found in INS/GPS are analyzed. In order to overcome these limitations, an on-line smoothing method was proposed, and field tests showed that its results were better than those obtained using Kalman Filter in about 60%.

In [18], the Hemispherical Resonator Gyro (HRG) was discussed. A milli-HRG has been accomplished that withstands a wide range of temperature from +5 to +50 °C. This milli-HRG can provide precise INS with lowered bias stability (0.00035°/hr) and angular Random Walk (ARW) of (0.0003°/√hr). So, it can hold the altitude performance over extended time duration and can be used in applications that require fast time response; since its alignment time is very short.

In [19], an invariant observer approach was applied to an aided-INS consists of magnetometer and GPS. Extended Kalman Filter (EKF) is usually used for such systems where the error dynamics are non-linear, then the equations are linearized and a Kalman Filter for the linearized model is built. Invariant observer, recently introduced, used to obtain a non-linear structure which possesses the same symmetries as the original model in a systematic way.

Invariant observer combined with invariant EKF methodology is more robust than a conventional EKF which makes it suitable for a large variety of applications.

In [20], a localization approach for an Omni-directional Automatic Guided Vehicle (AGV) with Mecanum wheels was proposed. The encoder attached to the Omni-wheels cannot be used because of the large slip the wheel experiences while in side motion. So, the encoder were used along with a gyro and accelerometer which proved to be efficient.

In [21], a combined system of GPS, Omnidirectional Vision sensor, Odometer, and INS was presented. A wide field of view can be obtained using Omnidirectional Vision sensors. This system was used with a ground vehicle to make its navigation possible in case of extended periods of GPS outage. Experiments showed that this approach can reduce the position, velocity, and attitude accumulation errors during GPS outages.

In [22], stereo visual odometry, and IMU were fused together using Kalman Filter to enable a Quad-Rotor UAV to navigate in an indoor environment where GPS signal is

weak or unavailable. Necessary equations of motion of the Quad-Rotor, along with the Kalman design process were shown. Both altitude and Yaw angle were stabilized using PD controllers. Flight tests showed the effectiveness of this approach.

In [23], a self-contained dynamics-aided error correction method was developed and used to correct the rapid drift occurring in Inertial Navigation Systems (INS) when aiding sensors, such as GPS, are not available. This method uses the dynamic equations of the carrier vehicle, i.e. land vehicle in this case, for updating the Kalman Filter, responsible of navigating the vehicle, when the main source of aiding the information is unavailable.

Vehicle dynamics were identified using an expert system based on fuzzy logic according to this method. The position accuracy was increased to about 15 m in field tests with GPS signal was not available for about 3 minutes when using the proposed method, which is small once compared to the unaided case which has an error larger than 100 m.

3.3 Calibration

In [24], a low-accuracy turn table was used to determine the parameters of a mathematical model of instrument errors of strapdown INS. The algorithm used here has a distinguished feature such that the characteristics of the turn table sensors are not directly used in it.

In [25], a fast and inexpensive method for calibrating an accelerometer-array is proposed, which can estimate the accelerometers' offset, scale factors, sensitive direction, and position on a rigid body. This method guarantees that the estimated accelerometers-array

parameters are globally optimum in the least-squares sense. It was experimentally tested and it showed that when it is used to compute the angular velocity of a rigid body from the acceleration measurements, the error can be significantly reduced. It is mainly composed of two steps, namely static and dynamic calibrations, where the dynamic calibration step do not add much to the results obtained in the static calibration.

In [26], a multi-position calibration method, which does not require the precise alignment of sensors with either local level frame or to the vertical direction, of a low-cost MEMS-based INS is described and discussed. This method is fast and efficient since the accelerometers' results converged rapidly. Bias and scale factors were found.

In [27], all-accelerometers INS method was implemented and fused with the vehicle dynamics using a Kalman filter to estimate true values. This method was tested in a 2-D motion and it gave reasonable results where the drift effect in velocity and position were reduced.

3.4 Errors

In [28], shearer dynamics positioning used in coal mining is discussed and analyzed. The usage of strapdown INS is suitable for such environment where the usage of other aiding devices is hard or impossible. The accuracy of the shearer positioning depends on the error value introduced by the following sources:

- Accelerometers and Gyroscopes drift errors.
- Vibration during operation which introduces acceleration and angular velocities.
- Truncation errors in attitude calculations.

- Initial alignment error of INS compared to the reference axes.

This paper only focused on the alignment problem, so a non-linear filter was used in initial alignment based on the shearer misalignment angle. A quaternion method rule was established to compensate for alignment errors found in INS and the derivation of non-linear EKF was shown.

In [29], an algorithm capable of compensating the biases of angular-rate sensors was presented. This algorithm integrates inertial sensors, GPS, magnetometer, and barometric altimeter. It was used mainly for low-cost Unmanned Aerial Vehicles (UAVs). The equations needed to retrieve vehicle attitude, velocity, and acceleration were derived using Euler-Rodrigues parameters.

3.5 Faults

In [30], an all accelerometers based, fault-tolerant IMU that consists of 13 single-axis linear accelerometers is presented. It uses a combination of redundant accelerometers, identification technique to identify faults, and a state-estimator to enable taking 6-DOF measurements. The initial value problems faced traditionally in almost all IMU is solved here by presenting an observer, where the issue of observability was also covered.

In [31], a fault-tolerant optimal robust filter for linear discrete time-varying systems is proposed. The algorithm solves Linear Matrix Inequality (LMI) to obtain the optimal robust H_∞ estimator, and uses H-index to maximize the minimum effect of faults on the

residual output of the filter. This makes the system robust to disturbances, and at the same time, sensitive to faults.

The Robust Fault-Detection Filter (RFDF) was investigated for Linear Discrete Time Variant (LDTV) systems and a simulation example proved the claims.

In [32], a method based on Least Absolute Deviations (LAD) for dynamic systems was used to detect jumps in the bias signal of gyros in INS. LAD is claimed to be more accurate, for the same purpose, than Kalman filter combined to least-squares method.

3.6 Build INS

In [33], an INS using one 3-axis rate gyro and three 2-axis linear accelerometers were used. Error analysis was implemented based only on accelerometers' position error and other sources of error were not investigated. The gravity was compensated using a 2-axis inclinometer.

In [34], a strapdown INS algorithm was developed using Geometric Algebra (GA). This method resulted in kinematic equations that can be solved using differential equation methods. Despite being stable for high-maneuver applications; it is very sensitive to the measurement noises, so a proper GA-based filtering algorithm is needed.

In [35], an instrumental error evaluation and optimization algorithm has been proposed. The result of testing this algorithm on several different benchmarks showed its good accuracy and efficiency for choosing the optimal sequence of elementary operations

execution (i.e. multiplication, division, etc.) and for the instrumental error estimation. This algorithm was used to increase the accuracy of a six single-axis accelerometer array used to build a gyro-free IMU. The minimum number of bits of the computation engine required was reduced from 16-18 bit to 13-14 bit with the same total instrumental error value.

3.7 Dead Reckoning

In [36], an approach which integrated the location estimation using Dead Reckoning techniques in step-based pedestrian navigation is addressed. GPS and INS information can be fused together through the usage of EKF which showed to be less efficient compared to a particle filter when both are used to extract navigation information from the same setup. Different types of Distance sensing devices were mentioned and a brief description for each one of them was included.

3.8 Center of Gravity Change

The position of Center of Gravity (CoG) is of great importance; since the attitude of the air vehicle is affected by the position of CoG. It is designed to be kept within certain limits known as “CoG limits”. A drastic change beyond those limits may drive the vehicle towards instability. So it is important to know how exactly this change will affect the maneuverability of the vehicle and towards what extent it can deteriorate its controllability.

In [8], an adaptive tracking controller based on output feedback linearization that compensates for dynamical changes in the center of gravity of the quad rotor was presented. The stability of the controller was proven using Lyapunov theory.

In [37], a spacecraft center of mass was estimated online using multi-accelerometers under the assumption of zero linear acceleration when the spacecraft is in steady mode and the position of center of mass is not changing, then the equations of motion can be very much simplified and the position of center of mass was estimated using a recursive least squares method.

In [6], different ways of finding the CoG position and finding the moment of a space craft on the ground were introduced. It explains the parallel axis theorem and how to use it in finding the inertia of a space craft.

3.9 ALL-Accelerometers Method

In [38], angular velocity/acceleration, and linear acceleration of a rigid body were obtained using simple matrix operation. The positioning of the four accelerometers in a frame was discussed and the sign ambiguity in angular velocity was solved. This method uses four 3-axis accelerometers, not installed at the CoG, and without gyros. Neither numerical integration nor differentiation was used, and the resulting angular velocity is bounded with no drift. Gravity effect was ignored.

In [39], an IMU was built using MEMS to find angular velocity/acceleration, and linear acceleration of a rigid body. It consists of two 3-axis accelerometers and a gyro. The alignment process is needed to remove the misalignment and the errors were analyzed. As in [38], neither numerical integration nor differentiation was used, and there was extra measurements but never been used. Different schemes for accelerometers distribution were considered and their effect on the invertibility of the structure matrix was examined.

The effects of sensors alignment, position, and instrumental errors were explored. Gravity effect was ignored.

In [40], the design, and calibration of IMU based on twelve 1-axis accelerometers were presented. The location and direction of these sensors are determined by optimizing the numerical condition number of structure matrix. Also, orientation installation errors of each sensor are identified, and angular velocity was obtained without integration. This method was more general than the previous methods; since it allows (m) number of accelerometers to be included, although it used 12 for a specified structure. Redundancy is mentioned but not utilized, and the angular acceleration tensor was obtained without differentiation and the gravity effect was removed.

In [41], differential sensing was used to cancel the contribution of gravity in the accelerometers' measurements. It is based on integration, and the error analysis was carried out.

In [42], Einstein well-defined principle was argued, showing that the gravity acceleration can be separated from body acceleration from within the accelerometers' measurements. A mathematical model relating gravity and motion was derived, and it states clearly that 6 accelerometers are enough.

In [43], angular velocity and linear acceleration were found using only three 1-axis accelerometers. Various types of deterministic misalignment errors were investigated, and sampling rate was found to affect the algorithm.

In [44], it was also found that, as in [52], only 6 accelerometers are required to completely define the kinematics of a rigid body, and it showed when this method can fail in practice so a nine accelerometers-based method was devised where it showed to be stable and superior compared to other methods. Gravity effect was ignored.

In [45], different configurations of linear accelerometers were tested and the corresponding IMU mechanization equations were derived which was not shown in other resources.

In [46], a gyro-free (all-accelerometers) IMU design was presented, where the position and orientation of the sensors were identified through a calibration scheme. An unscented Kalman filter (UKF) was used to fuse the angular acceleration and angular rate measurements to remove the ambiguity in the angular velocity sign. Measurements using a 3-D rotation table were collected, and an improvement in the results was clear.

Interestingly, it showed that out-of-plan accelerometer resulted in lower accuracy so this has to be checked when dealing with such configuration such that found in [7]. Also, the calibration procedure was unable to compensate for non-ideal sensor characteristics; simply because the sensor's model does not include them.

In [47], a constrained unscented Kalman filter (UKF) was designed to estimate the angular motion of a rigid body using all-accelerometers IMU. The results obtained were better than those obtained from an ordinary UKF; since it was not sensitive to drift errors. Gravity effect was ignored.

In [48], the feasibility of designing all-accelerometers based INS using accelerometers' measurements only to compute the angular velocity/acceleration, and linear acceleration of a rigid body was investigated and conditioned. The effects of accelerometers locations' errors were analyzed, and an algorithm that identifies and compensates these errors was developed.

In [49], the minimum number of single axis accelerometers used to implement the algorithm was nine, and the accelerometers used must not be collinear. Also, it showed the reasons why gyroscopes are avoided and replaced by accelerometers, and suggested using a mathematical integration method that does not depend on time, namely the square-rooting of the centripetal acceleration. At the end, it was recommended to keep the installed gyroscopes, in the UAVs under study, and not to replace them with accelerometers since the later did not give the expected accuracy obtained when using the gyroscopes for a 1 m wingspan UAV.

The error equations introduced can be used to compare an all-accelerometer design with an angular-rate sensor design.

3.10 Alignment

One, Two, and Three-axis accelerometers are available in the market and these components are used to build MEMS-based INS. At the micro-scale, the mass comprising each axis has misalignment, and on the IMU level the whole accelerometer package has misalignment and disorientation with respect to the assembly axes. It is the essence of INS built using these components to have the sensitive axis for each accelerometer aligned exactly with the assembly principle axis along which the acceleration is to be measured. Practically speaking, this is not possible so a compensation for any deviation from the ideal case has to be included to correct the readings from the all-accelerometer IMU. It is not to be mistakenly thought that no alignment is needed at the assembly stage, rather it is needed before assembly (coarse alignment), and after the assembly at the IMU level. Installing the INS on the Vehicle body needs another calibration (coarse and/or fine) to know the transformation matrix needed to compensate for the deviation from the vehicle body coordinate system. The appreciation of the alignment process will be enough, if it is known that even a 0.01° will result in large deviation in position in some cases when it is projected to the vehicle body coordinate system as time passes.

In [50], an initial alignment error model for in INS on a stationary base was derived based on lyapunov transformation. A drift estimator was implemented to remove the drift found in inertial sensors. A standard Kalman filter and a Multi-objective filter to deal with certain model and Gaussian noise, and with uncertain, non-Gaussian noise respectively.

In [51], a Lyapunov transformation was used this time to show the equivalence of strapdown INS (SINS) and Gimbal INS (GINS). Using this transformation, the results obtained when analyzing GINS errors can be applied to INS. It also shows that the INS is not completely observable, so a linear transformation is used to establish an observable subspace, thus the observable states and unobservable ones of INS error model can be dynamically decoupled.

In [27], an innovative estimation scheme to solve the initial and divergent problems for an all-accelerometers INS is presented. It also can provide an upper bound to initiate the platform attitude. Recursive least-squares (RLS) method was used to solve the problem of initial and divergent associated with all-accelerometer method. The velocity and position of the ship were estimated through the usage of Kalman filter.

In [52], a non-linear model for large initial azimuth alignment error for strapdown INS was derived. The accuracy of attitude error estimation using the unscented Kalman filter (UKF), the extended Kalman filter (EKF), and the 2nd order divided difference filter (DDF2) was determined showing the superiority of DDF2 over UKF, and EKF.

In [53], a marginalized unscented Kalman filter (MUKF) is proposed to deal with large initial alignment errors in strapdown INS under marine mooring condition. It was compared to Unscented-Kalman filter (UKF), and Extended-Kalman filter (EKF), and it showed through experiment and simulation that MUKF can achieve at least, if not better, a comparable results to traditional UKF at a considerable reduced computation. It used the same error model found in [52].

In [54], in a previous reference, alignment was done on a stationary base but in some cases this will not be the case; consider a car engine is started, or a plane preparing to take off, so there is a need to investigate the ability of doing the alignment under such conditions. In this paper, the vibrations' effects are treated as noises, so that they will not appear in the system and measurement matrices. Doing that, the fine alignment on a vibrating base on the ground can be done quickly and accurately.

In [55], the alignment of SINS is done during flight in such a way that the carrier aircraft (CA) provides the auxiliary information to the UAV in a scheme called In-Flight Transfer Alignment (TA) which requires usually about 10 minutes and the carrier aircraft is required to perform an S-turn maneuver. Usually, in TA only the velocity of CA is transferred to UAV, while in this paper, both the velocity and attitude information of CA were transferred to UAV resulting, as shown from the simulation results, in a better accuracy and reduced time interval for alignment process.

In [56], a fast and accurate stationary alignment method for SINS is proposed based on two-position alignment principle. The main difficulty associated with the self-alignment technique is that the system is not completely observable which can be solved using this method. Observability analysis was done and a model for the alignment error was derived.

The foundation of [56] is established in [57].

3.11 Numerical Methods

Almost all Inertial Navigation Systems needs to use integration at some point, which raise the concern about which integration method should be used. References [61-62] introduce interesting methods. In [58], it shows the numerical double integration of the noisy accelerometers measurements to extract the position information for which the error is proportional to the square root of the integration time cubic, and inversely proportional to the square root of the sampling frequency.

In [59], the error of real time numerical integration in INS was decreased using a method called “Subtractive Composite Simpson Method” (SCSM) which depends on Simpson’s 1/3 and 3/8 rules. The main disadvantage for this method is the huge consumption of memory since it requires all the sample from the beginning of the integration, so as a way around this defect it is combined with a 4th order Runge-Kutta method since it is stable and simple, but unfortunately its error also accumulate over time although it solves the memory consumption issue.

Interestingly, [49] promotes the usage of Square-Rooting the Centripetal Acceleration method which does not depend on time. The main problem with this method is that the error-bound blows up when the denominator is zero, so a combination between the previous methods is advised.

As in [60], a Kalman filter is used to avoid integrating the angular acceleration numerically to find the angular velocity.

3.12 Performance

In [60], the redundant IMUs with different sensor configurations were analyzed. Redundancy will increase the reliability of IMU measurements for extended period of time. This reliability is increased if a suitable geometric configuration for a given number of redundant sensors is achieved. This paper presents a general derivation to obtain such a configuration. It also gives information about the way to calculate the reliability of a sensor distribution, mean time to fail, performance index, geometric dilution of precision, and reliability.

In [61], the solution of the spacecraft navigation problem in the near-Earth space was presented. It means the determination of the coordinates, velocities, and orientation with respect to the navigation coordinate system (geocentric, geographical, or geodetic). SINS use data of the following types:

- Measured or Inertial data: from accelerometers and Gyros.
- Initial conditions determined during alignment.

Lately, Gravity Gradiometry and INS were combined together allowing the precise determination of gravitational field parameters and to solve the navigation problem as well. This system can be useful for flight to planets of the solar system whose gravitational field is known with low precision. The SINS dynamics with errors were derived in detail and a numerical analysis of its operation and errors were done, which helps in making the decision on inclusion or exclusion of the corresponding terms from the considered error model upon designing a navigation system, based on the estimation of higher order of smallness in error equations.

In [62], Error dynamics of all-accelerometers based IMU were analyzed. A compensator for each accelerometer was used to remove its scale error and bias found in its measurements. The configuration error caused by location and orientation errors can be compensated as well.

A larger cube (One configuration) achieves higher angular acceleration accuracy but structure flexibility may then contribute as an error source, while a small cube makes the accelerometers more sensitive to noise, so higher resolution accelerometers must be used. This approach does not involve integration of the angular acceleration numerically so it limits the growth of the angular rate error.

3.13 Simulation

Simulation plays an important role in many applications, and navigation is not an exception. Zhang, et al in his paper [63] used MATLAB and Simulink to build a free open-source simulation environment for testing the strapdown INS (SINS). This platform deals with air-vehicles in particular where six flight routines were used to validate this model, namely static, circle, line, s-shape “required for alignment procedure”, and two sets of real static data.

3.14 Testing

In [64], the methods and procedures used to check strapdown INS (SINS) device are presented. These methods and procedures are used to check the errors in SINS output orientation parameters under rolling, pitching, and yawing. It also estimate the accuracy of SINS alignment on a test bench and the accuracy of the test bench itself, so that the

errors generated to the test procedures can be calculated showing the real results of the SINS device.

3.15 Data Fusion

Having multiple sources for same/related data can be considered crucial for validating, error and fault detection, but at the same time if this information is not processed correctly, it may lead to erroneous results and conclusions. Data Fusion is one of the techniques used to deal with multiple data sources, which have the ability to combine it and increase the reliability and confidence in the measurements when it is implemented on sensors. Redundancy is one factor that may invite the usage of data fusion. In [7], the data fusion is described on the ring level and it is used to validate measurement and to detect faults at the same time, but no algorithm what so ever is described about the fusion of data between redundant rings.

Allerton, et al [65], described data fusion algorithms for inertial network systems that can be used for [7] at the ring level and at the redundant rings level. In his paper, he stated that these algorithms will increase the accuracy of estimates of inertial state vectors in all the network nodes including the navigation states. They also improve the fault-tolerance of inertial network system. Dynamic alignment and Calibration of distributed inertial systems is also a feature of these algorithms.

This paper focuses on the IMU level, so it does not consider the gravity compensation, and accelerometers/gyros errors and it also consider an ideal communication channels

which is not the case in real avionic data buses, so it is maybe worth investigating the effect and robustness of such algorithms in the case of drop-packets and latency.

One more thing to add, is that these algorithms depends on the fact that the center of gravity is well-known beforehand so that the master node will be fixed there against which all other slave nodes will align and correct themselves, a fact that can misled the system especially in varying center of gravity location.

3.16 Implementation

Implementing INS algorithm using hardware is one of the factors that affect the performance of INS device/algorithm. It is true that the inertial sensors play significant role in obtaining the dynamical states of a rigid body, as well as the hardware that does the signal acquisition and processing. Embedded computers facilitate the implementation of INS using a compact platform instead of bulky devices. Since the results of a navigation algorithm depends on the measurement, it is essential to consider the acquisition rate, processing time, round-off/truncation errors, the processing, and the computational power needed. Sequential execution consumes more time than parallel execution where the latter is more complex since of mutual dependency on variable in multiple threads may exist. Ordinary digital signal processing hardware, or for short DSP, is a good candidate for INS implementation but it lacks the parallel thread capabilities. Field Programmable Gate Array (FPGA) provides an alternative for the DSP devices in such cases [66].

The introduced complexities due to FPGA are analyzed in [66], and it is well-known that better performance may sometime result in more complex implementations.

3.17 INS Mechanization

Oliver J. Woodman [67], in his technical report “Introduction to inertial navigation”, did a great work starting from analyzing the MEMS components used mainly in most Strapdown INS (SINS), namely: gyroscopes and linear accelerometers, till modeling one of the INS devices available in the market, i.e. XSens Mtx device. It was shown that the accuracy of a gyro which limits the INS accuracy in general.

During the literature review phase of this thesis, a complete comparison between ordinary IMU (containing a gyro) and all-accelerometers (gyro-free) methods was not found.

3.18 Patents

Four patents were investigated, and the main objective of this thesis is to investigate [7] in more detail. Three of those patents were concerned about finding the position of center of gravity during flight; since it has direct impacts on the quality, stability, controllability, and maneuvering capabilities if immigrated outside its limits, known as “CoG limits”. Patents [68] and [69] are somehow simple; since they do not offer robustness or corrections against faults, while [7] is well-designed so it is capable to show some robustness against faults and some errors, while Patent [70], deals with the faults by introducing redundant units interacting with each other to form a fault-tolerant scheme.

CHAPTER 4

SIMULATING RIGID BODY DYNAMICS

In this chapter, the basic dynamic equations used to formulate the work in this thesis are presented. Despite being simple, they still have the potential to render the work done here possible and valuable, Thanks to ALLAH. The implementation of these equations was done using the SimMechanics library side by side with other MATLAB and Simulink features. In chapter five, the method presented in [7] is simulated in a more detail.

4.1 Rigid Body Dynamics equations

The motion of a rigid body in 3D space can be described as a combination between a translational, and a rotational motion. Everything starts by defining the position of a point in 3D space with respect to two frames, namely the inertial and non-inertial frames. This is essential in this work; since in flight navigation, the usage of different reference frames is involved for both types of frames. Assuming flat non-rotating earth model, the position of a point (P), see Figure 9, is given in 3D space as follows:

$$\vec{P}_I = \vec{R}_I + \vec{r}_v \quad (32)$$

Where, (P_I) is the position of point (P) with respect to the inertial frame $(O_n X_n Y_n Z_n)$, (R_I) is the position of the origin of the moving coordinate system, i.e. non-inertial frame $(O_b X_b Y_b Z_b)$ which is allowed to be translated and rotated, with respect to the inertial one,

and (r_v) is the position of point (P) with respect to the non-inertial frame. By taking the time derivate of equation (32), the velocity of point (P) will be given by:

$$\frac{d\vec{P}_I}{dt} = \frac{d\vec{R}_I}{dt} + \vec{\omega} \times \vec{r}_v \quad (33)$$

Where ($\vec{\omega}$) is the angular velocity of the non-inertial frame, and (\times) denote the cross product between two vectors.

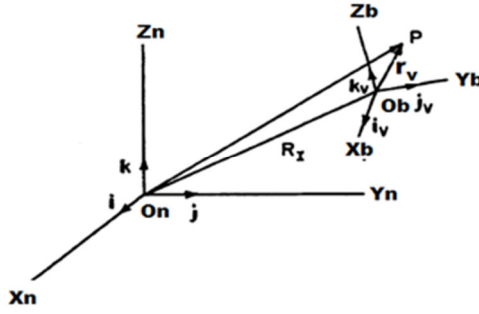


Figure 9: Inertial and non-inertial frames.

Taking the time derivate of equation (33) will result in the inertial acceleration (\vec{A}_I) of point (P) with respect to the inertial frame as given by (34).

$$\vec{A}_I = \ddot{\vec{R}}_I + \dot{\vec{\Omega}} \times \vec{r}_v + \ddot{\vec{r}}_v + 2\vec{\Omega} \times \dot{\vec{r}}_v + \vec{\Omega} \times (\vec{\Omega} \times \vec{r}_v) \quad (34)$$

Where, ($\ddot{\vec{R}}_I$) is the linear acceleration of the origin of the non-inertial coordinate system with respect to inertial frame (n) and ($\dot{\vec{\Omega}}$) is its angular acceleration. ($\ddot{\vec{r}}_v$) and ($\dot{\vec{r}}_v$) are the acceleration and velocity of point (P) respectively with respect to the non-inertial frame. Equation (34) is the main equation upon which the remaining work depends.

One last thing to mention here is that the angular acceleration and velocity are the same at each point of the object, and based on this fact the positioning of the proposed IMU will be flexible.

4.2 Simulating Rigid Body Dynamics using SimMechanics

SimMechanics is a multi-body dynamics simulation library found in Simulink simulation environment. It provides various approaches to handle dynamical problems. One of its simplest usages is shown in this thesis where it was used to simulate the dynamics of a rigid body in 3D space acted upon by several forces and moments. Despite the fact that these forces and moments may get several profiles, certain profiles for the forces and moments were adopted to make the simulation easy. In this section, only the blocks used from the library are briefly explained here. It is worthy to note that there is no need to write down any code that reflects the dynamical equations previously stated, and this enables the user to focus on the problem in his hand.

4.2.1 Machine Environment Block

A connected diagram formed of SimMechanics blocks is defined in SimMechanics as a Machine. Each machine must have one fixed frame (Ground Block) to which the machine is attached. Another block that is called the Environment block is essential in each SimMechanics diagram since it determines the way to simulate the machine, and how the simulation is visualized and linearized and to understand the way the blocks within the machine are related to each other, i.e. mechanical constraints and Degrees of Freedom (DoF) each block has relative to the block attached to it. The Machine Environment Block also accepts a Simulink signal as a Gravity signal. This feature is very important when considering the gravity compensation part introduced in later chapters, see Figure 10.

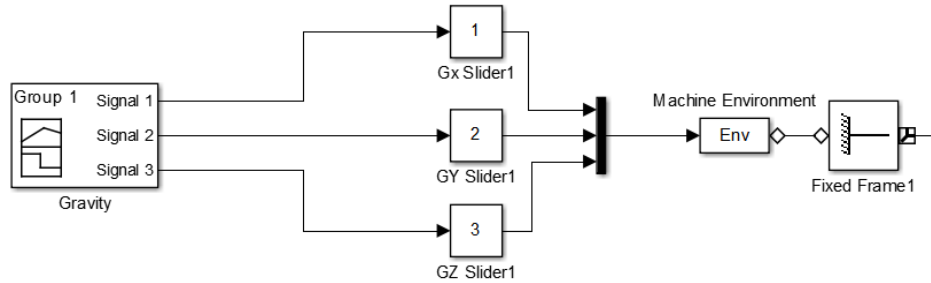


Figure 10: Machine Environment Block with gravity as a Simulink signal.

4.2.2 Six-DOF Mechanical Joint Block

The Six-DoF block, shown in Figure 11, consists of three translational joints forming three translational degrees of freedom and three rotational joints allowing the rotation about the translational axes. The Six-DOF Mechanical Joint Block enables the simulation of a rigid body, attached to a non-inertial frame $O_b X_b Y_b Z_b$, in 3D space by having a 6-DoF motion relative to the inertial frame $O_n X_n Y_n Z_n$.

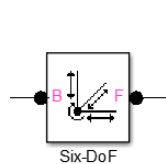


Figure 11: Six-DOF Mechanical Joint Block.

4.2.3 Weld Mechanical Joint Block

When two objects are attached to each other with no relative motion between them is allowed, they are said to be rigidly locked to each other. Such a constraint can be realized using a Weld joint block. This joint is equivalent to a motion with zero-DoF, see Figure 12.

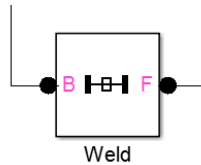


Figure 12: Weld Mechanical Joint Block.

4.2.4 Rigid Body Block

Using a Rigid Body Block, it is possible to define a rigid body with specified mass and moment of inertia tensor. Additional information such as the position of CoG within the body is needed as well as, at least, one extra body coordinate system to completely define a rigid body in SimMechanics. Additional body coordinate systems can be added to define the geometry of the rigid body, see Figure 13. This block also accepts STL (sterolithographic) file format to visualize its geometry. This STL file can be generated using the available CAD packages.

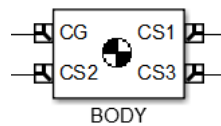


Figure 13: Body Block.

4.2.5 Body Actuator Block

The Body Actuator block is used to exert a generalized force consists of a linear force and a rotational torque which can be generated using the available Simulink signals. The generalized force is applied to the CoG in this work, see Figure 14.

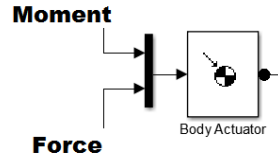


Figure 14: Body Actuator Block.

4.2.6 Body Sensor Block

The Body Sensor block, shown in Figure 15, is used to measure the position, linear velocity/acceleration, angular velocity/acceleration, and the rotation of the rigid body with relative to the reference selected from the dialog box as shown in Figure 16. The measurements generated by this block can be used in Simulink environment directly without any conversion or interfacing blocks.

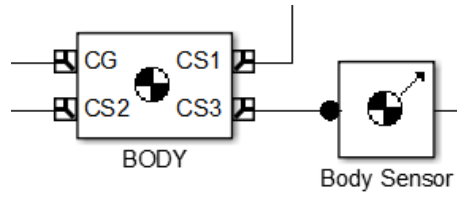


Figure 15: Body Sensor Block.

Measurements

With respect to CS:

- Position [x;y;z]
- Velocity [x';y';z'] Units: m/s
- Angular velocity [Rx';Ry';Rz'] Units: deg/s
- Rotation matrix [3 x 3]:
- Acceleration [x'';y'';z''] Units: m/s^2
- Angular acceleration [Rx'';Ry'';Rz''] Units: deg/s^2

Output selected parameters as one signal.

The dropdown menu for 'With respect to CS' shows the following options: Absolute (World), Absolute (World), and Local (Body CS).

Figure 16: Available measurements in a Body Sensor Block.

Next, the usage of SimMechanics library in modeling the main measuring device in the proposed IMU is presented.

4.3 Modeling a Tri-axis linear accelerometer using SimMechanics

The flexibility gained using SimMechanics Blocks enabled the modeling of a generic Tri-axis accelerometer model. Although it is simple; since it does not include the cross-coupling, directly, and scale-factor effects usually exist in real tri-axis accelerometers as well as other sources of errors, it is still capable of providing the possibility of introducing misalignments and disorientations usually involved in assembly process of such type of IMUs. The only source of error included was the measurement noise. To ensure the functionality of the identification routine presented in later chapters, the introduced noise was within the usual noise level found in real accelerometers and was modeled as a white noise.

Other sources of errors and non-linearity can be added, but it was not the objective of this thesis to investigate the performance of the proposed IMU through any of the available error analysis techniques. So, this can be considered as a part of the future work.

4.3.1 Accelerometer model

Figure 17 shows the tri-axis linear accelerometer model used in this thesis. It was completely parameterized to ensure its reusability later on. This model consists basically of two Body Sensor Blocks, shown in Figure 15, and three White Noise Blocks and other basic blocks. Faults were also included and they are allowed to be one of the following types: {None, No-Output, Wrong-Output}. These faults are also used to check the Fault

Detection and Isolation (FDI) procedure proposed by [7] although it was not reported in this thesis.

The simulation setup and results of the accelerometer model are shown in Figure 18 and Figure 19 respectively. There are two available measurements, one with respect to the inertial frame (A_e) and the other with respect to the body frame (A_b) to which the accelerometer is attached to. The later will be used, and it is the responsibility of the INS to provide the measurements in the desired frame by utilizing the available measurements provided by the IMU.

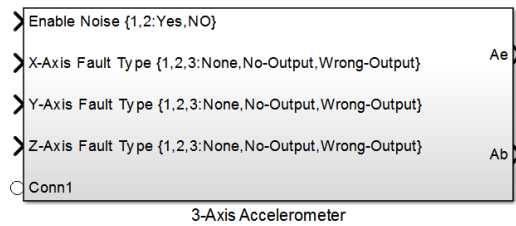


Figure 17: Tri-axis model used in the thesis, where measurements are provided with respect to: (Ae) Inertial, and (Ab) Body frames.

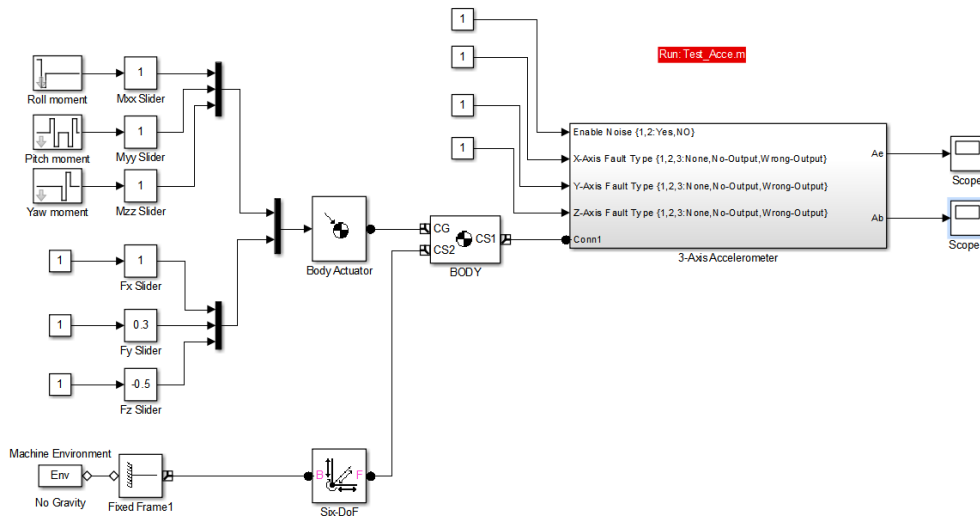
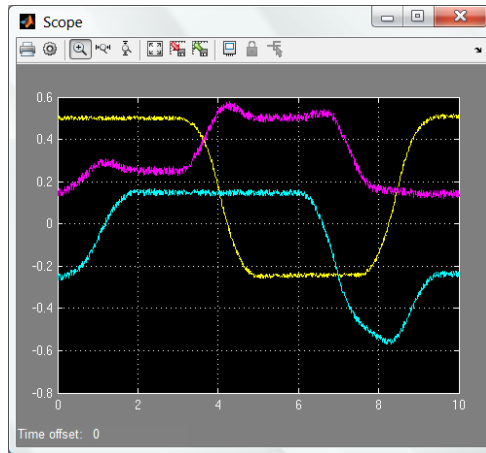
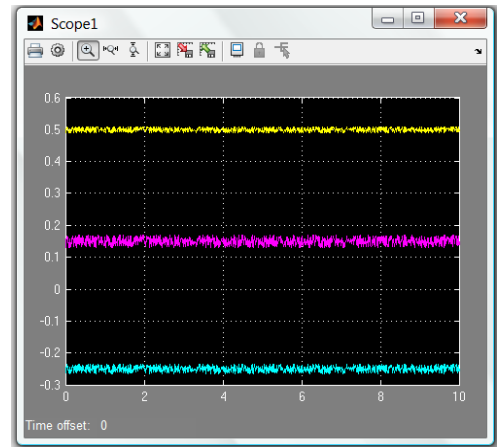


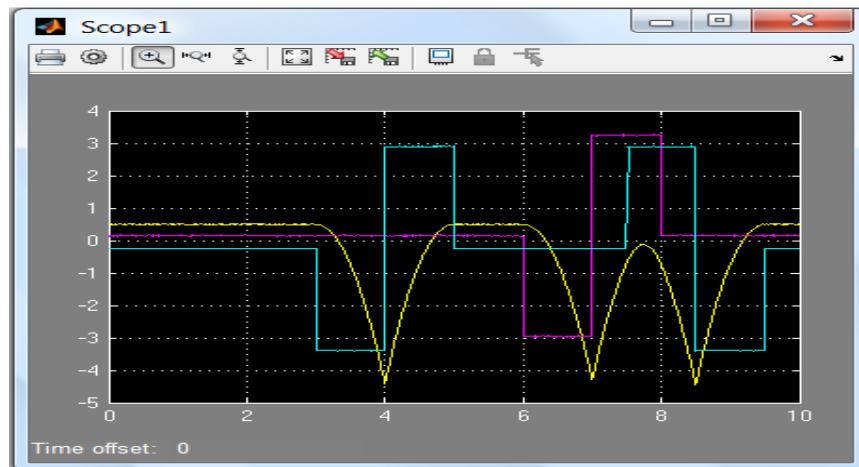
Figure 18: Simulation setup used to test the tri-axis accelerometer model.



(a)



(b)



(c)

Figure 19: Accelerometer measurements relative to: (a) world (b) body coordinate systems when located at CoG (c) same as (b) but when shifted 2 meters in the X-direction from CoG.

Figure 19.a shows the accelerometers measurements with respect to world (Inertial) frame. Both Figures 19.b and 19.c show the measurements but with respect to the body frame. The main difference between those two figures is that Figure 19.b shows the accelerometer's measurements when it coincides with the BODY CoG while Figure 19.c shows the accelerometer's measurement when it is shifted two meters in the X-direction from the BODY CoG.

Figure 19.c reflects the necessity of finding the position of CoG to compensate for such offset. Figures 19.a, 19.b and 19.c were obtained using the setup shown in Figure 18 and using the same applied torque and force.

CHAPTER 5

ALL-ACCELEROMETERS BASED IMU

The feasibility of designing All-accelerometers based IMU using only linear accelerometers' measurements to compute the linear/angular accelerations, and the angular velocity of a rigid body was investigated in [48]. It is possible to use different number of accelerometers to design All-accelerometers IMU where the issue of singularity must be taken into consideration when finding the optimum number of linear accelerometers arranged in a specific structure [40]. The accelerometers' measurements can be used to determine the angular velocity/acceleration and the linear acceleration of a rigid body using different approaches such as simple matrix operation [38], Geometric Algebra (GA) [34], or by using filters such as Unscented Kalman Filter (UKF) [46] just to name few. It is worth mentioning that IMUs based on both rate gyros and linear accelerometers are still under research, see [33].

In [71], Flat-Earth Model (FEM) and the more precise Around-Earth model (AEM) were used to check the induced error when using the simpler model (FEM) compared to (AEM) in designing a Strapdown Inertial Navigation System (SINS). The results were encouraging to adopt the simpler FEM model in the proposed IMUs.

Using linear accelerometers in certain configurations enables finding the angular acceleration of the body they are attached to when their outputs are treated in differential mode. One of those configurations is the diamond configuration by which two linear

accelerometers are separated equally about a point in three perpendicular directions, i.e. one pair per axis. The differential output can then be fed into a Kalman Filter (KF) or the like to estimate the body angular velocities from the noisy linear accelerometers' measurements. Redundant sensors are used to consolidate the accelerometers' measurements. In the IMU found in [7], only two pairs of linear tri-axial accelerometers were used in the Y and Z directions which make a total number of 12 accelerometers. The available accelerometers' channels in each tri-axial accelerometer are used to facilitate fault detection and isolating the faulty sensors.

In this Chapter, implementation of the IMU along with the procedure suggested by [7] is done and will serve as an evaluation of this version of IMU. Based on the results, other versions will be presented as can be found in Chapter 6.

The proposed IMU, found in [7], is used in the setup shown in Figure 20. This setup helps in improving guidance and control of aerial Vehicles, and more particularly to track the changes in the position of CoG of a moving vehicle due fuel consumption or changes in its payload. Redundancy is available at the IMU level and at the Ring level to increase the reliability of such instrument. The distribution of these rings is somehow flexible to overcome the constraints imposed on such instruments when installed in real vehicles. Although these IMUs can operate in centralized or distributed modes, the latter is adopted here and the former will be a subject of future work.

In Figure 20, all the accelerometers are arranged in a symmetric way around the point (m) at a distance (μ) forming a ring, from now on sometimes referred to as a Ring, where (P_i) is a 3-axis linear accelerometer's position, (O_b) is the position of Center of Gravity

(CoG), (O_n) is the origin of the inertial coordinate system, (R_0) is the vector from inertial frame origin (O_n) to CoG, and (R_{vj}) is the vector from the CoG O_b to origin of Ring (j), where $j = 1, 2, 3, \dots$ etc.

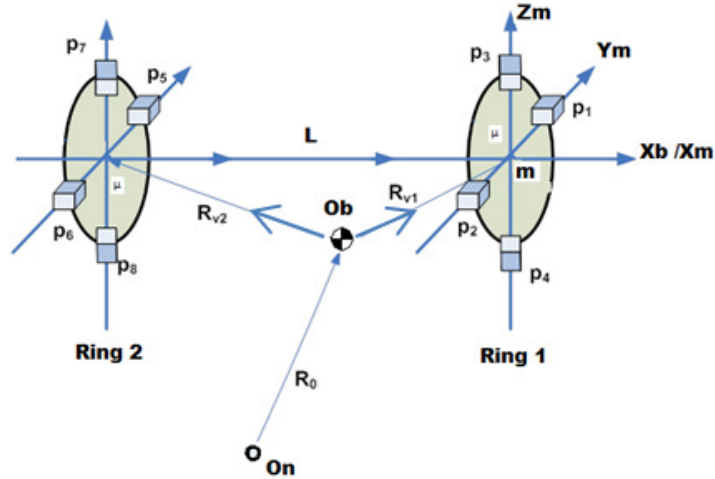


Figure 20: Two Rings approach based on the proposed IMU.

5.1 Mathematical Derivation

Rigid body dynamics equations can be used to describe the motion of a rigid body in 3-D space relative to a reference frame. A local non-inertial frame called the body frame (b), located at Center of Gravity (CoG) of the vehicle, and an inertial frame (n), located at center of Earth, are presented. Non-rotating Flat earth model is adopted to reduce the complexity of equations. Basic equation of motion for a point P, see Figure 9, with respect to the inertial frame is given by equation (34) in Chapter 4.

Now, if the CoG is stationary, i.e. $\ddot{r}_v = \dot{r}_v = 0$, then the acceleration of the point P is given by:

$$\vec{A}_I = \ddot{\vec{R}}_I + \dot{\vec{\Omega}} \times \vec{r}_v + \vec{\Omega} \times (\vec{\Omega} \times \vec{r}_v) \quad (35)$$

5.1.1 Estimation of Angular Velocities and Accelerations

The total inertial acceleration at point P1 with respect to body frame can be expressed as, see Figure 20 and by given $\vec{A}_I = \ddot{\vec{R}}_0$:

$$\vec{A}_1 = \vec{A}_I + \ddot{\vec{R}}_{v1} + \dot{\vec{\Omega}} \times (\vec{R}_{v1} + \mu\vec{j}) + 2\vec{\Omega} \times \dot{\vec{R}}_{v1} + \vec{\Omega} \times (\vec{\Omega} \times (\vec{R}_{v1} + \mu\vec{j})) \quad (36)$$

Or in matrix format as:

$$\begin{aligned} \begin{bmatrix} A_{1xb} \\ A_{1yb} \\ A_{1zb} \end{bmatrix} &= \begin{bmatrix} a_x \\ a_y \\ a_z \end{bmatrix} + \begin{bmatrix} \ddot{r}_{v1x} \\ \ddot{r}_{v1y} \\ \ddot{r}_{v1z} \end{bmatrix} + 2 \begin{bmatrix} 0 & -\Omega_z & \Omega_y \\ \Omega_z & 0 & -\Omega_x \\ -\Omega_y & \Omega_x & 0 \end{bmatrix} \begin{bmatrix} \dot{r}_{v1x} \\ \dot{r}_{v1y} \\ \dot{r}_{v1z} \end{bmatrix} \\ &+ \begin{bmatrix} 0 & -\dot{\Omega}_z & \dot{\Omega}_y \\ \dot{\Omega}_z & 0 & -\dot{\Omega}_x \\ -\dot{\Omega}_y & \dot{\Omega}_x & 0 \end{bmatrix} \begin{bmatrix} r_{v1x} \\ r_{v1y} + \mu \\ r_{v1z} \end{bmatrix} \\ &+ \begin{bmatrix} -\Omega_z^2 - \Omega_y^2 & \Omega_x \Omega_y & \Omega_x \Omega_z \\ \Omega_x \Omega_y & -\Omega_z^2 - \Omega_x^2 & \Omega_z \Omega_y \\ \Omega_x \Omega_z & \Omega_z \Omega_y & -\Omega_y^2 - \Omega_x^2 \end{bmatrix} \begin{bmatrix} r_{v1x} \\ r_{v1y} + \mu \\ r_{v1z} \end{bmatrix} \end{aligned} \quad (37)$$

The acceleration as measured by a tri-axial accelerometer at point 2 is given by:

$$\begin{aligned} \begin{bmatrix} A_{2xb} \\ A_{2yb} \\ A_{2zb} \end{bmatrix} &= \begin{bmatrix} a_x \\ a_y \\ a_z \end{bmatrix} + \begin{bmatrix} \ddot{r}_{v1x} \\ \ddot{r}_{v1y} \\ \ddot{r}_{v1z} \end{bmatrix} + 2 \begin{bmatrix} 0 & -\Omega_z & \Omega_y \\ \Omega_z & 0 & -\Omega_x \\ -\Omega_y & \Omega_x & 0 \end{bmatrix} \begin{bmatrix} \dot{r}_{v1x} \\ \dot{r}_{v1y} \\ \dot{r}_{v1z} \end{bmatrix} \\ &+ \begin{bmatrix} 0 & -\dot{\Omega}_z & \dot{\Omega}_y \\ \dot{\Omega}_z & 0 & -\dot{\Omega}_x \\ -\dot{\Omega}_y & \dot{\Omega}_x & 0 \end{bmatrix} \begin{bmatrix} r_{v1x} \\ r_{v1y} - \mu \\ r_{v1z} \end{bmatrix} \\ &+ \begin{bmatrix} -\Omega_z^2 - \Omega_y^2 & \Omega_x \Omega_y & \Omega_x \Omega_z \\ \Omega_x \Omega_y & -\Omega_z^2 - \Omega_x^2 & \Omega_z \Omega_y \\ \Omega_x \Omega_z & \Omega_z \Omega_y & -\Omega_y^2 - \Omega_x^2 \end{bmatrix} \begin{bmatrix} r_{v1x} \\ r_{v1y} - \mu \\ r_{v1z} \end{bmatrix} \end{aligned} \quad (38)$$

The subscript (b) denotes the body frame and it will be omitted since the remaining work in this thesis is in the body frame unless otherwise stated.

All the accelerometers are assumed to be perfectly aligned with respect to the body frame.

The differential output of the accelerometers at points P1 and P2 is given by:

$$\begin{aligned} \begin{bmatrix} A_{1x} \\ A_{1y} \\ A_{1z} \end{bmatrix} - \begin{bmatrix} A_{2x} \\ A_{2y} \\ A_{2z} \end{bmatrix} &= \begin{bmatrix} 0 & -\dot{\Omega}_z & \dot{\Omega}_y \\ \dot{\Omega}_z & 0 & -\dot{\Omega}_x \\ -\dot{\Omega}_y & \dot{\Omega}_x & 0 \end{bmatrix} \begin{bmatrix} 0 \\ 2\mu \\ 0 \end{bmatrix} \\ &+ \begin{bmatrix} -\Omega_z^2 - \Omega_y^2 & \Omega_x \Omega_y & \Omega_x \Omega_z \\ \Omega_x \Omega_y & -\Omega_z^2 - \Omega_x^2 & \Omega_z \Omega_y \\ \Omega_x \Omega_z & \Omega_z \Omega_y & -\Omega_y^2 - \Omega_x^2 \end{bmatrix} \begin{bmatrix} 0 \\ 2\mu \\ 0 \end{bmatrix} \end{aligned} \quad (39)$$

The difference of the accelerations of the points P3 and P4 is then given by:

$$\begin{aligned} \begin{bmatrix} A_{3x} \\ A_{3y} \\ A_{3z} \end{bmatrix} - \begin{bmatrix} A_{4x} \\ A_{4y} \\ A_{4z} \end{bmatrix} &= \begin{bmatrix} 0 & -\dot{\Omega}_z & \dot{\Omega}_y \\ \dot{\Omega}_z & 0 & -\dot{\Omega}_x \\ -\dot{\Omega}_y & \dot{\Omega}_x & 0 \end{bmatrix} \begin{bmatrix} 0 \\ 0 \\ 2\mu \end{bmatrix} \\ &+ \begin{bmatrix} -\Omega_z^2 - \Omega_y^2 & \Omega_x \Omega_y & \Omega_x \Omega_z \\ \Omega_x \Omega_y & -\Omega_z^2 - \Omega_x^2 & \Omega_z \Omega_y \\ \Omega_x \Omega_z & \Omega_z \Omega_y & -\Omega_y^2 - \Omega_x^2 \end{bmatrix} \begin{bmatrix} 0 \\ 0 \\ 2\mu \end{bmatrix} \end{aligned} \quad (40)$$

The differential output of the two accelerometers within the first ring on the body y-axis gives:

$$\frac{1}{2\mu} (A_{1x} - A_{2x}) = -\dot{\Omega}_z + \Omega_x \Omega_y \quad (41)$$

$$\frac{1}{2\mu} (A_{2y} - A_{1y}) = \Omega_z^2 + \Omega_x^2 \quad (42)$$

$$\frac{1}{2\mu} (A_{1z} - A_{2z}) = \dot{\Omega}_x + \Omega_y \Omega_z \quad (43)$$

The differential output of the two accelerometers within the first ring on the body z-axis gives:

$$\frac{1}{2\mu} (A_{3x} - A_{4x}) = \dot{\Omega}_y + \Omega_x \Omega_z \quad (44)$$

$$\frac{1}{2\mu} (A_{3y} - A_{4y}) = -\dot{\Omega}_x + \Omega_y \Omega_z \quad (45)$$

$$\frac{1}{2\mu}(A_{4z} - A_{3z}) = \Omega_y^2 + \Omega_x^2 \quad (46)$$

From (41) - (46), the state equations:

$$\dot{\Omega}_x = \frac{1}{4\mu}(A_{1z} - A_{2z} - A_{3y} + A_{4y}) \quad (47)$$

$$\dot{\Omega}_y = -\Omega_x\Omega_z + \frac{1}{2\mu}(A_{3x} - A_{4x}) \quad (48)$$

$$\dot{\Omega}_z = \Omega_x\Omega_y - \frac{1}{2\mu}(A_{1x} - A_{2x}) \quad (49)$$

While the remaining equations are as follows:

$$\frac{1}{2\mu}(A_{2y} - A_{1y}) = \Omega_z^2 + \Omega_x^2 \quad (50)$$

$$\frac{1}{2\mu}(A_{4z} - A_{3z}) = \Omega_y^2 + \Omega_x^2 \quad (51)$$

$$\frac{1}{2\mu}(A_{3y} - A_{4y} + A_{1z} - A_{2z}) = \Omega_y\Omega_z \quad (52)$$

Equations (47), (48), and (49) can be solved using numerical methods. Once these equations are solved, the values of the calculated angular velocities can be used to check the consistency of measurements by substituting them in equations (50-52). If the errors between the left side and right side of those equations are within a certain threshold, say a normal accelerometer noise level, then the available measurements are considered healthy and can be used for further stages. If they do not, then a fault detection algorithm will be used to point out the faulty measurements and to isolate the faulty sensors. This algorithm makes use of the available measurements from the redundant rings in the setup. It is apparent that this approach provides redundancy at the IMU level and the IMUs level as a whole. If the previous test is passed, then the angular velocities are re-estimated using all the healthy measurements by using a Kalman filter as follows:

Equations (47) to (52) can be linearized and discretized in the following state equations:

$$\begin{aligned}\vec{X}(k+1) &= A(k)\vec{X}(k) + B\vec{U}(k) + \vec{w}(k) \\ \vec{Y}(k) &= C(k)\vec{X}(k) + \vec{v}(k)\end{aligned}\quad (53)$$

Where, $w(k)$ and $v(k)$ are random white noises, and:

$$\begin{aligned}\vec{X} &= [\Omega_x, \Omega_y, \Omega_z]^T \\ \vec{U} &= \begin{bmatrix} \frac{1}{4\mu}(A_{1z} - A_{2z} - A_{3y} + A_{4y}) \\ \frac{1}{2\mu}(A_{3x} - A_{4x}) \\ \frac{1}{2\mu}(A_{1x} - A_{2x}) \end{bmatrix} \\ \vec{Y}(k) &= \begin{bmatrix} \frac{1}{2\mu}(A_{2y} - A_{1y}) \\ \frac{1}{2\mu}(A_{4z} - A_{3z}) \\ \frac{1}{4\mu}(A_{3y} - A_{4y} + A_{1z} - A_{2z}) \end{bmatrix}\end{aligned}$$

$$A(k) = \begin{bmatrix} 1 & 0 & 0 \\ 0 & 1 & -T\Omega_x \\ 0 & T\Omega_x & 1 \end{bmatrix}, \quad B = \begin{bmatrix} T & 0 & 0 \\ 0 & T & 0 \\ 0 & 0 & -T \end{bmatrix}, \quad C(k) = \begin{bmatrix} \Omega_x & 0 & \Omega_z \\ \Omega_x & \Omega_y & 0 \\ 0 & \Omega_z & 0 \end{bmatrix}$$

Where, T is the sampling rate in seconds.

The steps proceed as follows:

➤ Prediction

$$\hat{X}(k+1|k) = A(k)\hat{X}(k|k) + B\vec{U}(k)\quad (54)$$

➤ Correction

$$\hat{X}(k|k) = \hat{X}(k|k-1) + K(k)(\vec{Y}(k) - C\hat{X}(k|k-1))\quad (55)$$

Where:

$$K(k) = P(k)C^T(k)(R_{yy} + C(k)P(k)C^T(k))^{-1}$$

$$P(k+1) = A(k)P(k)A^T(k) + R_{xx} \\ - A(k)P(k)C^T(k) \left(R_{yy} + C(k)P(k)C^T(k) \right)^{-1} C(k)P(k)A^T(k)$$

Where, R_{xx} and R_{yy} are 3X3 weighing matrices.

This process is done within each ring, in the case of distributed IMUs configuration, and if the difference between the results obtained from all rings is within a certain threshold, then the angular velocities are consolidated using all the available measurements by simply taking their average.

5.1.2 Estimation of CoG position and inertial acceleration

The angular velocities and accelerations were previously found by utilizing the difference in the accelerometers' measurements coexist on the same axis. It is possible to show that the addition of those measurements will help in finding a relation that reflects the kinematics of the CoG. At the moment, it is the position of CoG to be found. By adding the accelerometers' measurements at points P1 and P2 the following equation will result:

$$\begin{aligned}
\begin{bmatrix} A_{1x} \\ A_{1y} \\ A_{1z} \end{bmatrix} + \begin{bmatrix} A_{2x} \\ A_{2y} \\ A_{2z} \end{bmatrix} &= \begin{bmatrix} a_x \\ a_y \\ a_z \end{bmatrix} + \begin{bmatrix} \ddot{r}_{v1x} \\ \ddot{r}_{v1y} \\ \ddot{r}_{v1z} \end{bmatrix} + 2 \begin{bmatrix} 0 & -\Omega_z & \Omega_y \\ \Omega_z & 0 & -\Omega_x \\ -\Omega_y & \Omega_x & 0 \end{bmatrix} \begin{bmatrix} \dot{r}_{v1x} \\ \dot{r}_{v1y} \\ \dot{r}_{v1z} \end{bmatrix} \\
&+ \begin{bmatrix} 0 & -\dot{\Omega}_z & \dot{\Omega}_y \\ \dot{\Omega}_z & 0 & -\dot{\Omega}_x \\ -\dot{\Omega}_y & \dot{\Omega}_x & 0 \end{bmatrix} \begin{bmatrix} r_{v1x} \\ r_{v1y} \\ r_{v1z} \end{bmatrix} \\
&+ \begin{bmatrix} -\Omega_z^2 - \Omega_y^2 & \Omega_x \Omega_y & \Omega_x \Omega_z \\ \Omega_x \Omega_y & -\Omega_z^2 - \Omega_x^2 & \Omega_z \Omega_y \\ \Omega_x \Omega_z & \Omega_z \Omega_y & -\Omega_y^2 - \Omega_x^2 \end{bmatrix} \begin{bmatrix} r_{v1x} \\ r_{v1y} \\ r_{v1z} \end{bmatrix}
\end{aligned} \tag{56}$$

Moreover, the previous addition will give the acceleration at the center of the ring by using six accelerometers virtually located at the center of the ring, which cannot be practically possible; because each accelerometer has a finite size and they cannot share the same position. The same result can also be obtained when adding the measurements of the other pair of accelerometers found on the Z axis which will help in providing the first level of sensor validation within the IMU itself. Equation (57) reflects this fact clearly.

$$(\vec{A}_1 + \vec{A}_2) = (\vec{A}_3 + \vec{A}_4) \tag{57}$$

Comparing both sides of equation (57) over a short window of time may help in avoiding wrong decisions resulted because of the noisy measurements.

It is clear, from equation (56), that the body linear acceleration cannot be retrieved simply, although the angular velocities and accelerations were found previously, because of the unknown kinematics of the CoG.

To simplify the situation, the rate of change in the position of CoG is assumed to be much less than the rate of change of the body inertial acceleration. In this case, it can be safely assumed equal to zero. Equation (56) can then be simplified to:

$$\begin{aligned} \begin{bmatrix} A_{1x} \\ A_{1y} \\ A_{1z} \end{bmatrix} + \begin{bmatrix} A_{2x} \\ A_{2y} \\ A_{2z} \end{bmatrix} &= \begin{bmatrix} a_x \\ a_y \\ a_z \end{bmatrix} + \begin{bmatrix} 0 & -\dot{\Omega}_z & \dot{\Omega}_y \\ \dot{\Omega}_z & 0 & -\dot{\Omega}_x \\ -\dot{\Omega}_y & \dot{\Omega}_x & 0 \end{bmatrix} \begin{bmatrix} r_{v1x} \\ r_{v1y} \\ r_{v1z} \end{bmatrix} \\ &+ \begin{bmatrix} -\Omega_z^2 - \Omega_y^2 & \Omega_x \Omega_y & \Omega_x \Omega_z \\ \Omega_x \Omega_y & -\Omega_z^2 - \Omega_x^2 & \Omega_z \Omega_y \\ \Omega_x \Omega_z & \Omega_z \Omega_y & -\Omega_y^2 - \Omega_x^2 \end{bmatrix} \begin{bmatrix} r_{v1x} \\ r_{v1y} \\ r_{v1z} \end{bmatrix} \end{aligned} \quad (58)$$

In (58), only the inertial acceleration and CoG position with respect to the first ring are to be found, using for example a Recursive Least-Squares (RLS) method or the like.

Equation (58) can be written in a vector form as:

$$\vec{f} = \vec{A}_I + B\vec{R}_{v1} \quad (59)$$

Where:

$$\vec{f} = (\vec{A}_1 + \vec{A}_2 + \vec{A}_3 + \vec{A}_4)/4 \quad (60)$$

$$\begin{aligned} B &= \begin{bmatrix} b_{11} & b_{12} & b_{13} \\ b_{21} & b_{22} & b_{23} \\ b_{31} & b_{32} & b_{33} \end{bmatrix} = [\dot{\Omega}] + [\Omega \times] \\ &= \begin{bmatrix} 0 & -\dot{\Omega}_z & \dot{\Omega}_y \\ \dot{\Omega}_z & 0 & -\dot{\Omega}_x \\ -\dot{\Omega}_y & \dot{\Omega}_x & 0 \end{bmatrix} + \begin{bmatrix} -\Omega_z^2 - \Omega_y^2 & \Omega_x \Omega_y & \Omega_x \Omega_z \\ \Omega_x \Omega_y & -\Omega_z^2 - \Omega_x^2 & \Omega_z \Omega_y \\ \Omega_x \Omega_z & \Omega_z \Omega_y & -\Omega_y^2 - \Omega_x^2 \end{bmatrix} \end{aligned}$$

\vec{A}_i is the acceleration measured at point P_i , $i = 1,2,3, \text{ and } 4$.

The formulation of the RLS method, discussed in more detail in chapter 8, is given as follows:

Rearrange (59) in the form of:

$$\vec{f} = D\vec{x} \quad (61)$$

Where:

$$\vec{x} = [r_{v1x}, r_{v1y}, r_{v1z}, a_x, a_y, a_z]^T$$

$$D = \begin{bmatrix} b_{11} & b_{12} & b_{13} & 1 & 0 & 0 \\ b_{21} & b_{22} & b_{23} & 0 & 1 & 0 \\ b_{31} & b_{32} & b_{33} & 0 & 0 & 1 \end{bmatrix}$$

The procedure then proceeds as follows:

- Initialize: λ_0 and x_0 .
- Recursion:

$$\beta = 1 + \text{trace}(DD^T)\lambda_0$$

$$K_t = (\lambda_0 D^T) / \beta \quad (62)$$

$$E_t = f_t - D_t x_t$$

$$x_{t+1} = x_t + K_t E_t$$

The same calculations are done independently for all rings. As in the case of estimated angular velocities and accelerations, the best estimate of the position of CoG with respect to say, Ring 1, is given for the two ring case by:

$$\hat{R}_{v1} = \frac{1}{2}(\hat{R}_{v11} + \hat{R}_{v12}) = \frac{1}{2}(\hat{R}_{v1} + \hat{R}_{v2} + L\vec{l}) \quad (63)$$

Where, $\hat{R}_{v11} = \hat{R}_{v1}$ is the estimation of the CoG position relative to the first ring calculated using the measurements of the first ring, while $\hat{R}_{v12} = \hat{R}_{v2} + L\vec{l}$ is the estimation of the CoG position relative to the first ring calculated using the measurements of the second ring.

Using more rings can improve further the reliability, accuracy and precision of the measurements, and hence the navigation parameters values along with the position of CoG. Figure 21, shows a three-Ring configuration that can be used to determine the position of CoG of an F-15 jet fighter plane. Each ring can be placed anywhere within the plane body and all what is needed to know is the relative distances between the rings (L_{12}, L_{23}, L_{31}) and the position of each ring with respect to the vehicle datum which can be considered possible to have.

The modified version of the IMU found in [7] is shown in Figure 22 where it is apparent that the main difference is the additional pair of linear accelerometers on the vehicle's X-axis. The effect of this addition will be appreciated later on through the simulation results in this chapter. The underlying equations governing the behavior of this version as well as others will be presented in more detail in Chapter 6.

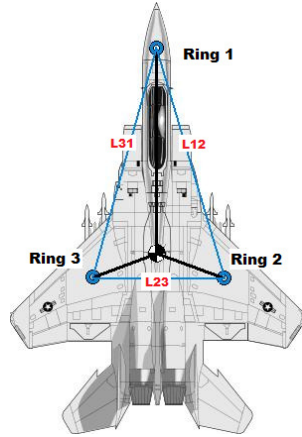


Figure 21: F-15 jet fighter with three-Ring configuration. [18]

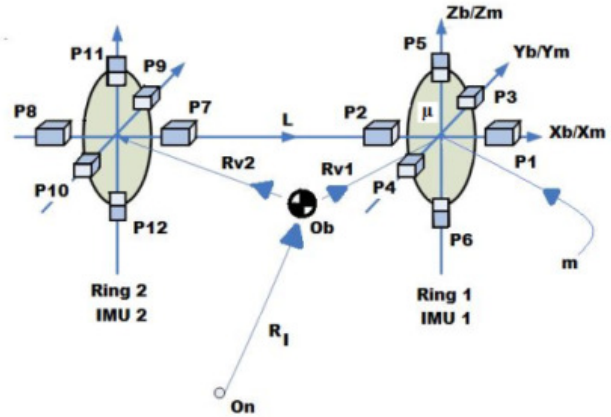


Figure 22: Two Rings approach based on the proposed IMU using 18-accelerometer/Ring version.

5.2 Simulating All-accelerometers Based IMU

In this part, the simulation results obtained when simulating the proposed IMUs are presented, following the same procedure previously introduced. The SimMechanics Library has been used to model an arbitrary object in 3D space subjected to various Forces and Torques. SimMechanics blocks were used since they give more freedom in the design process as well as different situations can be investigated such as misalignments and disorientation in the accelerometers when they are assembled to form a ring.

The accelerometer model, shown in Figure 17, was used in the simulation model shown in Figure 23 to form the two rings. Figure 23 shows a SimMechanics machine that resembles a composite rigid body in the form of cube whose mass is (0.5Kg) and the length of its side is (1m) with (1Kg) added masses at each corner subjected to force and moment acting at its equivalent CoG and it is allowed to move in 6-DOF motion in the

space where no gravity force is active. Figure 24 clearly represents this composite body shape.

It can be seen from equation (60) that the B matrix depends totally on the angular motion of the body. So, it is a must to have sufficient rotational motion to obtain a good estimation of the position of CoG using this approach. Next, different scenarios for applied moment, and force are used to cover larger number of possibilities that may include the change in torque, force, and CoG position. Figure 25 shows the force and moment profiles used in this simulation.

The CoG position of the composite body was found using the following equation:

$$CoG = \frac{\sum_1^N m_i \vec{r}_i}{\sum_1^N m_i} \quad (64)$$

Where (N) is the total number of additional masses, that is 8, (m_i) is the value of the added mass taken here to be (1 Kg), and (\vec{r}_i) is its position relative to the cube geometric center in meters.

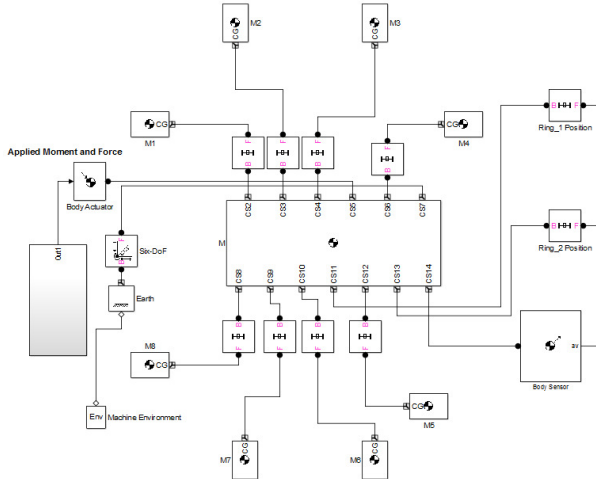


Figure 23: Composite rigid body SimMechanics Machine.

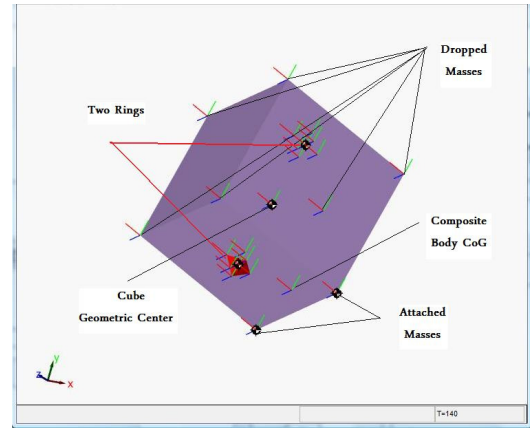
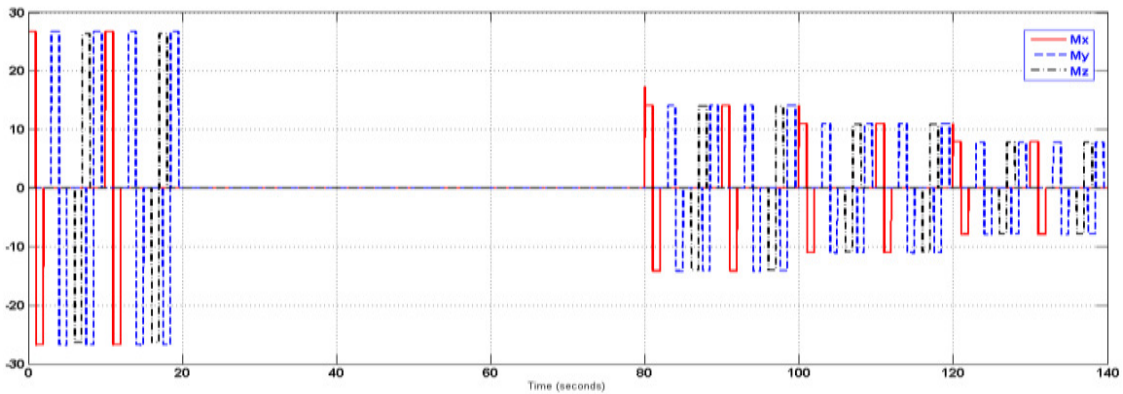
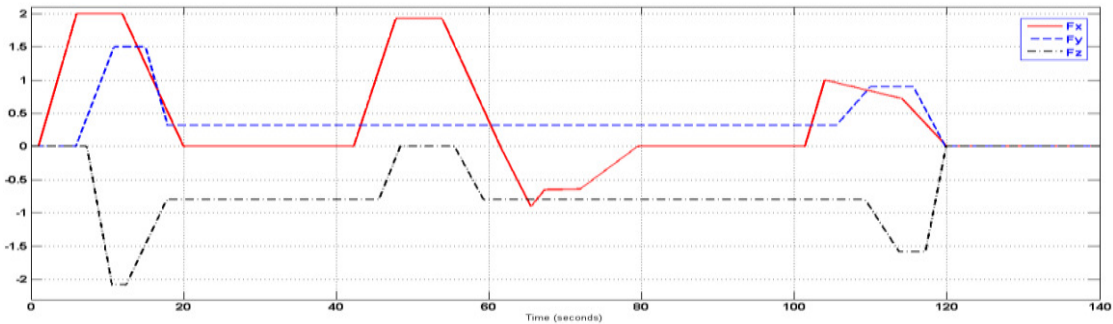


Figure 24: SimMechanics visualization of the composite rigid body given in the example.



(a)



(b)

Figure 25: (a) Applied Moment (N.m), (b) Force (N) profiles used in the simulation.

The position of the composite body CoG, relative to the cube geometric center (0,0,0), was forced to change by dropping one added mass at the end of each interval, an interval equals 20 seconds in simulation time. The effect is resembled by abrupt changes in its

position as can be seen in Figure 26. The new composite inertia is calculated by SimMechanics and the resulting dynamic equation is solved internally. The two Rings were located at (0.5,0,0) meters and (-0.5,0,0) meters respectively. Table 1 shows the schedule used in dropping the additional masses and the resulting CoG position.

Table 1: Simulation Schedule.

Total Mass (Kg)	Composite Body CoG Position (m)	Dropped Mass Position (m)	Time Interval (seconds)
8.5	(0,0,0)	-	0-20
7.5	(-0.0667,-0.0667,-0.0667)	(0.5, 0.5, 0.5)	20-40
6.5	(-0.1538,0,0)	(0.5, -0.5, -0.5)	40-60
5.5	(-0.2727,-0.0909,0.0909)	(0.5, 0.5, -0.5)	60-80
4.5	(-0.4444,0,0)	(0.5, -0.5, 0.5)	80-100
3.5	(-0.4286,-0.1429,0.1429)	(-0.5, 0.5, -0.5)	100-120
2.5	(-0.4,-0.4,0)	(-0.5, 0.5, 0.5)	120-140

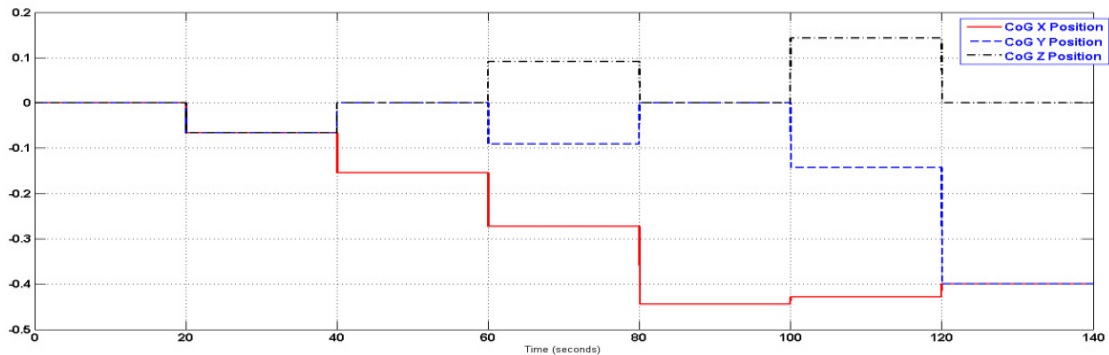


Figure 26: Composite Object CoG Position (m) relative to the Geometric Center (0, 0, 0).

5.2.1 Simulating All-accelerometers Based IMU with 12-accelerometers

Figures 27-30 shows the errors in the estimations using the 12-accelerometer version as found in [7] by taking ($\mu = 0.1$ m). Another modified version of the IMU proposed in [7] is simulated, and will be covered in more detail in Chapter 6.

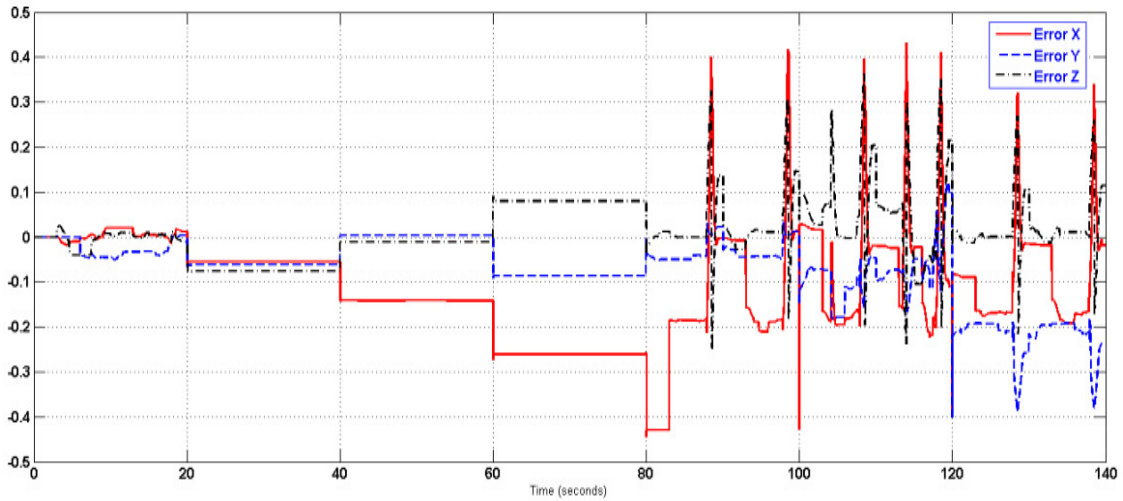


Figure 27: Estimation error of the position of the composite body CoG (m) using 12-accelerometer IMU version in Two-Rings Configuration.

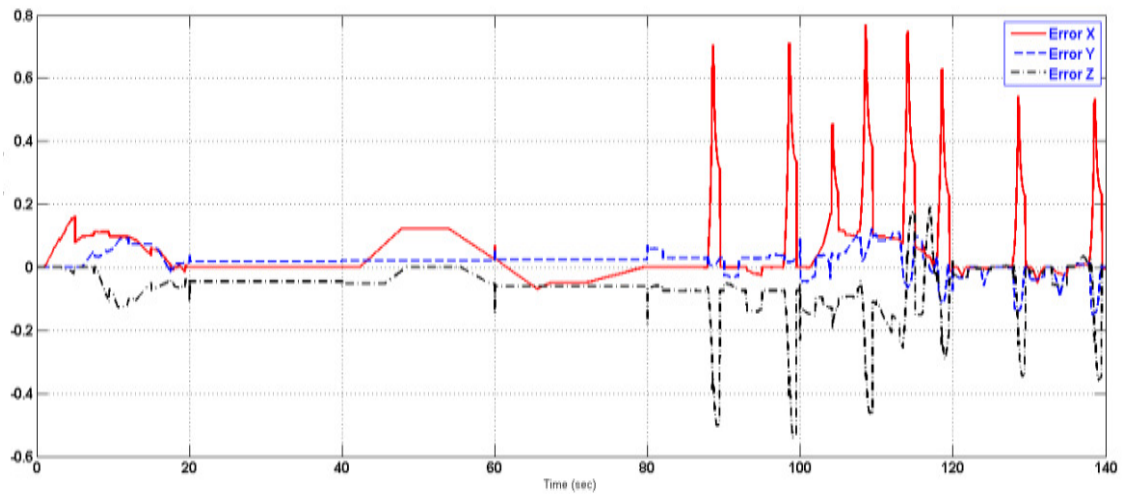


Figure 28: Estimation error of the acceleration of the composite body (m/sec²) using 12-accelerometer IMU version in Two-Rings Configuration.

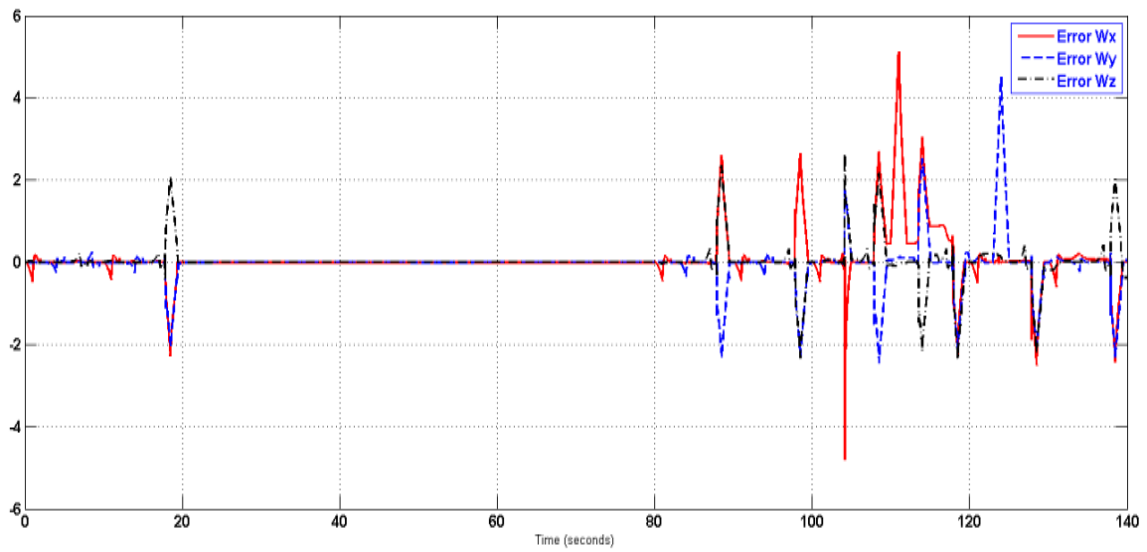


Figure 29: Estimation error of the angular velocity of the composite body (rad/sec) using 12-accelerometer IMU version in Two-Rings Configuration.

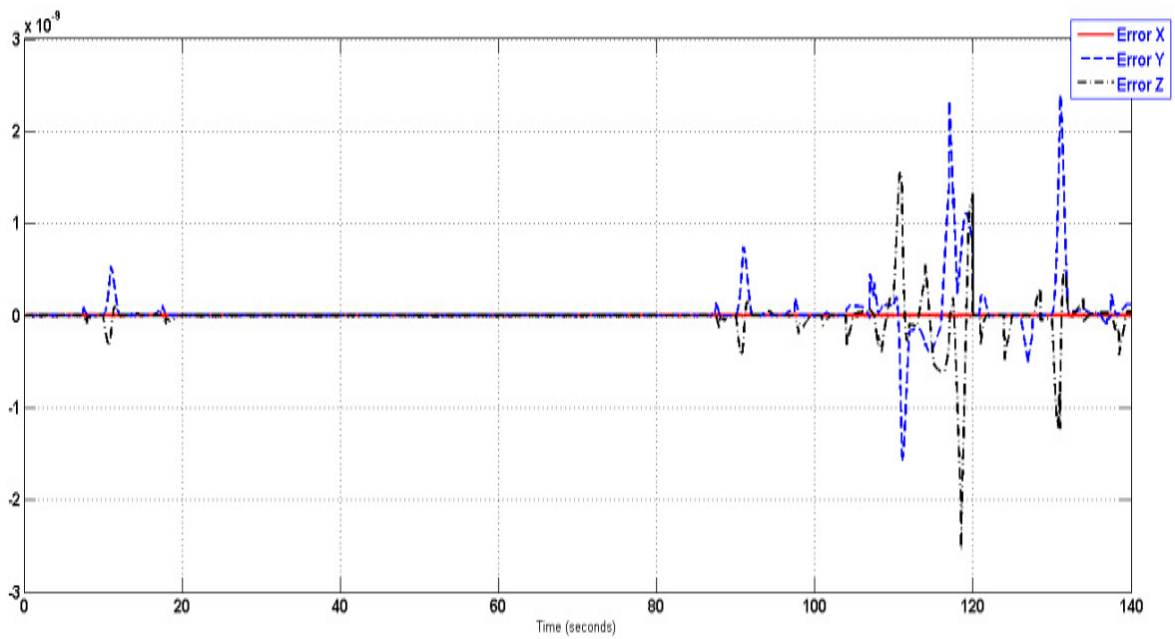


Figure 30: Estimation error of the angular acceleration of the composite body (rad/sec²) in the range of 10^{-9} using 12-accelerometer IMU version in Two-Rings Configuration.

5.2.2 Simulating All-accelerometers Based IMU with 18 accelerometers

The simulation results of the second modified version with noise enabled, and by taking ($\mu = 0.1 \text{ m}$), are shown next. Better results were obtained using this version which reflects the effect of the additional pair of linear accelerometers on the vehicle's X-axis.

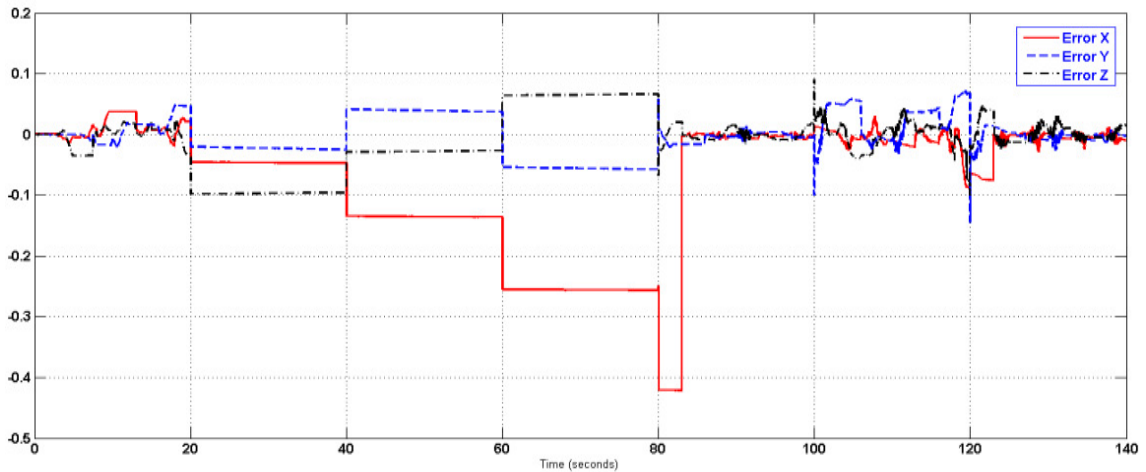


Figure 31: Estimation error of the position of the composite body CoG (m) using second modified version in Two-Rings Configuration.

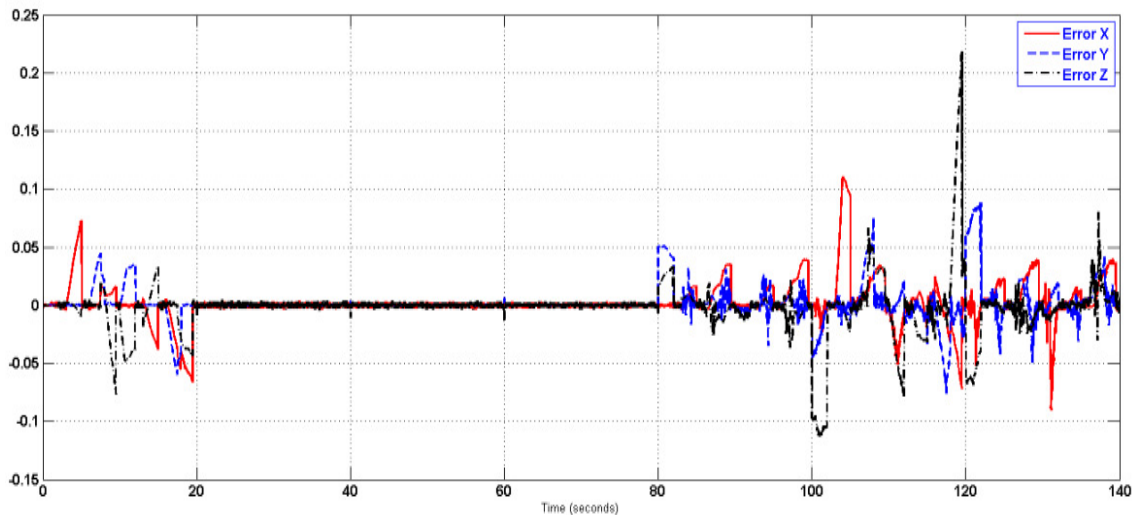


Figure 32: Estimation error of the acceleration of the composite body (m/sec²) using second modified version in Two-Rings Configuration.

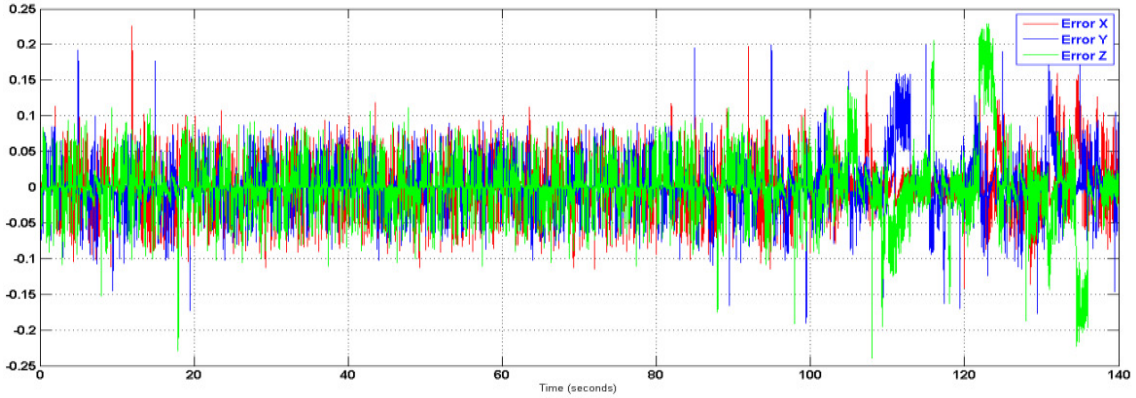


Figure 33: Estimation error of the angular velocity of the composite body (rad/sec) using second modified version in Two-Rings Configuration.

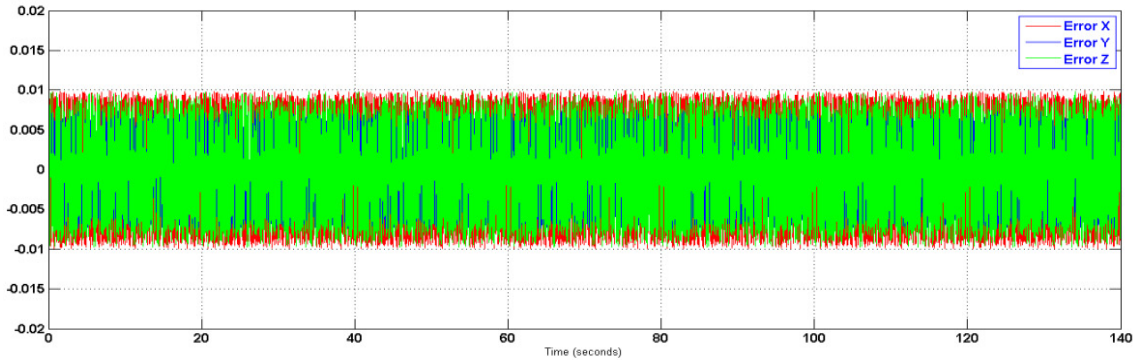


Figure 34: Estimation error of the angular acceleration of the composite body (rad/sec²) using second modified version in Two-Rings Configuration.

The usage of SimMechanics library facilitates a lot of things and makes the analysis and design of IMUs easier. It is worth mentioning that the addition of a third ring does not add much to this problem so the results were not presented.

It is clear that the whole performance of the proposed IMUs totally depends on the angular motion availability, i.e. angular velocity and/or acceleration, and that can be seen from the estimation results in the period 20-80 seconds where no angular motion is present. Additionally, the abrupt changes of the CoG position caused by dropping the

additional masses caused deterioration in the estimations of CoG position and body linear acceleration using simple RLS approach. Moreover, the more accelerometers' measurements used the better the estimation will be and that can be seen from Figures 27 and 31 where the later reflects the effect of the additional accelerometers pair attached to the X-axis in the second modified version. To obtain better results, the number of accelerometers involved in CoG position estimation can be increased by using additional Rings (IMUs) and then fuses the estimation results obtained from the individual Rings. In the previous context, this was done using simply the average value although more sophisticated techniques can be used to fuse those estimations. Another approach to consider using the proposed IMUs is the Centralized estimation where all the accelerometers' measurements are fed into one central estimation unit which utilizes all the measurements and obtain better estimation results. The centralized approach will introduce coupling between the Rings and will raise a concern about the sensor network capacity and efficiency. This coupling will make the formulation of the problem a little bit more complicated but it deserves the investigation. Also, the previous points raise questions about the minimum angular motion needed to facilitate good CoG estimation as well as the most suitable estimation technique that can be used to handle abrupt and gradual changes in CoG position.

5.3 Summary

In both [1] and [2], the estimation of the CoG position depends on the position and mass of the individual objects causing the CoG and mass variations such as cargo and passengers. This knowledge, if possible to have, may lack accuracy and cause a bad

estimation in both the mass and CoG position of the aircraft. While in [5], a dynamic model of the helicopter was used along its weight and balance, i.e. CoG position, to build an EKF that was used to enable estimating both the gross weight and CoG location of that helicopter. Unlike the previously mentioned methods, the proposed IMUs do not need the aircraft dynamic model to facilitate its job, yet it can be used to enhance the estimation results obtained, which broaden the range of application they can be used in. In [35], a spacecraft center of mass was estimated online using multi-accelerometers under the assumption of zero linear acceleration when the spacecraft is in steady mode and the position of center of mass is not changing, then equation (34) can be very much simplified and the position of center of mass was estimated using a recursive least squares method. Here, the CoG is allowed to move and inertial acceleration may or may not exist. In the case where there is no angular motion, an estimation of CoG position may be flagged as unavailable, and the flight controller may keep the previous position. The error covariance is an indication of the estimation quality so that it can be checked before critical decisions can be taken.

The main contribution of this technique, besides finding the linear and angular accelerations and angular velocity, is the ability to use it in CoG position estimation which was not tackled before using this approach in such configurations, to the best of the author's knowledge.

The performance of the proposed IMU in [7], will be improved as well be shown in the next chapter.

CHAPTER 6

FILTER DESIGN

This part is very important in the sense that it provides an extraction method to retrieve the angular motion, needed to facilitate the CoG kinematics estimation and other INS tasks, from the available accelerometers measurements. As all-accelerometers IMUs depend only on the usage of linear accelerometers in certain configurations; hence no rate gyros are involved here as may be found in other IMUs. As a result of that, a dedicated filter is needed to extract the vehicle's angular motion from the accelerometers measurements. The structure of the needed filter depends heavily upon the equations representing the angular motion. Different dynamical systems were stated; however only some of them were actually used to build different types of filters. In the previous Chapter, a quick overview of the IMU presented by [7], and the newly proposed one was given including a filter based on forward-finite difference approximation for which the performance was shown in the associated figures. Here, more details about different types of filters are presented and evaluated to facilitate implementing some of them in later stages. Next, a brief literature review about the usage of filters in IMUs and INS in general to solve various problems is presented.

6.1 Literature Review

In [72], a matrix Kalman Filter (MKF) for a non-linear integrated navigation system using magnetic, inertial, and visual sensors was implemented and a pseudo-linear model was obtained. Lie derivatives were used to find the observability conditions of the non-linear system.

Calibration of INS errors was done through the usage of other sensors, such as magnetic and cameras sensors, since GPS is not available indoor. The magnetic sensor is able to, by sensing the earth's magnetic field; provide a drift-free estimate of the heading direction.

In [73], the non-linearity of Kalman Filter measurements resulting from the ultra-tight integration of INS and GPS will seriously affect the filtering results. Both a traditional and Extended Kalman Filters (EKF) are designed for such systems where the design of the Extended Kalman Filter depends upon its performance on stability, controllability, and observability obtained from the theoretical analysis of the traditional one. Implementation of EKF resulted in better estimation of all navigation parameters.

GPS/INS integrated systems can be operating in three modes, namely: loose, tight, and ultra-tight, where in the:

- 1- Loose mode: INS and GPS work separately and treated as independent navigation sensors.
- 2- Tight mode: GPS receiver must zone at least four satellites steadily to ensure the system operates the same as the loose mode, through the usage of data fusion.
- 3- Ultra-tight: Software and hardware are combined through data fusion, and it:

- Gives better performance than loose and tight modes.
- Navigation output can be provided with less than four satellites.
- Improved noise rejection and dynamic robustness of the entire system.
- Can be realized through direct/indirect methods.

In [74], the simulation of a robust H_∞ filter showed a quick transient response and a more accurate estimate than Kalman Filter designed to solve the problem of initial alignment of an integrated strapdown INS.

The traditional Kalman Filter expects dealing with white noises, and that requires the system and measurement noises to be with well-known statistical properties, which is practically difficult to have. It was shown that the Kalman Filter is better than that of H_∞ Filter for white noise, and the opposite is true for colored and uncertain noise.

In [75], a 2D navigation for land vehicle is achieved by integrating a low-cost single-axis, MEMS-based gyroscope, the vehicle odometer, and a GPS in a loosely integration configuration. The gyroscope and odometer are used to build a low-cost reduced inertial sensor system (RISS), which suffers from the non-stationary stochastic sensor errors and non-linear inertial sensors errors which cannot be handled by a Kalman Filter (KF) and its linearized error models. First order approximation on non-linear systems is used in the Extended Kalman Filter (EKF) which, as stated in [75], may cause poor performance and sometimes the divergence of the filter for systems with high non-linearity, while an Unscented Kalman Filter (UKF) is considered a better alternative that can provide better performance in the expense of increased computing time compared to EKF.

A Fast Orthogonal Search (FOS) algorithm with augmented KF was presented in [75] to deal with the non-stationary stochastic sensor errors problem. FOS needs to have some information about the system needed to be modeled which is not the case in Parallel Cascade Identification (PCI) technique.

Sensors' errors are of two types, namely: the deterministic parts and the stochastic parts, the former should be compensated for in navigation algorithm, whereas the later like bias drift is usually modeled as random processes. FOS was introduced by Korenberg (1987) and it is a numerical technique used to find the difference equations of a non-linear system. It can also be used in non-linear system identification.

In [76], a Robust Kalman Filter (RKF) structure was used to facilitate in-motion alignment for a low-cost strapdown IMU. Strapdown Inertial Navigation Systems (SINS) error model was derived with velocity, attitude, position, and sensor errors as the state vector. GPS measurements were used to provide velocity information was employed as a measurement to the filter. Navigation parameters were better estimated.

Outliers deteriorate the performance of a Kalman Filter, so a RKF have to meet two objectives, namely:

- 1- Be nearly optimal when outliers are absent.
- 2- Immune to outliers when they exist.

In [77], an innovation based on adaptive EKF, for adopting dynamics model covariance matrix Q and measurement noise covariance matrix R , was used to improve navigation system performance during GPS signal outages. This approach takes care of the varying

errors found in INS by adaptively varying the Q and R matrices used in EKF resulting in smaller estimation error once compared to a standard EKF.

In [78], an Adaptive Two-stage Extended Kalman Filter (ATEKF) for a fault-tolerant INS-GPS loosely coupled system was introduced. This ATEKF estimated the unknown bias effectively. An EKF may not be able to estimate effectively the time-varying unknown parameters while an ATEKF can do that efficiently.

6.2 Filter Design

As can be seen from the previous literature, the usage of filters is highly involved when solving problems related to INS. However, in this thesis the main focus regarding the usage of filters can be summarized in Figure 35. Future work may include other types of filters to solve other problems usually encountered when strapdown IMUs are used.

In the proposed IMU, filters are needed at the following stages:

1. Filter accelerometer measurements by removing bias, drift, cross couplings, disorientations, misalignments, and geometric problems (i.e. vibration, etc.).
2. Find Ω_x , Ω_y , and Ω_z (angular velocities) estimation in the body frame.
3. Use Ω_x , Ω_y , and Ω_z to find the vehicle attitude (using quaternion or Directional Cosine Matrix DCM).
4. Find vehicle's inertial velocity and position:
 - a. With respect to body frame \rightarrow projects them onto the navigation frame using quaternion or DCM.

- b. Project the acceleration onto the navigation frame → finds them with respect to the navigation frame.

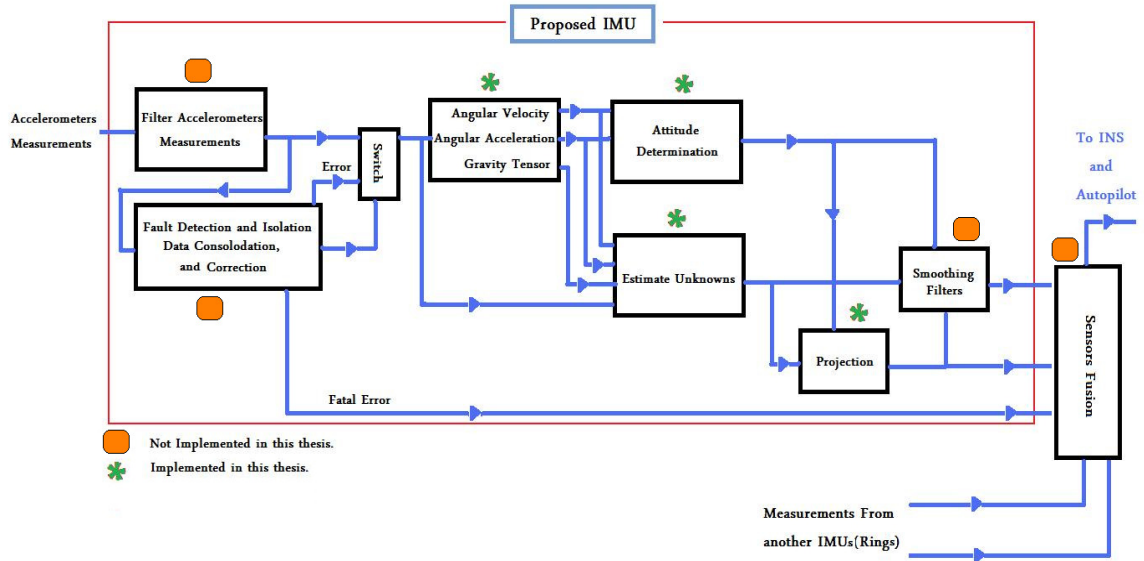


Figure 35: The usage of Filters within the proposed IMU.

Note: the previous options must be chosen according to error analysis, where the less erroneous method should be used.

5. Optimal Smoothers to refine the estimated parameters.
6. Distributed Sensors Data Fusion (at IMU, i.e. Rings, level).

Next, the possible differential equations that can be used in Filter design for both the IMU presented in [7] and the one proposed here are presented along with a modified version of the IMU presented in [7]. The possible equations have been stacked in 3×3 matrix format to ease equations manipulation.

- Formulation of System equations using the setup proposed in [7]:

Reference should be made to Figure 20.

Table 2: IMU Kinematics Equations for Systems 1 and 2.

$\begin{bmatrix} 0 & \frac{\vec{A}_1 - \vec{A}_2}{2\mu} & \frac{\vec{A}_3 - \vec{A}_4}{2\mu} \end{bmatrix} = \left(\begin{bmatrix} 0 & -\dot{\Omega}_z & \dot{\Omega}_y \\ 0 & 0 & -\dot{\Omega}_x \\ 0 & \dot{\Omega}_x & 0 \end{bmatrix} + \begin{bmatrix} 0 & \Omega_x \Omega_y & \Omega_x \Omega_z \\ 0 & -\Omega_z^2 - \Omega_x^2 & \Omega_z \Omega_y \\ 0 & \Omega_z \Omega_y & -\Omega_y^2 - \Omega_x^2 \end{bmatrix} \right)$	
System 1 (Unstable-nonlinear)	System 2 (Unstable-nonlinear)
$\dot{\Omega}_x = \frac{1}{4\mu} (A_{1z} - A_{2z} - A_{3y} + A_{4y})$	$\dot{\Omega}_x = -\Omega_z \Omega_y + \frac{1}{2\mu} (A_{1z} - A_{2z})$
$\dot{\Omega}_y = -\Omega_x \Omega_z + \frac{1}{2\mu} (A_{3x} - A_{4x})$	$\dot{\Omega}_y = -\Omega_x \Omega_z + \frac{1}{2\mu} (A_{3x} - A_{4x})$
$\dot{\Omega}_z = \Omega_x \Omega_y - \frac{1}{2\mu} (A_{1x} - A_{2x})$	$\dot{\Omega}_z = \Omega_x \Omega_y - \frac{1}{2\mu} (A_{1x} - A_{2x})$

From the above table, where \vec{A}_i denotes a 3×1 vector, two systems can be obtained one is marginally stable and the other is unstable. New system is described mathematically in Table 3.

- New formulation of System equations using the setup proposed in [7]:

Reference should be made to Figure 20.

Table 3: IMU Kinematics Equations for Systems 3 and 4.

$\begin{bmatrix} \frac{\vec{A}_1 - \vec{A}_5}{L} & \frac{\vec{A}_1 - \vec{A}_2}{2\mu} & \frac{\vec{A}_3 - \vec{A}_4}{2\mu} \end{bmatrix} = ([\dot{\Omega}] + [\Omega \times])$	
$\begin{bmatrix} \frac{\vec{A}_1 - \vec{A}_5}{L} & \frac{\vec{A}_1 - \vec{A}_2}{2\mu} & \frac{\vec{A}_3 - \vec{A}_4}{2\mu} \end{bmatrix} = \left(\begin{bmatrix} 0 & -\dot{\Omega}_z & \dot{\Omega}_y \\ \dot{\Omega}_z & 0 & -\dot{\Omega}_x \\ -\dot{\Omega}_y & \dot{\Omega}_x & 0 \end{bmatrix} + \begin{bmatrix} -\Omega_z^2 - \Omega_y^2 & \Omega_x \Omega_y & \Omega_x \Omega_z \\ \Omega_x \Omega_y & -\Omega_z^2 - \Omega_x^2 & \Omega_z \Omega_y \\ \Omega_x \Omega_z & \Omega_z \Omega_y & -\Omega_y^2 - \Omega_x^2 \end{bmatrix} \right)$	
System 3 (Unstable-nonlinear)	System 4 (stable-linear)
$\dot{\Omega}_x = -\Omega_z \Omega_y + \frac{1}{2\mu} (A_{1z} - A_{2z})$	$\dot{\Omega}_x = \frac{1}{4\mu} (A_{1z} - A_{2z} - A_{3y} + A_{4y})$

$\dot{\Omega}_y = -\Omega_x\Omega_z + \frac{1}{2\mu}(A_{3x} - A_{4x})$	$\dot{\Omega}_y = \frac{-1}{2L}(A_{1z} - A_{5z}) + \frac{1}{4\mu}(A_{3x} - A_{4x})$
$\dot{\Omega}_z = -\Omega_x\Omega_y + \frac{1}{L}(A_{1y} - A_{5y})$	$\dot{\Omega}_z = \frac{1}{2L}(A_{1y} - A_{5y}) - \frac{1}{4\mu}(A_{1x} - A_{2x})$
(1-D) Measurements Equations (nonlinear)	(3-D) Measurements Equations (nonlinear)
$\frac{1}{L}(A_{5x} - A_{1x}) = \Omega_z^2 + \Omega_y^2$	$\frac{1}{4\mu L}(4\mu(A_{5x} - A_{1x}) + L(A_{3y} - A_{4y} + A_{1z} - A_{2z}))$ $= \Omega_z^2 + \Omega_y^2 + \Omega_z\Omega_y$
$\frac{1}{2\mu}(A_{2y} - A_{1y}) = \Omega_z^2 + \Omega_x^2$	$\frac{1}{4\mu L}(LA_{3x} - LA_{4x} + 2L(A_{2y} - A_{1y}) + 2\mu(A_{1z} - A_{5z}))$ $= \Omega_x^2 + \Omega_z^2 + \Omega_z\Omega_x$
$\frac{1}{2\mu}(A_{4z} - A_{3z}) = \Omega_y^2 + \Omega_x^2$	$\frac{1}{4\mu L}(LA_{1x} - LA_{2x} + 2\mu(A_{1y} - A_{5y}) + 2L(A_{4z} - A_{3z}))$ $= \Omega_x^2 + \Omega_y^2 + \Omega_x\Omega_y$

As can be seen from Table 3, the new system formulation, namely System 3 suffers from the same problem of instability, while System 4 dynamics depends on the accelerometers' measurements and this system will be stable as long as those measurements are bounded; so System 4 will be used in this Chapter.

- Formulation of the IMU equations Proposed in this thesis:

Reference should be made to Figure 22.

Table 4: IMU Kinematics Equations for Systems 5 and 6.

$\begin{bmatrix} \frac{\vec{A}_1 - \vec{A}_2}{2\mu} & \frac{\vec{A}_3 - \vec{A}_4}{2\mu} & \frac{\vec{A}_5 - \vec{A}_6}{2\mu} \end{bmatrix} = ([\dot{\Omega}] + [\Omega \times])$
$\begin{bmatrix} \frac{\vec{A}_1 - \vec{A}_2}{2\mu} & \frac{\vec{A}_3 - \vec{A}_4}{2\mu} & \frac{\vec{A}_5 - \vec{A}_6}{2\mu} \end{bmatrix} = \left(\begin{bmatrix} 0 & -\dot{\Omega}_z & \dot{\Omega}_y \\ \dot{\Omega}_z & 0 & -\dot{\Omega}_x \\ -\dot{\Omega}_y & \dot{\Omega}_x & 0 \end{bmatrix} + \begin{bmatrix} -\Omega_z^2 - \Omega_y^2 & \Omega_x\Omega_y & \Omega_x\Omega_z \\ \Omega_x\Omega_y & -\Omega_z^2 - \Omega_x^2 & \Omega_z\Omega_y \\ \Omega_x\Omega_z & \Omega_z\Omega_y & -\Omega_y^2 - \Omega_x^2 \end{bmatrix} \right)$

System 5 (Unstable-nonlinear)	System 6 (stable-linear)
$\dot{\Omega}_x = -\Omega_z\Omega_y + \frac{1}{2\mu}(A_{3z} - A_{4z})$	$\dot{\Omega}_x = \frac{1}{4\mu}(A_{3z} - A_{4z} - A_{5y} + A_{6y})$
$\dot{\Omega}_y = -\Omega_x\Omega_z + \frac{1}{2\mu}(A_{5x} - A_{6x})$	$\dot{\Omega}_y = \frac{1}{4\mu}(A_{5x} - A_{6x} - A_{1z} + A_{2z})$
$\dot{\Omega}_z = -\Omega_x\Omega_y + \frac{1}{2\mu}(A_{1y} - A_{2y})$	$\dot{\Omega}_z = \frac{1}{4\mu}(A_{1y} - A_{2y} - A_{3x} + A_{4x})$
(1-D) Measurements Equations (nonlinear)	(3-D)Measurements Equations (nonlinear)
$\frac{1}{2\mu}(A_{2x} - A_{1x}) = \Omega_z^2 + \Omega_y^2$	$\frac{1}{4\mu}(2A_{2x} - 2A_{1x} + A_{5y} - A_{6y} + A_{3z} - A_{4z}) = \Omega_z^2 + \Omega_y^2 + \Omega_z\Omega_y$
$\frac{1}{2\mu}(A_{4y} - A_{3y}) = \Omega_z^2 + \Omega_x^2$	$\frac{1}{4\mu}(A_{5x} - A_{6x} + 2A_{4y} - 2A_{3y} + A_{1z} - A_{2z}) = \Omega_x^2 + \Omega_z^2 + \Omega_z\Omega_x$
$\frac{1}{2\mu}(A_{6z} - A_{5z}) = \Omega_y^2 + \Omega_x^2$	$\frac{1}{4\mu}(A_{3x} - A_{4x} + A_{1y} - A_{2y} + 2A_{6z} - 2A_{5z}) = \Omega_x^2 + \Omega_y^2 + \Omega_x\Omega_y$

System 5 is also unstable and that actually was reported in [45]; hence the same procedure done before with System 4 is done again to produce a stable version of the proposed IMU resulting in System 6 as can be found in Table 4, so System 6 will be used in the remainder of this thesis.

- Comparison between System 4 and System 6:

The new formulation of System 4 introduces a coupling between the measurements of the two rings which puts a demand over the used network that connects them to provide the measurements without considerable latency. This will raise the concern about the network availability and latency which must also be reflected on the filter design problem. Such problems are beyond the objective of this thesis. Other than this coupling,

the main difference between systems 4 and 6 is that system 4 depends on the values of (L), i.e. the separation between the two rings, and (μ). In this case, some analysis must be done to determine the effect of (L) and its relation with (μ); since they affect the quality of angular acceleration estimated using the accelerometers' measurements. As (μ) increases, the estimation of angular acceleration would be better and the opposite is true. The increased value of (μ) comes on the expenses of increased sensitivity to structural vibrations and design sizing limitation, so the problem is not that easy as it may seems from the first glance. Now, the effect of ($L \gg \mu$) can be reflected on Systems 4 as follows:

Table 5: IMU Kinematics Equations for Systems 4 when ($L \gg \mu$).

System 4* (stable-linear)	
$\dot{\Omega}_x = \frac{1}{4\mu} (A_{1z} - A_{2z} - A_{3y} + A_{4y})$	
$\dot{\Omega}_y \approx \frac{1}{4\mu} (A_{3x} - A_{4x})$	
$\dot{\Omega}_z \approx -\frac{1}{4\mu} (A_{1x} - A_{2x})$	
(1-D) Measurements Equations* (nonlinear)	(3-D) Measurements Equations* (nonlinear)
$0 \approx \Omega_z^2 + \Omega_y^2$	$\frac{1}{4\mu} (A_{3y} - A_{4y} + A_{1z} - A_{2z}) \approx \Omega_z^2 + \Omega_y^2 + \Omega_z \Omega_y$
$\frac{1}{2\mu} (A_{2y} - A_{1y}) \approx \Omega_z^2 + \Omega_x^2$	$\frac{1}{4\mu} (A_{3x} - A_{4x} + 2(A_{2y} - A_{1y})) \approx \Omega_x^2 + \Omega_z^2 + \Omega_z \Omega_x$
$\frac{1}{2\mu} (A_{4z} - A_{3z}) \approx \Omega_y^2 + \Omega_x^2$	$\frac{1}{4\mu} (A_{1x} - A_{2x} + 2(A_{4z} - A_{3z})) \approx \Omega_x^2 + \Omega_y^2 + \Omega_x \Omega_y$

As ($L \gg \mu$), the coupling between the two Rings is reduced. So, once System 4 is considered, it is worth investigating such condition. In fact, the error analysis is essential

to see the full picture each parameter is affecting the System with, and this will be a subject for future work, see Chapter 10.

6.2.1 Models used in Filter Design

In this chapter, the following filters are to be investigated, namely:

1. Extended Kalman Filter EKF.
2. Unscented Kalman Filter UKF.

System 4 and 6 are of concern in this chapter; since System 4 is considered an improvement for what was proposed originally in [7] and its performance need to be examined, while System 6 is the one to be used in the proposed IMU in this thesis.

Since the interest is in implementing the filter on a digital computer, one have to use the discrete version of Kalman Filters (KFs) but before that the previous systems must be converted into difference equations.

- Discrete Version of System 4:

Using the backward finite-difference approximation for the first derivative, System 4 can be discretized as shown in Table 6.

Table 6: Discrete Version of System 4

System 4 (linear)	Measurements Equations (nonlinear)
$\Omega_x(k) = \Omega_x(k-1) + \frac{T}{4\mu}(A_{1z} - A_{2z} - A_{3y} + A_{4y})$	$\frac{1}{L}(A_{5x} - A_{1x}) = \Omega_z^2(k) + \Omega_y^2(k)$
$\Omega_y(k) = \Omega_y(k-1) - \frac{T}{2L}(A_{1z} - A_{5z}) + \frac{T}{(4\mu)}(A_{3x} - A_{4x})$	$\frac{1}{2\mu}(A_{2y} - A_{1y}) = \Omega_z^2(k) + \Omega_x^2(k)$
$\Omega_z(k) = \Omega_z(k-1) + \frac{T}{2L}(A_{1y} - A_{5y}) - \frac{T}{4\mu}(A_{1x} - A_{2x})$	$\frac{1}{2\mu}(A_{4z} - A_{3z}) = \Omega_y^2(k) + \Omega_x^2(k)$

- Discrete Version of System 6:

Using the backward finite-difference approximation for the first derivative, System 6 can also be discretized as shown in Table 7.

Table 7: Discrete Version of System 6

System 6 (linear)	Measurements Equations (nonlinear)
$\Omega_x(k) = \Omega_x(k-1) + \frac{T}{4\mu}(A_{3z} - A_{4z} - A_{5y} + A_{6y})$	$\frac{1}{2\mu}(A_{2x} - A_{1x}) = \Omega_z^2(k) + \Omega_y^2(k)$
$\Omega_y(k) = \Omega_y(k-1) + \frac{T}{4\mu}(A_{5x} - A_{6x} - A_{1z} + A_{2z})$	$\frac{1}{2\mu}(A_{4y} - A_{3y}) = \Omega_z^2(k) + \Omega_x^2(k)$
$\Omega_z(k) = \Omega_z(k-1) + \frac{T}{4\mu}(A_{1y} - A_{2y} - A_{3x} + A_{4x})$	$\frac{1}{2\mu}(A_{6z} - A_{5z}) = \Omega_y^2(k) + \Omega_x^2(k)$

➤ Extended Kalman Filter:

Since the system equations are linear and the measurements equations are non-linear in both systems 4 and 6, an EKF can be used to retrieve the angular velocities. Different measurements model will be investigated, namely: 1-D, 2-D, and 3-D measurement models. The previously shown discrete versions of Systems 4 and 6 are used along the procedure depicted in Figure 36 to build the intended first-order discrete-EKFs.

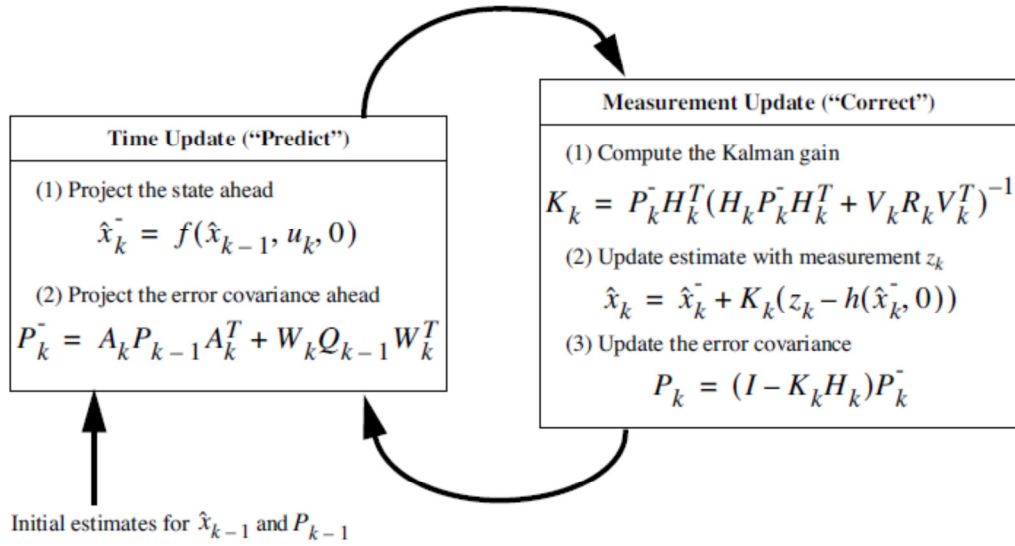


Figure 36: Extended Kalman Filter Layout. ^[80]

For both Systems 4 and 6, the matrices found in Figure 36 are given as follows:

$$A_k = W_k = V_k = eye(3)$$

$$R_k = \sigma_1^2 eye(3), \quad Q_k = \sigma_2^2 eye(3) \quad (65)$$

Where: σ_1^2 and σ_2^2 are the measurement and process noise variances respectively.

The available measurement models for both Systems 4 and 6 are given as follows:

➤ System 4 Measurements Models:

Reference must be made to Figure 20.

Note that for the equations in the second Ring, every (L) must be replaced with (-L).

• 1-D Measurements Model:

Table 8: 1-D Measurement Model for System 4.

(1-D) Measurements Equations (nonlinear)
$\frac{1}{L}(A_{5x} - A_{1x}) = \Omega_z^2(k) + \Omega_y^2(k)$
$\frac{1}{2\mu}(A_{2y} - A_{1y}) = \Omega_z^2(k) + \Omega_x^2(k)$
$\frac{1}{2\mu}(A_{4z} - A_{3z}) = \Omega_y^2(k) + \Omega_x^2(k)$

• 2-D Measurements Model:

Table 9: 2-D Measurement Model for System 4.

(2-D) Measurements Equations (nonlinear)
$\frac{1}{4\mu}(A_{3y} - A_{4y} + A_{1z} - A_{2z}) = \Omega_z\Omega_y$
$\frac{1}{4\mu L}(L(A_{3x} - A_{4x}) + 2\mu(A_{1z} - A_{5z})) = \Omega_z\Omega_x$
$\frac{1}{4\mu L}(L(A_{1x} - A_{2x}) + 2\mu(A_{1y} - A_{5y})) = \Omega_x\Omega_y$

• 3-D Measurements Model:

Table 10: 3-D Measurement Model for System 4.

(3-D) Measurements Equations (nonlinear)
$\frac{1}{4\mu L} (4\mu(A_{5x} - A_{1x}) + L(A_{3y} - A_{4y} + A_{1z} - A_{2z})) = \Omega_z^2 + \Omega_y^2 + \Omega_z\Omega_y$
$\frac{1}{4\mu L} (L(A_{3x} - A_{4x}) + 2L(A_{2y} - A_{1y}) + 2\mu(A_{1z} - A_{5z})) = \Omega_x^2 + \Omega_z^2 + \Omega_z\Omega_x$
$\frac{1}{4\mu L} (L(A_{1x} - A_{2x}) + 2\mu(A_{1y} - A_{5y}) + 2L(A_{4z} - A_{3z})) = \Omega_x^2 + \Omega_y^2 + \Omega_x\Omega_y$

➤ System 6 Measurements Models:

Reference must be made to Figure 22.

- 1-D Measurements Model:

Table 11: 1-D Measurement Model for System 6.

(1-D) Measurements Equations (nonlinear)
$\frac{1}{2\mu} (A_{2x} - A_{1x}) = \Omega_z^2 + \Omega_y^2$
$\frac{1}{2\mu} (A_{4y} - A_{3y}) = \Omega_z^2 + \Omega_x^2$
$\frac{1}{2\mu} (A_{6z} - A_{5z}) = \Omega_y^2 + \Omega_x^2$

- 2-D Measurements Model:

Table 12: 2-D Measurement Model for System 6.

(2-D) Measurements Equations (nonlinear)
$\frac{1}{4\mu}(A_{5y} - A_{6y} + A_{3z} - A_{4z}) = \Omega_z\Omega_y$
$\frac{1}{4\mu}(A_{5x} - A_{6x} + A_{1z} - A_{2z}) = \Omega_z\Omega_x$
$\frac{1}{4\mu}(A_{3x} - A_{4x} + A_{1y} - A_{2y}) = \Omega_x\Omega_y$

- 3-D Measurements Model:

Table 13: 3-D Measurement Model for System 6.

(3-D)Measurements Equations (nonlinear)
$\frac{1}{4\mu}(2A_{2x} - 2A_{1x} + A_{5y} - A_{6y} + A_{3z} - A_{4z}) = \Omega_z^2 + \Omega_y^2 + \Omega_z\Omega_y$
$\frac{1}{4\mu}(A_{5x} - A_{6x} + 2A_{4y} - 2A_{3y} + A_{1z} - A_{2z}) = \Omega_x^2 + \Omega_z^2 + \Omega_z\Omega_x$
$\frac{1}{4\mu}(A_{3x} - A_{4x} + A_{1y} - A_{2y} + 2A_{6z} - 2A_{5z}) = \Omega_x^2 + \Omega_y^2 + \Omega_x\Omega_y$

The measurement matrix (H) for Systems 4 and 6 obtained after linearization are given as follows:

Table 14: Measurement Matrix for Systems 4 and 6, linearized version.

1-D	2-D	3-D
$H = 2 \begin{bmatrix} 0 & \Omega_y & \Omega_z \\ \Omega_x & 0 & \Omega_z \\ \Omega_x & \Omega_y & 0 \end{bmatrix}$	$H = \begin{bmatrix} 0 & \Omega_z & \Omega_y \\ \Omega_z & 0 & \Omega_x \\ \Omega_y & \Omega_x & 0 \end{bmatrix}$	$H = \begin{bmatrix} 0 & 2\Omega_y + \Omega_z & 2\Omega_z + \Omega_y \\ 2\Omega_x + \Omega_z & 0 & 2\Omega_z + \Omega_x \\ 2\Omega_x + \Omega_y & 2\Omega_y + \Omega_x & 0 \end{bmatrix}$

6.2.2 Simulation Results of System 4 with different Measurement Models Using EKF

A Simulink model, shown in Figure 37, was used to simulate System 4 in which the coupling between the two Rings is clearly shown. The two Rings were added to the SimMechanics Machine previously shown in Figure 23.

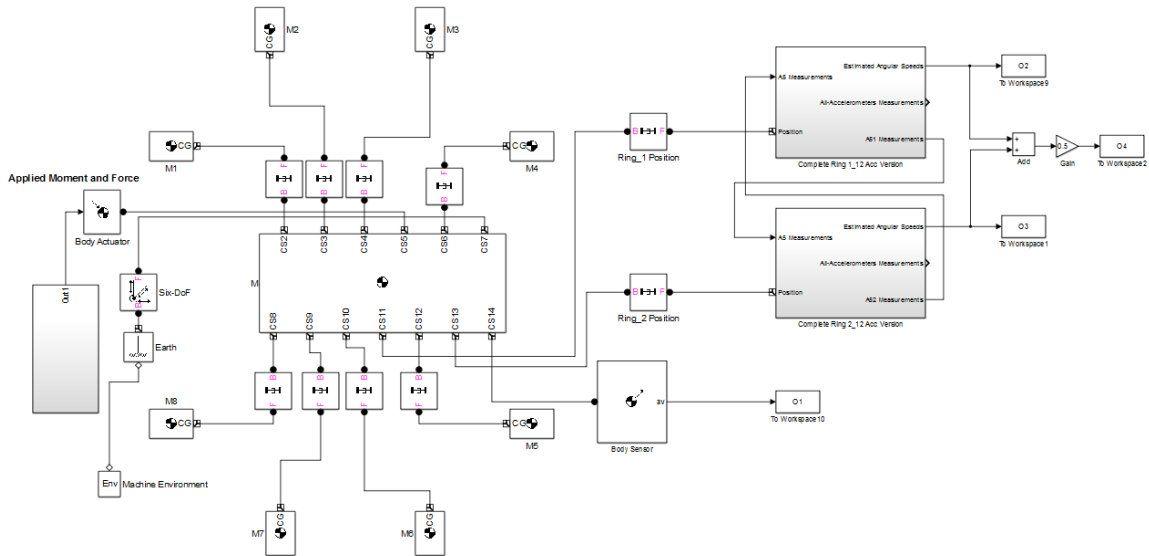


Figure 37: Simulink Model Used to Test System 4 with Different Measurement Models.

- System 4: ($L = 1\text{ m}$, $\mu = 0.1\text{ m}$) with (1-D) Measurements Equations

Next, only the results obtained from the first ring are displayed; since they are similar to those obtained from the second ring and from the averaged values. Figure 37 clearly shows the coupling between the measurements of the two Rings which put a demand on the sensor network used as was previously discussed.

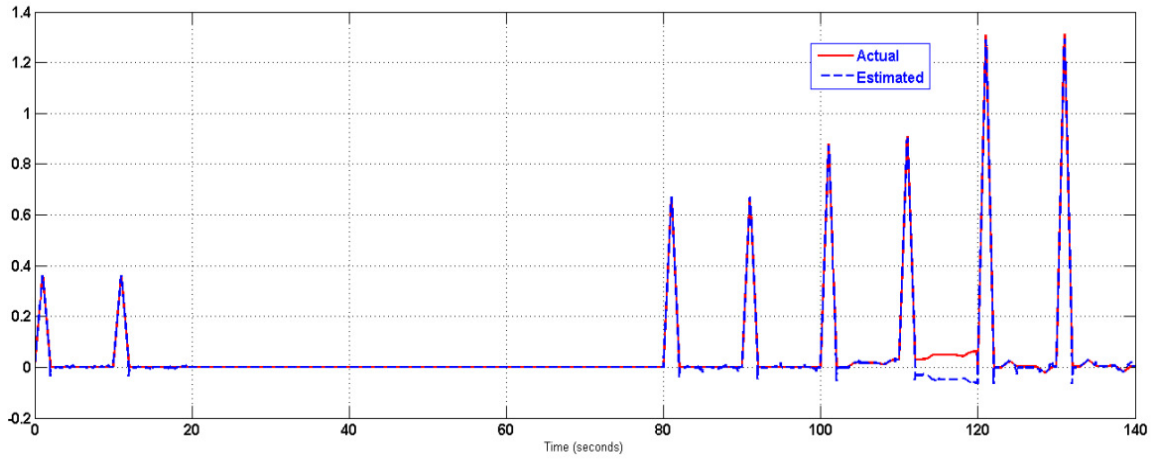


Figure 38: Composite Body Angular Velocity about X-axis (rad/sec) using 12-accelerometer/Ring in Two-Ring Configuration.

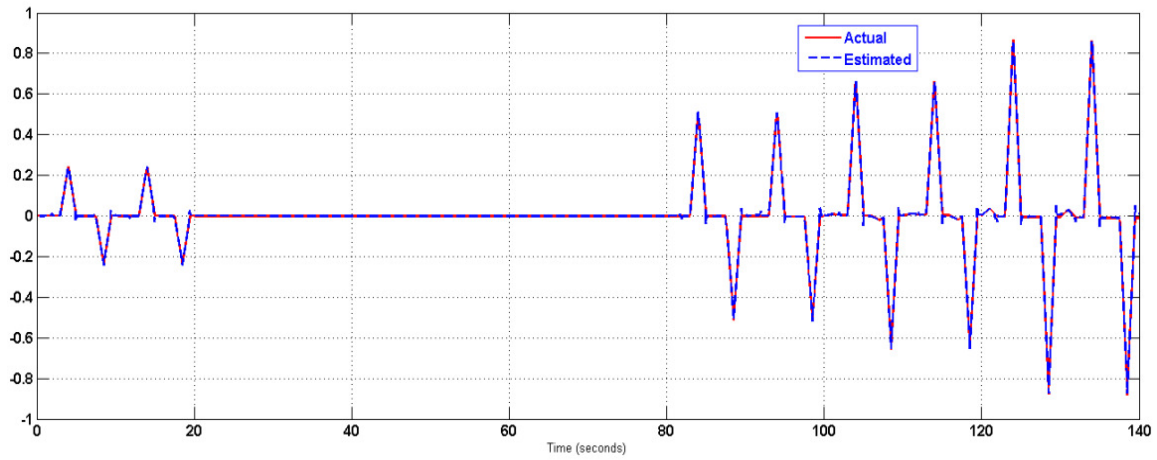


Figure 39: Composite Body Angular Velocity about Y-axis (rad/sec) using 12-accelerometer/Ring in Two-Ring Configuration.

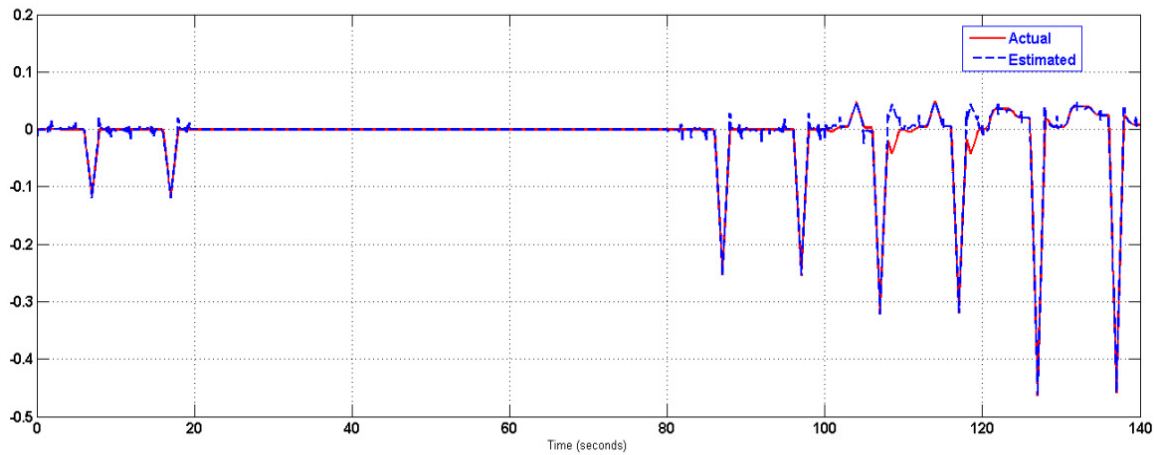


Figure 40: Composite Body Angular Velocity about Z-axis (rad/sec) using 12-accelerometer/Ring in Two-Ring Configuration.

It is obvious that the performance of System 4 using the EKF is very good except in the interval [112-120] seconds where there is an inversion in the estimation for the X and Z angular velocities, a closer view on the Z angular velocity is shown within this interval where the symmetry is obvious, see Figure 41. This problem is due to the angular velocity sign ambiguity which cannot be determined using the available non-linear terms.

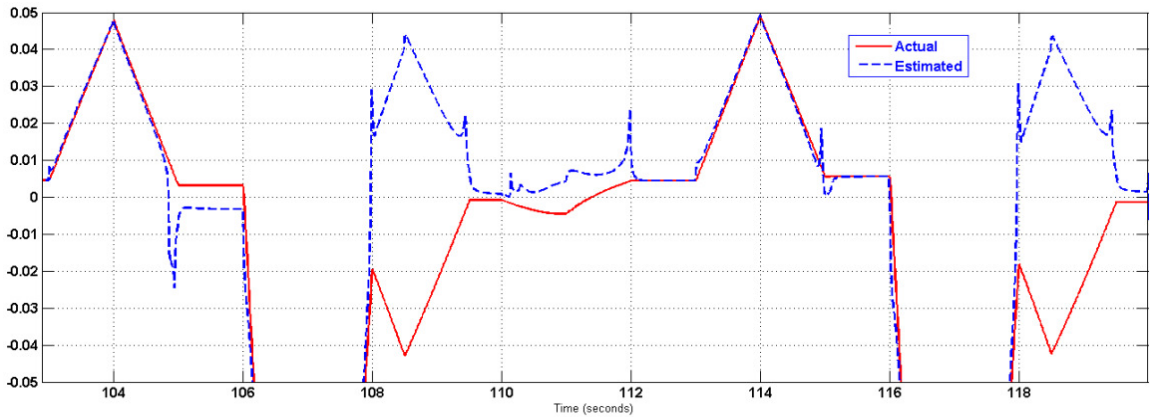


Figure 41: Composite Body Angular Velocity about Z-axis (rad/sec) using 12-accelerometer/Ring in Two-Ring Configuration, a close view.

➤ Second-order discrete-EKFs

It was shown in [81] that the state prediction of the second-order discrete-EKF is given by:

$$\hat{x}_{k+1}^- = f(\hat{x}_k^+, u_k, k) + \frac{1}{2} \sum_{i=1}^n \phi_i Tr \left[\left. \frac{\partial^2 f_i}{\partial x^2} \right|_{\hat{x}_k^+} P_k^+ \right] \quad (66)$$

$$F = \left. \frac{\partial f}{\partial x} \right|_{\hat{x}_k^+} = \begin{bmatrix} 1 & 0 & 0 \\ 0 & 1 & 0 \\ 0 & 0 & 1 \end{bmatrix}$$

From the above equations, it is clear that the second-order EKF will be equivalent to the first-order discrete-time EKF; so it will not be implemented here.

Now, instead of using the usual approach of discretization that depends on the usage of gradients, the backward finite-difference approximation for the first derivative, given in equation (65), see [82], is used as follows:

$$\dot{f}(x_i) = \frac{f(x_{i-2}) - 4f(x_{i-1}) + 3f(x_i)}{2T} \quad (67)$$

Where, (T) is the sampling interval. Now, proceed as follows:

$$\text{Define } X = [\Omega_x \quad \Omega_y \quad \Omega_z]^T \quad (68)$$

$$X(k) = \frac{4}{3}X(k-1) - \frac{1}{3}X(k-2) + \frac{2}{3}Tm(k)$$

Where, $m(k)$ is the vector containing the accelerometers' measurements inputs.

Define,

$$X_1(k) = X(k-2), \quad X_1(k+1) = X(k-1) = X_2(k)$$

$$X_2(k+1) = X(k) = \frac{4}{3}X_2(k) - \frac{1}{3}X_1(k) + \frac{2}{3}Tm(k)$$

$$\begin{bmatrix} X_1(k+1) \\ X_2(k+1) \end{bmatrix} = \begin{bmatrix} \text{zeros}(3) & \text{eye}(3) \\ -\frac{1}{3} * \text{eye}(3) & \frac{4}{3} * \text{eye}(3) \end{bmatrix} \begin{bmatrix} X_1(k) \\ X_2(k) \end{bmatrix} + \begin{bmatrix} \text{zeros}(3) \\ \frac{2}{3}T * \text{eye}(3) \end{bmatrix} m(k) \quad (69)$$

$$Y(k) = \begin{bmatrix} 0 & 1 & 1 \\ 1 & 0 & 1 \\ 1 & 1 & 0 \end{bmatrix} * \text{diag}(X_1(k)) * X_1(k) = C * \text{diag}(X_1(k)) * X_1(k)$$

Now, the system is given by:

$$\begin{bmatrix} X_1(k+1) \\ X_2(k+1) \end{bmatrix} = \begin{bmatrix} \text{zeros}(3) & \text{eye}(3) \\ -\frac{1}{3} * \text{eye}(3) & \frac{4}{3} * \text{eye}(3) \end{bmatrix} \begin{bmatrix} X_1(k) \\ X_2(k) \end{bmatrix} + \begin{bmatrix} \text{zeros}(3) \\ \frac{2}{3}T * \text{eye}(3) \end{bmatrix} m(k) \quad (70)$$

$$Y(k) = \begin{bmatrix} Y_1(k) \\ Y_2(k) \end{bmatrix} = \begin{bmatrix} C_1 & \text{zeros}(3) \\ \text{zeros}(3) & \text{zeros}(3) \end{bmatrix} \begin{bmatrix} X_1(k) \\ X_2(k) \end{bmatrix}$$

$$A = \begin{bmatrix} \text{zeros}(3) & \text{eye}(3) \\ -\frac{1}{3} * \text{eye}(3) & \frac{4}{3} * \text{eye}(3) \end{bmatrix}, B = \begin{bmatrix} \text{zeros}(3) \\ \frac{2}{3} T * \text{eye}(3) \end{bmatrix}$$

$$H = \begin{bmatrix} C_1 & \text{zeros}(3) \\ \text{zeros}(3) & \text{zeros}(3) \end{bmatrix}, C_1 = \begin{bmatrix} 0 & \Omega_y & \Omega_z \\ \Omega_x & 0 & \Omega_z \\ \Omega_x & \Omega_y & 0 \end{bmatrix}$$

By applying the EKF equations, as previously shown in Figure 36 using the matrices given in (70), System 4 gives approximately the same results and it did not solve the sign ambiguity problem. The results are as follows:

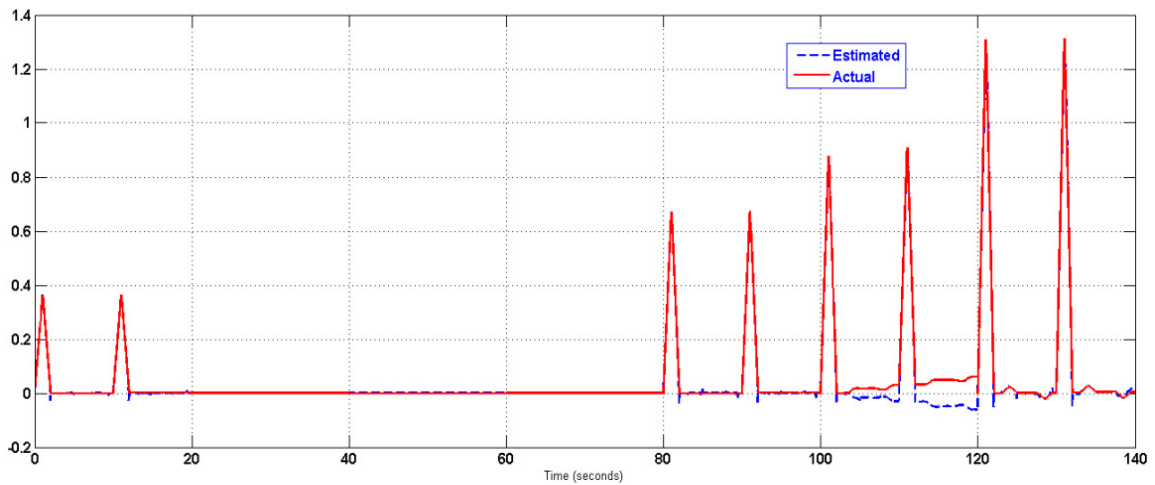


Figure 42: Composite Body Angular Velocity about X-axis (rad/sec) using 12-accelerometer/Ring in Two-Ring Configuration, L = 1m, with 1-D measurement model.

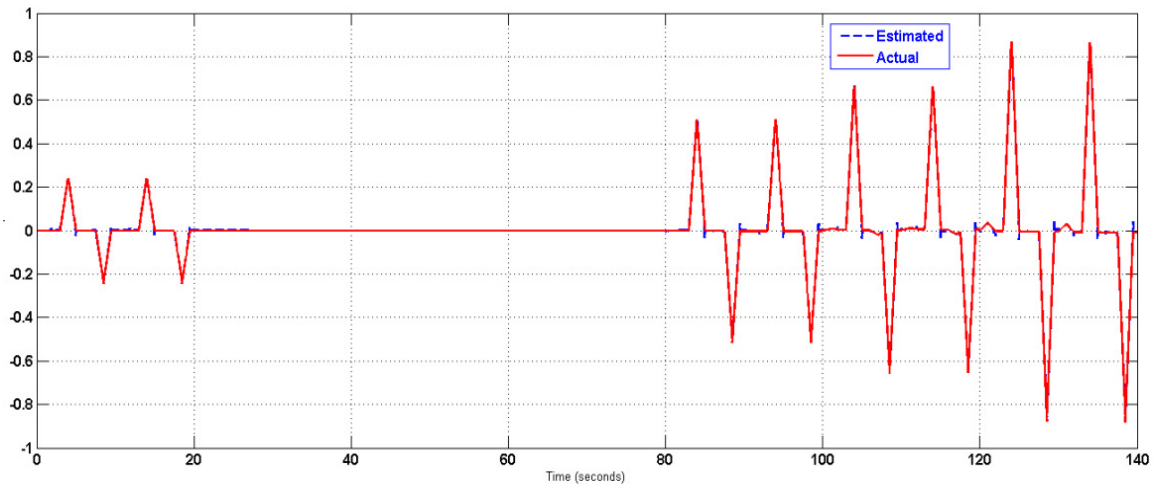


Figure 43: Composite Body Angular Velocity about Y-axis (rad/sec) using 12-accelerometer/Ring in Two-Ring Configuration, $L = 1m$, with 1-D measurement model.

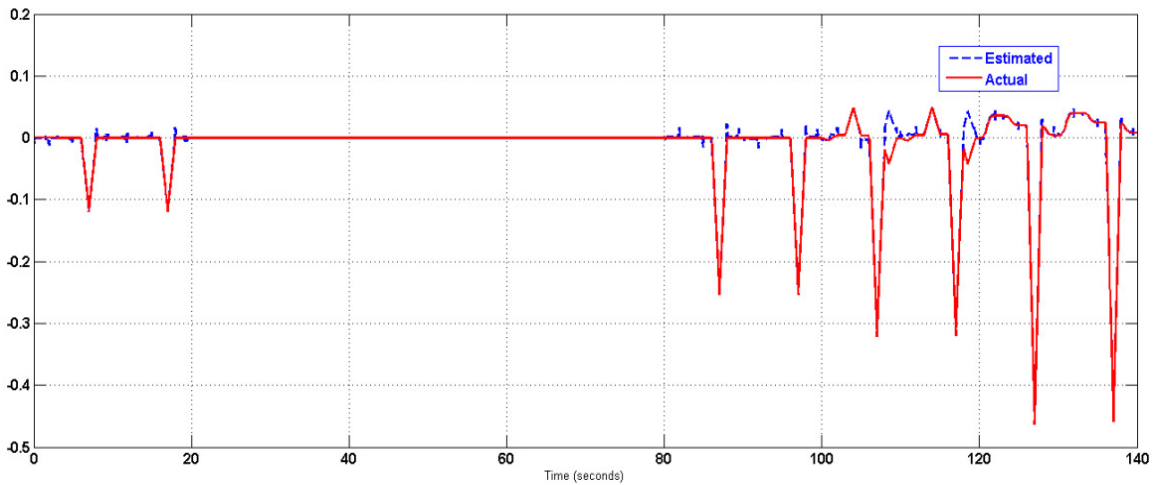


Figure 44: Composite Body Angular Velocity about Z-axis (rad/sec) using 12-accelerometer/Ring in Two-Ring Configuration, $L = 1m$, with 1-D measurement model.

- System 4: ($L = 100 m, \mu = 0.1 m$) with (1-D) Measurements Equations

The effect of increased value of (L , i.e. the separation between the two rings) on the previous system is shown in the following figures:

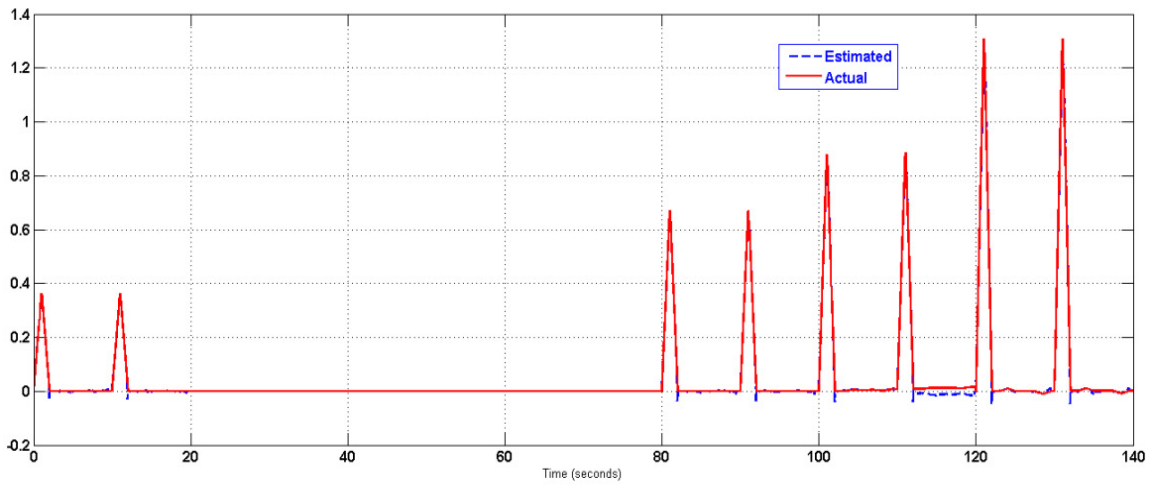


Figure 45: Composite Body Angular Velocity about X-axis (rad/sec) using 12-accelerometer/Ring in Two-Ring Configuration, $L = 100m$, with 1-D measurement model.

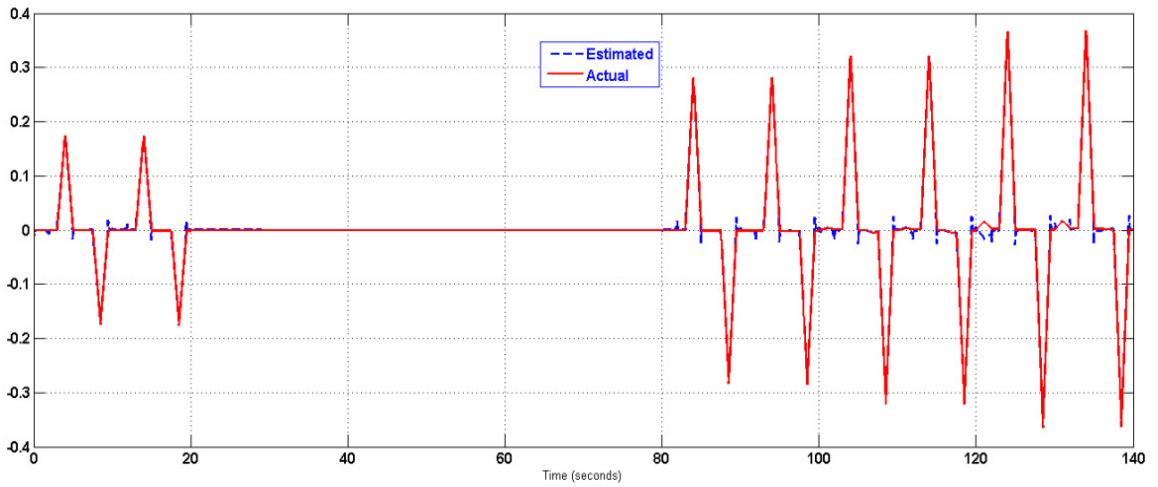


Figure 46: Composite Body Angular Velocity about Y-axis (rad/sec) using 12-accelerometer/Ring in Two-Ring Configuration, $L = 100m$, with 1-D measurement model.

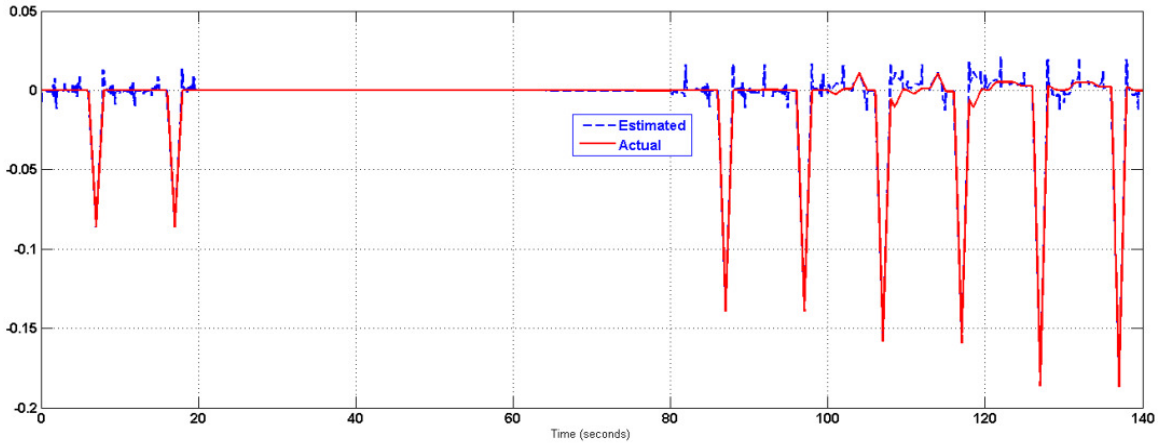


Figure 47: Composite Body Angular Velocity about Z-axis (rad/sec) using 12-accelerometer/Ring in Two-Ring Configuration, $L = 100m$, with 1-D measurement model.

- System 4: ($L = 1 m, \mu = 0.1 m$) with (2-D) Measurements Equations

As not expected, the increased measurements were unable to provide better estimation than 1-D measurement model for the same process and measurement noise matrices, because of the added nonlinear complexities. The results, obtained using 2-D measurement model, are shown in the following figures:

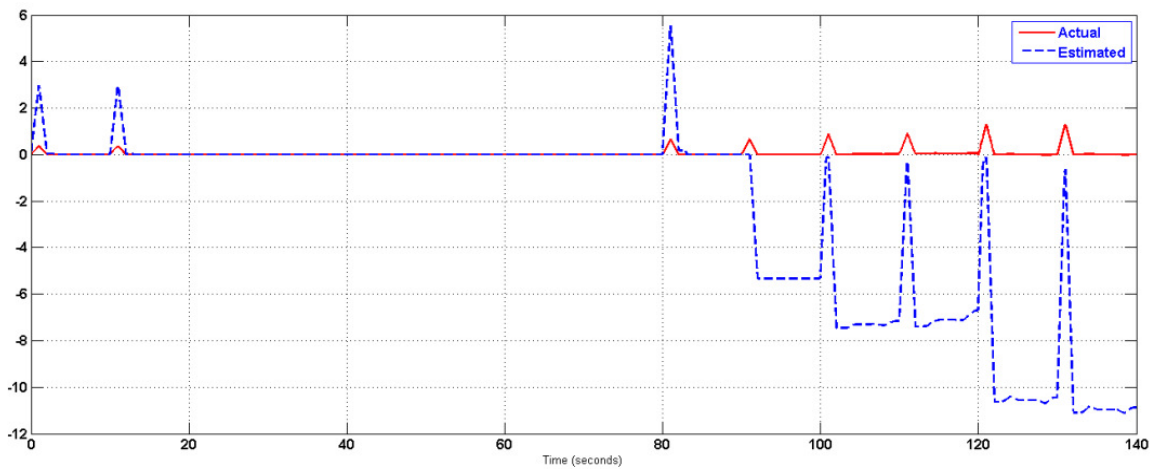


Figure 48: Composite Body Angular Velocity about X-axis (rad/sec) using 12-accelerometer/Ring in Two-Ring Configuration, $L = 1m$, with 2-D measurement model.

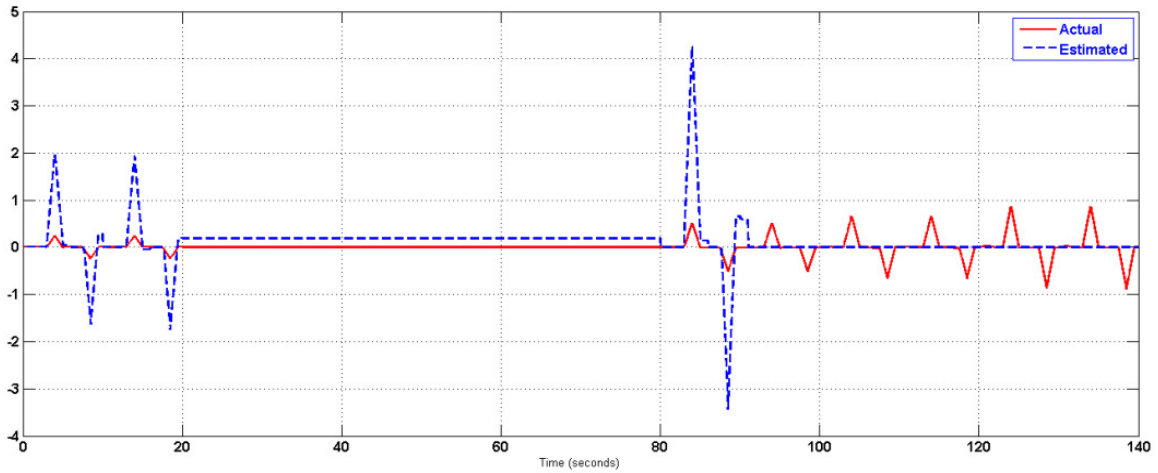


Figure 49: Composite Body Angular Velocity about Y-axis (rad/sec) using 12-accelerometer/Ring in Two-Ring Configuration, $L = 1m$, with 2-D measurement model.

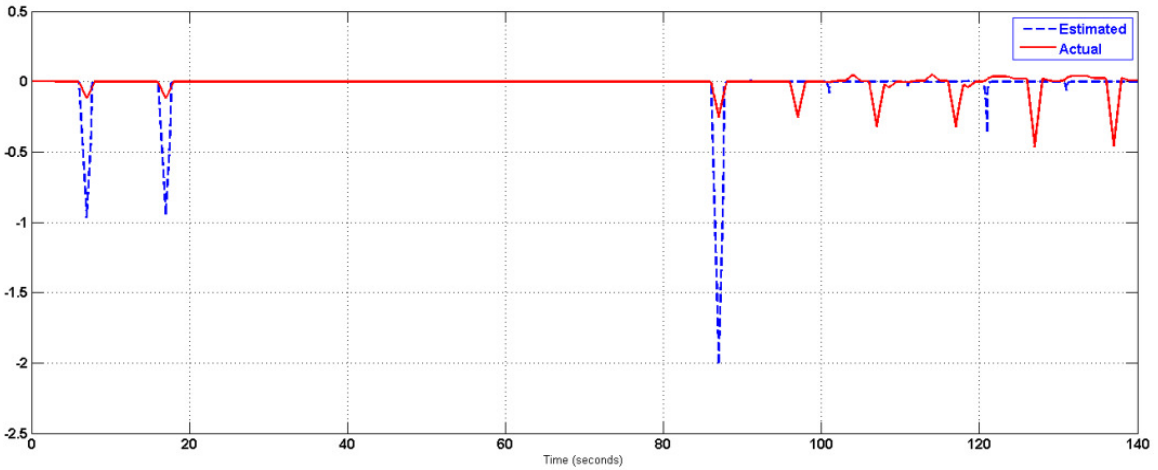


Figure 50: Composite Body Angular Velocity about Z-axis (rad/sec) using 12-accelerometer/Ring in Two-Ring Configuration, $L = 1m$, with 2-D measurement model.

- System 4: ($L = 1 m, \mu = 0.1 m$) with (3-D) Measurements Equations

The same as in 2-D measurement model, the 3-D measurement model was unable to provide better estimation of the angular velocity for the same process and measurement noise matrices, because of the added nonlinear complexities. The results were as follows:

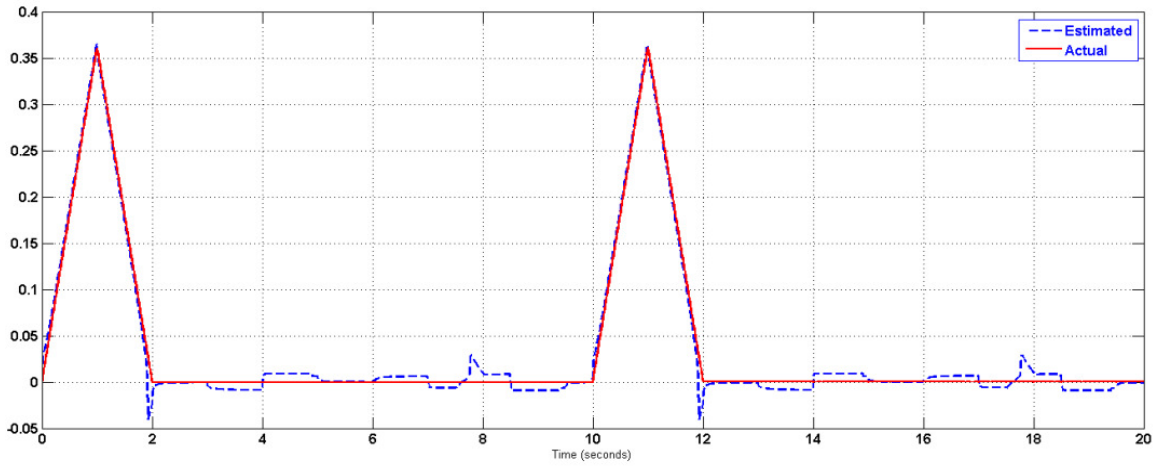


Figure 51: Composite Body Angular Velocity about X-axis (rad/sec) using 12-accelerometer/Ring in Two-Ring Configuration, $L = 1\text{m}$, with 3-D measurement model.

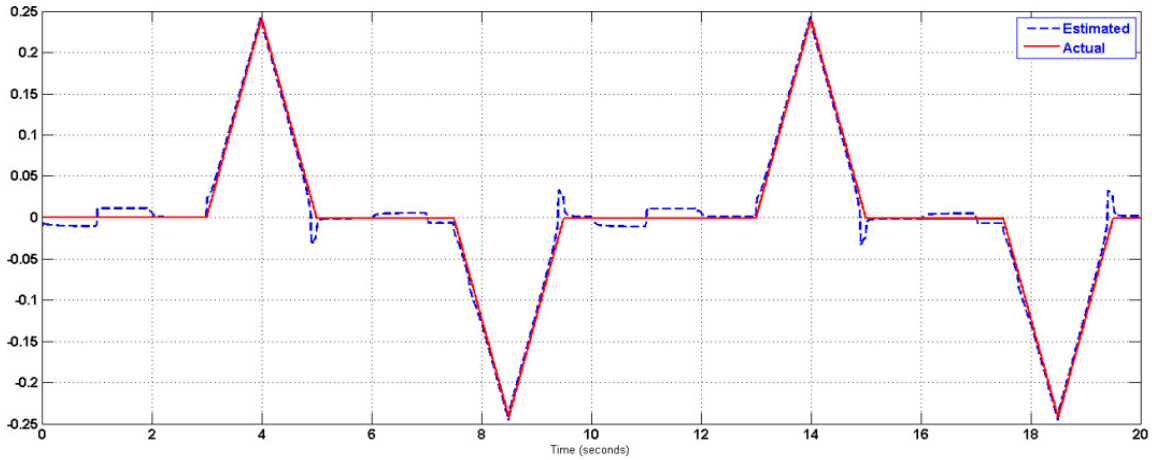


Figure 52: Composite Body Angular Velocity about Y-axis (rad/sec) using 12-accelerometer/Ring in Two-Ring Configuration, $L = 1\text{m}$, with 3-D measurement model.

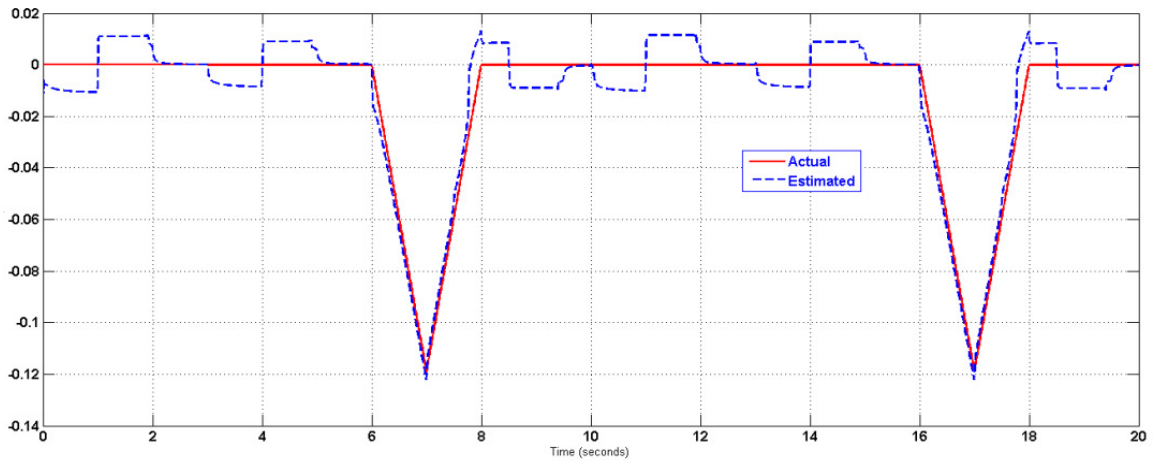


Figure 53: Composite Body Angular Velocity about Z-axis (rad/sec) using 12-accelerometer/Ring in Two-Ring Configuration, $L = 1\text{m}$, with 3-D measurement model.

6.2.3 Simulation Results of System 6 with different Measurement Models

Using EKF

Here, the simulation results will only be presented without further comments. The effect of various measurements model will be clear once the observability of each system is checked. The Simulink model shown in Figure 54 was used to simulate System 6 with different measurement models.

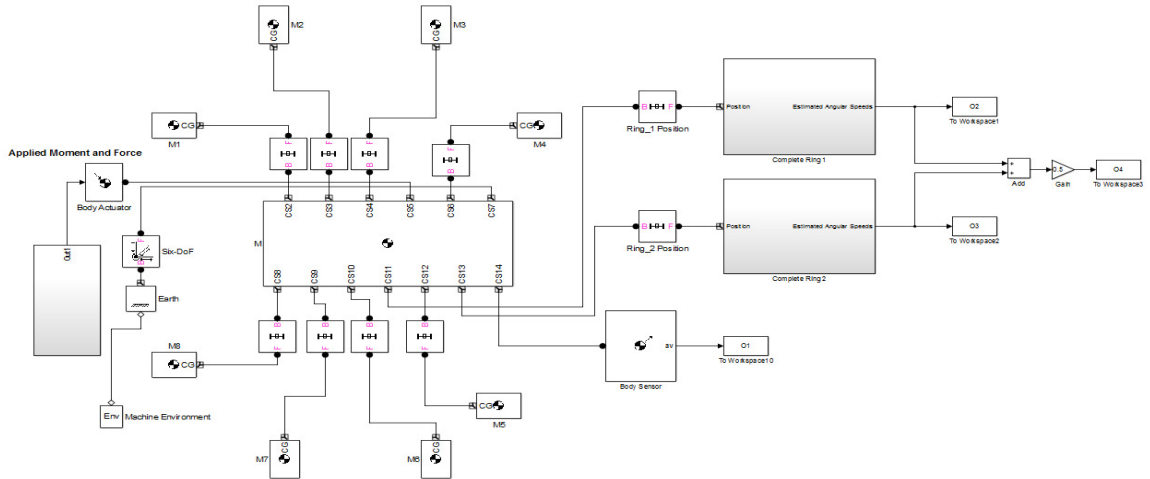


Figure 54: Simulink Model Used to Test System 6 with Different Measurement Models.

The simulation results are as follows:

- System 6: ($L = 1\text{ m}$, $\mu = 0.1\text{ m}$) with (1-D) Measurements Equations

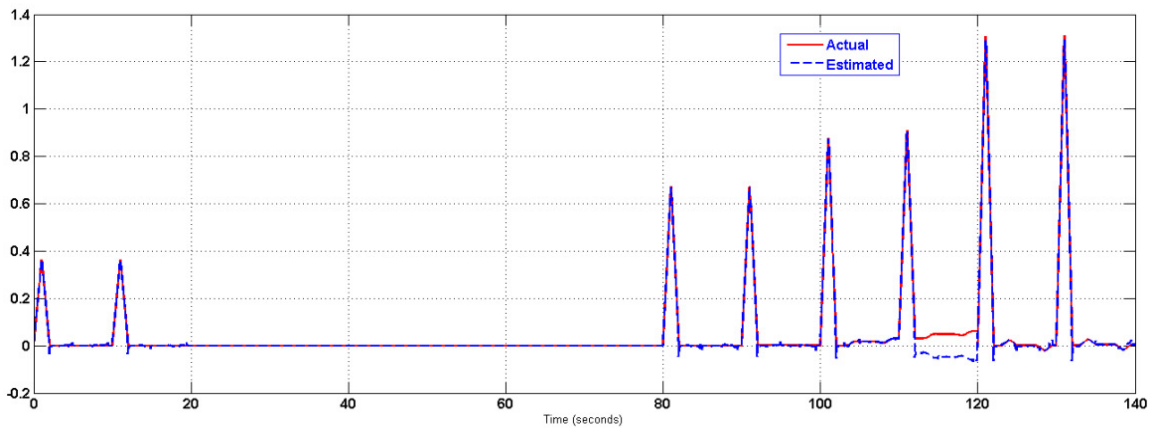


Figure 55: Composite Body Angular Velocity about X-axis (rad/sec) using 18-accelerometer/Ring in Two-Ring Configuration, $L = 1\text{ m}$, with 1-D measurement model.

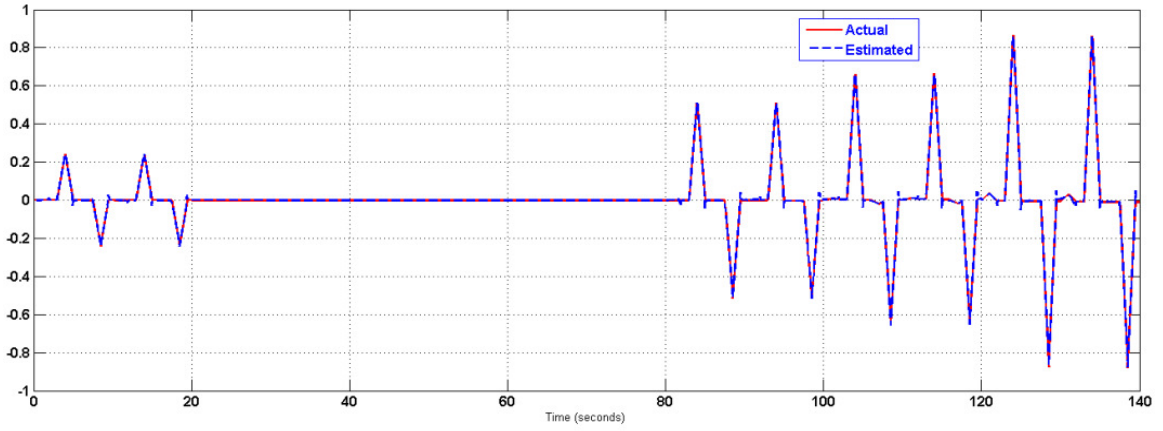


Figure 56: Composite Body Angular Velocity about Y-axis (rad/sec) using 18-accelerometer/Ring in Two-Ring Configuration, $L = 1m$, with 1-D measurement model.

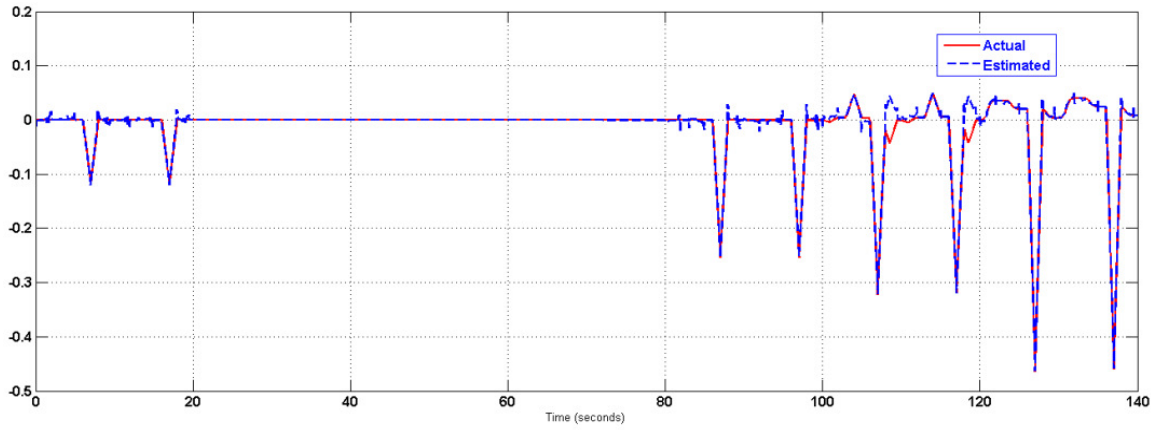


Figure 57: Composite Body Angular Velocity about Z-axis (rad/sec) using 18-accelerometer/Ring in Two-Ring Configuration, $L = 1m$, with 1-D measurement model.

- System 6: ($L = 1 m, \mu = 0.1 m$) with (2-D) Measurements Equations

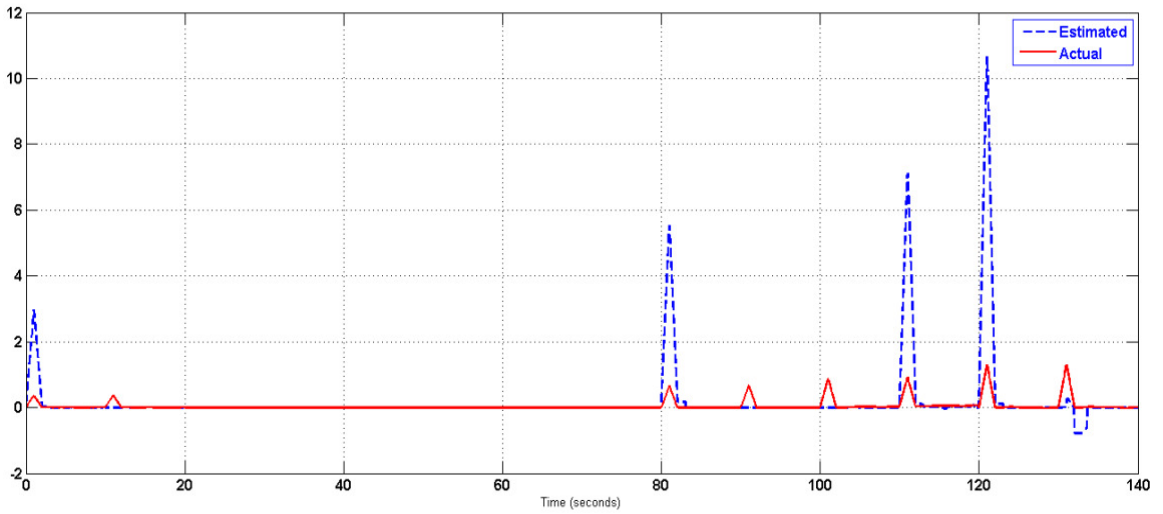


Figure 58: Composite Body Angular Velocity about X-axis (rad/sec) using 18-accelerometer/Ring in Two-Ring Configuration, $L = 1\text{m}$, with 2-D measurement model.

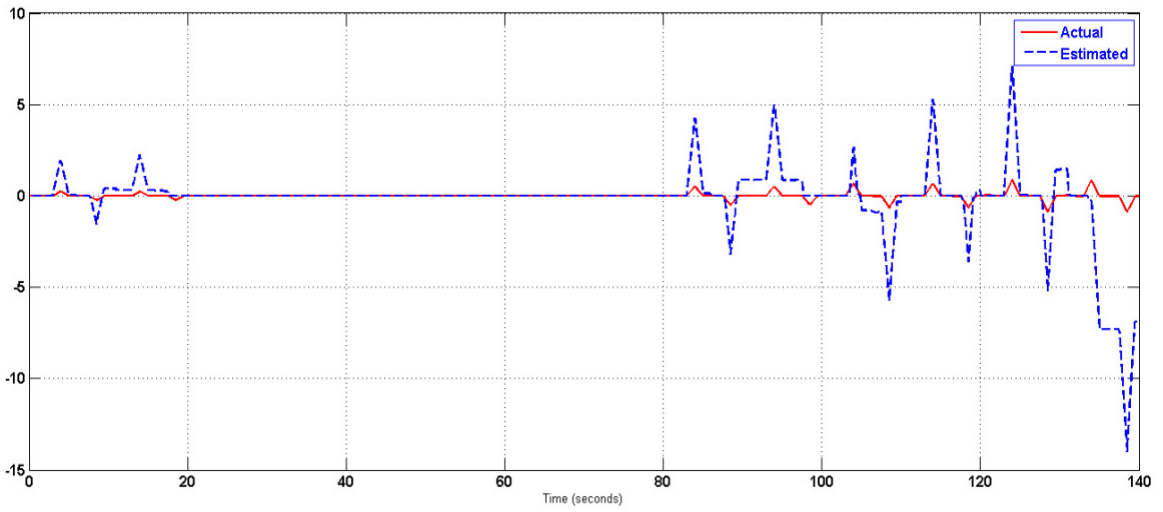


Figure 59: Composite Body Angular Velocity about Y-axis (rad/sec) using 18-accelerometer/Ring in Two-Ring Configuration, $L = 1\text{m}$, with 2-D measurement model.

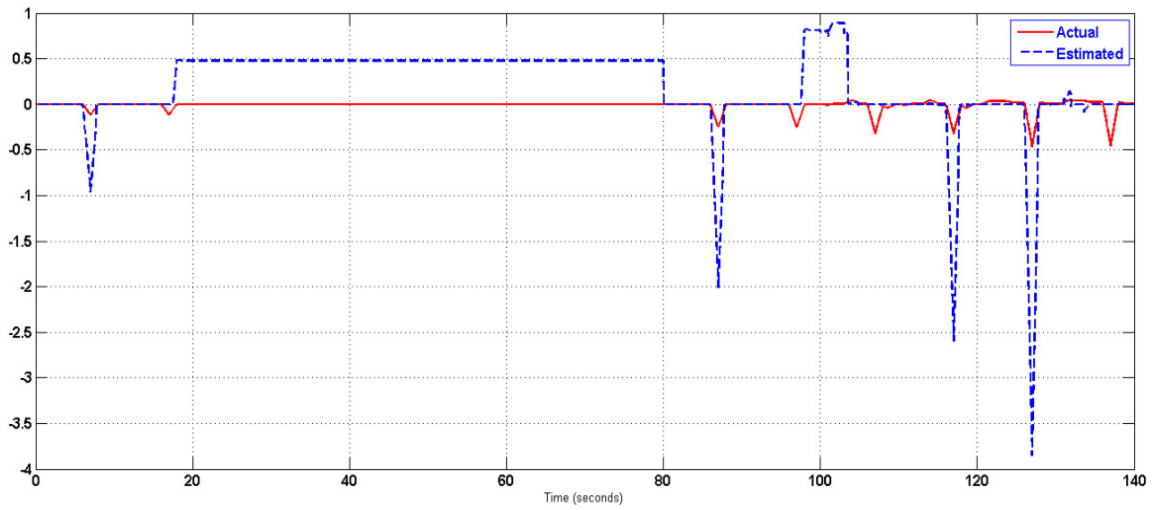


Figure 60: Composite Body Angular Velocity about Z-axis (rad/sec) using 18-accelerometer/Ring in Two-Ring Configuration, $L = 1\text{ m}$, with 2-D measurement model.

- System 6: ($L = 1\text{ m}$, $\mu = 0.1\text{ m}$) with (3-D) Measurements Equations

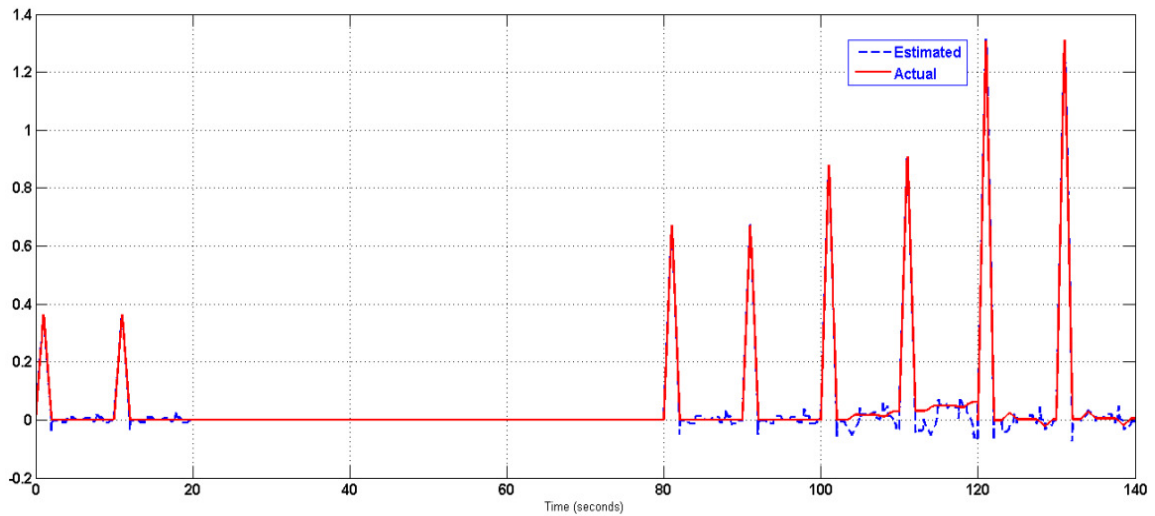


Figure 61: Composite Body Angular Velocity about X-axis (rad/sec) using 18-accelerometer/Ring in Two-Ring Configuration, $L = 1\text{ m}$, with 3-D measurement model.

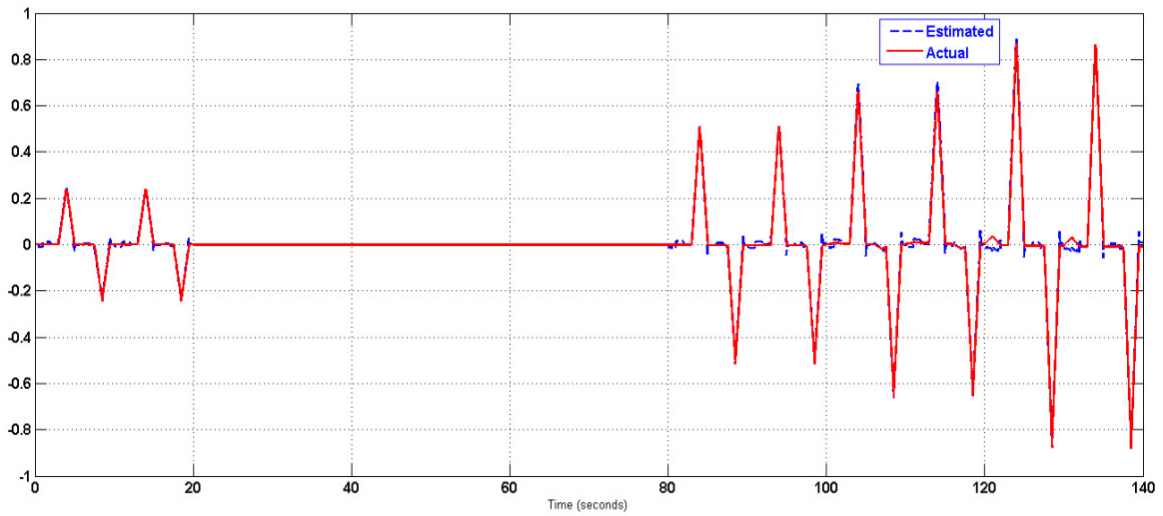


Figure 62: Composite Body Angular Velocity about Y-axis (rad/sec) using 18-accelerometer/Ring in Two-Ring Configuration, $L = 1m$, with 3-D measurement model.

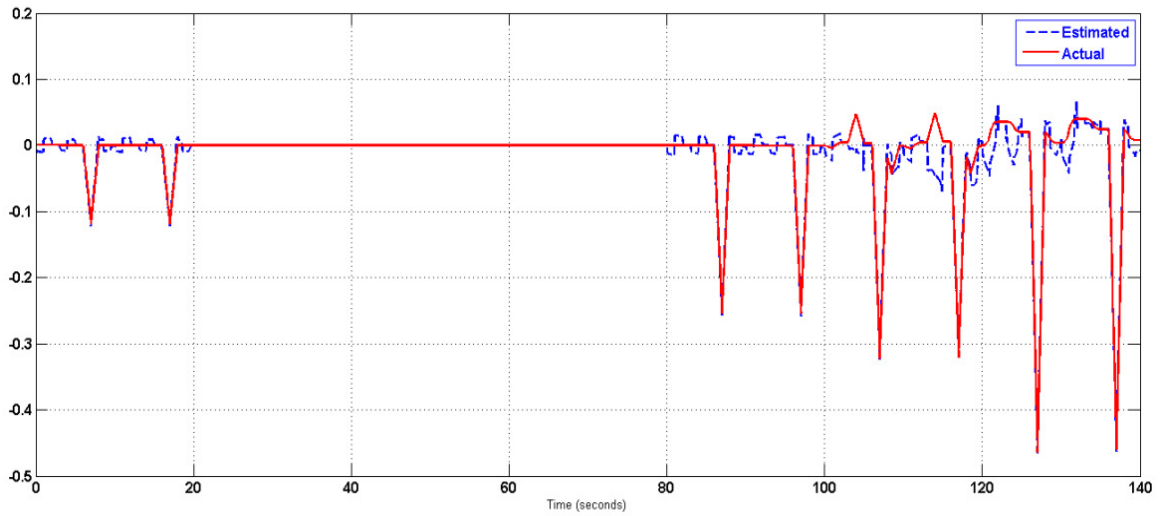


Figure 63: Composite Body Angular Velocity about Z-axis (rad/sec) using 18-accelerometer/Ring in Two-Ring Configuration, $L = 1m$, with 3-D measurement model.

From all the previous simulation results, it is apparent that the best model is the linear state model with 1-D measurement model. The main problem to be solved here is the sign ambiguity, as stated before. The following algorithm provides the solution:

Integrate the state equations using numerical techniques, and then determine the sign of each “AngularVelocity” then feed them to the EKF and correct for the sign of the “Estimated_AngularVelocity” using the following pseudo code, example given here for the X-axis angular velocity but it is applicable to other axes as well:

```
If (sign(AngularVelocity_X)*Estimated_AngularVelocity_X < 0) % different  
  
    Then Estimated_AngularVelocity_X = -1* Estimated_AngularVelocity_X;  
    Elseif sign(AngularVelocity_X) == 0  
        Then Estimated_AngularVelocity_X = 0  
End
```

This will reduce the sign ambiguity to the level of the noise available after integrating the angular acceleration obtained directly using the accelerometers’ readings as found in Systems 4 and 6. Similar approach to overcome sign ambiguity was also used in [38]. The results obtained, using the sign ambiguity algorithm in conjunction with EKF, are shown only for System 6.

The performance of System 6 along with the 1-D measurement Model and the sign ambiguity algorithm is shown in the following figures:

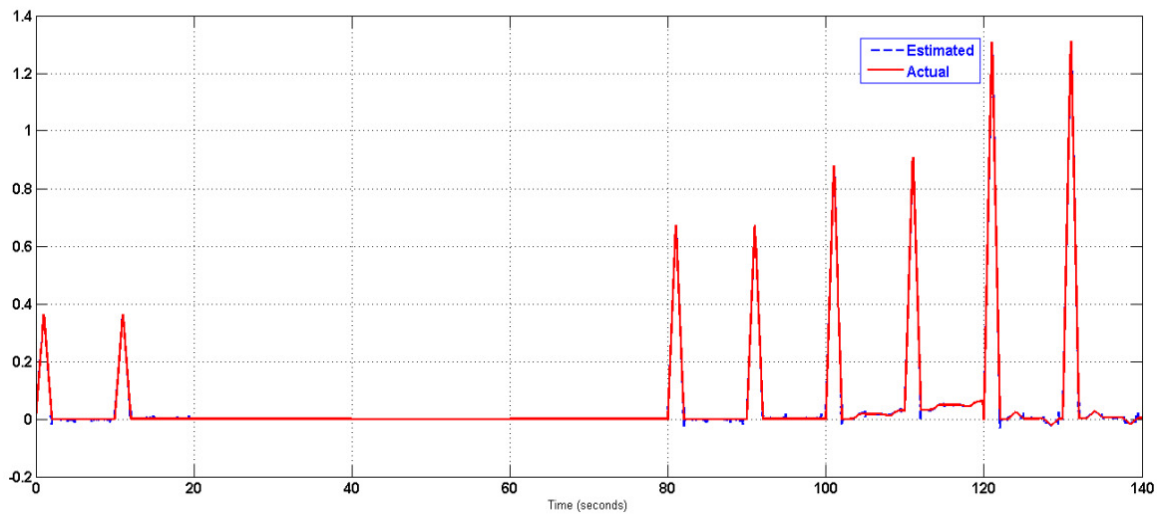


Figure 64: Composite Body Angular Velocity about X-axis (rad/sec) using 18-accelerometer/Ring in Two-Ring Configuration, $L = 1\text{m}$, with 1-D measurement model, and Sign ambiguity algorithm.

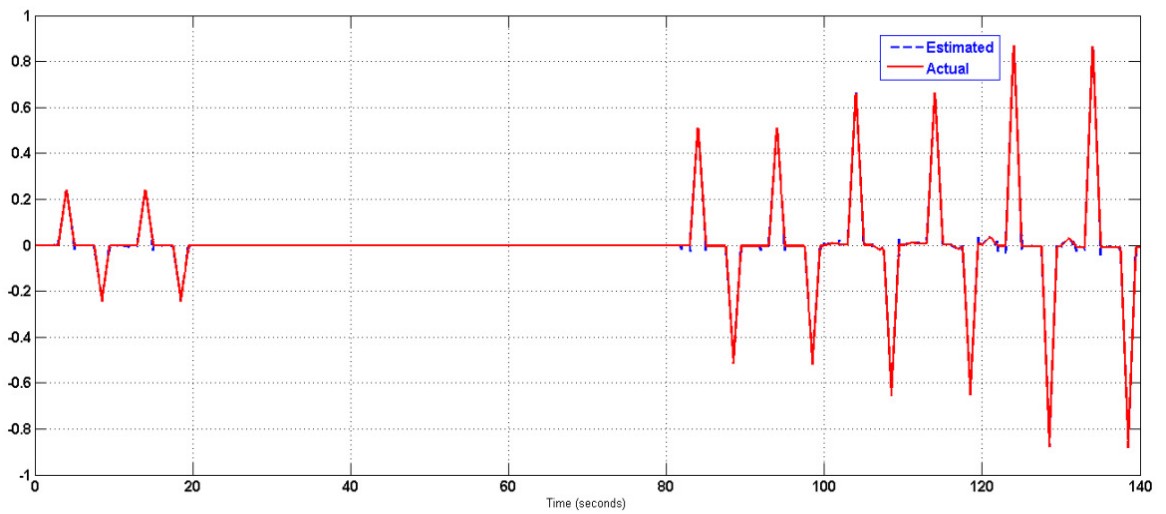


Figure 65: Composite Body Angular Velocity about Y-axis (rad/sec) using 18-accelerometer/Ring in Two-Ring Configuration, $L = 1\text{m}$, with 1-D measurement model, and Sign ambiguity algorithm.

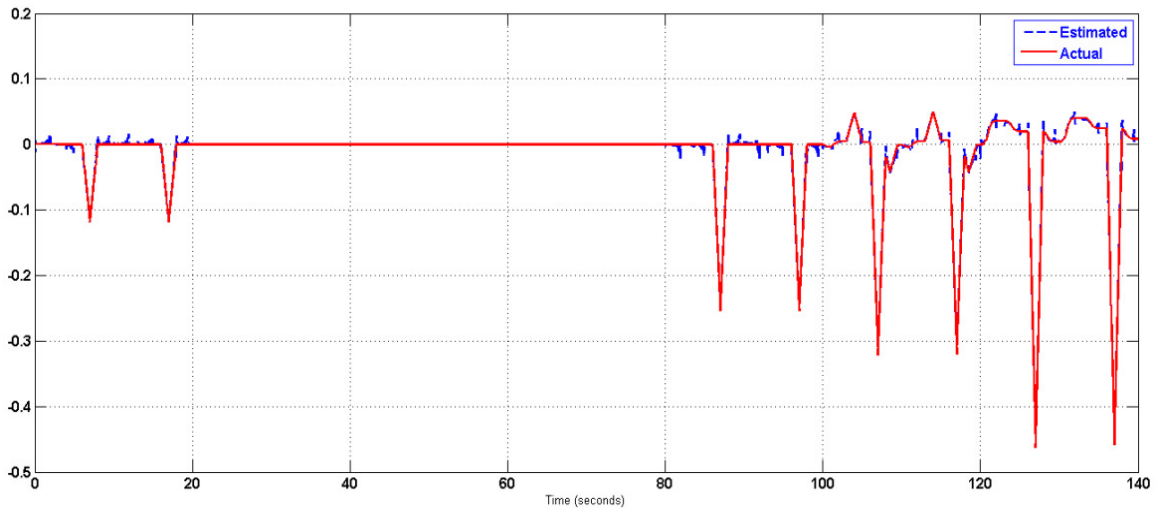


Figure 66: Composite Body Angular Velocity about Z-axis (rad/sec) using 18-accelerometer/Ring in Two-Ring Configuration, $L = 1\text{m}$, with 1-D measurement model, and Sign ambiguity algorithm.

Both Systems 4 and 6 allow the offline calculation for A, B, Q_k matrices where the only changing matrix is (H) . Now, before preceding further it is recommended to check the observability of these linearized time-varying models (LTV) using different measurement models to have some insight about the simulation results shown so far which reflect the performance of the EKF using such models.

6.2.4 Observability Check using different Measurement Models

Mainly, Systems 4 and 6 treated in this thesis are non-linear time-varying systems in measurements. Both have been linearized and then discretized to make them usable within the framework of EKF as was shown previously in Figure 36. The resulting measurement matrices for different measurement models are as given in Table 14. The observability of a discrete and linear time-varying or a linearized and then discretized system with no process or measurement noise vectors can be defined as follows [83]:

Definition 1: A LTV or linearized system with no process or measurement noise vectors is observable at time t_N if the state vector at time t_N , x_N can be determined from operations on the measurement sequence $Z_N = [z_0, \dots, z_N]$ where $t_N > t_0$ and $t_N < \infty$.

The observability of such systems can be assessed by calculating the rank of the Observability Grammian, defined as follows [84]:

$$\mathcal{M}(t_d) = \sum_{k=1}^d \Phi^T(t_k, t_1) H^T(t_k) H(t_k) \Phi(t_k, t_1) \quad (72)$$

Equation (72) can also be written in a recursive form as follows [84]:

$$\mathcal{M}(t_d) = \mathcal{M}(t_d) + \Phi^T(t_d, t_1) H^T(t_d) H(t_d) \Phi(t_d, t_1) \quad (73)$$

Along with, $\mathcal{M}(t_0) = 0$ as the initial condition.

This test is based on evaluating the rank of 3×3 $\mathcal{M}(t_d)$ matrix whose dimensions depend only on the dimensions of the state vector and not on the dimensions of the measurement vector or number of measurements [85].

The state equation for both Systems 4 and 6 are given as follows:

$$X(t_{k+1}) = \Phi(t_k) X(t_k) + B(t_k) U(t_k) \quad (74)$$

$$X = [\Omega_x, \Omega_y, \Omega_z]^T, \quad \Phi(t_k) = \text{eye}(3)$$

And their output equation is given by:

$$Y(t_d) = H(t_k) X(t_k) \quad (75)$$

Where, $H(t_k)$ depends on the measurement model used as was given in Table 14.

Making use of equation (74), equation (73) can be rewritten as follows:

$$\mathcal{M}(t_d) = \mathcal{M}(t_d) + H^T(t_d)H(t_d) \quad (76)$$

It is obvious from equation (76) that for the rank of the Observability Grammian $\mathcal{M}(t_d)$ to be full, i.e. equals 3, the term $H^T(t_d)H(t_d)$ must be full rank at each time instant t_d . One way to ensure that is to check the positive definiteness of that term. A positive definite matrix is invertible, i.e. nonsingular, [86]. Knowing the fact that an invertible matrix must have a full rank enables insuring the observability of the system according to this condition.

Next, the observability of both systems, using different measurement models, is investigated which can be used to understand the simulation results previously shown in more detail.

- Observability of Systems 4 and 6 using 1-D measurement Model

The linearized (H) matrix for this model is given as follows:

$$H = 2 * \begin{bmatrix} 0 & \Omega_y & \Omega_z \\ \Omega_x & 0 & \Omega_z \\ \Omega_x & \Omega_y & 0 \end{bmatrix}$$

Now, the positive definiteness of the symmetric matrix $H^T(t_d)H(t_d)$ is checked as follows:

A symmetric $n \times n$ real matrix M is said to be positive definite if $(Z^T M Z)$ is positive for every non-zero column vector Z of n real numbers.

- Define a vector $Z = [a \quad b \quad c]^T$
- Check whether $\vec{Z}^T (\mathbf{C}^T \mathbf{C}) \vec{Z} > 0, \forall \vec{Z} \neq \vec{0}$

- If the previous step was valid, then the matrix is positive definite for all time instances and hence the system is observable.

It can be shown that the result will be given by:

$$(a\Omega_x + b\Omega_y)^2 + (a\Omega_x + c\Omega_z)^2 + (b\Omega_y + c\Omega_z)^2 > 0, \quad \forall \vec{Z} \neq \vec{0} \quad (77)$$

Then, both systems are observable using this measurement model.

- Observability of Systems 4 and 6 using 2-D measurement Model

Similarly, the observability of both Systems 4 and 6 can be checked when they utilize the 2-D measurement model. The linearized (H) matrix is given as follows:

$$H = \begin{bmatrix} 0 & \Omega_z & \Omega_y \\ \Omega_z & 0 & \Omega_x \\ \Omega_y & \Omega_x & 0 \end{bmatrix}$$

The same steps can be implemented to show that the Observability Gramian is given as follows:

$$(a\Omega_z + c\Omega_x)^2 + (a\Omega_y + b\Omega_x)^2 + (b\Omega_z + c\Omega_y)^2 > 0, \quad \forall \vec{Z} \neq \vec{0} \quad (78)$$

Then, both systems are observable using this measurement model.

- Observability of Systems 4 and 6 using 3-D measurement Model

The linearized (H) matrix is given as follows:

$$H = \begin{bmatrix} 0 & 2\Omega_y + \Omega_z & 2\Omega_z + \Omega_y \\ 2\Omega_x + \Omega_z & 0 & 2\Omega_z + \Omega_x \\ 2\Omega_x + \Omega_y & 2\Omega_y + \Omega_x & 0 \end{bmatrix}$$

The same steps can be implemented to show that the Observability Gramian is given as follows:

$$\begin{aligned} & [(2\Omega_x + \Omega_y)a + (2\Omega_y + \Omega_x)b]^2 + [(2\Omega_y + \Omega_z)b + (2\Omega_z + \Omega_y)c]^2 \\ & + [(2\Omega_x + \Omega_z)a + (2\Omega_z + \Omega_x)c]^2 > 0, \quad \forall \vec{Z} \neq \vec{0} \end{aligned} \quad (79)$$

Then, both systems are observable using this measurement model.

In light of the previous discussion, in order to explain the performance of the EKF built for Systems 4 and 6 utilizing the 2-D and 3-D measurement model it is good to remember that this observability, for Systems 4 and 6 using the 2-D and 3-D measurement model, was checked while neglecting the process and measurement noise vectors.

Figure 36 shows how the evolution of the state covariance matrix depends on the state transition matrix Φ , denoted by (A) in Figure 36, the sensor matrix H , the process noise Q , the measurement noise R , and finally the statistics of the initial state vector P_0 . The later three matrices can cause the state covariance matrix P to exceed a predetermined threshold value or even to become unbounded, even though the pair (Φ, H) is observable; hence Observability is necessary but not sufficient [85]. Other types of Observability tests may be used to deepen the understanding of the situation in hand such as Stochastic Observability [85] which is beyond the scope of this thesis.

It is worth noting that the observability test of System 4 will be different if non-ideal network was assumed to connect either the two Rings, or many Rings, together which is, as well, beyond the objective of this thesis.

➤ Unscented Kalman Filter Design

This type of filters can be used if the system is highly non-linear which may cause EKF performance to deteriorate. Because EKF depends on linearization, a linearization error can result in errors in the transformation of means and covariance when a random variable is operated on by a non-linear function [81].

Figure 67 shows the UKF layout that can be followed to design such a filter for the systems proposed here. To ensure the compactness of the thesis body, a detail explanation for the UKF is avoided since it can be easily located in literature. So, in this section, the main concern will be about the performance of System 6 once an UKF is designed to utilize different measurement models.

6.2.5 Simulation Results of System 6 with different Measurement Models Using UKF

In this section, the simulation results obtained using the same previously presented Simulink model are shown for System 6 with 1-D and 3-D measurement models only; since the results obtained using UKF designed for System 6 utilizing 2-D measurements were unsatisfactory.

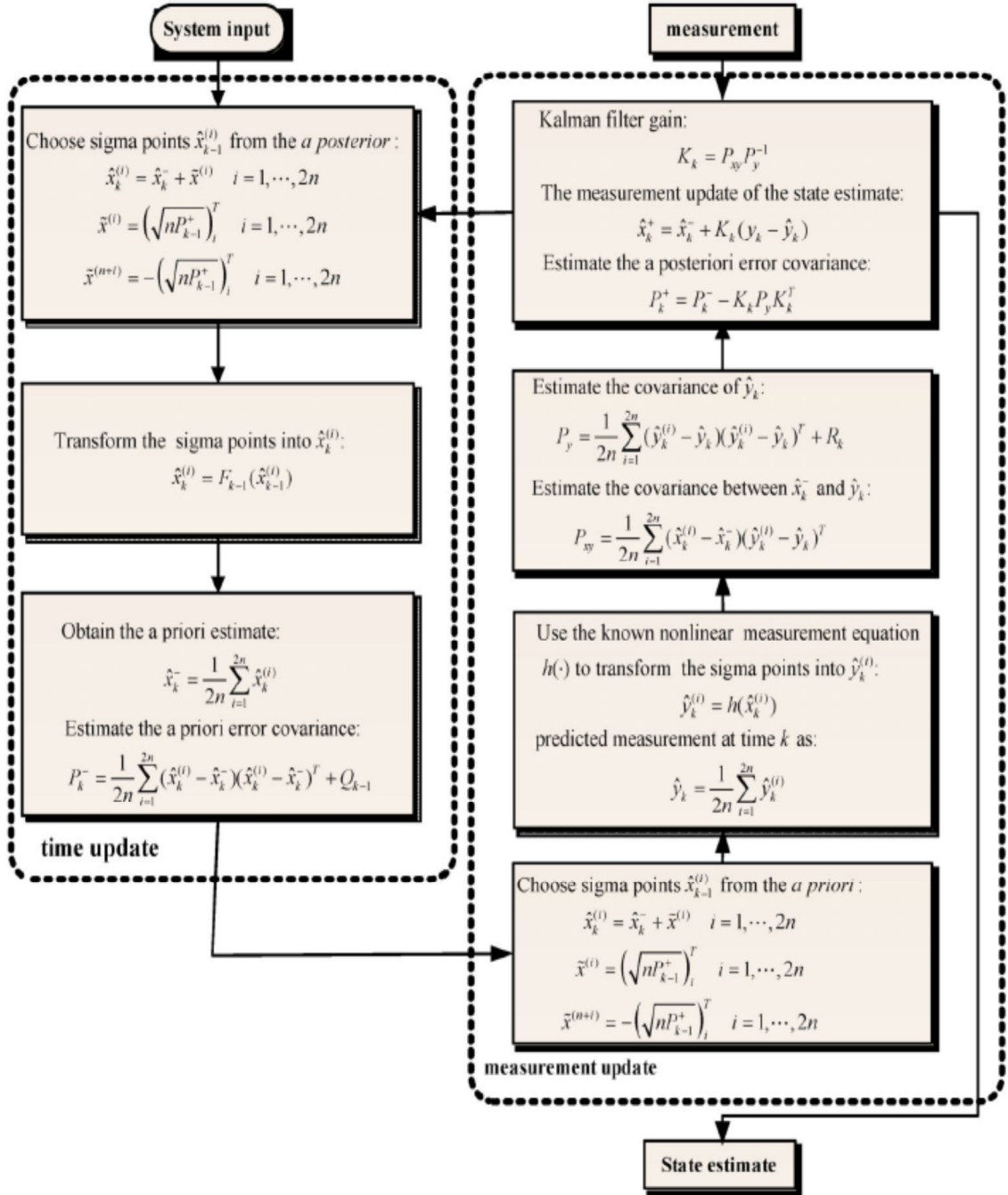


Figure 67: UKF layout. ^[87]

- System 6: ($L = 1, \mu = 0.1$) with (1-D) Measurements Equations and Sign Correction and noise enabled.

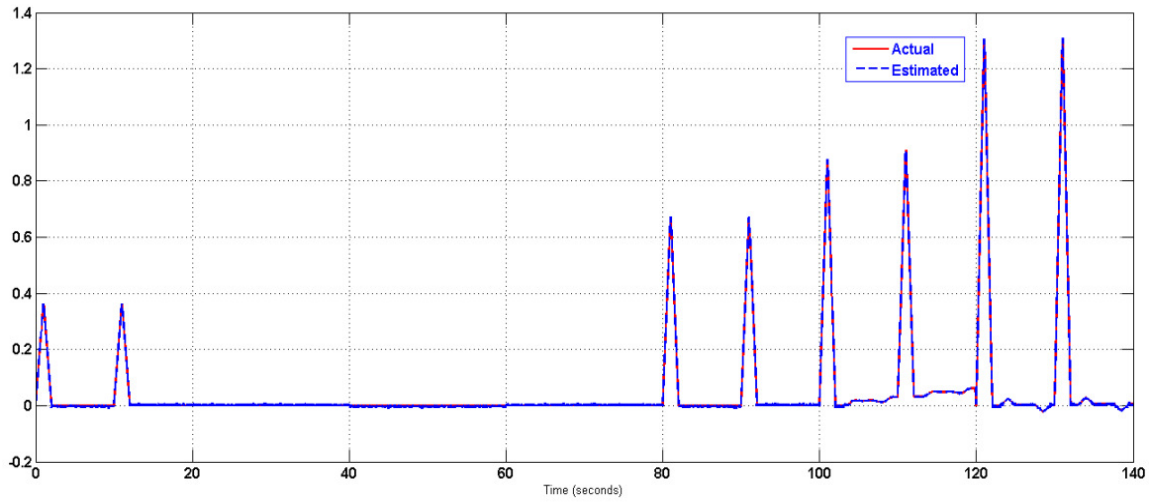


Figure 68: Composite Body Angular Velocity about X-axis (rad/sec) using 18-accelerometer/Ring in Two-Ring Configuration, with 1-D measurement model, and Sign ambiguity algorithm with UKF.

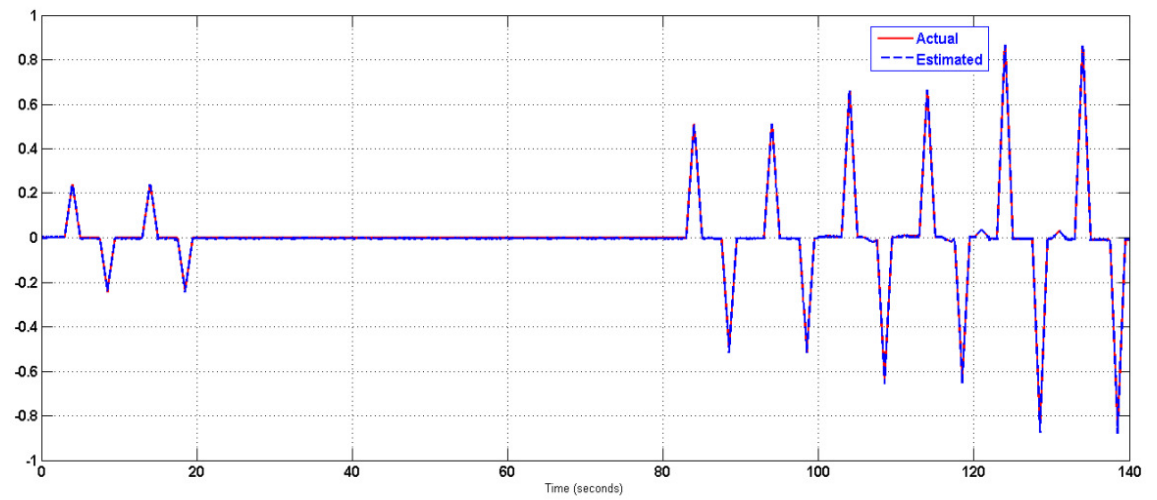


Figure 69: Composite Body Angular Velocity about Y-axis (rad/sec) using 18-accelerometer/Ring in Two-Ring Configuration, with 1-D measurement model, and Sign ambiguity algorithm with UKF.

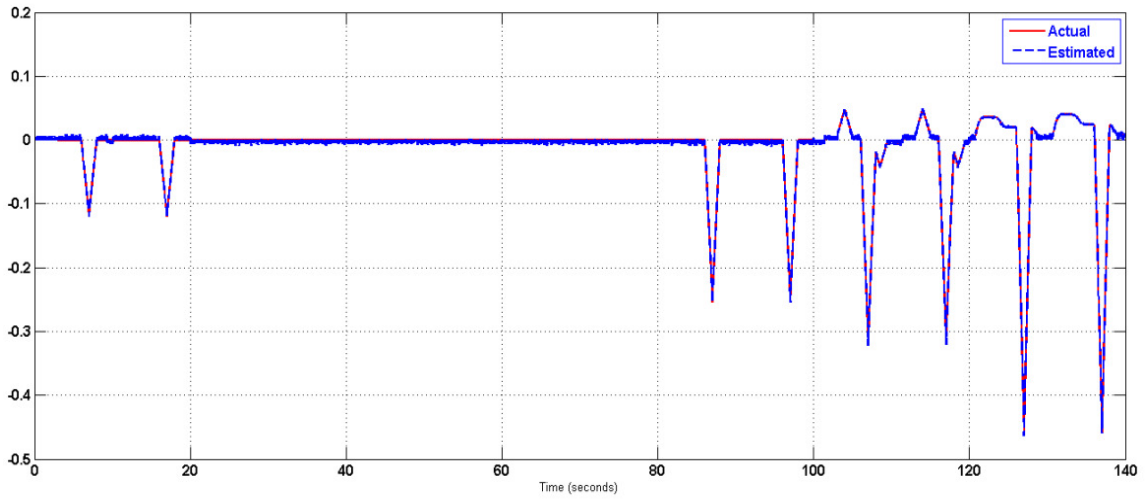


Figure 70: Composite Body Angular Velocity about Z-axis (rad/sec) using 18-accelerometer/Ring in Two-Ring Configuration, with 1-D measurement model, and Sign ambiguity algorithm with UKF.

- System 6: ($L = 1\text{ m}, \mu = 0.1\text{ m}$) with (3-D) Measurements Equations and Sign Correction and noise enabled.

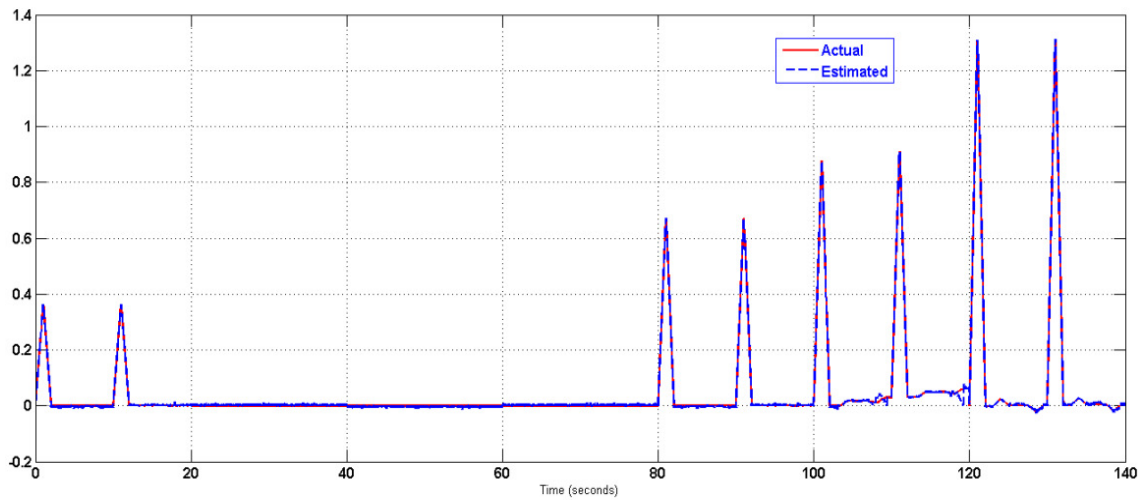


Figure 71: Composite Body Angular Velocity about X-axis (rad/sec) using 18-accelerometer/Ring in Two-Ring Configuration, with 3-D measurement model, and Sign ambiguity algorithm with UKF.

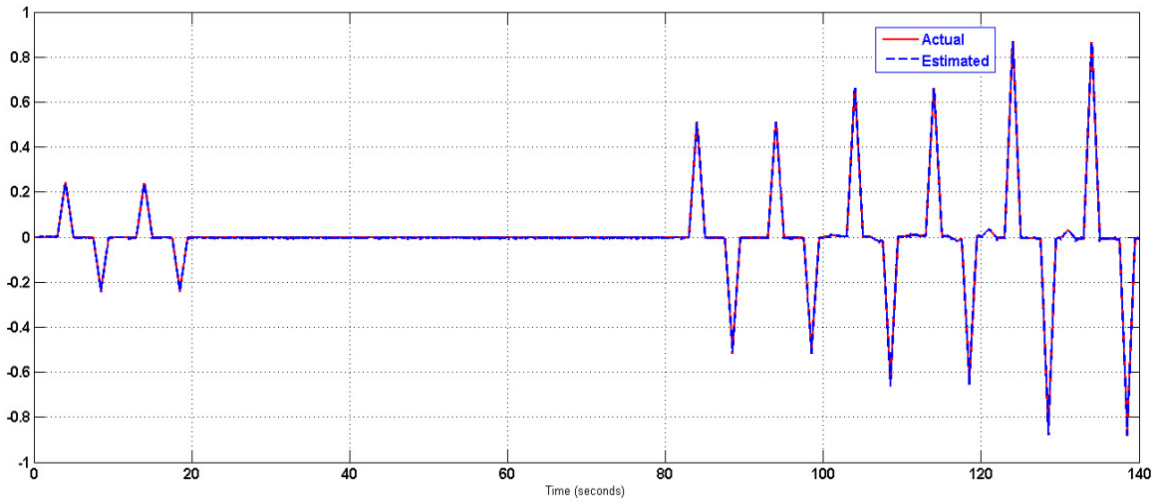


Figure 72: Composite Body Angular Velocity about Y-axis (rad/sec) using 18-accelerometer/Ring in Two-Ring Configuration, with 3-D measurement model, and Sign ambiguity algorithm with UKF.

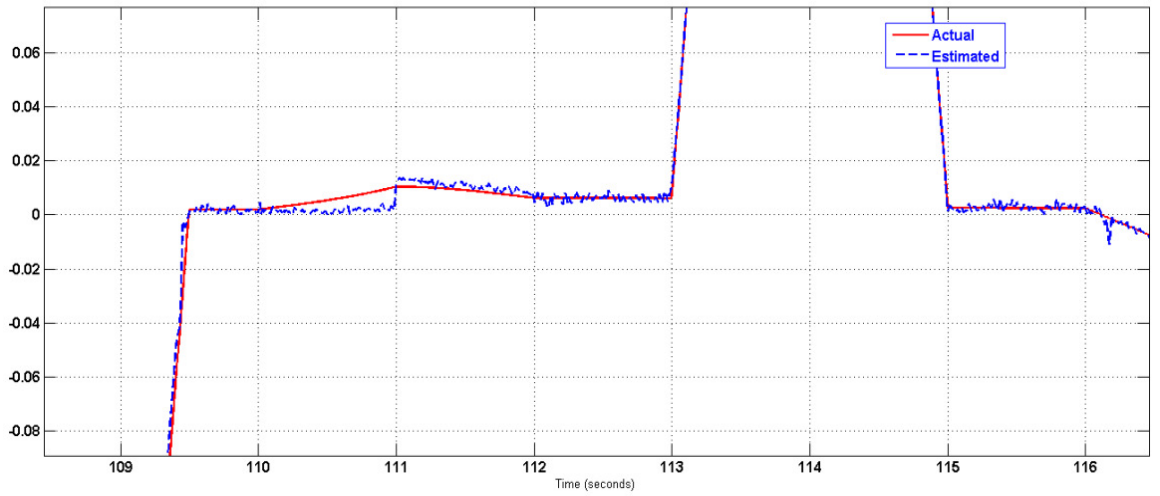


Figure 73: Composite Body Angular Velocity about Y-axis (rad/sec) using 18-accelerometer/Ring in Two-Ring Configuration, with 3-D measurement model, and Sign ambiguity algorithm with UKF, close view.

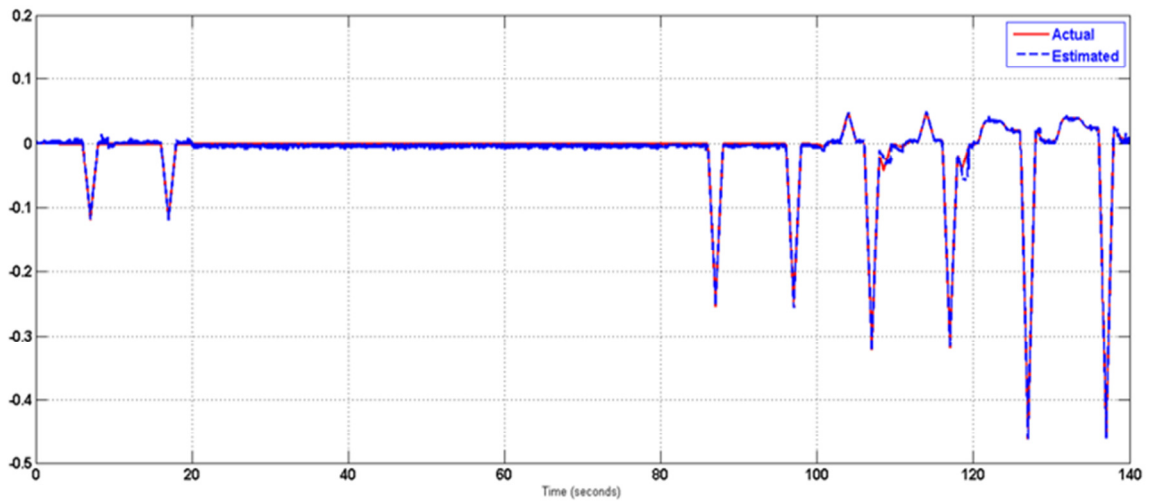


Figure 74: Composite Body Angular Velocity about Z-axis (rad/sec) using 18-accelerometer/Ring in Two-Ring Configuration, with 3-D measurement model, and Sign ambiguity algorithm with UKF.

The following figures reflect the performance of the UKF designed for System 6 utilizing 3-D measurement model. It can be clearly seen that the performance is deteriorated when sign correction algorithm is ignored and that makes the performance of the UKF similar to the EKF when this problem is considered. The following section discusses the question: Which non-linear filter to choose, UKF or EKF?

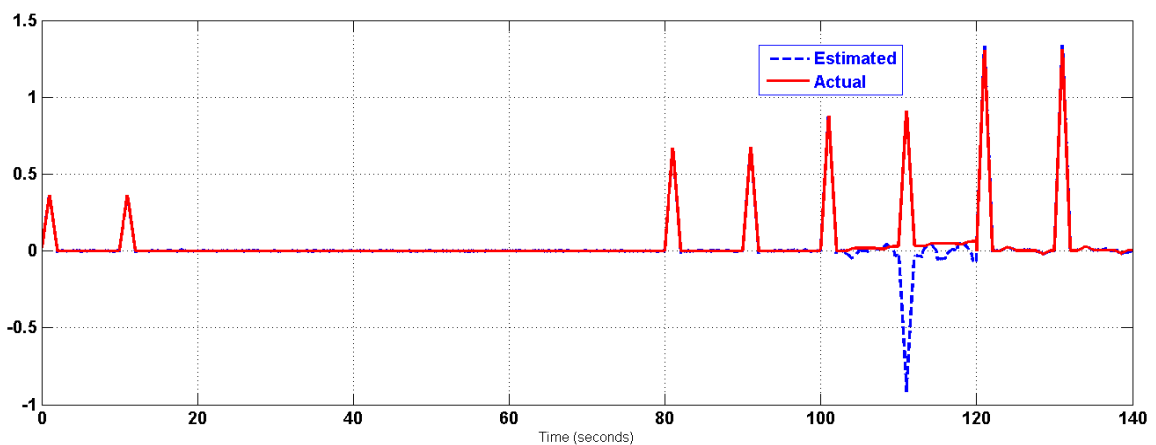


Figure 75: Composite Body Angular Velocity about X-axis (rad/sec) using 18-accelerometer/Ring in Two-Ring Configuration, with 3-D measurement model, and Without Sign ambiguity algorithm with UKF.

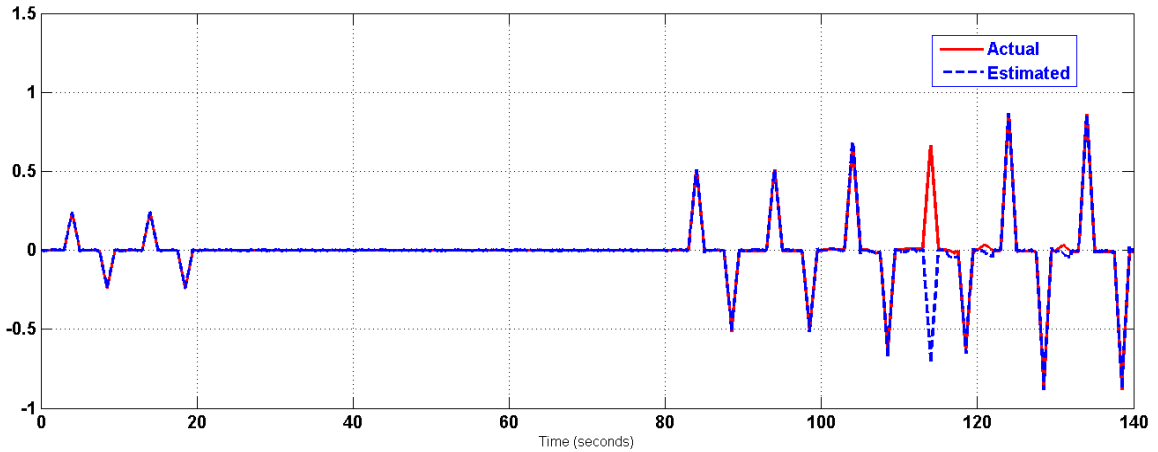


Figure 76: Composite Body Angular Velocity about Y-axis (rad/sec) using 18-accelerometer/Ring in Two-Ring Configuration, with 3-D measurement model, and Without Sign ambiguity algorithm with UKF.

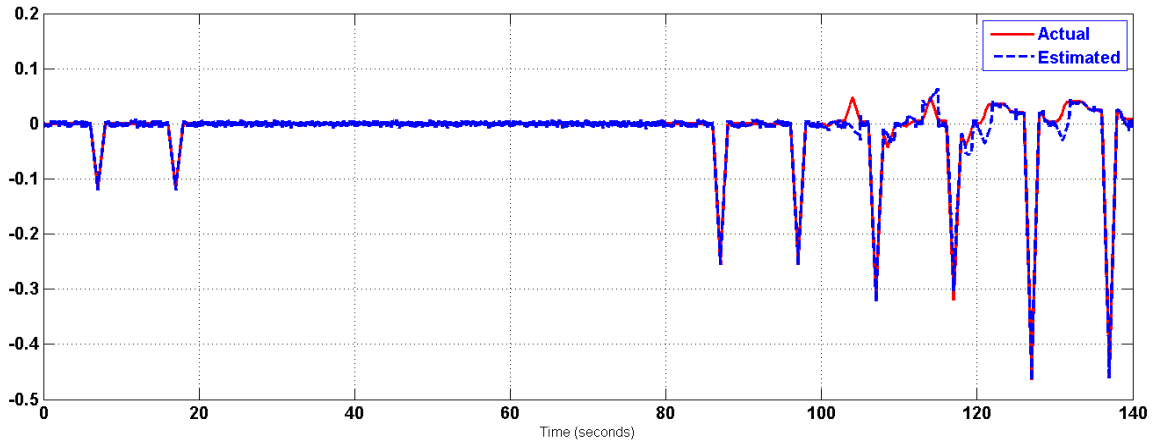


Figure 77: Composite Body Angular Velocity about Z-axis (rad/sec) using 18-accelerometer/Ring in Two-Ring Configuration, with 3-D measurement model, and Without Sign ambiguity algorithm with UKF.

It is obvious from the previous figures, that the UKF is unable to uniquely determine the sign of the angular velocity especially when allowing the CoG position to change. So, the corporation between the sign ambiguity algorithm and the UKF resolves this problem.

6.2.6 Comparison between EKF and UKF

Mainly, the measurement models suggested in Systems 4 and 6 were the motivation behind choosing the Extended and Unscented Kalman Filter versions to handle the non-

linearity inherited by choosing such measurement models. Further investigation of the problem formulation and deeper understanding of the problem will result in a linear time-invariant version of Systems 4 and 6, which will be discussed in the next section.

However, the UKF is capable of handling more non-linearities within the system dynamics which the EKF cannot do. It was clear from Figures 53 and 63 that the EKF failed in retrieving the angular velocity when the 3-D measurement model was used with System 4 and System 6 respectively. On the opposite, the UKF was able to handle these non-linearities once applied to System 6 utilizing the 3-D measurement model as can be seen in Figures 71-74 with the aid of sign ambiguity algorithm.

The main difference between 1-D and 3-D measurement models is the added accelerometers' measurements in the case of the 3-D measurement model. This addition was the source of increased non-linearities found in the 3-D measurement models once compared to those found in the 1-D counterpart. This will make the estimation of the angular velocity more robust especially in the case of accelerometer failure provided that a utility capable of removing the outliers in the accelerometers' measurements is involved, as can be seen in Chapter 9.

Once the implementation of those filters within a finite precision device is considered, the computational power needed with each type must be evaluated. Once compared from this perspective, both filters share the same level of computational complexity [88].

In opposition to UKF, the EKF computation involves finding the Jacobian which makes it difficult to implement the EKF for non-linear systems which are not given analytically. In such cases, the computation of the Jacobian numerically will be difficult [81]. A more

detailed comparison between UKF and EKF can be found in [89] and specifically in navigation can be found in [90].

So, it seems clear that when additional measurements, i.e. increased accuracy and robustness, are needed, the best choice would be using the 3-D measurement model along with the UKF. However, if it is intended to reduce the complexity of the overall design, then an EKF can be used along with 1-D measurement model.

6.2.7 Is a non-linear Filter really needed?

By examining the continuous time state equations of Systems 4 and 6, it is clear that a simpler approach can be taken to retrieve the angular velocity from the accelerometers' measurements. In such an approach, the result will be a linear time-invariant system. Recall the state equations of system 6; they can be given in a state-space representation as follows:

$$\begin{aligned}
 \dot{\Omega}_x &= \frac{1}{4\mu} (A_{3z} - A_{4z} - A_{5y} + A_{6y}) \\
 \dot{\Omega}_y &= \frac{1}{4\mu} (A_{5x} - A_{6x} - A_{1z} + A_{2z}) \\
 \dot{\Omega}_z &= \frac{1}{4\mu} (A_{1y} - A_{2y} - A_{3x} + A_{4x})
 \end{aligned} \tag{80}$$

$$\begin{bmatrix} \dot{\Omega}_x \\ \dot{\Omega}_y \\ \dot{\Omega}_z \end{bmatrix} (t) = B\vec{U}(t) = \vec{\dot{\Omega}}(t)$$

$$\begin{bmatrix} y_1 \\ y_2 \\ y_3 \end{bmatrix} (t) = \begin{bmatrix} 1 & 0 & 0 \\ 0 & 1 & 0 \\ 0 & 0 & 1 \end{bmatrix} \begin{bmatrix} \Omega_x \\ \Omega_y \\ \Omega_z \end{bmatrix} (t) = \vec{y}(t)$$

This system, System 7, can be discretized and a standard Kalman Filter (KF) can be designed. To maintain compactness of the thesis body, discussing the KF will be avoided and reference can be made to [81] for further details. The discretized version of the system given by (81) is shown below:

$$\begin{aligned}\bar{\Omega}(k+1) &= \bar{\Omega}(k) + TB\bar{U}(k) \\ \bar{y}(k) &= \bar{\Omega}(k)\end{aligned}\tag{81}$$

Where, T denotes the sampling period in seconds.

The IMU proposed by this thesis, previously referred to as System 6, is investigated using this system and the results were as follows:

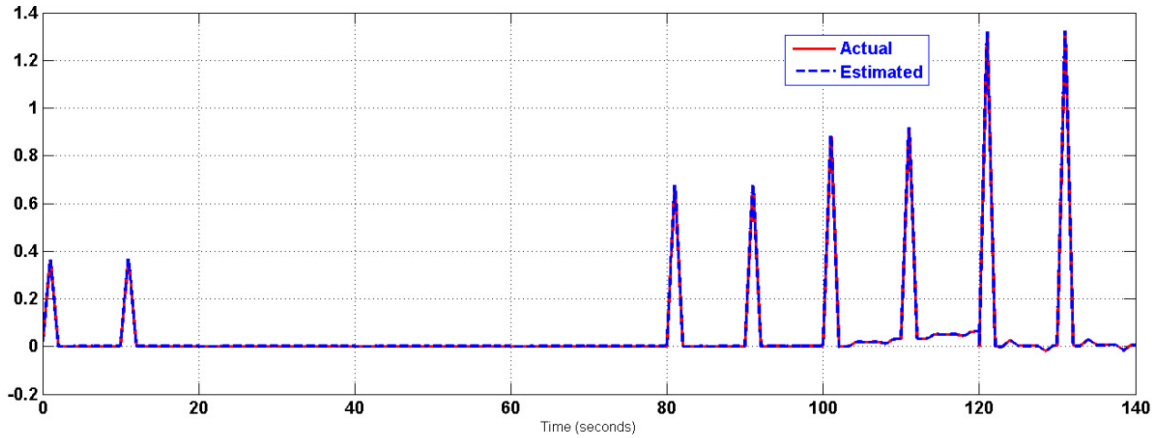


Figure 78: Composite Body Angular Velocity about X-axis (rad/sec) using 18-accelerometer/Ring in Two-Ring Configuration, with Standard Kalman Filter and without noise.

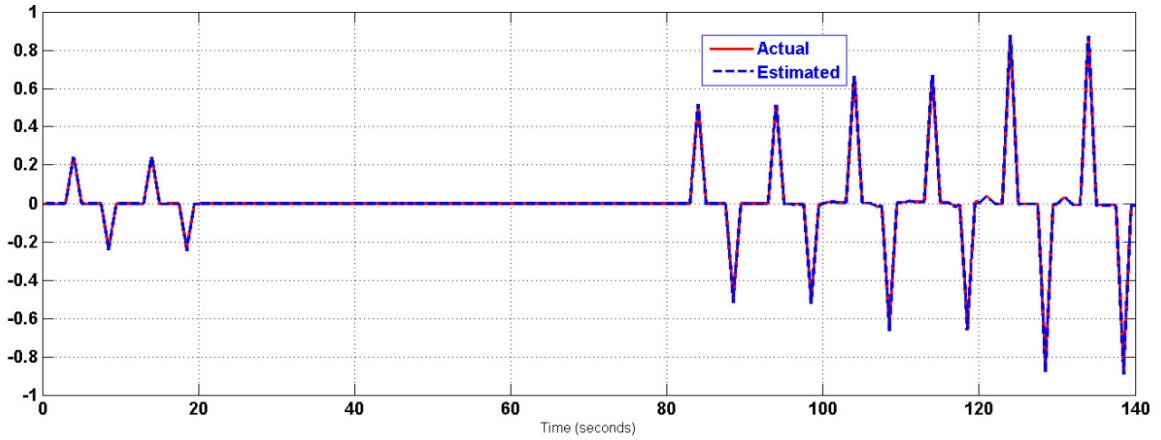


Figure 79: Composite Body Angular Velocity about Y-axis (rad/sec) using 18-accelerometer/Ring in Two-Ring Configuration, with Standard Kalman Filter and without noise.

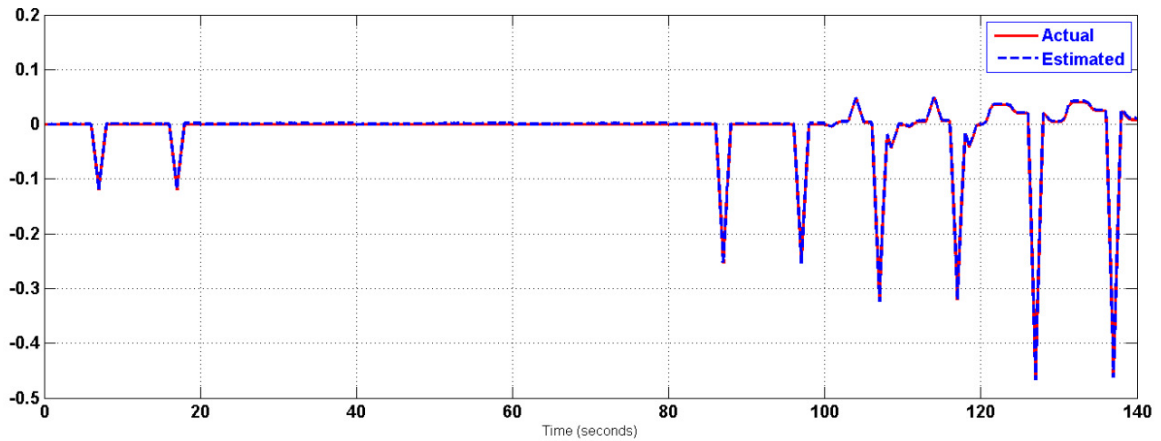


Figure 80: Composite Body Angular Velocity about X-axis (rad/sec) using 18-accelerometer/Ring in Two-Ring Configuration, with Standard Kalman Filter and without noise.

Now, the results obtained when noise, greater than what have been used in UKF just to show the point of interest, was added are shown in Figure 81. It is clear that the noise, once integrated, will introduce a drift in the estimated angular velocity, so it is maybe essential to design a complementary filter or to introduce redundant measurements to enhance the performance of the standard Kalman Filter and the quality of the estimated angular velocity as can be found in [62].

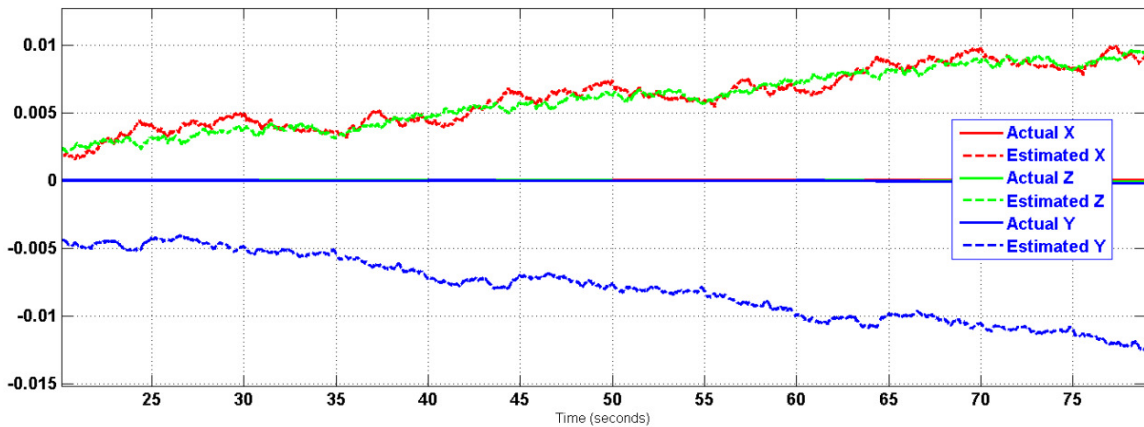


Figure 81: Composite Body Angular Velocities (rad/sec) using 18-accelerometer/Ring in Two-Ring Configuration, with Standard Kalman Filter and with noise.

This system was provided only for sake of completeness and it seems attractive especially when implemented in real hardware devices. In such a case, the redundant accelerometers' measurements can still be used in fault detection, CoG position estimation, and gravity tensor determination.

6.3 Summary

In this chapter, different systems have been formulated to make the best out of the available measurements in order to retrieve the angular velocity from the available accelerometers' measurements. It was shown that for System 6, an UKF can preferably be used along with 1-D and 3-D measurement models. The observability of Systems 4 and 6 was investigated and a conclusion was made that the observability is necessary but not sufficient for an EKF to operate nicely. System 7 was also introduced to complete the picture where a standard Kalman Filter simply acts as an integrator for the angular acceleration to retrieve the angular velocity. This approach suffers from the drift caused

by the noise available in the measurements so a solution is needed and can be found in [62]. System 7 can be of use once the gravity tensor is estimated as can be seen in Chapter 7.

Table 15 shows the maximum percentage error quantifying the performance of different filters used to retrieve the angular velocity using the proposed IMU. It is clear that the standard Kalman Filter exhibits the best performance, then UKF, and Finally EKF.

Table 15: Maximum Percentage Error of the estimated angular velocity obtained using different Filters

Filter Type			Maximum Percentage Error %		
			Non-Linear Measurement model		
			1-D	2-D	3-D
System 6 Linear System	EKF	Without Sign ambiguity Solution	17.5239	500.1133	18.1712
		With Sign ambiguity Solution	8.6870	189.6023	8.8964
	UKF	Without Sign ambiguity Solution	5.0590	283.3059	5.8795
		With Sign ambiguity Solution	3.1458	85.8435	3.8833
System 7 Linear System	KF		Linear Measurement model		
			1.1679		

CHAPTER 7

GRAVITY COMPENSATION

Inertial Navigation Systems (INS) depend on inertial sensors. The accelerometer is the only inertial sensor used in All-accelerometers IMUs. The measurements of the accelerometers are affected by the gravity force that must be compensated for before the measurements of the accelerometers are used further in other calculations. Equation (82) shows the relation between the inertial accelerometer measurements (\vec{A}_i), for an accelerometer located at the stationary CoG, and the acceleration due to gravity (\vec{g}).

$$\vec{A}_i = \vec{A}_b - \vec{g} \quad (82)$$

Where, \vec{A}_b is the acceleration of the body to which the accelerometer is attached, and \vec{g} is commonly known to be equal to (9.81 m/sec²). In fact it is different from place to place and it depends on many factors which makes a gravity model hard to be built. In addition, as the accelerometers' accuracy is increasing, due to new fabrication techniques, it was found that the error in the value of gravity acceleration contributes most in the overall navigation error; hence there is a need to reduce this error [94].

The gravitational field can be measured using a gravimeter, i.e. gravity meter, or a gradiometer. The later has a number of advantages because of which its usage becomes more frequent. Different types of gravity gradiometer devices are available, such as gradiometers based on electrostatic or rotating accelerometers.

Airborne gravity gradiometers are becoming popular in natural resources prospecting and in mining surveys as well; since aircraft can reach areas easily than a ground survey can do [91].

The feasibility of using an airborne gravity gradiometer in high precision INS is investigated in [92]. It is worth noting, at this point, that the sole focus of this thesis is on all-accelerometers based IMU that can be used with the available INS. So, the integration of gradiometer within INS is utilized through the all-accelerometers based IMU proposed here.

As was shown previously in section 2.2, there are two main types of INS, namely: the stabilized platform and the strapdown INS. In the former, the angular motion of the carrier vehicle will not participate in the overall equations as was shown in [92]. In [93], the gravity gradiometer based on stabilized INS was presented, and the governing equations were derived in more detail where the cases of aided INS that combines INS measurements with low and high bandwidths from two IMUs with different qualities are included.

The errors associated with integrated INS and a gravity gradiometer were analyzed in [94] where it shows that the errors associated with gravitation can be reduced to about 5 meters after one hour of free-inertial navigation. It should be clear that the more precise acceleration and angular measurements are, the less error they will have once compared to gravity model errors which must be compensated for.

The effect of the earth model adopted in this thesis, namely FEM, is investigated in [95] where it shows that such a simple model will not be sufficient to accurately obtain the gravitational field using gradiometers in stabilized systems. So, the earth rotation must be included into the governing equations, or at least investigated in a strapdown INS, which will be a part of future work as will be shown in Chapter 10.

The basic idea of using All-accelerometers based IMU in a strapdown configuration as a gravity gradiometer was presented in [44].

In [96], the usage of accelerometer-based gravity gradiometer is formulated and accordingly, the governing equations of Bell/Aero gravity gradiometer were derived. This part is very essential in this thesis; because one of its objectives is to compensate for gravity. It is intended to compensate for the gravity using only the accelerometers' readings available from all-accelerometers IMU, so no gravity models or tables are used nor needed.

In [74], a strapdown Inertial Navigation System (SINS) for an air vehicle was developed using the Flat-Earth model (FEM) and the NED coordinate system. The earth acceleration and rotation effects were neglected; since those generated from the aircraft is too large once compared to the earth's counterparts, knowing that gravity is assumed to be constant. This approach can produce wrong results if the results presented in a stabilized system are considered as can be found in [95].

In [97], the usage of 18 accelerometers was demonstrated to show how to extract angular velocity, angular/linear acceleration, and the gravitational gradient. Instrumental error analysis was done which showed that a gravitational field affects the errors in position, velocity and acceleration so that they increase without bound all the time.

In [103-106], a correctable model of INS, which can be corrected via external means such as GPS and the like, to determine the earth's gravitational field, was presented. It also show the reason why most the time gravimetry and INS are combined with each other.

In [102], a Kalman filter is used to find the values of magnetic and gravitational fields from gyro measurements individually. INS was considered in Laparoscopic Surgery due to line of sight constraints where optical tracking is not possible. The gravity effect was removed from the accelerometers' measurements using Kalman filter where a dynamic model of gravity estimation is presented.

In [100], all-accelerometers and gravity gradiometer relationship was derived, and also the Bell/Aero gradiometer equations were derived. The advantages of using a gradiometer over using gravimeter were mentioned to be:

- 1- Gravity gradient sensitivity to the high frequency information of earth is higher.
- 2- Gravimeter can give gravity information in one direction only, where gradiometer can give five components of the symmetric and traceless gravity gradient tensor.
- 3- It has more anti-jamming capabilities.

- 4- The gravimeter is affected by the movement of its carrier because it cannot distinguish the acceleration due to gravity and that of its carrier, where gradiometer is not.

In [103], the All-Accelerometer based Gradiometer is assumed to be located at the CoG while in thesis, such assumption is not forced.

The main participation of this thesis regarding the gravity compensation is to find the acceleration due to varying gravity under the assumption of varying CoG using an identification scheme which was not tackled before as far as the author is aware of.

7.1 Problem Formulation

Referring to Figure 22, the ideal accelerometer's measurements can be given by the following equation:

$$\vec{A}_i = \vec{A}_b + \ddot{\vec{R}}_{vk} + \dot{\vec{\Omega}} \times (\vec{R}_{vk} + \mu\hat{s}) + 2\vec{\Omega} \times \dot{\vec{R}}_{vk} + \vec{\Omega} \times (\vec{\Omega} \times (\vec{R}_{vk} + \mu\hat{s})) - \vec{g}_i \quad (83)$$

Where (i) denotes the accelerometer index within the (kth) ring, (\vec{A}_b) is the vehicle acceleration at the CoG relative to the inertial frame measured in the body frame, (\vec{R}_{vk}) is the vector from the CoG to the center of the (kth) ring, ($\ddot{\vec{R}}_{vk}$) is the acceleration of the CoG relative to the (kth) ring, ($\dot{\vec{R}}_{vk}$) is the velocity of the CoG relative to the (kth) ring, (μ_i) is the distance of the (ith) accelerometer from the center of the (kth) ring which is assumed to be equal for all the accelerometers within the same ring and it is assumed to be less than 1 meter, ($\vec{\Omega}$) is the angular velocity of the body, ($\dot{\vec{\Omega}}$) is its angular acceleration, (\times) denotes the cross product between two vectors, and (\hat{s}) is the unit vector

in the X, Y, or Z directions corresponding to the axis where the accelerometer is attached to. Finally, (\vec{g}_i) is the gravity vector measured in the body frame affecting the measurements of the (i^{th}) accelerometer in the (k^{th}) ring.

Practically speaking, these measurements are subjected to various sources of errors that make the ideal measurements impossible to have. Despite this fact, this chapter will use the ideal measurements just for simplicity of derivation of the remaining equations. Error analysis can be a part of future work, see Chapter 10.

The actual measurements obtained from an accelerometer, i.e. a tri-axis one, are given by the following equation:

$$\vec{\tilde{A}}_i = \mathbf{A}_{SFCC(i)}\vec{A}_i + \vec{A}_{bias(i)} + \overline{noise}_i \quad (84)$$

Where, $(\mathbf{A}_{SFCC(i)})$ denotes a (3X3) matrix whose diagonal represents the Scale Factor for each channel of the tri-axis accelerometers, namely: x, y, and z channels, and its off diagonal are the Cross Coupling between the other two axes denoted by (M) . $(A_{bias(i)})$ represents the bias each channel has which may vary with time. (\overline{noise}_i) represents the noise each channel has, and most the time it is considered as a white noise for simplicity.

$(\mathbf{A}_{SFCC(i)})$ is given as follows:

$$\mathbf{A}_{SFCC(i)} = \begin{bmatrix} 1 + S_{xi} & M_{yi} & M_{zi} \\ M_{xi} & 1 + S_{yi} & M_{zi} \\ M_{xi} & M_{yi} & 1 + S_{zi} \end{bmatrix} \quad (85)$$

Recall that all the accelerometers within each ring are arranged in a diamond configuration, i.e. two accelerometers spaced equally about the ring's center with a distance equal to μ in each axis.

When taking the difference between each pair of accelerometers in one direction, i.e. X, Y, or Z axis, the following will result:

For the tri-axis accelerometers pair in the X-axis of any ring, drop the ring index (k) and assume all rings are aligned to the body reference frame:

$$\vec{A}_1 - \vec{A}_2 = 2\dot{\vec{\Omega}} \times \mu\hat{i} + 2\vec{\Omega} \times (\vec{\Omega} \times \mu\hat{i}) - (\vec{g}_1 - \vec{g}_2) \quad (86)$$

For the accelerometers pair in the Y-axis of any ring:

$$\vec{A}_3 - \vec{A}_4 = 2\dot{\vec{\Omega}} \times \mu\hat{j} + 2\vec{\Omega} \times (\vec{\Omega} \times \mu\hat{j}) - (\vec{g}_3 - \vec{g}_4) \quad (87)$$

For the accelerometers pair in the Z-axis of any ring:

$$\vec{A}_5 - \vec{A}_6 = 2\dot{\vec{\Omega}} \times \mu\hat{k} + 2\vec{\Omega} \times (\vec{\Omega} \times \mu\hat{k}) - (\vec{g}_5 - \vec{g}_6) \quad (88)$$

Where, \hat{i} , \hat{j} , and \hat{k} are the units vector in the ring X, Y, and Z axes respectively.

The gravity vector is a function of the position, so it may be given as follows [93]:

$$\vec{g} = [G_x(x(t), y(t), z(t)) \quad G_y(x(t), y(t), z(t)) \quad G_z(x(t), y(t), z(t))]^T \quad (89)$$

The difference between two gravity vectors is considered as the gravity gradient which changes within a large distance in space that may reach kilometers [110,111]. The symmetric gravity gradient with respect to body frame is given by [44]:

$$\Gamma^a = \nabla g / (2\mu) = \begin{bmatrix} \Gamma_{xx} & \Gamma_{xy} & \Gamma_{xz} \\ \Gamma_{xy} & \Gamma_{yy} & \Gamma_{yz} \\ \Gamma_{xz} & \Gamma_{yz} & \Gamma_{zz} \end{bmatrix} \quad (90)$$

Rearranging the previous equations and taking the appropriate part of the gravity gradient according to the axes of concern, then the previous equations will be given by:

$$\frac{\vec{A}_1 - \vec{A}_2}{2\mu} = ([\dot{\Omega}] + [\Omega \times] - \Gamma^a) \begin{bmatrix} 1 \\ 0 \\ 0 \end{bmatrix} \quad (91)$$

$$\frac{\vec{A}_3 - \vec{A}_4}{2\mu} = ([\dot{\Omega}] + [\Omega \times] - \Gamma^a) \begin{bmatrix} 0 \\ 1 \\ 0 \end{bmatrix} \quad (92)$$

$$\frac{\vec{A}_5 - \vec{A}_6}{2\mu} = ([\dot{\Omega}] + [\Omega \times] - \Gamma^a) \begin{bmatrix} 0 \\ 0 \\ 1 \end{bmatrix} \quad (93)$$

Where the cross product was replaced by the multiplication of a skew symmetric matrix and a vector in the right order, and the matrices $([\dot{\Omega}])$, $([\Omega \times])$ are given as follows:

$$[\dot{\Omega}] = \begin{bmatrix} 0 & -\dot{\Omega}_z & \dot{\Omega}_y \\ \dot{\Omega}_z & 0 & -\dot{\Omega}_x \\ -\dot{\Omega}_y & \dot{\Omega}_x & 0 \end{bmatrix}, \quad [\Omega \times] = \begin{bmatrix} -\Omega_z^2 - \Omega_y^2 & \Omega_x \Omega_y & \Omega_x \Omega_z \\ \Omega_x \Omega_y & -\Omega_z^2 - \Omega_x^2 & \Omega_z \Omega_y \\ \Omega_x \Omega_z & \Omega_z \Omega_y & -\Omega_y^2 - \Omega_x^2 \end{bmatrix} \quad (94)$$

Although the gravity gradient is traceless; because it satisfies the Laplace's equation assuming free air and the fact that gravitation is a conservative force [93], it is still impossible to determine the five elements uniquely using only the All-accelerometer configuration proposed in [7], so it was necessary to introduce another pair of accelerometers to render the needed elements observable. Arranging the previous three equations into one system yields:

$$\left[\frac{\vec{A}_1 - \vec{A}_2}{2\mu} \quad \frac{\vec{A}_3 - \vec{A}_4}{2\mu} \quad \frac{\vec{A}_5 - \vec{A}_6}{2\mu} \right] = ([\dot{\Omega}] + [\Omega \times] - \Gamma^a) \quad (95)$$

The previous system of equations contains nine equations need to be solved to determine the elements of gravity tensor, and both the angular velocity and acceleration. One approach to handle this system is to solve for the angular accelerations at the beginning, then through integrating the results the angular velocities can be obtained provided that their initial conditions are known [44]. After that, the elements of gravity tensor can be calculated. Implementing the previously stated procedure, the following equations can be solved and the results are as follows:

$$\dot{\Omega}_x(kT) = \frac{(A_{3z}(kT) - A_{4z}(kT)) - (A_{5y}(kT) - A_{6y}(kT))}{4\mu}, k = 0, 1, 2, \dots \infty \quad (96)$$

$$\dot{\Omega}_y(kT) = \frac{(A_{5x}(kT) - A_{6x}(kT)) - (A_{1z}(kT) - A_{2z}(kT))}{4\mu}, k = 0, 1, 2, \dots \infty \quad (97)$$

$$\dot{\Omega}_z(kT) = \frac{(A_{1y}(kT) - A_{2y}(kT)) - (A_{3x}(kT) - A_{4x}(kT))}{4\mu}, k = 0, 1, 2, \dots \infty \quad (98)$$

$$\Omega_x(kT) \cong \Omega_x(0) + \sum_{k=1}^N \int_{kT}^{(k+1)T} \dot{\Omega}_x \cdot dt, k = 0, 1, 2, \dots \infty \quad (99)$$

$$\Omega_y(kT) \cong \Omega_y(0) + \sum_{k=1}^N \int_{kT}^{(k+1)T} \dot{\Omega}_y \cdot dt, k = 0, 1, 2, \dots \infty \quad (100)$$

$$\Omega_z(kT) \cong \Omega_z(0) + \sum_{k=1}^N \int_{kT}^{(k+1)T} \dot{\Omega}_z \cdot dt, k = 0, 1, 2, \dots \infty \quad (101)$$

$$\Gamma_{xx}(kT) \cong -\frac{(A_{1x}(kT) - A_{2x}(kT))}{2\mu} - \Omega_z^2(kT) - \Omega_y^2(kT), k = 0, 1, 2, \dots \infty \quad (102)$$

$$\Gamma_{yy}(kT) \cong -\frac{(A_{3y}(kT) - A_{4y}(kT))}{2\mu} - \Omega_z^2(kT) - \Omega_x^2(kT), k = 0, 1, 2, \dots \infty \quad (103)$$

$$\Gamma_{zz}(kT) \cong -\frac{(A_{5z}(kT) - A_{6z}(kT))}{2\mu} - \Omega_x^2(kT) - \Omega_y^2(kT), k = 0, 1, 2, \dots \infty \quad (104)$$

$$\Gamma_{xy}(kT) \cong -\frac{(A_{3x}(kT) - A_{4x}(kT)) + (A_{1y}(kT) - A_{2y}(kT))}{4\mu} + \Omega_x(kT)\Omega_y(kT), k = 0, 1, 2, \dots \infty \quad (105)$$

$$\Gamma_{xz}(kT) \cong -\frac{(A_{5x}(kT) - A_{6x}(kT)) + (A_{1z}(kT) - A_{2z}(kT))}{4\mu} + \Omega_x(kT)\Omega_z(kT), k = 0, 1, 2, \dots \infty \quad (106)$$

$$\Gamma_{yz}(kT) \cong -\frac{(A_{3z}(kT) - A_{4z}(kT)) + (A_{5y}(kT) - A_{6y}(kT))}{4\mu} + \Omega_z(kT)\Omega_y(kT), k = 0, 1, 2, \dots \infty \quad (107)$$

Where, (T) is the sampling period. It is worth noting that the quality of results depends on the way the angular velocity is retrieved with using equations (99-101). System 7, previously shown in Chapter 6, can be used to retrieve the angular velocities, or a numerical integration technique can be used once the angular acceleration is calculated using equations (96-98). The results obtained using this approach depends on the numerical technique used, such as Trapezoidal or Simpson's rules for example. More details can be found in [85]. Another way is to solve a system of non-linear algebraic equations as can be found in [106].

Now, recall the ideal accelerometer measurements' equation:

$$\vec{A}_i = \vec{A}_b + \ddot{\vec{R}}_{vk} + \dot{\vec{\Omega}} \times (\vec{R}_{vk} + \mu_i \hat{s}) + 2\vec{\Omega} \times \dot{\vec{R}}_{vk} + \vec{\Omega} \times (\vec{\Omega} \times (\vec{R}_{vk} + \mu_i \hat{s})) - \vec{g}_i$$

Three cases can be considered, namely:

- Case (1): the CoG position is known, along with its acceleration and velocity, in such case equation (1) will be given as:

$$\vec{A}_i - \ddot{\vec{R}}_{vk} - \dot{\vec{\Omega}} \times (\vec{R}_{vk} + \mu_i \hat{s}) - 2\vec{\Omega} \times \dot{\vec{R}}_{vk} - \vec{\Omega} \times (\vec{\Omega} \times (\vec{R}_{vk} + \mu_i \hat{s})) = \vec{A}_b - \vec{g}_i \quad (108)$$

- Case (2): the CoG position is unknown and is moving with unknown constant velocity, in such case equation (83) will be given as:

$$\vec{A}_i = \vec{A}_b + \dot{\vec{\Omega}} \times (\vec{R}_{vk} + \mu_i \hat{s}) + 2\vec{\Omega} \times \dot{\vec{R}}_{vk} + \vec{\Omega} \times (\vec{\Omega} \times (\vec{R}_{vk} + \mu_i \hat{s})) - \vec{g}_i \quad (109)$$

- Case (3): the CoG position is unknown and is accelerating, in such case equation (83) will be given as:

$$\vec{A}_i = \vec{A}_b + \ddot{\vec{R}}_{vk} + \dot{\vec{\Omega}} \times (\vec{R}_{vk} + \mu_i \hat{s}) + 2\vec{\Omega} \times \dot{\vec{R}}_{vk} + \vec{\Omega} \times (\vec{\Omega} \times (\vec{R}_{vk} + \mu_i \hat{s})) - \vec{g}_i \quad (110)$$

In all the previous cases, the angular velocities and accelerations are known and it is now intended to find the unknown variables using the available accelerometers' measurements. Before proceeding further, the concept of redundant rings will be presented and utilized to reflect the position of CoG into the previous three cases. This approach will help in increasing the availability and reliability of measurements and estimation of the unknowns and make the configuration less dependent on a particular ring which allows excluding a ring's results once it is deemed faulty. Another thing to mention is that once such a configuration is established, a Centralized or Decentralized approach can be used to fuse the measurements and estimations of the available rings. Avionic networks, or the like, can be used to connect the rings to each other and to a

processing unit which makes the process more complicated if non-ideal network behavior is considered, which is beyond the scope of this thesis.

Since the equations are to be derived with respect to the ring level, it is better to refer to its center instead of referring to individual accelerometers within the same ring. This approach will also increase the reliability of measurements within the same ring even in the case of a particular accelerometer failure. For example, the health of each channel in an accelerometer within a ring can be checked using the procedure described in [7]. It is also obvious that once this approach is used, then the data processing within a Ring will not be dependent on its radius (μ). However, the design process of a Ring is more concerned about reducing the sizing effect by choosing its radius (μ) in an optimal fashion that complies with the vehicle's constraints and the desired measurements' sensitivity.

If all the accelerometers' measurements are correct, i.e. have been checked as described in [7], the acceleration at the center of the (k^{th}) Ring is given by:

$$\vec{a}_{rk} = \frac{\sum_{i=1}^6 \vec{A}_{ik}}{6}, k = 1, 2, \dots, N \quad (111)$$

Where, (N) is the number of redundant rings.

Figure 82 shows a Three-Ring configuration from which the following equations can be derived:

$$\vec{R}_1 - \vec{R}_G = \vec{R}_{v1} \quad (112)$$

$$\vec{R}_2 - \vec{R}_G = \vec{R}_{v2} \quad (113)$$

$$\vec{R}_3 - \vec{R}_G = \vec{R}_{v3} \quad (114)$$

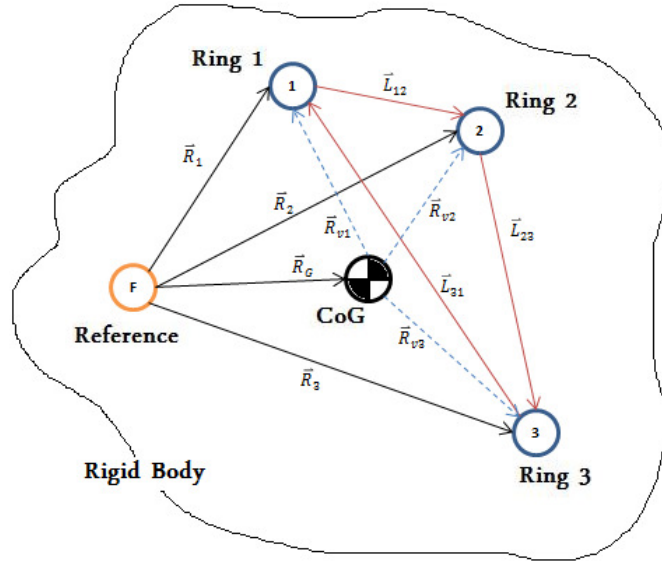


Figure 82: Rings Arrangement within a rigid body.

Substituting equations (111-114) into (108-110) will change the previously mentioned cases as follows; where results are shown only for Ring 1:

- Case (1):

$$\begin{aligned} \ddot{\vec{a}}_{r1} + \ddot{\vec{R}}_G - \dot{\vec{\Omega}} \times (\vec{R}_1 - \vec{R}_G) + 2\vec{\Omega} \times \dot{\vec{R}}_G - \vec{\Omega} \times (\vec{\Omega} \times (\vec{R}_1 - \vec{R}_G)) \\ = \vec{A}_b - \vec{g}_1 \end{aligned} \quad (115)$$

- Case (2):

$$\begin{aligned} \ddot{\vec{a}}_{r1} - \dot{\vec{\Omega}} \times \vec{R}_1 - \vec{\Omega} \times (\vec{\Omega} \times \vec{R}_1) = \vec{A}_b - \dot{\vec{\Omega}} \times \vec{R}_G - 2\vec{\Omega} \times \dot{\vec{R}}_G - \vec{\Omega} \times \\ (\vec{\Omega} \times \vec{R}_G) - \vec{g}_1 \end{aligned} \quad (116)$$

- Case (3):

$$\begin{aligned} \ddot{\vec{a}}_{r1} - \dot{\vec{\Omega}} \times \vec{R}_1 - \vec{\Omega} \times (\vec{\Omega} \times \vec{R}_1) \\ = \vec{A}_b + \ddot{\vec{R}}_G - \dot{\vec{\Omega}} \times \vec{R}_G - 2\vec{\Omega} \times \dot{\vec{R}}_G - \vec{\Omega} \times (\vec{\Omega} \times \vec{R}_G) - \vec{g}_1 \end{aligned} \quad (117)$$

Now, it is clear that the previous equations heavily dependent on the angular motion of the vehicle, that may not be available for some interval depending on the flight path, flight conditions, and the type of the vehicle, i.e. car on a flat surface.

Recall that the gravitational gradient is given by (90) from which the gravity vector can be retrieved, in the body frame, as follows [93]:

$$\begin{bmatrix} g_x \\ g_y \\ g_z \end{bmatrix} = \vec{g}_0 + \int_0^t \Gamma^a \vec{V}_b . dt \quad (118)$$

Where (\vec{V}_b) is the body inertial velocity evaluated in the body frame, and (\vec{g}_0) is the gravity vector given at the initial position which is assumed to be known to certain accuracy in the body frame as well. If (\vec{V}_b) is small so that it does not violate the assumption of constant gravitational gradient within a finite number of successive sampling intervals, then the gravity vector may be given by:

$$\begin{bmatrix} g_x \\ g_y \\ g_z \end{bmatrix} = \vec{g}_0 + \Gamma^a \vec{S} \quad (119)$$

Where, (\vec{S}) is the inertial position of the vehicle measured in the body frame and its second derivative is the linear inertial acceleration of the vehicle (\vec{A}_b) measured at the center of gravity with respect to the body frame. The general equation is given as follows making use of (118):

$$\begin{aligned} \vec{a}_{ri} - \dot{\vec{\Omega}} \times \vec{R}_i - \vec{\Omega} \times (\vec{\Omega} \times \vec{R}_i) + \vec{g}_0 = \ddot{\vec{S}} - \ddot{\vec{R}}_G - \dot{\vec{\Omega}} \times (\vec{R}_G) - 2\vec{\Omega} \times \dot{\vec{R}}_G \\ - \vec{\Omega} \times (\vec{\Omega} \times (\vec{R}_G)) - \int_0^t \Gamma^a V . dt = m(t) \end{aligned} \quad (120)$$

Now, equation (120) will be discretized to reflect the exact relations between the unknown variable where four models are presented. A sampling interval equals to (h) is chosen, and backward finite-divided-difference formulas for the first and second derivatives are used to obtain a numerical accuracy equals to $O(h^2)$ and the integral part is simplified first using the trapezoidal rule followed by the derivatives approximations. These equations are given as follows [85]:

$$\dot{f}(x_i) = \frac{3f(x_i) - 4f(x_{i-1}) + f(x_{i-2})}{2h} \quad (121)$$

$$\ddot{f}(x_i) = \frac{2f(x_i) - 5f(x_{i-1}) + 4f(x_{i-2}) - f(x_{i-3})}{h^2} \quad (122)$$

$$\int_0^t \Gamma^a V. dt \cong \sum_{i=1}^N \frac{h}{2} \left\{ \int_{t_i}^{t_{i+1}} \Gamma^a(t_i) \dot{S}(t_i) + \Gamma^a(t_{i-1}) \dot{S}(t_{i-1}) \right\} \quad (123)$$

- Model I:

Equation (120) can be simplified more by utilizing equations (121-123), and then equation (120) can be given as a discrete equation as follows:

$$\begin{aligned} 2h^2 m(k) = & \left\{ 4\vec{S}(k) + \left(4I - 2h^2([\dot{\Omega}](k) + [\Omega \times](k)) - 6h[\Omega](k) \right) \vec{R}_G(k) \right\} \\ & - \left\{ 10\vec{S}(k-1) + (10I - 8h[\Omega](k)) \vec{R}_G(k-1) \right\} \\ & + \left\{ 8\vec{S}(k-2) + (8I - 2h[\Omega](k)) \vec{R}_G(k-2) \right\} \\ & - \left\{ 2\vec{S}(k-3) + 2\vec{R}_G(k-3) \right\} \\ & - \frac{h^2}{2} \sum_{i=1}^k \left\{ 3\Gamma^a(i) \vec{S}(i) + (3\Gamma^a(i-1) - 4\Gamma^a(i)) \vec{S}(i-1) \right. \\ & \left. + (\Gamma^a(i) - 4\Gamma^a(i-1)) \vec{S}(i-2) + \Gamma^a(i-1) \vec{S}(i-3) \right\} \end{aligned} \quad (124)$$

Where $I_{3 \times 3}$ identity matrix, and $k = 0, 1, 2, \dots, \infty$

$$\begin{aligned}
2h^2m(k) + \frac{h^2}{2} \sum_{i=1}^{k-1} & \{3\Gamma^a(i)\vec{S}(i) + (3\Gamma^a(i-1) - 4\Gamma^a(i))\vec{S}(i-1) \\
& + (\Gamma^a(i) - 4\Gamma^a(i-1))\vec{S}(i-2) + \Gamma^a(i-1)\vec{S}(i-3)\} \\
& = \left\{ \left(4I - \frac{3h^2}{2}\Gamma^a(k)\right)\vec{S}(k) \right. \\
& + \left. \left(4I - 2h^2([\dot{\Omega}](k) + [\Omega \times](k)) - 6h[\Omega](k)\right)\vec{R}_G(k) \right\} \\
& - \left\{ \left(10I + \frac{h^2}{2}(3\Gamma^a(k-1) - 4\Gamma^a(k))\right)\vec{S}(k-1) \right. \\
& + \left. (10I - 8h[\Omega](k))\vec{R}_G(k-1) \right\} \\
& + \left\{ \left(8I - \frac{h^2}{2}(\Gamma^a(k) - 4\Gamma^a(k-1))\right)\vec{S}(k-2) \right. \\
& + \left. (8I - 2h[\Omega](k))\vec{R}_G(k-2) \right\} \\
& - \left\{ \left(2I + \frac{h^2}{2}\Gamma^a(k-1)\right)\vec{S}(k-3) + 2\vec{R}_G(k-3) \right\}
\end{aligned}$$

$$\text{Where, } [\Omega] = \begin{bmatrix} 0 & -\Omega_z & \Omega_y \\ \Omega_z & 0 & -\Omega_x \\ -\Omega_y & \Omega_x & 0 \end{bmatrix} \quad (125)$$

- Model II:

Additionally, the numerical accuracy can be sacrificed to simplify the problem formulation and computation, by using backward finite-divided-difference formulas for the first and second derivatives that gives a numerical accuracy equals to $O(h)$ instead as follows [85]:

$$\dot{f}(x_i) = \frac{f(x_i) - f(x_{i-1})}{h} \quad (126)$$

$$\ddot{f}(x_i) = \frac{f(x_i) - 2f(x_{i-1}) + 2f(x_{i-2}))}{h^2} \quad (127)$$

Then, equation (120) is given as follows:

$$\begin{aligned}
h^2 m(k) = & \left\{ \vec{S}(k) + \left(I - h^2 \left([\dot{\Omega}](k) + [\Omega \times](k) \right) - 2h[\Omega](k) \right) \vec{R}_G(k) \right\} \\
& - \left\{ 2\vec{S}(k-1) + (2I - 2h[\Omega](k)) \vec{R}_G(k-1) \right\} \\
& + \left\{ \vec{S}(k-2) + \vec{R}_G(k-2) \right\} \\
& - \frac{h^2}{2} \sum_{i=1}^k \left\{ \Gamma^a(i) \vec{S}(i) + (\Gamma^a(i-1) - \Gamma^a(i)) \vec{S}(i-1) \right. \\
& \left. - \Gamma^a(i-1) \vec{S}(i-2) \right\}
\end{aligned} \tag{128}$$

Where $I_{3 \times 3}$ identity matrix, and $k = 0, 1, 2, \dots \infty$

$$\begin{aligned}
h^2 m(k) + \frac{h^2}{2} \sum_{i=1}^{k-1} \left\{ \Gamma^a(i) \vec{S}(i) + (\Gamma^a(i-1) - \Gamma^a(i)) \vec{S}(i-1) - \Gamma^a(i-1) \vec{S}(i-2) \right\} = & \left\{ \left(I - \frac{h^2}{2} \Gamma^a(k) \right) \vec{S}(k) + \left(I - h^2 \left([\dot{\Omega}](k) + [\Omega \times](k) \right) - 2h[\Omega](k) \right) \vec{R}_G(k) \right\} \\
& - \left\{ \left(2I + \frac{h^2}{2} (\Gamma^a(k-1) - \Gamma^a(k)) \right) \vec{S}(k-1) + \left(2I - 2h[\Omega](k) \right) \vec{R}_G(k-1) \right\} \\
& + \left\{ \left(I + \frac{h^2}{2} \Gamma^a(k-1) \right) \vec{S}(k-2) + \vec{R}_G(k-2) \right\}
\end{aligned}$$

If the special case is considered, namely when the gravity tensor is constant, then the following two models can be obtained:

- Model III:

Equation (120) can be simplified more by utilizing equations (119, 121-122), and then equation (120) can be given as a discrete equation as follows taking the gravity tensor as constant:

$$\begin{aligned}
2h^2 m(k) = & \left\{ (4I - 2h^2 \Gamma^a(k)) \vec{S}(k) \right. \\
& + \left(4I - 2h^2 \left([\dot{\Omega}](k) + [\Omega \times](k) \right) - 6h[\Omega](k) \right) \vec{R}_G(k) \left. \right\} \\
& - \left\{ 10\vec{S}(k-1) + (10I - 8h[\Omega](k)) \vec{R}_G(k-1) \right\} \\
& + \left\{ 8\vec{S}(k-2) + (8I - 2h[\Omega](k)) \vec{R}_G(k-2) \right\} \\
& - \left\{ 2\vec{S}(k-3) + 2\vec{R}_G(k-3) \right\}
\end{aligned} \tag{129}$$

Where $I_{3 \times 3}$ identity matrix, and $k = 0, 1, 2, \dots \infty$

- Model IV:

Using equations (119) and (126-127), then equation (120) is given as follows:

$$\begin{aligned}
 h^2 m(k) = & \left\{ (I - h^2 \Gamma^a(k)) \vec{S}(k) \right. \\
 & + \left(I - h^2 ([\dot{\Omega}](k) + [\Omega \times](k)) - 2h[\Omega](k) \right) \vec{R}_G(k) \left. \right\} \\
 & - \left\{ 2\vec{S}(k-1) + (2I - 2h[\Omega](k)) \vec{R}_G(k-1) \right\} \\
 & + \left\{ \vec{S}(k-2) + \vec{R}_G(k-2) \right\}
 \end{aligned} \tag{130}$$

Where $I_{3 \times 3}$ identity matrix, and $k = 0, 1, 2, \dots, \infty$

Finally, the regression forms of the previous four models will be given in Chapter 8. One of the previous models can be used according to the problem in hand, for example Model I can be used with Air vehicles having large MACH numbers where the gravity tensor cannot be approximated as a constant while Model II can be used for the same case with reduced computations especially when the CoG acceleration is not an added information to the problem. On the opposite, Models III and IV can be used with air vehicles having low MACH numbers.

7.2 Simulating the Gravity Gradient

In this chapter, the Gradiometer device was presented. The structure of the proposed IMU facilitates incorporating the Gradiometer into its functionality. “Significant research has been conducted in recent decades on developing a practical all-accelerometer inertial navigation system and on developing a practical moving base gravity gradiometer. The former strives to measure kinematic motion in the presence of unwanted variations in gravity; the latter endeavors to measure variations in gravity in the presence of unwanted motion. Thus, goes the adage, *one person’s signal is another person’s noise*”^[42].

The European Space Agency (ESA) has launched a number of space missions serving the purpose of earth exploration among them is the Gravity field and Ocean Circulation Explorer (GOCE) Earth Explorer [131]. GOCE aims to measure the gravitational field and it is built about a Gradiometer instrument as shown in Figure 83. The resolution of the accelerometers' measurements is less than $2.0^{-12} \frac{m}{s^2\sqrt{Hz}}$.

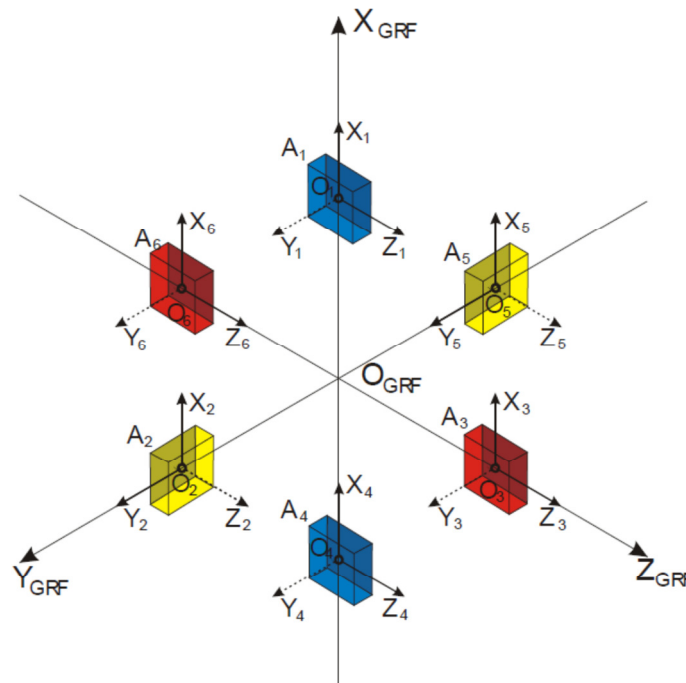


Figure 83: Nomenclature and location of the 6 accelerometers of the GOCE Gradiometer in the Gradiometer Reference Frame (GRF) and with all Accelerometer Reference Frame (ARF) [132].



Figure 84: Electrostatic Gravity Gradiometer (EGG) [133].

The main objective of Electrostatic Gravity Gradiometer (EGG) is to measure the three components of the GGT (Gravity-Gradient Tensor). The EGG instrument, designed and developed at ONERA (Office National d'Etudes et de Recherches Aérospatiales) and manufactured at Thales Alenia Space, France, is based on an ambient temperature, closed loop, capacitive accelerometer concept.

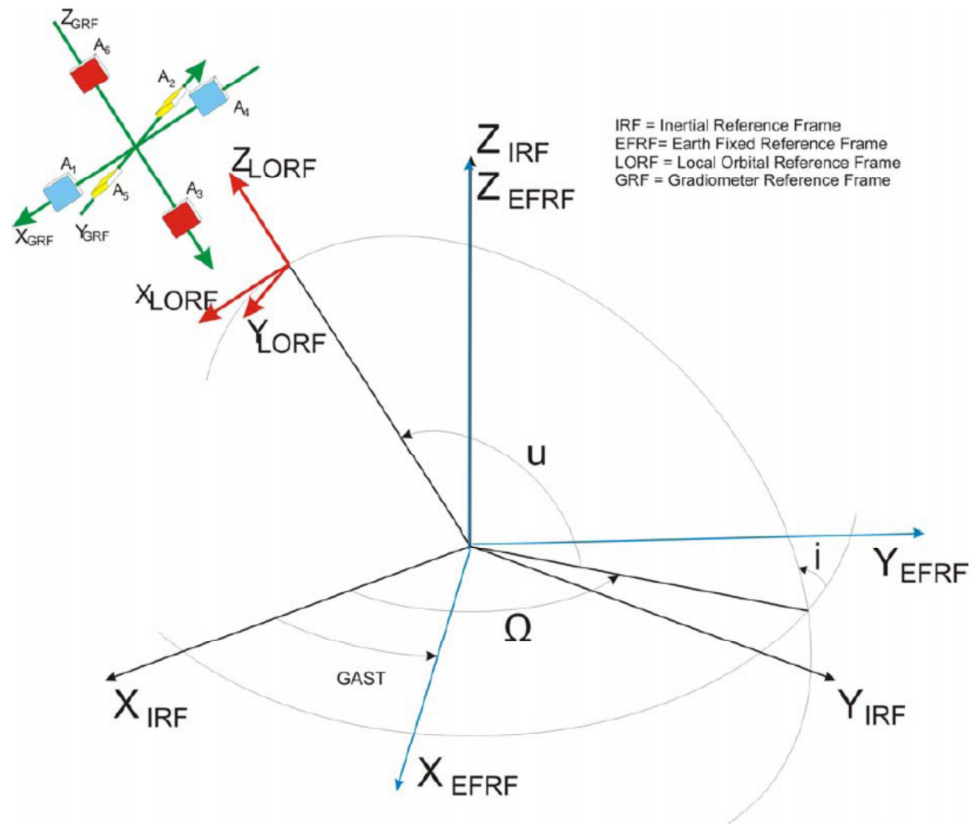


Figure 85: Major Reference Frames for Gradiometry [132].

The Gradiometer was attached to the GOCE spacecraft shown in Figure 86.



Figure 86: GOCE spacecraft [131].

7.2.1 Simulating Gravity Gradient using EGG

Making use of the available data from the ESA website, the following figures show sample gravity gradient measurement along with the calculated gravity gradient using the equations described in this chapter. The units used are Eötvös, which is a non-SI unit named for Loránd Eötvös, a Hungarian physicist: $1 E = 10^{-9} s^{-2}$ [93]. A MATLAB reader downloaded from ESA facilitates reading a GOCE EGG_NOM_1b product file containing the following data:

- Time GPS
- Common (CCM) and Differential (CDM) accelerations for each accelerometer pair.
- Gravity Gradient Tensor components $\Gamma_{xx}, \Gamma_{yy}, \Gamma_{zz}, \Gamma_{xy}, \Gamma_{xz}, \Gamma_{yz}$ in EGG frame.
- Gradiometer Inertial Attitude Quaternions (IAQ)
- Quality

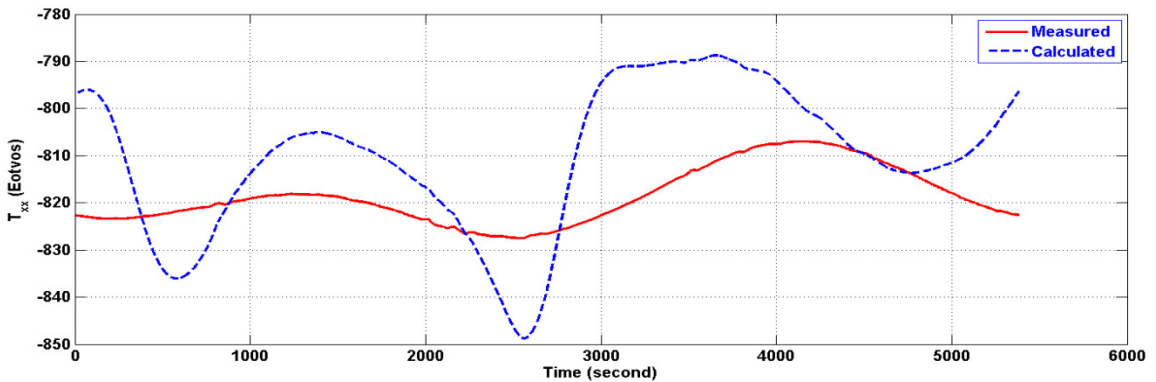


Figure 87: Γ_{xx} gravity gradient component.

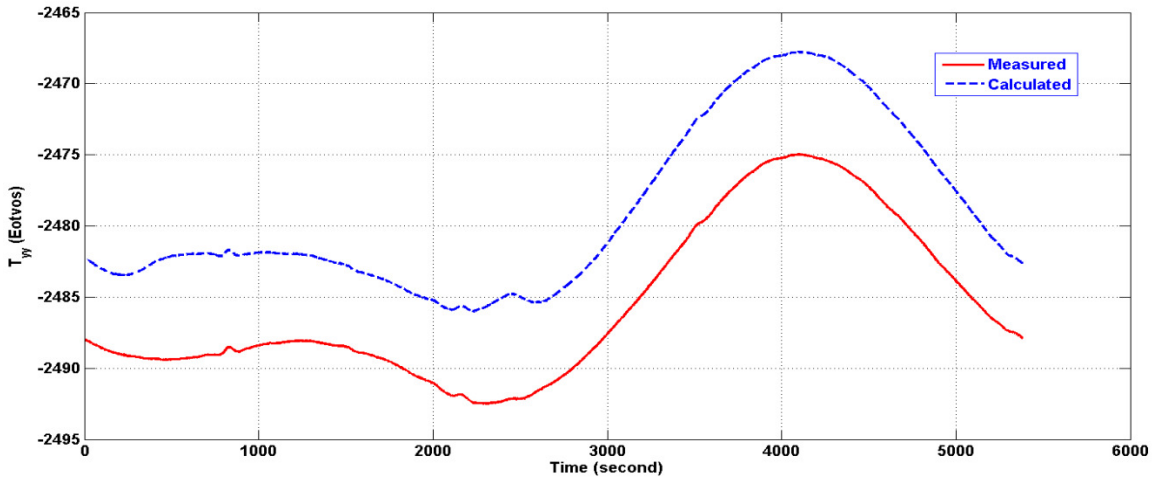


Figure 88: Γ_{yy} gravity gradient component.

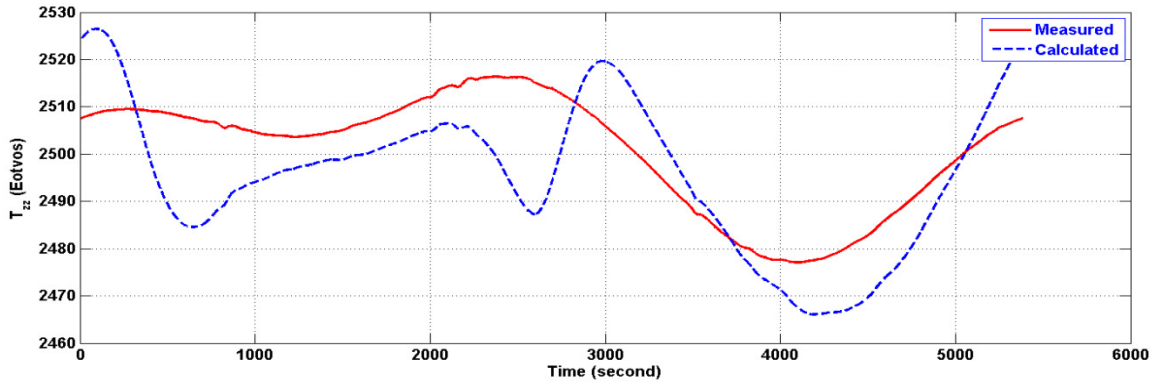


Figure 89: Γ_{zz} gravity gradient component.

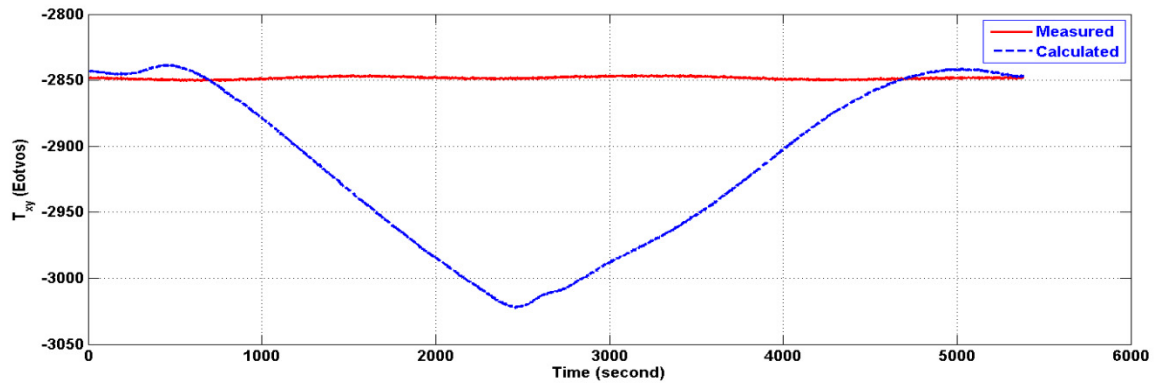


Figure 90: Γ_{xy} gravity gradient component.

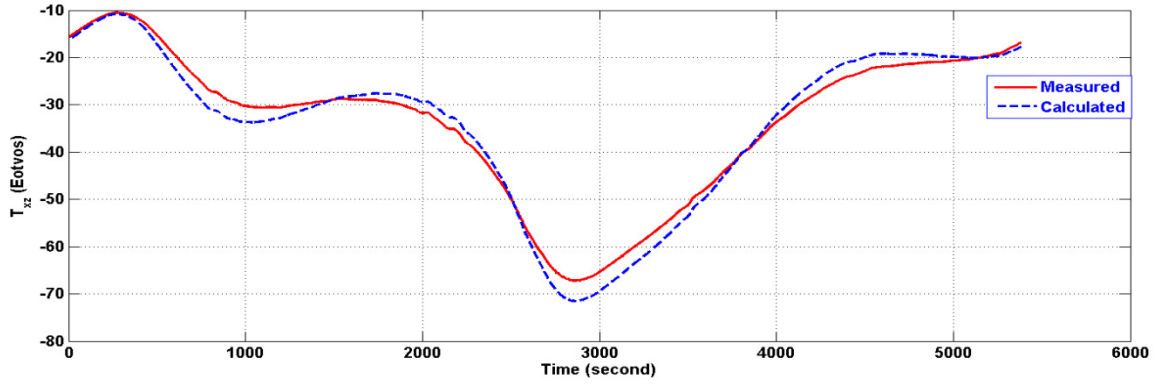


Figure 91: Γ_{xz} gravity gradient component.

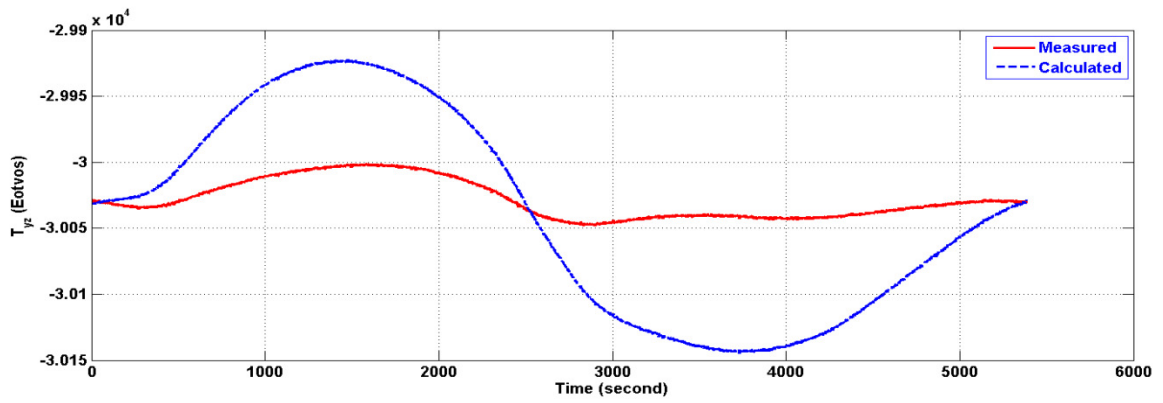


Figure 92: Γ_{yz} gravity gradient component in order of 10^4 .

The following values were used to generate the calculated curves [134]:

$$\begin{bmatrix} \Omega_x \\ \Omega_y \\ \Omega_z \end{bmatrix} = \begin{bmatrix} 0 \\ 1.17 \\ 0 \end{bmatrix} * 10^{-3} \text{ rad/sec}$$

$$\begin{bmatrix} \dot{\Omega}_x \\ \dot{\Omega}_y \\ \dot{\Omega}_z \end{bmatrix} = \begin{bmatrix} 0 \\ 0 \\ 0 \end{bmatrix} \text{ rad/sec}^2 \quad (131)$$

$$L = 0.5 \text{ m}$$

7.2.2 Simulating Gravity Gradient using SimMechanics/Simulink

Figure 93 shows the Simulink model used to simulate the gradient. Making use of the SimMechanics library features, the following figures were obtained.

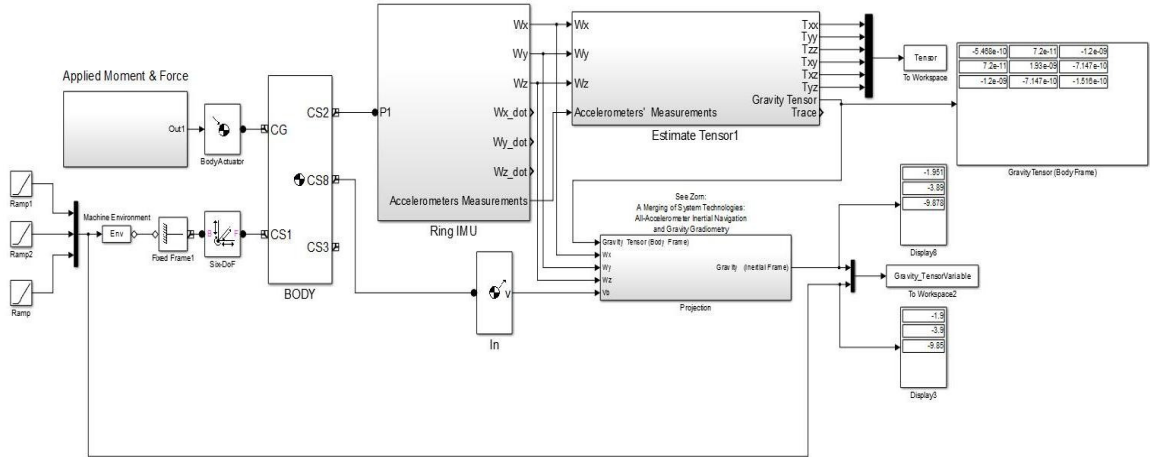


Figure 93: Simulink model used to simulate the gravity gradient.

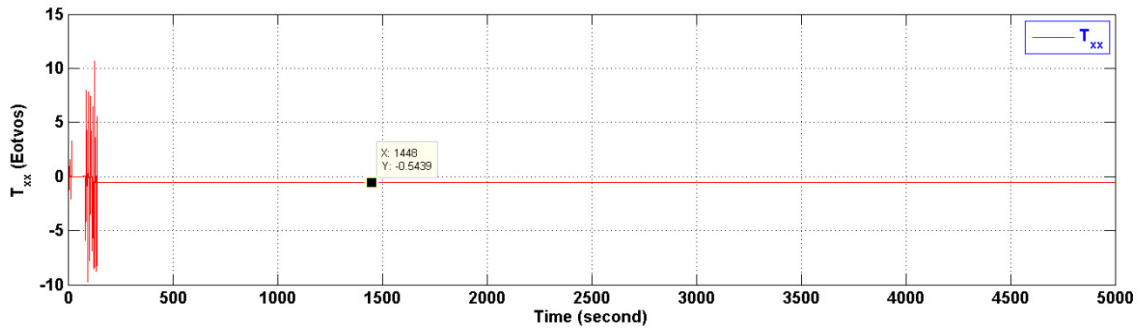


Figure 94: Γ_{xx} simulated gravity gradient component.

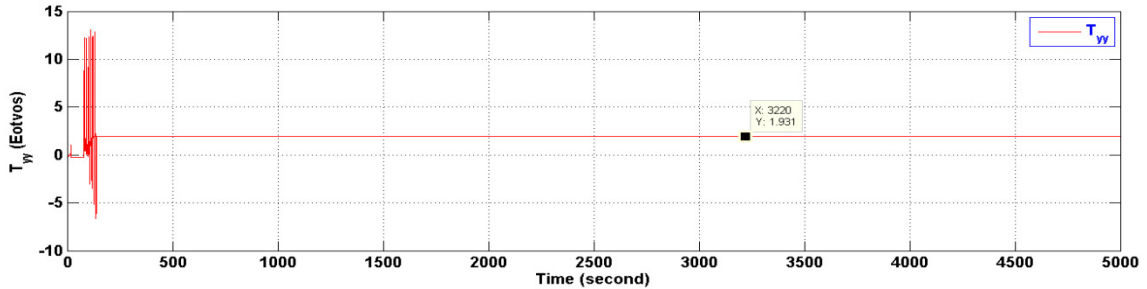


Figure 95: Γ_{yy} simulated gravity gradient component.

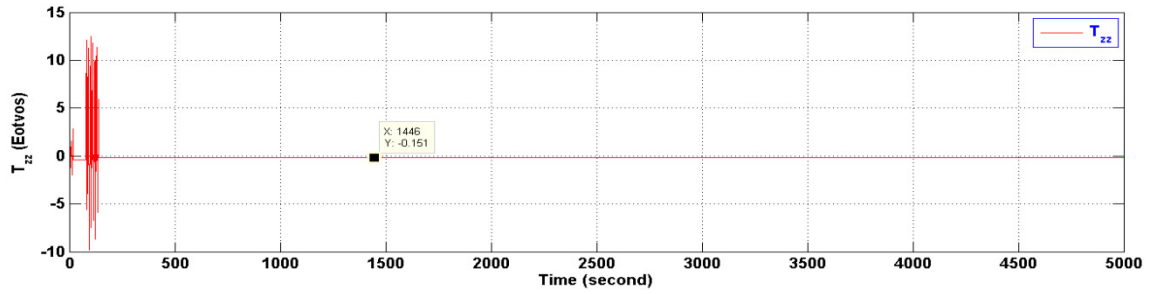


Figure 96: Γ_{zz} simulated gravity gradient component.

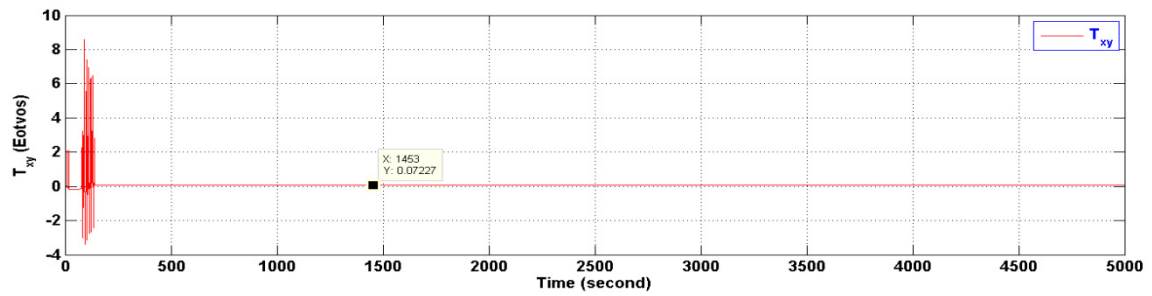


Figure 97: Γ_{xy} simulated gravity gradient component.

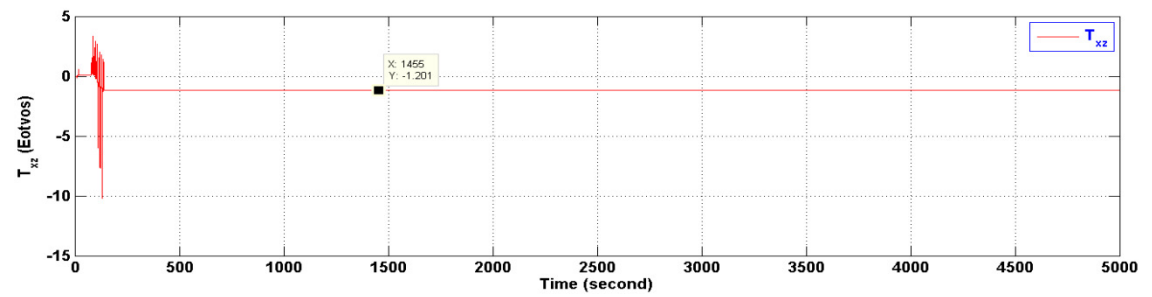


Figure 98: Γ_{xz} simulated gravity gradient component.

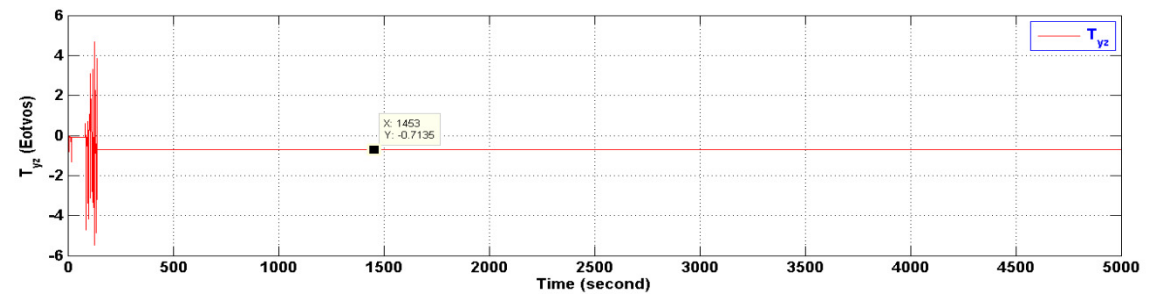


Figure 99: Γ_{yz} simulated gravity gradient component.

7.2.3 Gravity Compensation Implementation

The Simulink model shown in Figure 93 in which equation (119) was implemented since the gradient was constant as shown in Figures 94-99 was used to simulate the Gravity Compensation. Using a BODY Sensor Block to retrieve the body's inertial velocity, the following results show the results:

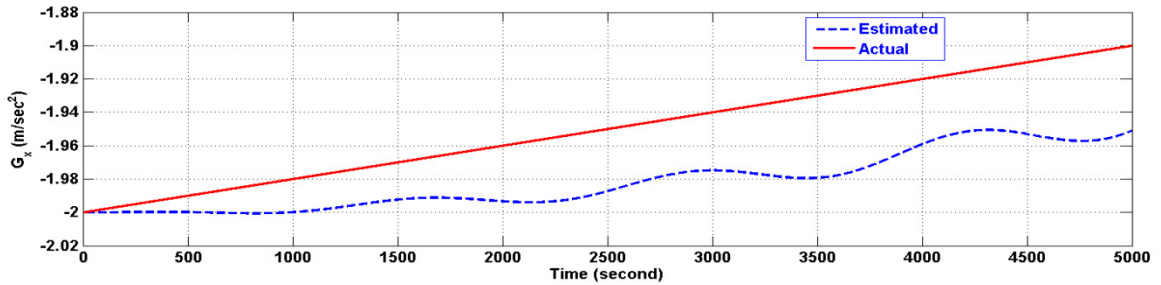


Figure 100: G_x gravity component.

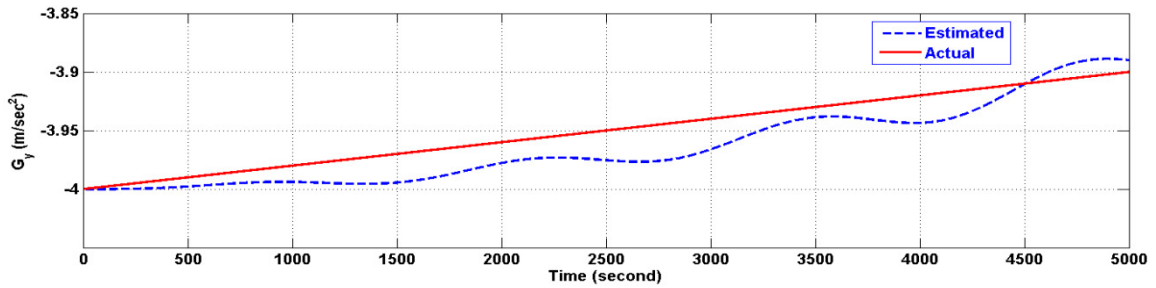


Figure 101: G_y gravity component.

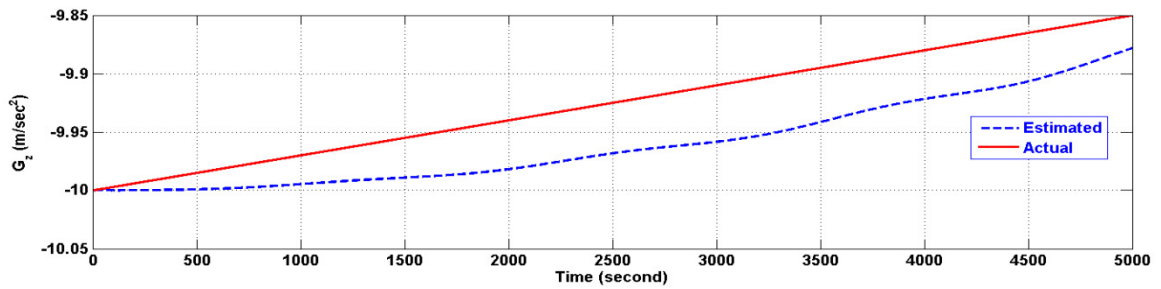


Figure 102: G_z gravity component.

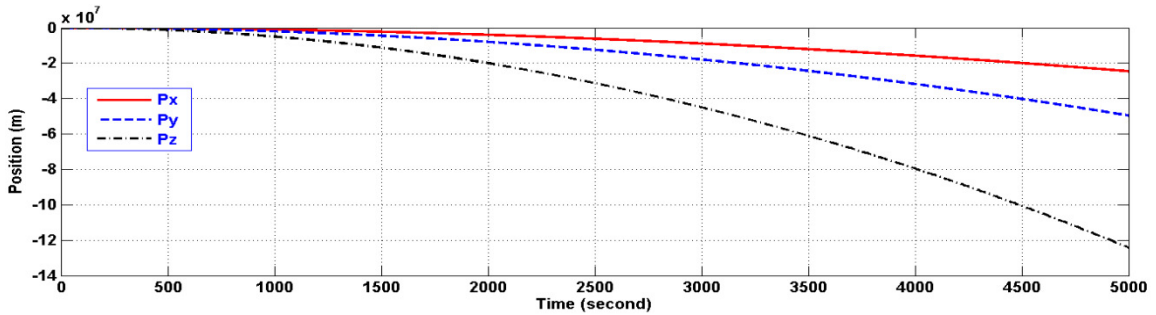


Figure 103: Body position (m)

In Chapter 9, the Gravity Compensation will be a part of an identification problem where the effect of CoG position immigration will be shown clearly.

7.3 Summary

In the previous chapter, the gravity effect on the accelerometers' measurements was ignored. However, it was shown in this chapter that this neglecting is not appropriate; since the acceleration due to gravity seriously affects the measurements. The governing equations by which this acceleration can be retrieved from the available accelerometers' measurements were shown. First, the angular acceleration is found, from which the angular velocity can then be determined allowing the gravity tensor to be calculated. After the gravity tensor is calculated, the angular velocity can be re-estimated using one of the filters previously presented in Chapter 6.

CHAPTER 8

SYSTEM IDENTIFICATION

In this Chapter, the resulting equations obtained in Gravity Compensation Chapter, Chapter 7, will be revisited and formulated in different forms that enable identifying the unknown parameters found mainly in equation (120) under various assumptions. Different identification techniques will be used and the results will be presented and discussed when appropriate. In order to focus mainly on the identification problem, a Body Sensor available in the SimMechanics Library is used to retrieve the actual angular velocity and acceleration values needed in the estimation routines. It will be shown in the next chapter that the quality of parameters' estimation is dependent on the quality of the angular motion that can be obtained using the filters presented in Chapter 6.

8.1 System models used in Identification problem

The importance of equation (120) is raised because it shows the relationship between the main parts of this thesis, namely: Gravity Compensation, CoG position estimation, and finding the inertial vehicle acceleration all represented in the body frame. Using the skew matrix representation instead of cross product representation, equation (120) can be given as follows:

$$\vec{m}(k) = \vec{a}_{ri} - ([\dot{\Omega}] + [\Omega \times])\vec{R}_i + \vec{g}_0 = \ddot{\vec{S}} - \ddot{\vec{R}}_G - 2[\dot{\Omega}]\dot{\vec{R}}_G - ([\dot{\Omega}] + [\Omega \times])\vec{R}_G - \int_0^t \Gamma^a \vec{V}_b \cdot dt \quad (132)$$

Where:

\vec{a}_{ri} : is the acceleration measurement at the center of the i^{th} Ring, given by equation (111).

$[\dot{\Omega}]$ and $[\Omega \times]$: are given by equation (94), and both are known.

$[\Omega]$: is given by equation (38), and it is also known.

\vec{g}_0 : is the initial gravity vector at time (t_0), and it is known provided that the initial vehicle attitude and gravity vector in the inertial space are known which can be possible to have. It will be shown in the next chapter that this vector must be appropriately defined in the body frame to facilitate Gravity Compensation, so the Direction Cosine Matrix (DCM), as can be obtained as will be shown in Chapter 9, can be used to map the initial gravity vector in the world coordinate to the body frame. This step is very important to render the objectives of this thesis possible.

$\ddot{\vec{S}}$: is the inertial acceleration of the vehicle measured at CoG in the body frame, which is to be identified.

$\ddot{\vec{R}}_G$ and $\dot{\vec{R}}_G$: are the acceleration and the velocity of the CoG respectively, which are to be identified, if appropriate.

\vec{R}_G : is the position of CoG, which is to be identified.

Γ^a : is the gravity gradient measured in the body frame given by equation (90), and it is measured.

\vec{V}_b : is the inertial velocity of the vehicle measured in the body frame, which is to be identified.

Equation (132) is an Integral-Differential equation, which in general non-identifiable, so approximations are needed to bring about identifiability [107]. Since this is the case, equation (132) will be discretized using equations (121-123) and equations (126-127) which in fact is one reason why there are many models appearing in this Chapter. The four models previously shown in Chapter 7 are revisited and formulated in regression forms that can be easily used later in identification methods. The complexity of those models is justified by the inclusion of the gravity effect into the picture. To avoid such a complexity, further handling of the identification problem in this Chapter will neglect the direct contribution of the gravity effect; in order to ease focusing on the identification problem as well as to ease Simulating Models using Simulink and SimMechanics, although its existence is respected through the necessity of discretization. The second reason for presenting many models is that there is a need to investigate the possibility of retrieving all the information about the CoG, i.e. its position, velocity, and acceleration, as was depicted in Figure 7.

Next, the models are investigated closely. The whole picture in which all the thesis objectives come together will be presented in the following Chapter.

- Model I:

Equation (132) can be discretized by utilizing equations (121-123). In this model, the exact equation given by (132) is discretized were all the CoG information, Gravity effect, and the inertial acceleration terms are preserved. The assumption made here was that the

gravity tensor is not constant and all the CoG information is needed to be identified. It will be shown later, through the simulation results, that such a demand cannot be fulfilled; since the CoG acceleration cannot be determined uniquely as can be clearly seen from equation (132) and hence the proposed IMU loses one of its claims shown in Figure 7, namely finding the CoG acceleration. This model is given as follows:

$$\begin{aligned}
2h^2\bar{m}(k) + \frac{h^2}{2} \sum_{i=1}^{k-1} \{ & 3\Gamma^\alpha(i)\vec{S}(i) + (3\Gamma^\alpha(i-1) - 4\Gamma^\alpha(i))\vec{S}(i-1) + (\Gamma^\alpha(i) - 4\Gamma^\alpha(i-1))\vec{S}(i-2) \\
& + \Gamma^\alpha(i-1)\vec{S}(i-3) \} \\
= & \left\{ \left(4I - \frac{3h^2}{2}\Gamma^\alpha(k) \right) \vec{S}(k) + \left(4I - 2h^2 \left([\dot{\Omega}](k) + [\Omega \times](k) \right) - 6h[\Omega](k) \right) \vec{R}_G(k) \right\} \\
& - \left\{ \left(10I + \frac{h^2}{2} (3\Gamma^\alpha(k-1) - 4\Gamma^\alpha(k)) \right) \vec{S}(k-1) + (10I - 8h[\Omega](k)) \vec{R}_G(k-1) \right\} \\
& + \left\{ \left(8I - \frac{h^2}{2} (\Gamma^\alpha(k) - 4\Gamma^\alpha(k-1)) \right) \vec{S}(k-2) + (8I - 2h[\Omega](k)) \vec{R}_G(k-2) \right\} \\
& - \left\{ \left(2I + \frac{h^2}{2} \Gamma^\alpha(k-1) \right) \vec{S}(k-3) + 2\vec{R}_G(k-3) \right\}
\end{aligned} \tag{133}$$

And the Regression Form:

$$\begin{aligned}
\bar{M}(k) = & \{a1(k)\vec{S}(k) + b1(k)\vec{R}_G(k)\} - \{a2(k)\vec{S}(k-1) + b2(k)\vec{R}_G(k-1)\} \\
& + \{a3(k)\vec{S}(k-2) + b3(k)\vec{R}_G(k-2)\} - \{a4(k)\vec{S}(k-3) + 2\vec{R}_G(k-3)\} \\
\bar{M}(k) = & [a1(k), -a2(k), a3(k), -a4(k), b1(k), -b2(k), b3(k), -2]\theta^T(k) \\
\theta^T(k) = & [\vec{S}(k), \vec{S}(k-1), \vec{S}(k-2), \vec{S}(k-3), \vec{R}_G(k), \vec{R}_G(k-1), \vec{R}_G(k-2), \vec{R}_G(k-3)]
\end{aligned} \tag{134}$$

Where $\bar{M}(k)$ is defined from above.

- Model II:

$$\begin{aligned}
h^2m(k) = & \left\{ \vec{S}(k) + \left(I - h^2 \left([\dot{\Omega}](k) + [\Omega \times](k) \right) - 2h[\Omega](k) \right) \vec{R}_G(k) \right\} \\
& - \left\{ 2\vec{S}(k-1) + (2I - 2h[\Omega](k)) \vec{R}_G(k-1) \right\} + \left\{ \vec{S}(k-2) + \vec{R}_G(k-2) \right\} \\
& - \frac{h^2}{2} \sum_{i=1}^k \left\{ \Gamma^\alpha(i)\vec{S}(i) + (\Gamma^\alpha(i-1) - \Gamma^\alpha(i))\vec{S}(i-1) - \Gamma^\alpha(i-1)\vec{S}(i-2) \right\}
\end{aligned} \tag{135}$$

Where $I_{3 \times 3}$ identity matrix, and $k = 0, 1, 2, \dots, \infty$

$$\begin{aligned}
h^2 m(k) + \frac{h^2}{2} \sum_{i=1}^{k-1} \{ & \Gamma^a(i) \vec{S}(i) + (\Gamma^a(i-1) - \Gamma^a(i)) \vec{S}(i-1) - \Gamma^a(i-1) \vec{S}(i-2) \} \\
= & \left\{ \left(I - \frac{h^2}{2} \Gamma^a(k) \right) \vec{S}(k) \right. \\
& + \left(I - h^2 \left([\dot{\Omega}](k) + [\Omega \times](k) \right) - 2h[\Omega](k) \right) \vec{R}_G(k) \left. \right\} \\
& - \left\{ \left(2I + \frac{h^2}{2} (\Gamma^a(k-1) - \Gamma^a(k)) \right) \vec{S}(k-1) + (2I - 2h[\Omega](k)) \vec{R}_G(k-1) \right\} \\
& + \left\{ \left(I + \frac{h^2}{2} \Gamma^a(k-1) \right) \vec{S}(k-2) + \vec{R}_G(k-2) \right\}
\end{aligned}$$

$$\begin{aligned}
\vec{M}(k) &= [a1(k), -a2(k), a3(k), b1(k), -b2(k), 1] \theta^T(k) \\
\theta^T(k) &= [\vec{S}(k), \vec{S}(k-1), \vec{S}(k-2), \vec{R}_G(k), \vec{R}_G(k-1), \vec{R}_G(k-2)]
\end{aligned}$$

- Model III:

Equation (132) can be simplified more by utilizing equations (121,122), and by taking the gravity tensor as a constant, Model III is given as follows:

$$\begin{aligned}
2h^2 m(k) = & \left\{ (4I - 2h^2 \Gamma^a(k)) \vec{S}(k) + \left(4I - 2h^2 \left([\dot{\Omega}](k) + [\Omega \times](k) \right) - 6h[\Omega](k) \right) \vec{R}_G(k) \right\} \\
& - \left\{ 10\vec{S}(k-1) + (10I - 8h[\Omega](k)) \vec{R}_G(k-1) \right\} \\
& + \left\{ 8\vec{S}(k-2) + (8I - 2h[\Omega](k)) \vec{R}_G(k-2) \right\} - \left\{ 2\vec{S}(k-3) + 2\vec{R}_G(k-3) \right\}
\end{aligned} \tag{136}$$

Where $I_{3 \times 3}$ identity matrix, and $k = 0, 1, 2, \dots, \infty$

$$\begin{aligned}
\vec{M}(k) &= [a1(k), -10, 8, b1(k), -b2(k), b3(k), -2] \theta^T(k) \\
\theta^T(k) &= [\vec{S}(k), \vec{S}(k-1), \vec{S}(k-2), \vec{R}_G(k), \vec{R}_G(k-1), \vec{R}_G(k-2), \vec{W}_G(k)] \\
\vec{W}_G(k) &= \vec{S}(k-3) + \vec{R}_G(k-3)
\end{aligned}$$

- Model IV:

Using equations (126-127), and by taking the gravity tensor as a constant, Model IV is given as follows:

$$\begin{aligned}
h^2 m(k) = & \left\{ \left(I - h^2 \Gamma^a(k) \right) \vec{S}(k) + \left(I - h^2 \left([\dot{\Omega}](k) + [\Omega \times](k) \right) - 2h[\Omega](k) \right) \vec{R}_G(k) \right\} \\
& - \left\{ 2\vec{S}(k-1) + (2I - 2h[\Omega](k)) \vec{R}_G(k-1) \right\} + \left\{ \vec{S}(k-2) + \vec{R}_G(k-2) \right\}
\end{aligned} \tag{137}$$

Where, $I_{3 \times 3}$ identity matrix, and $k = 0, 1, 2, \dots \infty$

$$\begin{aligned}\bar{M}(k) &= [a1(k), -2, b1(k), -b2(k), 1]\theta^T(k) \\ \theta^T(k) &= [\bar{S}(k), \bar{S}(k-1), \bar{R}_G(k), \bar{R}_G(k-1), \bar{W}_G(k)] \\ \bar{W}_G(k) &= \bar{S}(k-2) + \bar{R}_G(k-2)\end{aligned}$$

Using the Backwards Finite-Difference approximation for the differential terms, the following models will result as stated in Table 16, taking (h) equals 1 time unit and neglecting the gravity contribution.

Table 16: Various Models used in Identification parameters.

1	Include $\ddot{\bar{R}}_G$ and approximate the derivative terms using $O(h^2)$ approximations.
	$M(k) = 2\bar{S}(k) - 5\bar{S}(k-1) + 4\bar{S}(k-2) - \bar{S}(k-3) + (2I + 3[\Omega] + [\dot{\Omega}] + [\Omega \times])\bar{R}_G(k) \\ + (4[\Omega] + 5I)\bar{R}_G(k-1) - (4I - [\Omega])\bar{R}_G(k-2) + \bar{R}_G(k-3)$
2	Neglect $\ddot{\bar{R}}_G$ and approximate the derivative terms using $O(h^2)$ approximations.
	$M(k) = 2\bar{S}(k) - 5\bar{S}(k-1) + 4\bar{S}(k-2) - \bar{S}(k-3) - (3[\Omega] + [\dot{\Omega}] + [\Omega \times])\bar{R}_G(k) \\ + (4[\Omega])\bar{R}_G(k-1) + ([\Omega])\bar{R}_G(k-2)$
3	Neglect $\ddot{\bar{R}}_G$ and $\dot{\bar{R}}_G$ approximate $\ddot{\bar{S}}$ term using $O(h^2)$ approximations.
	$M(k) = 2\bar{S}(k) - 5\bar{S}(k-1) + 4\bar{S}(k-2) - \bar{S}(k-3) - ([\dot{\Omega}] + [\Omega \times])\bar{R}_G(k)$
4	Neglect $\ddot{\bar{R}}_G$, $\dot{\bar{R}}_G$, and do not approximate $\ddot{\bar{S}}$ term.
	$M(k) = \bar{S}(k) - ([\dot{\Omega}] + [\Omega \times])\bar{R}_G(k)$
5	Neglect $\ddot{\bar{R}}_G$, and do not approximate any term.

	$M(k) = \ddot{S}(k) - 2[\Omega]\dot{\bar{R}}_G(k-1) - ([\dot{\Omega}] + [\Omega \times])\bar{R}_G(k)$
6	Neglect $\ddot{\bar{R}}_G$, approximate $\dot{\bar{R}}_G$ using $O(h)$, and do not approximate \ddot{S} term.
	$M(k) = \ddot{S}(k) - (2[\Omega] + [\dot{\Omega}] + [\Omega \times])\bar{R}_G(k) + 2[\Omega]\bar{R}_G(k-1)$
7	Neglect $\ddot{\bar{R}}_G$, approximate $\dot{\bar{R}}_G$ using $O(h^2)$, and do not approximate \ddot{S} term.
	$M(k) = \ddot{S}(k) - (3[\Omega] + [\dot{\Omega}] + [\Omega \times])\bar{R}_G(k) + 4[\Omega]\bar{R}_G(k-1) - [\Omega]\bar{R}_G(k-2)$
8	Neglect $\ddot{\bar{R}}_G$, approximate \ddot{S} using $O(h^2)$, and do not approximate $\dot{\bar{R}}_G$ term.
	$M(k) = 2\ddot{S}(k) - 5\ddot{S}(k-1) + 4\ddot{S}(k-2) - \ddot{S}(k-3) - 2[\Omega]\dot{\bar{R}}_G(k-1) - ([\dot{\Omega}] + [\Omega \times])\bar{R}_G(k)$
9	Neglect $\ddot{\bar{R}}_G$, approximate \ddot{S} using $O(h)$, and do not approximate $\dot{\bar{R}}_G$ term.
	$M(k) = \ddot{S}(k) - 2\ddot{S}(k-1) + \ddot{S}(k-2) - 2[\Omega]\dot{\bar{R}}_G(k-1) - ([\dot{\Omega}] + [\Omega \times])\bar{R}_G(k)$
10	Neglect $\ddot{\bar{R}}_G$, approximate \ddot{S} using $O(h^2)$, and approximate $\dot{\bar{R}}_G$ using $O(h)$.
	$M(k) = 2\ddot{S}(k) - 5\ddot{S}(k-1) + 4\ddot{S}(k-2) - \ddot{S}(k-3) - (2[\Omega] + [\dot{\Omega}] + [\Omega \times])\bar{R}_G(k) + 2[\Omega]\bar{R}_G(k-1)$
11	Neglect $\ddot{\bar{R}}_G$, approximate \ddot{S} using $O(h)$, and approximate $\dot{\bar{R}}_G$ using $O(h^2)$.
	$M(k) = \ddot{S}(k) - 2\ddot{S}(k-1) + \ddot{S}(k-2) - (3[\Omega] + [\dot{\Omega}] + [\Omega \times])\bar{R}_G(k) + 4[\Omega]\bar{R}_G(k-1) - [\Omega]\bar{R}_G(k-2)$
12	Neglect $\ddot{\bar{R}}_G$, approximate \ddot{S} using $O(h)$, and approximate $\dot{\bar{R}}_G$ using $O(h)$.

	$M(k) = \vec{S}(k) - 2\vec{S}(k-1) + \vec{S}(k-2) - (2[\Omega] + [\dot{\Omega}] + [\Omega \times])\vec{R}_G(k) + 2[\Omega]\vec{R}_G(k-1)$
13	Neglect $\ddot{\vec{R}}_G$ and $\dot{\vec{R}}_G$ approximate $\ddot{\vec{S}}$ term using $O(h)$ approximations.
	$\vec{S}(k) - 2\vec{S}(k-1) + \vec{S}(k-2) - ([\dot{\Omega}] + [\Omega \times])\vec{R}_G(k)$

The previous models can be grouped as follows: models {4, 5, 6, and 7} can be used when the gravity can be found by external means other than the proposed IMU and when the CoG information is the concern. The remaining models, which are useful to meet the objectives of this thesis, can be used when CoG information, Gravity Estimation, and Inertial acceleration are needed to be determined simultaneously. It is worth mentioning that model 4 was proposed by [7] and was simulated in Chapter 5.

The regression vectors for the models of interest can be generated using the following formats:

$$[\vec{R}_G(k), \vec{R}_G(k-1), \dots, \vec{S}(k), \vec{S}(k-1), \dots] \quad (138)$$

Or

$$[\vec{S}(k), \vec{S}(k-1), \dots, \vec{R}_G(k), \vec{R}_G(k-1), \dots] \quad (139)$$

The following Simulink Model, utilizing a Body Sensor to retrieve the angular motion needed, was used to test the identification results using the previously stated models. The entire models were tested using the same conditions so that the results can be compared with each other's.

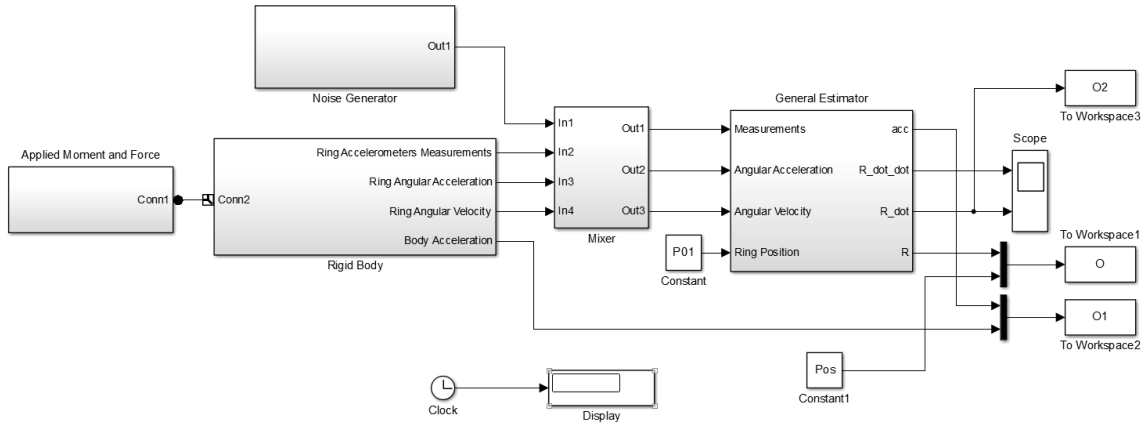


Figure 104: Simulink Model used in Parameter Identification.

8.2 Recursive Identification methods used

In general, there are two methods in use for parameter identification, namely: the Recursive Least-Squares (RLS), and the Maximum Likelihood Estimation (MLE) [108]. Mainly, three RLS identification techniques were investigated in this thesis despite the fact that other methods may have better advantages over the used techniques. Namely Standard Recursive-Least Squares RLS, Weighted RLS with Covariance Resetting, and the Normalized Least Mean Square (NLMS) methods were used to identify the parameters. Since these methods are well-known in literature, no description is provided here for Normalized LMS method but further details can be found in [109].

The following are the steps used to implement the QR-D based WRLS:

1. Find the QR-Decomposition of regression expression matrix D to enhance its condition number. This can be done using different methods such as Householder or Givens Rotations. In this work, the (qr) MATLAB function was used.

2. Update the Regression Expression as follows:

$$\vec{f} = D\vec{x} = Q * R * \vec{x} \rightarrow Q^T * \vec{f} = R * \vec{x} \quad (140)$$

$$Q^T * \vec{f} = R * \vec{x} \rightarrow \vec{w} = R * \vec{x}$$

3. Now, use the modified Regression Expression in a WRLS scheme as follows

[109]:

$$K_{ki} = \frac{P_{(k-1)i} R_{ki}^T}{FF + \text{trace}(R_{ki} P_{(k-1)i} R_{ki}^T)}$$

$$\vec{e}_{ki}(k) = \vec{w}(k) - R_{ki} \vec{\hat{x}}_{ki}(k-1)$$

$$\vec{\hat{x}}_{ki}(k) = \vec{\hat{x}}_{ki}(k-1) + K_{ki} \vec{e}_{ki}(k) \quad (141)$$

$$P_{ki} = \frac{1}{FF} (I - K_{ki} R_{ki}) P_{(k-1)i}$$

The following expression will help to keep the covariance matrix positive [81]:

$$P_{ki} = 0.5 * (P_{ki}^T + P_{ki})$$

Where, (i) denotes the Ring index and k is the iteration index.

4. Now, check the trace of the covariance matrix as follows:

$$\text{if } (\text{Trace}(P_{ki}) > TH) \quad \text{then} \quad (142)$$

$$P_{ki} = \beta * \text{eye}(6)$$

Where, \vec{f} is the measurements vector, FF is the Forgetting Factor, TH is the Threshold used to decide whether to reset the covariance matrix or not, and β is a large positive number. In this work FF , TH and β were chosen based on trial and error basis.

For the standard RLS, equation (141) is only used with $FF = 1$.

Next, the simulation results will show the performance of the used recursive techniques in identifying the desired parameters using different models. Models {4, 5, 6, and 7} are ignored.

8.3 Simulation Results

In this part, the simulation results of the previous models using the three identification methods will be presented when appropriate. These results will put forward a number of candidate models, and identification methods to be used in the next chapter where the complete picture is presented. The sampling period used was 0.01 seconds. The regression forms used were generated according to the form given by (138). A similar Simulink model to what was described in Chapter 5 was used to simulate those models.

I. Simulation Results using Standard RLS Method:

Here, the standard RLS proofed to be deficient in identifying the parameters of the LTV models; since it has an infinite memory which makes it unable to adopt for the various and rapid changes available in the LTV models. As a result, this method was excluded from the candidate methods for identification. However, the results obtained for models {1, 2, 3, and 8} are shown.

- Model #1:

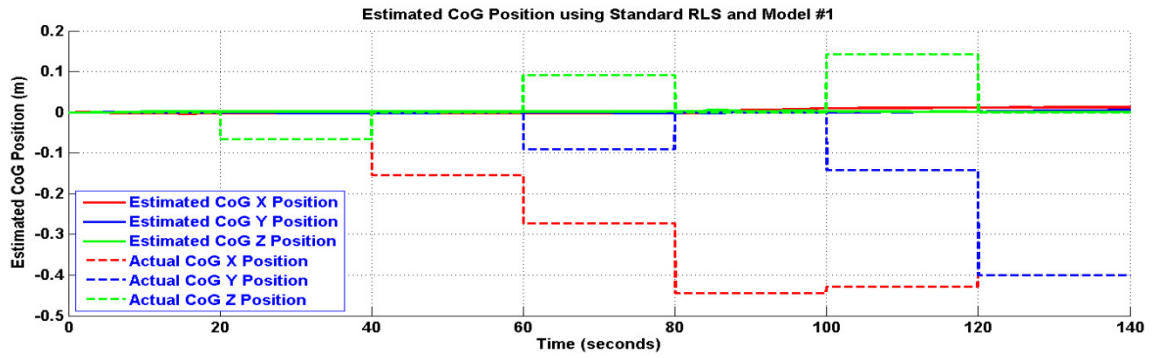


Figure 105: Estimated CoG Position using Standard RLS and Model #1.

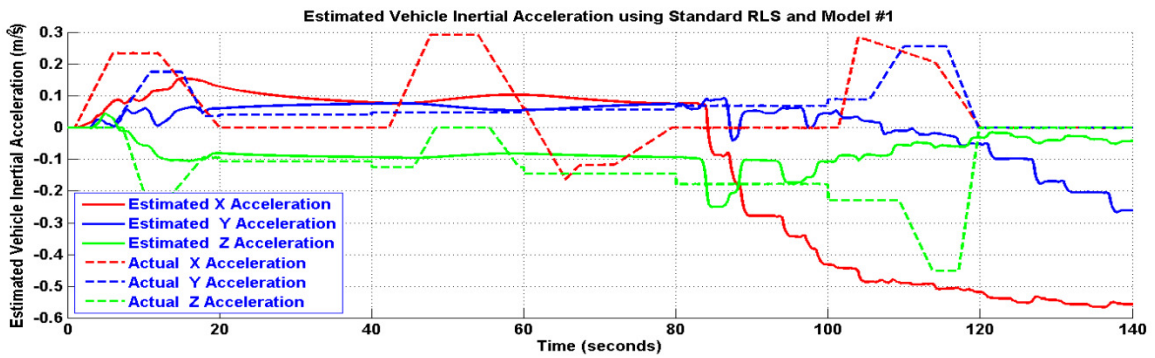


Figure 106: Estimated Vehicle Inertial Acceleration using Standard RLS and Model #1.

- Model #2:

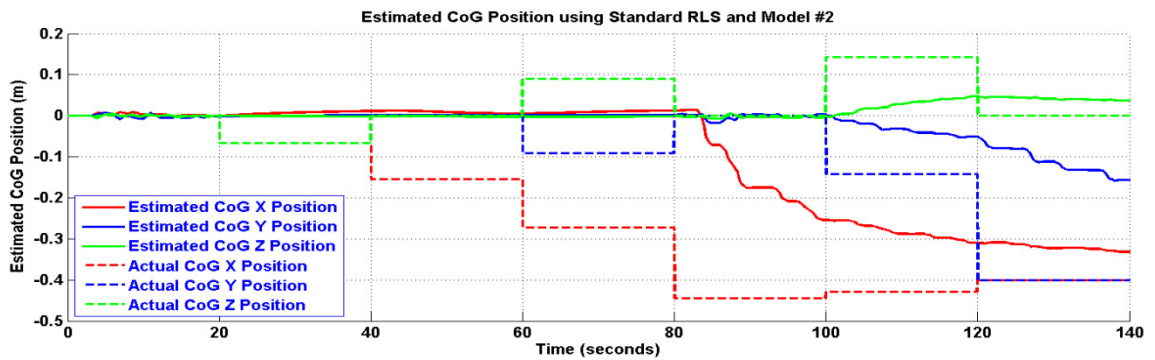


Figure 107: Estimated CoG Position using Standard RLS and Model #2.

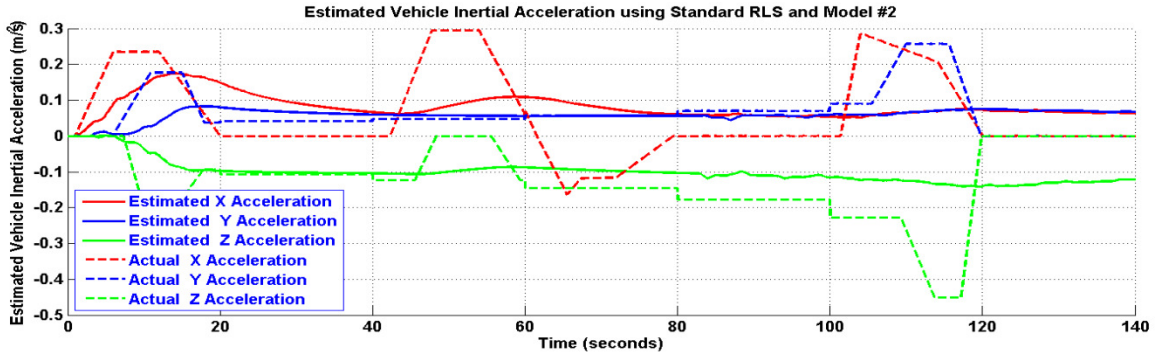


Figure 108: Estimated Vehicle Inertial Acceleration using Standard RLS and Model #2.

- Model #3:

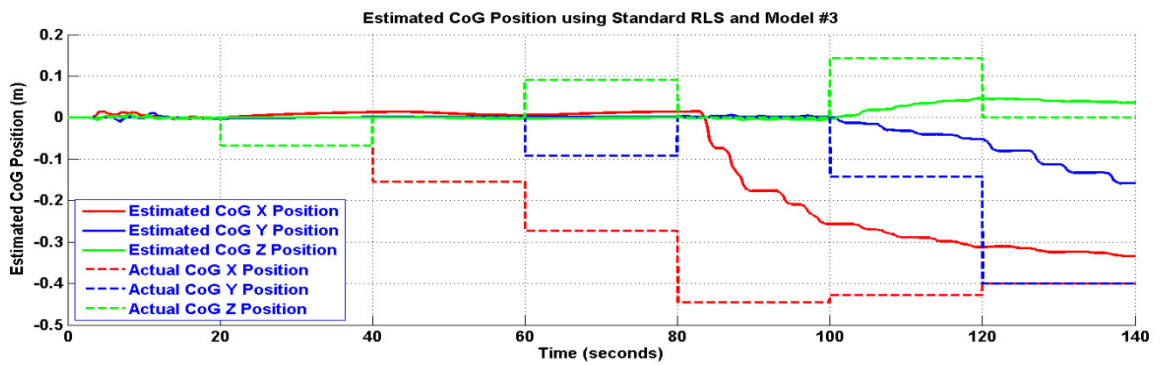


Figure 109: Estimated CoG Position using Standard RLS and Model #3.

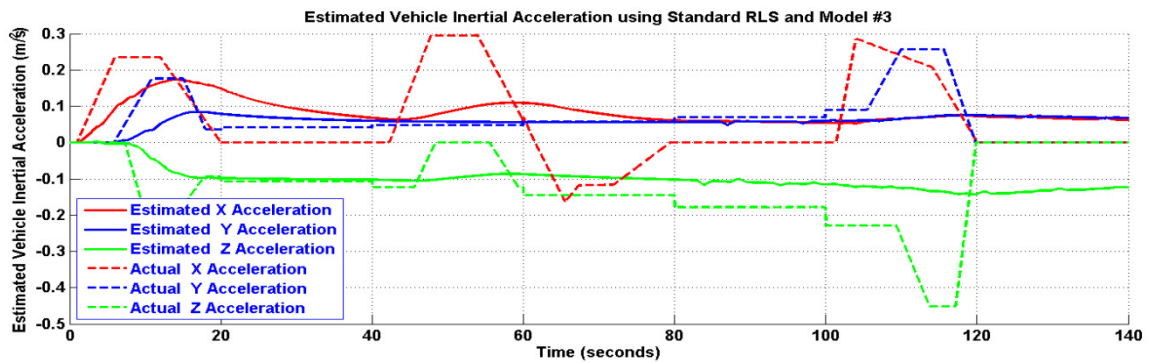


Figure 110: Estimated Vehicle Inertial Acceleration using Standard RLS and Model #3.

- Model #8:

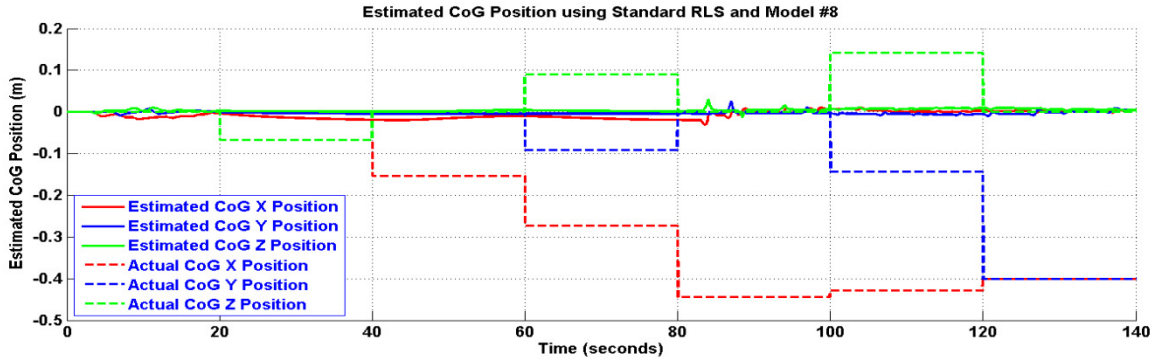


Figure 111: Estimated CoG Position using Standard RLS and Model #4.

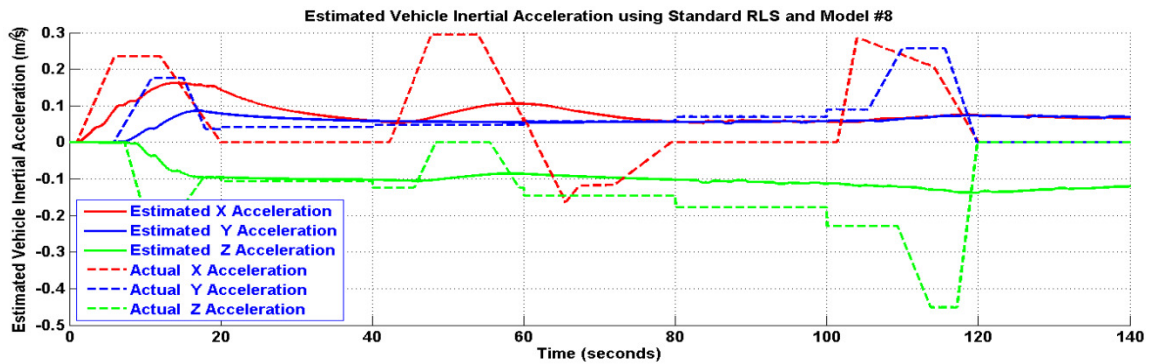


Figure 112: Estimated Vehicle Inertial Acceleration using Standard RLS and Model #8.

II. Simulation Results using Weighted RLS with Covariance Resetting Method:

To keep the thesis body neat, the results obtained using this methods for models {1, 2, 3, and 8} are shown. Other models are just the same as the chosen ones except with different order of approximation.

- Model #1:

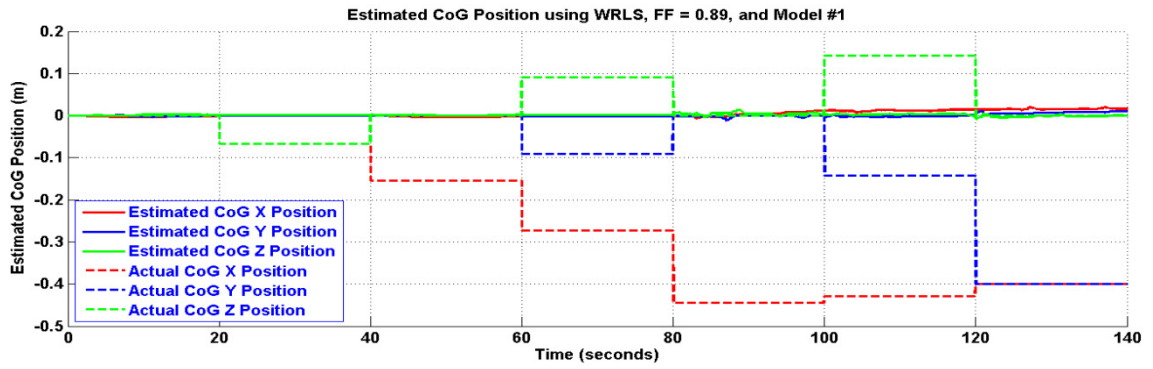


Figure 113: Estimated CoG Position using Weighted RLS and Model #1.

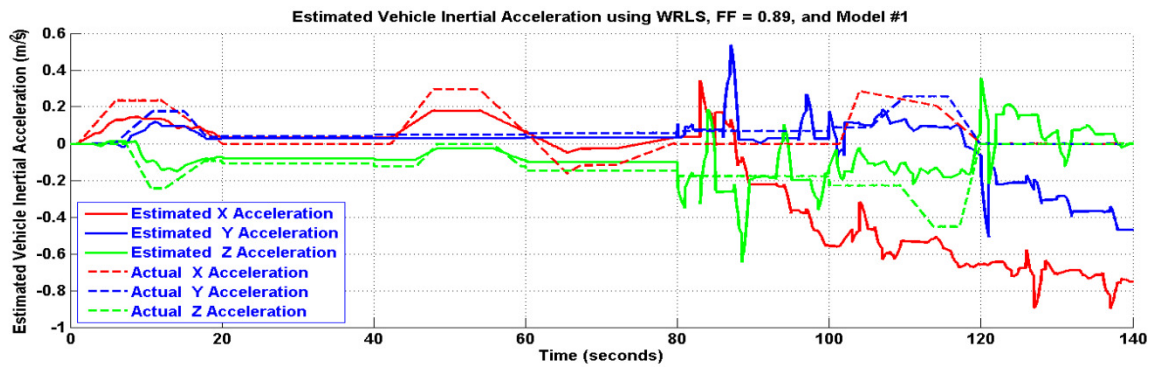


Figure 114: Estimated Vehicle Inertial Acceleration using Weighted RLS and Model #1.

- Model #2:

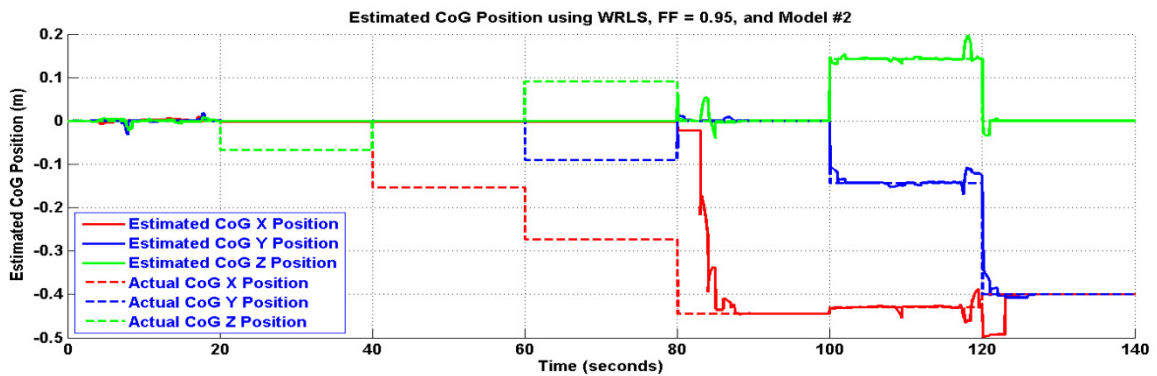


Figure 115: Estimated CoG Position using Weighted RLS and Model #2.

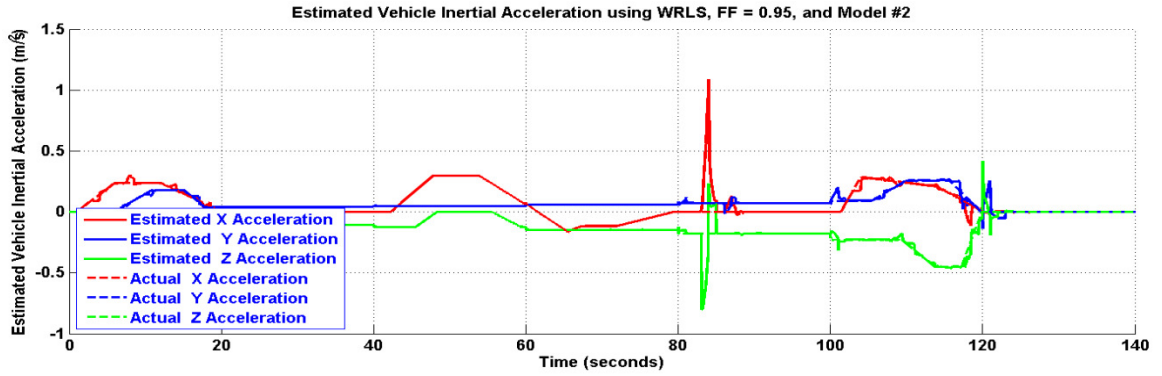


Figure 116: Estimated Vehicle Inertial Acceleration using Weighted RLS and Model #2.

- Model #3:

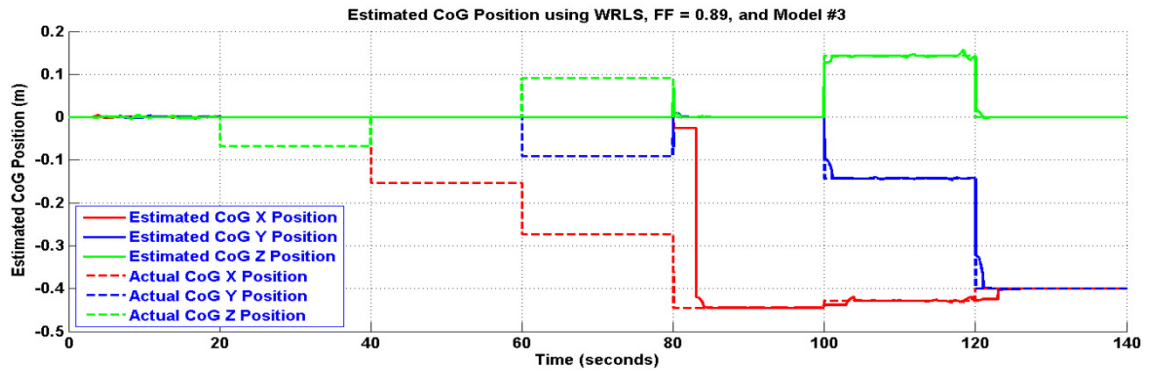


Figure 117: Estimated CoG Position using Weighted RLS and Model #3.

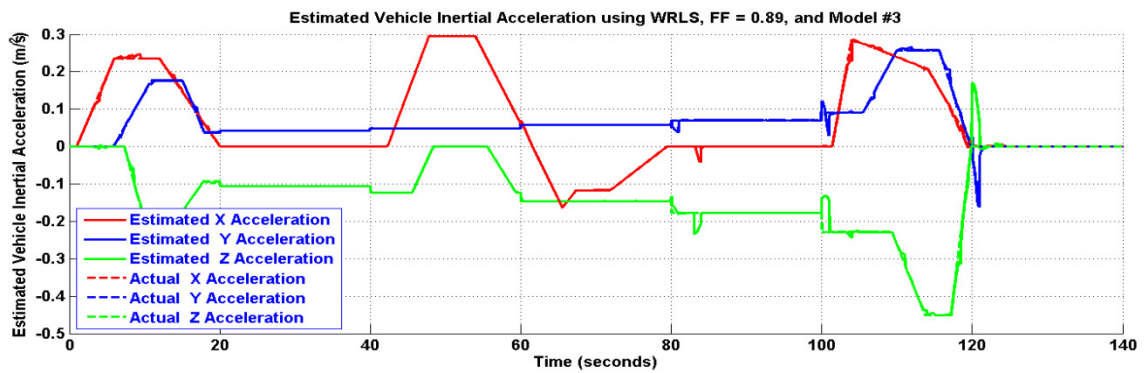


Figure 118: Estimated Vehicle Inertial Acceleration using Weighted RLS and Model #3.

- Model #8:

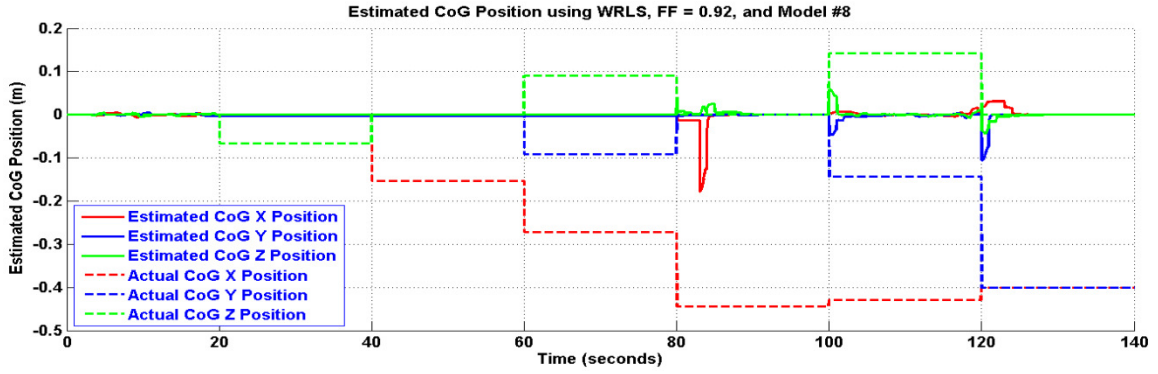


Figure 119: Estimated CoG Position using Weighted RLS and Model #4.

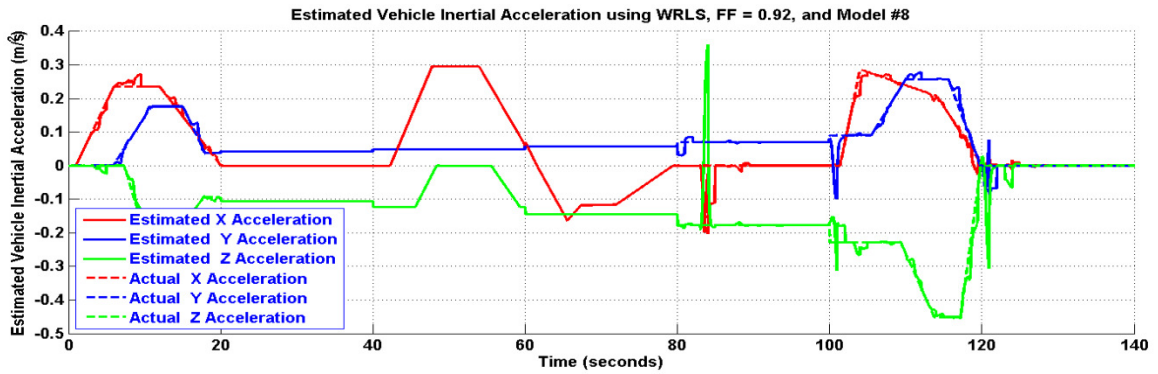


Figure 120: Estimated Vehicle Inertial Acceleration using Weighted RLS and Model #8.

III. Simulation Results using NLMS Method:

As done before, only the results obtained for models {1, 2, 3, and 8} are shown.

- Model #1:

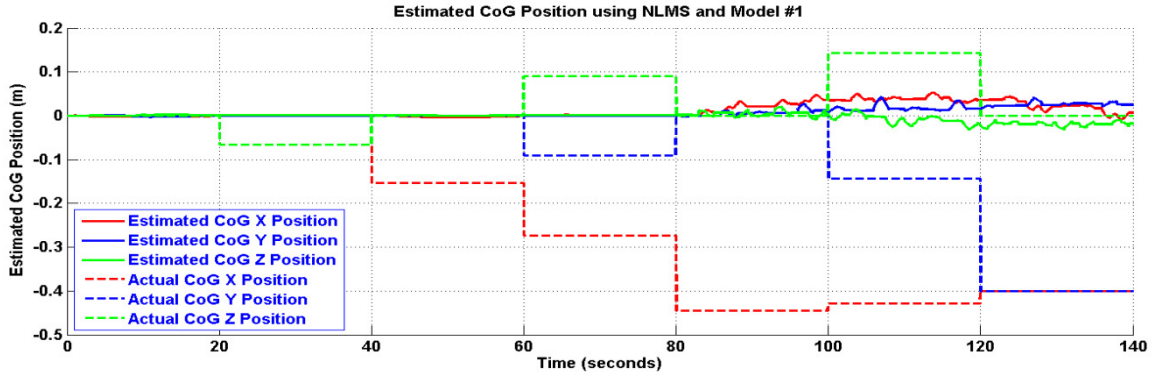


Figure 121: Estimated CoG Position using NLMS and Model #1.

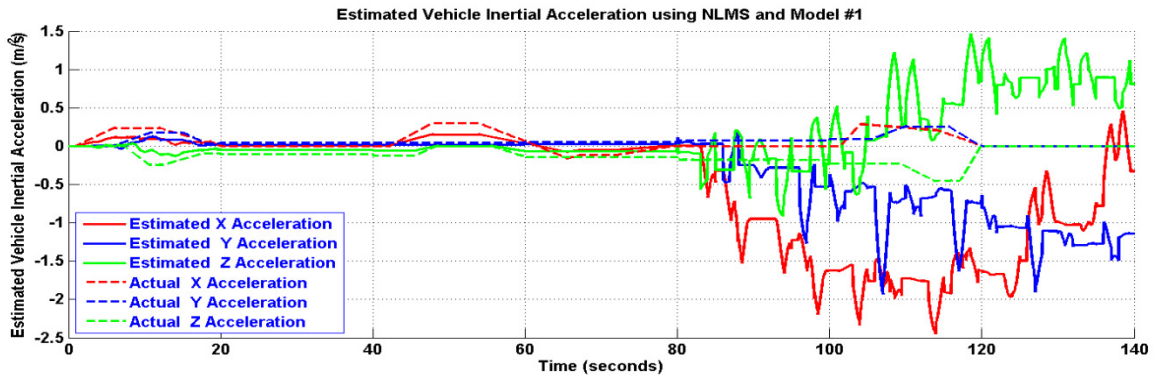


Figure 122: Estimated Vehicle Inertial Acceleration using NLMS and Model #1.

- Model #2:

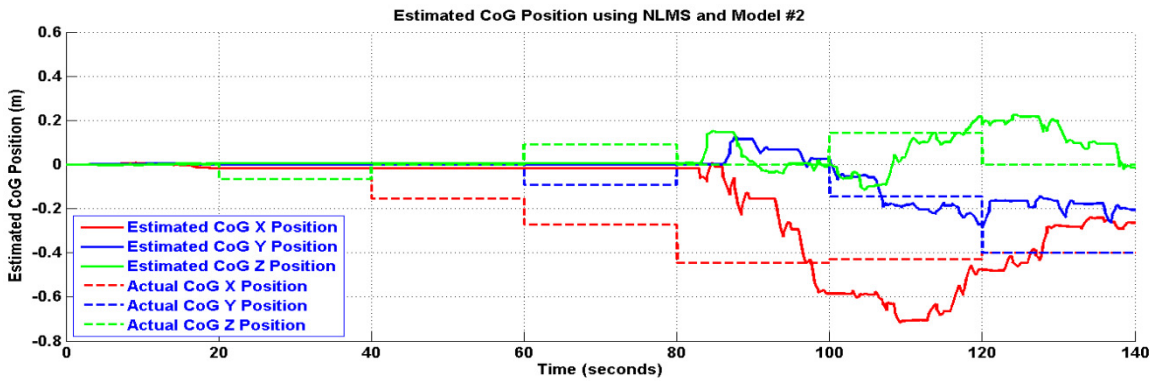


Figure 123: Estimated CoG Position using NLMS and Model #2.

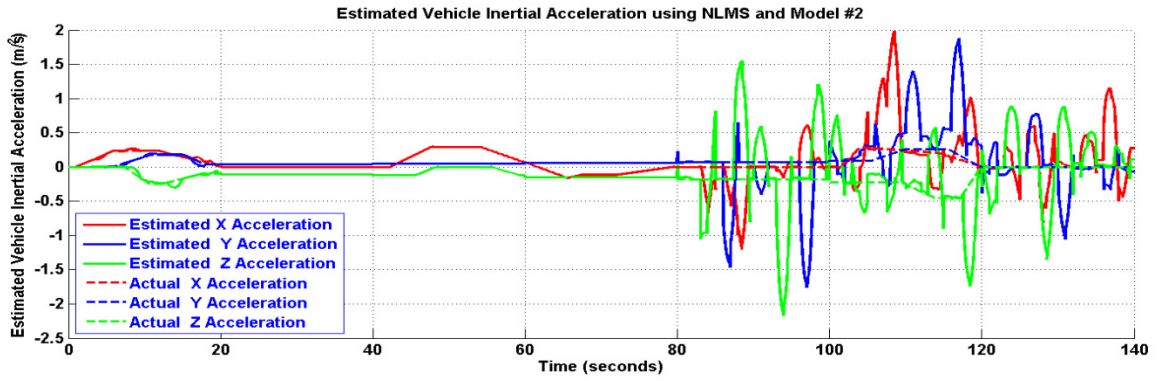


Figure 124: Estimated Vehicle Inertial Acceleration using NLMS and Model #2.

- Model #3:

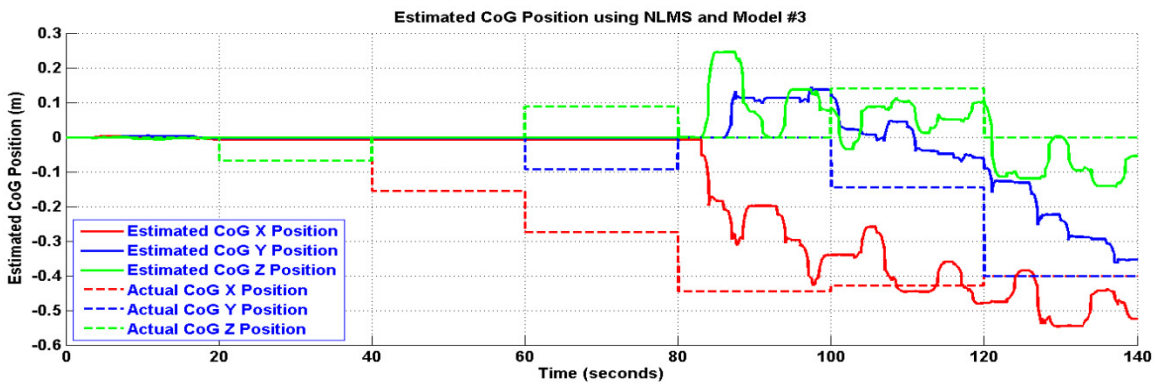


Figure 125: Estimated CoG Position using NLMS and Model #3.

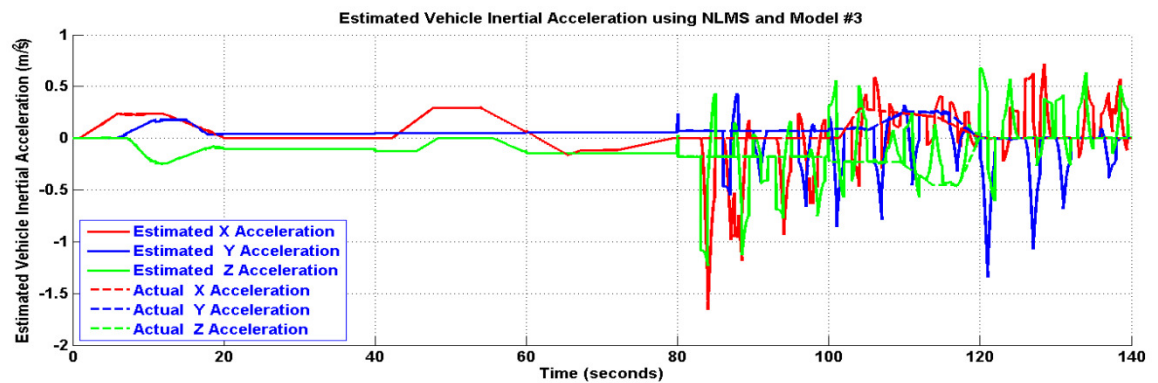


Figure 126: Estimated Vehicle Inertial Acceleration using NLMS and Model #3.

- Model #8:

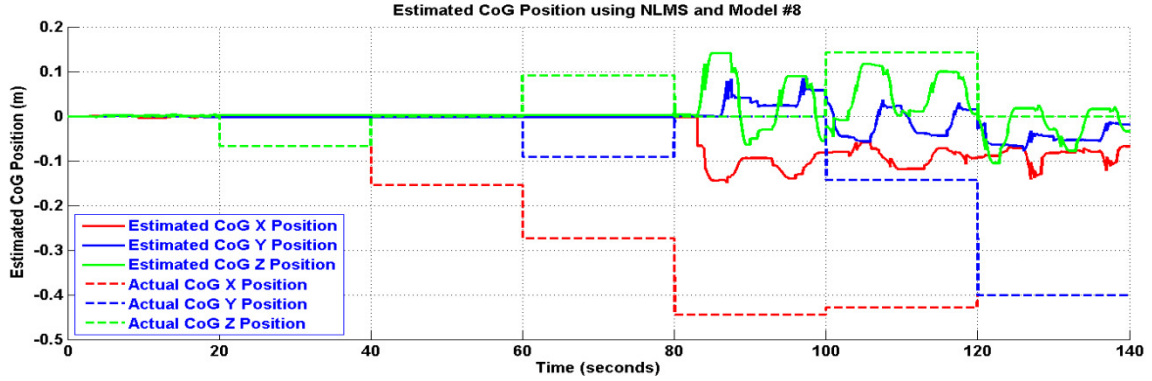


Figure 127: Estimated CoG Position using NLMS and Model #4.

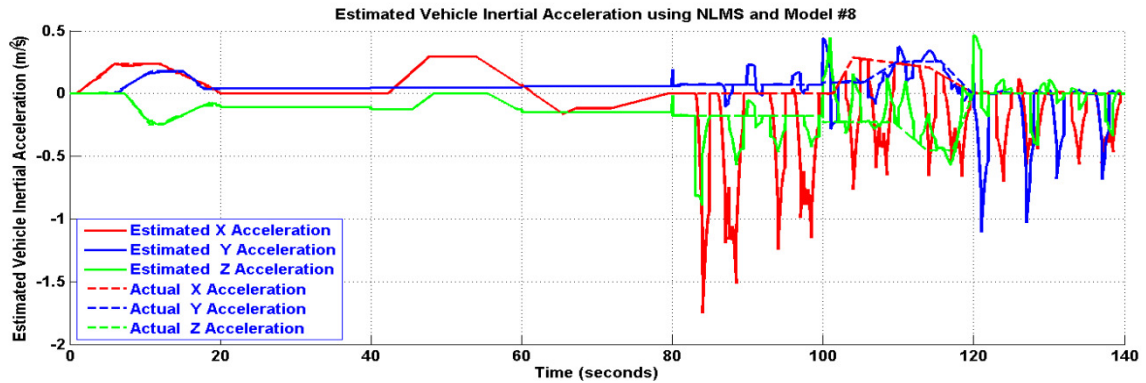


Figure 128: Estimated Vehicle Inertial Acceleration using NLMS and Model #8.

The following table shows a quantitative analysis for the previous results. The Maximum Percent Error (MPE) is obtained for each identification method and for each model inside the interval (90-140) seconds.

Table 17: System Identification MPE for CoG position Estimation

		Standard RLS	Weighted RLS	NLMS
Model #1	X	102.1121	102.7192	110.7243
	Time	100.0000	99.5000	98.5000
	Y	101.4482	102.7504	110.3182
	Time	137.9800	121.0000	127.0100
	Z	99.5438	100.8855	122.2956
	Time	120.0000	120.0000	118.5100
Model #2	X	60.6850	22.0332	65.1889
	Time	93.0000	120.0600	92.0000
	Y	87.1672	61.2335	63.7798
	Time	120.0100	120.0100	127.6500
	Z	102.9022	91.3019	180.1168

	Time	100.0100	120.0100	104.6600
Model #3	X	60.2622	6.3358	55.4748
	Time	93.0000	120.0200	92.0600
	Y	86.8984	35.2361	79.3716
	Time	120.0100	120.0100	120.0100
	Z	103.2529	50.0668	123.3972
	Time	100.0100	100.0100	103.0000
Model #8	X	102.2500	100.1517	83.1525
	Time	98.8400	119.5000	104.0000
	Y	102.0974	100.0103	97.0912
	Time	137.3000	128.5200	137.5000
	Z	97.1833	106.1809	131.7474
	Time	101.0100	118.5300	101.0000

8.4 Selecting an Identification Method and a Model

It is clear from the previous results, Figures 86-109 and Table 17, that the best method to choose is the Weighted-RLS (WRLS) method. Model 3 is considered the best model to choose; since it does not include the effects of CoG acceleration nor its velocity, as may be found in models {1, 2, 8, 9, 10, 11, and 12}.

An attempt to make use of the state-space form of different models to build a discrete EKF was done but not reported here since its results are lacking and it is scheduled to be investigated in a future work. Model 13 is similar to model 3 but with reduced order of approximation.

The performance of the WRLS can be improved by incorporating the QR-Decomposition which helps in improving the condition number of the regression matrix used if it is generated using the form given by (138). A QL-Decomposition can be used if the regression matrix is generated using the form given by (139). The results obtained using a QR-Decomposition based WRLS with Covariance Resetting utilizing model 3 are shown in Figures 110 and 111.

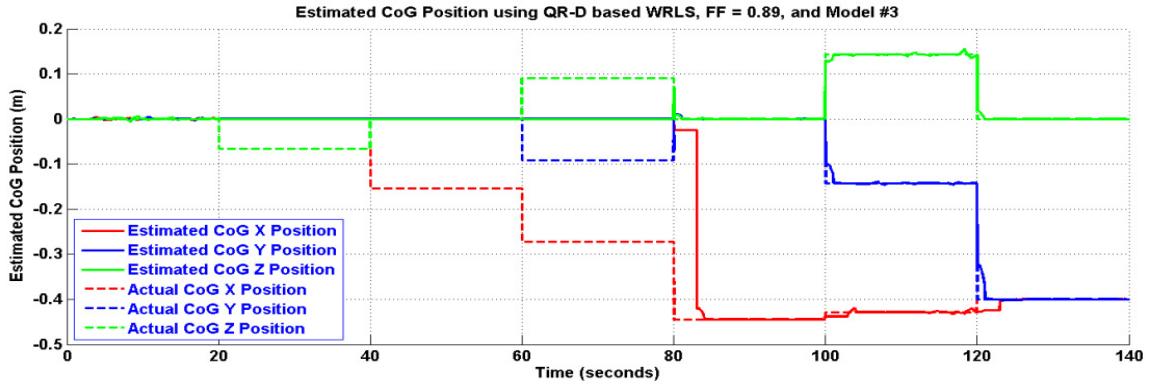


Figure 129: Estimated CoG Position using QR-D base WRLS and Model #3.

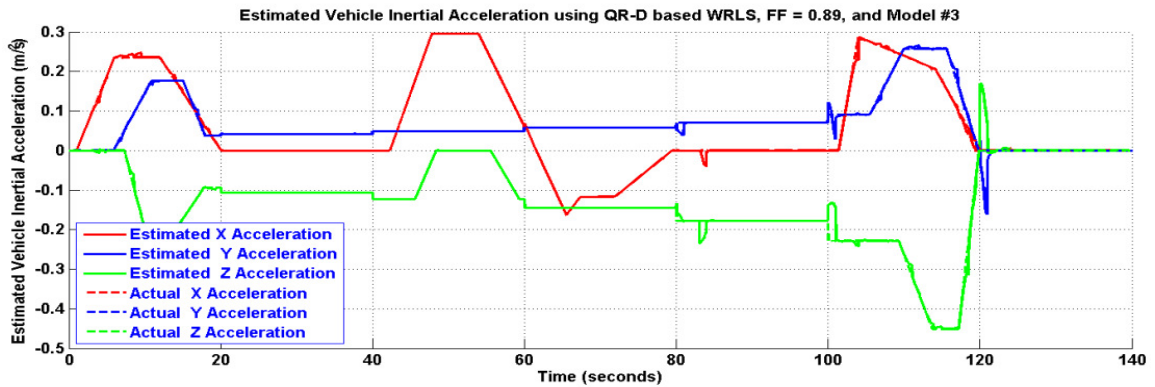


Figure 130: Estimated Vehicle Inertial Acceleration using QR-D based WRLS and Model #3.

It is worth mentioning that the most suitable value of the forgetting factor (FF) was found through trial and error procedure. This fact motivates the adaptive FF version of the QR-Decomposition based WRLS method which is a subject of future work.

Next, four identification schemes are proposed and only the first two were implemented due to time limitation.

8.4.1 Competitive QR-Decomposition based WRLS Identification Scheme

Basically, this scheme consists of two QR-Decomposition based WRLS filters, one of them estimates in forward direction and the other in the backward direction. The two results are averaged.

$$\text{FW: } M(k) = -\vec{S}(k+3) + 4\vec{S}(k+2) - 5\vec{S}(k+1) + 2\vec{S}(k) - ([\dot{\Omega}] + [\Omega \times])\vec{R}_G(k) \quad (143)$$

$$\text{BW: } M(k) = 2\vec{S}(k) - 5\vec{S}(k-1) + 4\vec{S}(k-2) - \vec{S}(k-3) - ([\dot{\Omega}] + [\Omega \times])\vec{R}_G(k) \quad (144)$$

The forgetting factor of the forward QR-D WRLS is 0.88 while that for the backward QR-D WRLS is 0.9. The results obtained, using this identification scheme, are shown in Figures 131 and 132. Figure 133 shows the Simulink blocks representing this scheme.

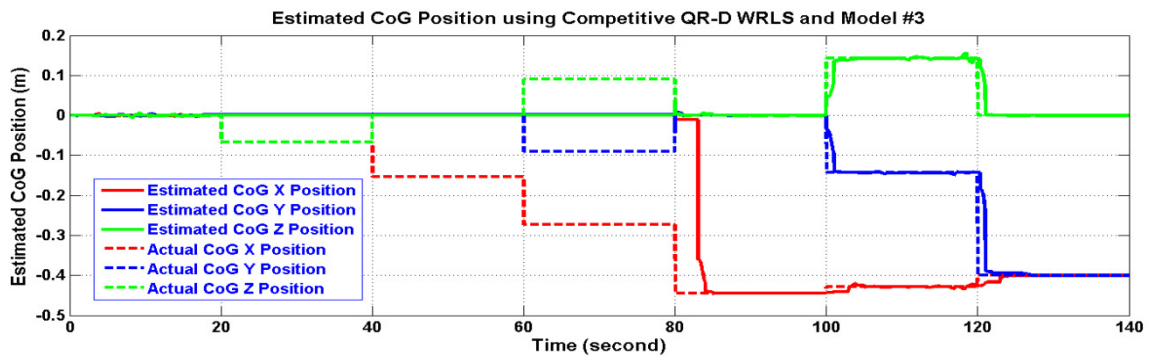


Figure 131: Estimated CoG Position using Competitive QR-D base WRLS and Model #3.

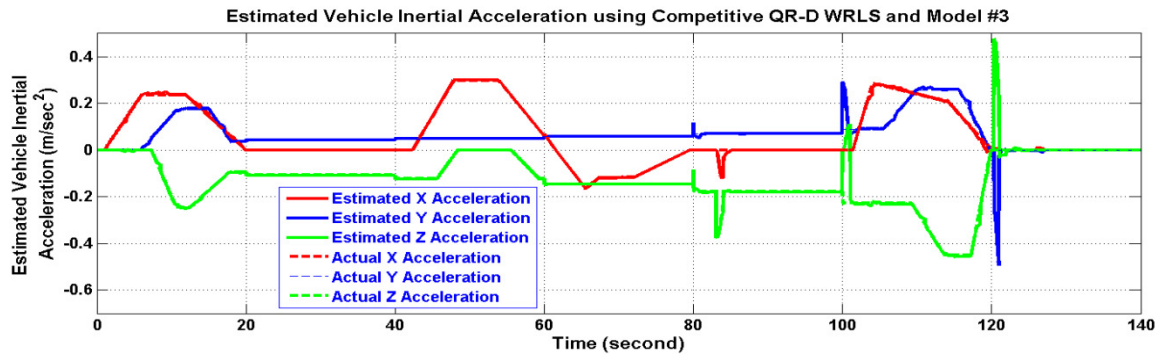


Figure 132: Estimated Vehicle Inertial Acceleration using Competitive QR-D based WRLS and Model #3.

It is worth noting that the spikes at 100 and 120 seconds are due to simulation initialization problems and are not because of the identification scheme itself.

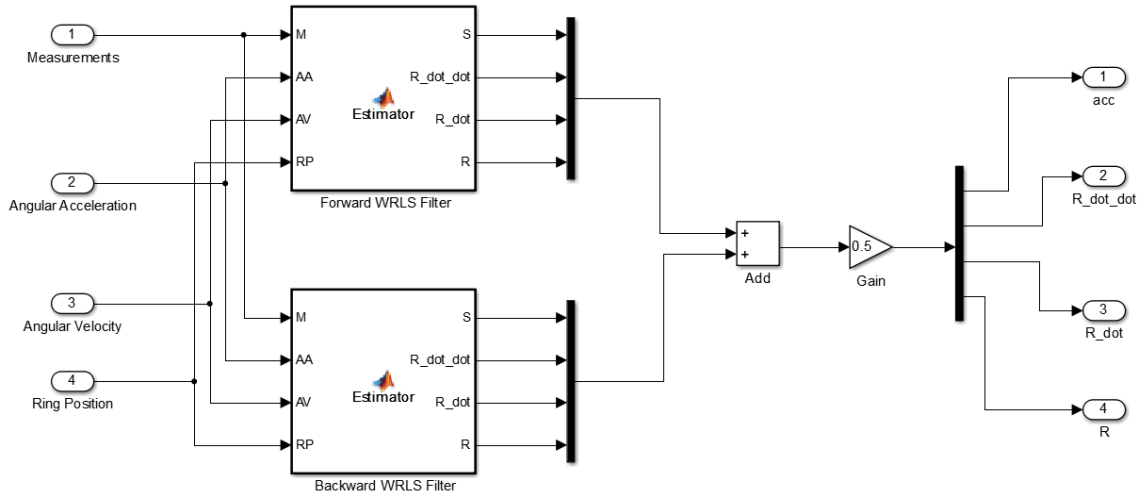


Figure 133: Simulink Blocks representing the Competitive QR-D based WRLS Identification Scheme.

8.4.2 QR-Decomposition based WRLS Bank and Maximum Likelihood Estimation Identification Scheme

In Chapter 5, the governing equations upon which this thesis is built were derived. A diamond arrangement, referred to as a Ring, was presented and its center was the main concern in those equations. Here, a similar derivation will be presented but this time will focus on the accelerometers' positions within the same Ring to provide larger set of observations that will be fed into a Maximum Likelihood Estimator (MLE) to provide the best estimate using those observations, Figure 134 visualizes this arrangement. MLE consistency property depends heavily on the number of samples involved; hence it is preferable to increase this number if possible. The accelerometers used in the proposed IMU are all tri-axial linear accelerometers whose axes are assumed to be perfectly aligned with the vehicle principle axes. In addition, there positions within the airframe are assumed to be precisely known, in fact that may lead to consider the following cases:

- 1- Handling the measurements of each individual channel within an accelerometer {x, y, and z-channels} and use it to identify the unknowns. This configuration will result in 21 1-D identification problems including the virtual measurements at the Ring's Center given by equation (111).

- 2- Handling the measurements of each individual accelerometer as pairs, (i.e. x-y, x-z, y-z). This configuration will result in 21 2-D identification problems including the virtual measurements at the Ring's Center.

- 3- Handling the measurement of each accelerometer as one unit, i.e. xyz measurements at once. This will result in 7 3-D identification problems including the virtual measurements at the Ring's Center. This case will be implemented next.

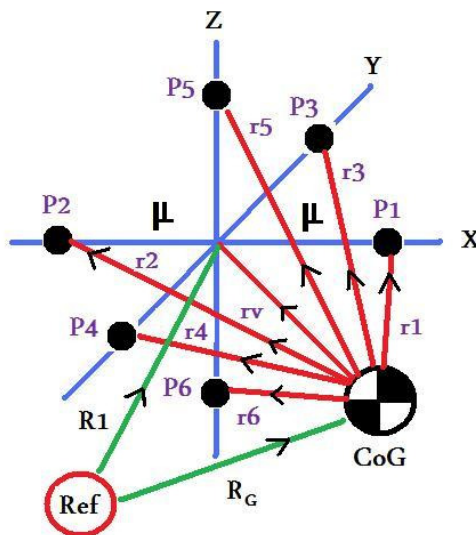


Figure 134: Schematic Diagram illustrating the principle of QR-D based WRLS Bank Identification Scheme.

By considering the gravity acceleration to be the same within the Ring's region, assuming the separation between the individual accelerometers is considerably small and by adopting model 3, the individual equations for each accelerometer is given as follows:

$$\vec{a}_i + \vec{g}_0 = \ddot{\vec{S}} + ([\dot{\Omega}] + [\Omega \times])\vec{r}_i - \int_0^t \Gamma^a V. dt \quad (145)$$

$$\vec{a}_{Ri} + \vec{g}_0 = \ddot{\vec{S}} + ([\dot{\Omega}] + [\Omega \times])\vec{r}_v - \int_0^t \Gamma^a V. dt \quad (146)$$

Where, \vec{a}_i denotes the 3x1 measurements of the i^{th} accelerometer, \vec{r}_i its position relative to the CoG, and the remaining are defined as before. Since the focus in this chapter is on the identification problem, the last terms from the right and left are set to zeroes. \vec{a}_{Ri} is given by equation (111). Figure 134 can be used to find the position of CoG \vec{R}_G relative to the reference by using the Ring position \vec{R}_1 and the i^{th} accelerometer position within the Ring. This information will be used in the MLE.

- **MLE Derivation**

“MLE is a standard approach to parameter estimation and inference in statistics. MLE has many optimal properties in estimation: sufficiency, consistency, efficiency, and parameterization invariance. The principle of maximum likelihood estimation (MLE) states that the desired probability distribution is the one that makes the observed data “most likely,” which means that one must seek the value of the parameter vector that maximizes the likelihood function” [108]. There are two types of MLE functions models that can be used here, namely the power and exponential maximum likelihood functions (MLF). The latter will be used to find the best estimate of the parameters provided that a

QR-D based WRLS Bank of size (N) is used to provide the observations. The idea here is to maximize this MLF and that can be done as follows:

The MLF, or the joint probability density function of all observations, is given by

$$f(\vec{x}, z, \sigma^2) = \frac{1}{(2\pi)^{\frac{N}{2}} (\sigma^2)^{\frac{N}{2}}} \exp\left(\frac{-1}{2\sigma^2} \sum_{n=0}^{N-1} (x(n) - z)^2\right) \quad (147)$$

Where, \vec{x} ($N \times 1$) denotes the estimations, obtained using the QR-D based WRLS Bank identification scheme as per equations (145-146), which are assumed to be independent with Gaussian distribution, z is their mean and σ^2 is the associated variance.

In order to minimize this function, it is easier to deal with its logarithmic version, i.e. $\ln(f)$, which will be continuously differentiable. Hence; the maximization problem will be given as follows:

$$\max_{z, \sigma^2} \ln(f) = -\frac{N}{2} \ln(2\pi\sigma^2) - \frac{-1}{2\sigma^2} \sum_{n=0}^{N-1} (x(n) - z)^2 \quad (148)$$

Taking the partial derivatives of $\ln(f)$ with respect to both z , and σ^2 and equating them to zeroes will give rise to the following results, for scalar observations:

$$\begin{aligned} \hat{z} &= \frac{1}{N} \sum_{n=0}^{N-1} x(n) \\ \sigma^2 &= \frac{1}{N} \sum_{n=0}^{N-1} (x(n) - \hat{z})^2 \end{aligned} \quad (149)$$

Where, $x(n)$ denotes the n^{th} observation. For of the estimated position of CoG using the estimated value of the vector \vec{r}_i as was depicted in Figure 134, the covariance matrix will be given as follows, where the diagonal elements represent the variance:

$$\sigma^2 = \frac{1}{N} \sum_{n=0}^{N-1} (\vec{x}(n) - \hat{z})(\vec{x}(n) - \hat{z})^T \quad (150)$$

Considering the 3-D identification problems configuration, these observations are given as follows:

$$\begin{aligned} \vec{R}_{G1} &= \vec{R}_1 + \mu\hat{i} - \vec{r}_1 & \vec{R}_{G5} &= \vec{R}_1 + \mu\hat{k} - \vec{r}_5 \\ \vec{R}_{G2} &= \vec{R}_1 - \mu\hat{i} - \vec{r}_2 & \vec{R}_{G6} &= \vec{R}_1 - \mu\hat{k} - \vec{r}_6 \\ \vec{R}_{G3} &= \vec{R}_1 + \mu\hat{j} - \vec{r}_3 & \vec{R}_{G7} &= \vec{R}_1 - \vec{r}_v \\ \vec{R}_{G4} &= \vec{R}_1 - \mu\hat{j} - \vec{r}_4 \end{aligned} \quad (151)$$

As was expected, the result will turn to be the ordinary mean and variance usually encounter in similar problems. However, the MLE is an asymptotically unbiased estimator and as a result it will be unbiased if the number of observations involved tends to be significantly large and that can explain the introduction of the three cases in this section.

Increasing the number of observation can be done by utilizing the three cases previously described, or the like if possible, but that will come with the expenses of increased computational complexity due to the increased number of QR-D based WRLS problems involved in such a scheme. So, a compromise must be done especially when such a scheme can be argued about because of the small separation of the accelerometer within

the Ring itself so that it may not provide additional information. However, such a scheme may be useful when a channel within an accelerometer or a whole accelerometer is deemed faulty. If this scheme proofed itself, it will eliminate the need for other Rings distributed along the airframe.

Other additional features to mention about this scheme are as follows:

- a. It can be used in open/closed loop configuration.
- b. It can be implemented locally at the Ring Level and globally at the Rings Level.
- c. It can be running in parallel threads once implemented in real hardware.

Figures 135 and 136 illustrate this concept, clearly.

This method depends on resetting the covariance matrix when the estimation may diverge. The trace of the error covariance matrix is used as a criterion to decide whether to reset the covariance matrix or not once it exceeds a predetermined value which was picked on trial and error basis. Another way to determine the quality of estimation during the process itself is to apply constraints, i.e. providing constraints to check against them the estimated parameters' values and to correct accordingly. "It was shown that the unique solutions to linear-equality constrained and the unconstrained LS problems, respectively, always have exactly the same recursive form. Their only difference lies in the initial values" ^[110]. The same thing can be considered as well for inequality constraints as can be found in [111]. In such a case, the individual units within the QR-D based WRLS bank may provide an estimate of the related accelerometer position, i.e. \vec{r}_i and \vec{r}_v and the following linear constraints can be applied and a correction can be made to

the estimation found by the individual units as can be seen from Figure 135. Those constraints come from the Geometric design of the Ring and they are as follows:

$$\begin{aligned} \vec{r}_1 - \vec{r}_2 &= 2\mu\hat{i} \\ \vec{r}_3 - \vec{r}_4 &= 2\mu\hat{j} \\ \vec{r}_5 - \vec{r}_6 &= 2\mu\hat{k} \end{aligned} \quad (152)$$

Where, μ denotes the relative position of all accelerometers in the designated directions measured from the Ring center.

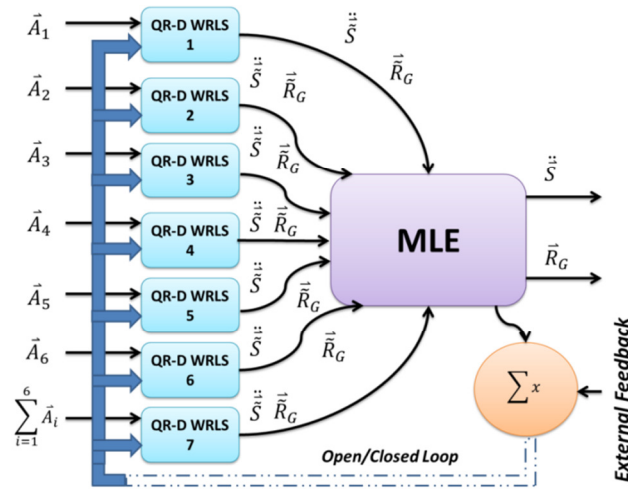


Figure 135: QR-Decomposition based WRLS Bank and Maximum Likelihood Estimation Identification Scheme Implemented locally within the proposed IMU in open/closed loop configuration.

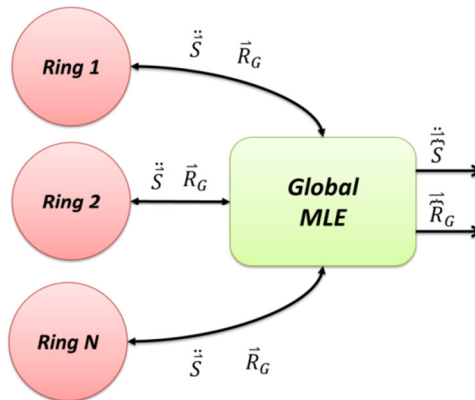


Figure 136: Global implementation of the MLE in open/closed loop configuration assuming ideal sensor network.

Simulating the previous scheme locally in open loop configuration resulted in the following figures:

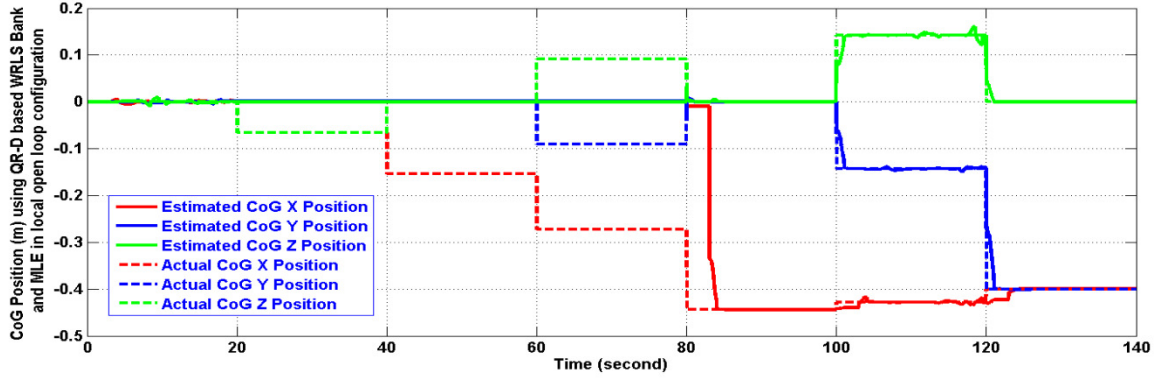


Figure 137: Estimated CoG Position using QR-D based WRLS Bank and MLE in local open loop configuration.

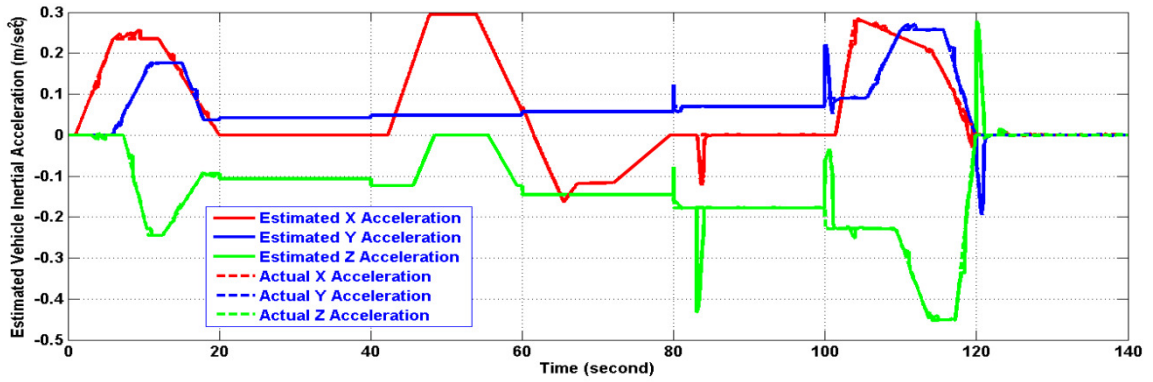


Figure 138: Estimated Vehicle Acceleration using QR-D based WRLS Bank and MLE in local open loop configuration.

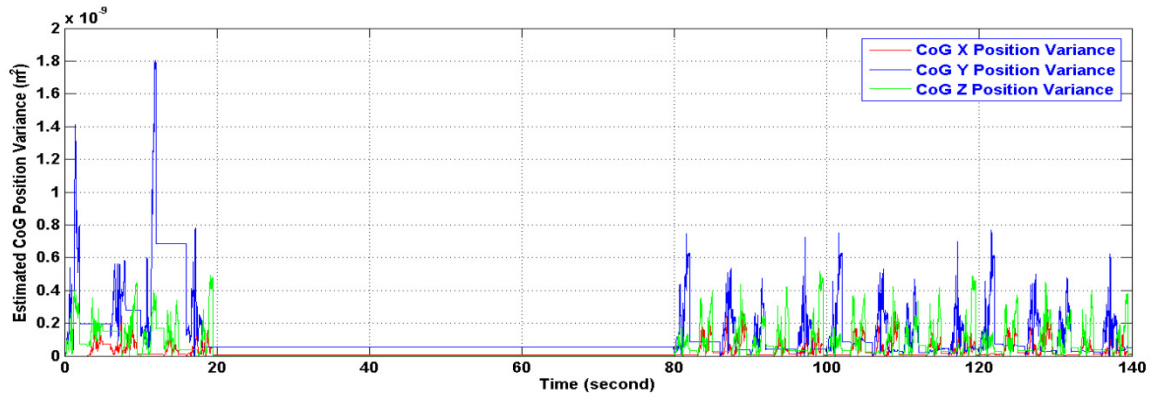


Figure 139: CoG Position Variance, in order of $1e-9$.

Inspired by the previous idea, the following scheme is proposed.

8.4.3 Geometric Optimization with linear constraints and MLE Identification Scheme

Neglecting the gravity contribution, the objective function is given as follows:

$$\begin{aligned}
 J &= J_1 + J_2 + J_3 \\
 J_1 &= \int_0^t \{(A_1 - \ddot{S} - Wr_1)^T Q_1 (A_1 - \ddot{S} - Wr_1) + (A_2 - \ddot{S} - Wr_2)^T Q_2 (A_2 - \ddot{S} - Wr_2)\} . dt \\
 J_2 &= \int_0^t \{(A_3 - \ddot{S} - Wr_3)^T Q_3 (A_3 - \ddot{S} - Wr_3) + (A_4 - \ddot{S} - Wr_4)^T Q_4 (A_4 - \ddot{S} - Wr_4)\} . dt \\
 J_3 &= \int_0^t \{(A_5 - \ddot{S} - Wr_5)^T Q_5 (A_5 - \ddot{S} - Wr_5) + (A_6 - \ddot{S} - Wr_6)^T Q_6 (A_6 - \ddot{S} - Wr_6)\} . dt
 \end{aligned} \tag{153}$$

The problem is to minimize J subjected to the constraints given by equations (152) then following the procedure given in MLE.

Combining the two previously schemes results in the following scheme.

8.4.4 Modified Geometric Optimization with linear constraints Identification Scheme

Figure 140 shows the block diagram of this identification scheme where the cooperation between the previous identification schemes is obvious. The role of the QR-D based WRLS Bank Identification scheme is to provide the initial estimates for the Geometric Constrained Optimization scheme which then feeds its estimation to a MLE which corrects the estimations as was previously shown and provides a mechanism to correct the estimation of the WRLS identification scheme in case a feedback loop is established.

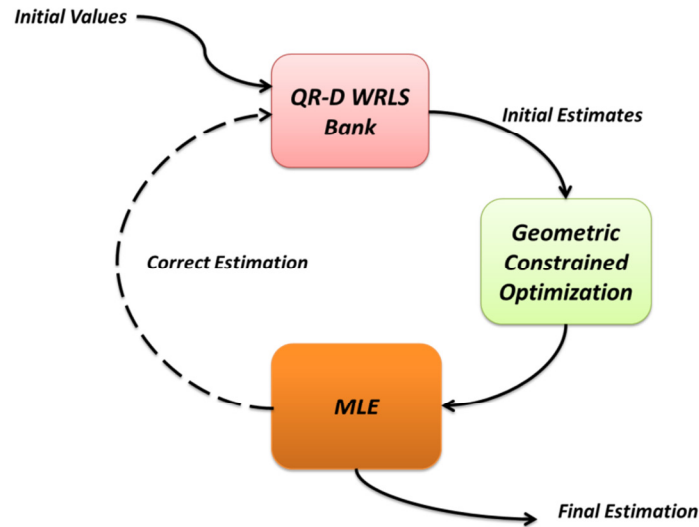


Figure 140: Block diagram of the Modified Geometric Optimization with linear constraints Identification Scheme.

8.5 Minimum Angular Motion Needed for CoG Position Determination

Such a question is very important to be answered; since it determines the applicability of the procedure proposed in this thesis within real air vehicles. The proposed IMU must go with the limitations imposed on different types of air vehicles. For example, a free rotating missile is allowed to have angular motion about its Body Axes freely, while a commercial airliner angular motion is restricted to a certain bound to ensure the comfort of passengers onboard. By examining the regression matrix given in model 3, for instant, it can be easily told due to the nature of the angular motion matrix, namely $([\dot{\Omega}] + [\Omega \times])$ that a sufficient angular velocity and/or acceleration, about any principle axis of the air vehicle enables identifying the coordinates of CoG position on the other two axes. So, an angular motion about at least two principle axes is needed to completely identify the CoG position. Table 18 gives a brief description about this situation. The estimation of the inertial acceleration is partially affected and in the case of adaptive forgetting factor version of the QR-D based WRLS this effect can be reduced further.

Table 18: Angular Motion plan To Identify CoG position

CoG Change	Roll	Pitch	Yaw
X-Axis			
Y-Axis			
Z-Axis			
X-Y Plane			
X-Z Plane			
Y-Z Plane			
X-Y-Z			
X-Y-Z			
X-Y-Z			
	AND		
	OR		

The previous conclusion depends as well on the magnitude of the available angular motion needed to render the parameters identifiable. Such a magnitude can be determined through the consistency and bias analysis of the estimator used, which is beyond the scope of this thesis. It should be clear that the reaction of the flight controller must be considered in the sense that any change in CoG position will be considered as a disturbance which the controller tries to cancel.

Basically, the proposed IMU may benefit from the instantaneous angular motion resulting from the change in the CoG position to estimate its position and then the controller will compensate for it, or it may totally depend on a planned angular motion by the controller (manned/unmanned vehicle) to determine the change in CoG position considered by the

controller as a disturbance which was cancelled. The latter approach comes to help in reducing the energy consumed to handle such a disturbance, as was mentioned in Chapter 1. Both cases depend on the way the controller is interacting with the proposed IMU.

The following figures illustrates the previous passages were an angular motion is restricted to be about one axis at a time. The QR-D based WRLS utilizing model 3 is used to simulate these cases.

1- Angular Motion about X-axis only (Roll):

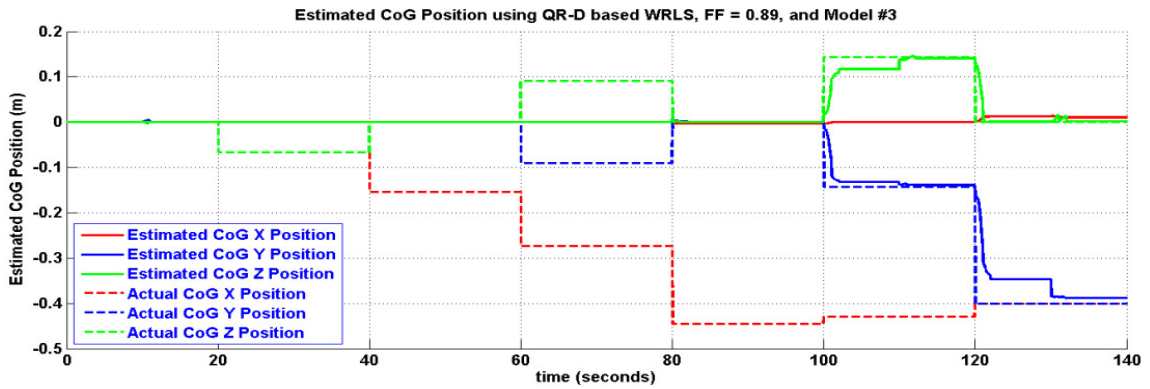


Figure 141: Estimated CoG Position when only angular motion about X-axis is present.

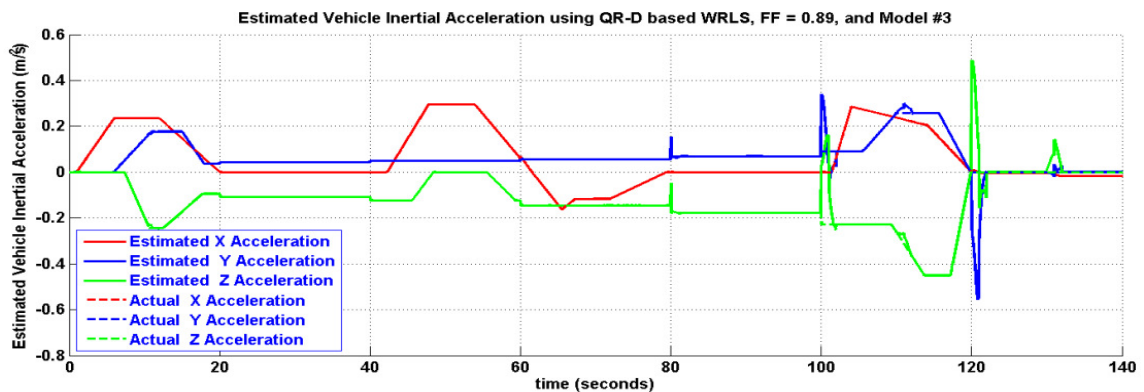


Figure 142: Estimated Inertial acceleration when only angular motion about X-Axis is present.

2- Angular Motion about Y-axis only (Pitch):

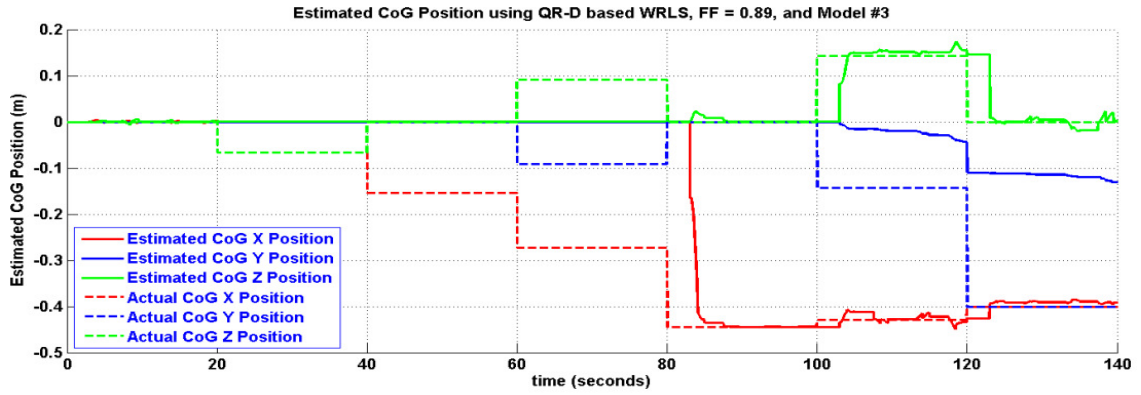


Figure 143: Estimated CoG Position when only angular motion about Y-axis is present.

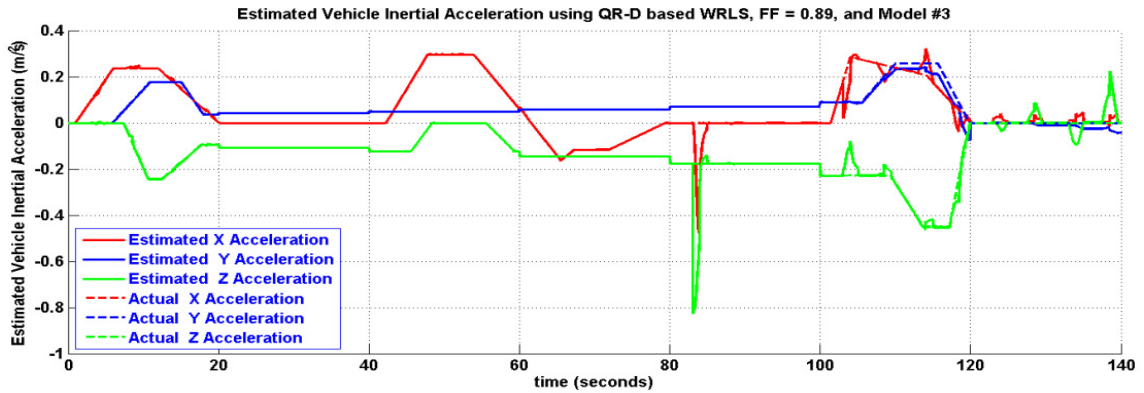


Figure 144: Estimated Inertial acceleration when only angular motion about Y-Axis is present.

3- Angular Motion about Z-axis only (Yaw):

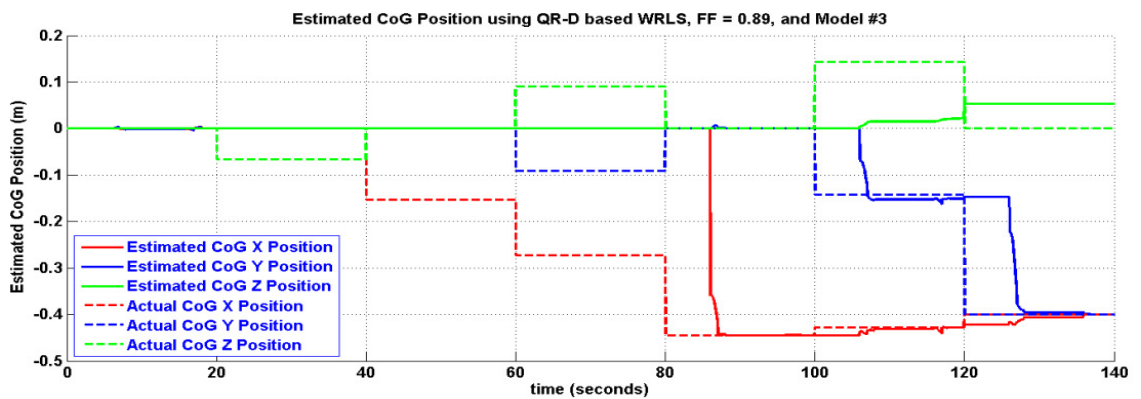


Figure 145: Estimated CoG Position when only angular motion about Z-axis is present.

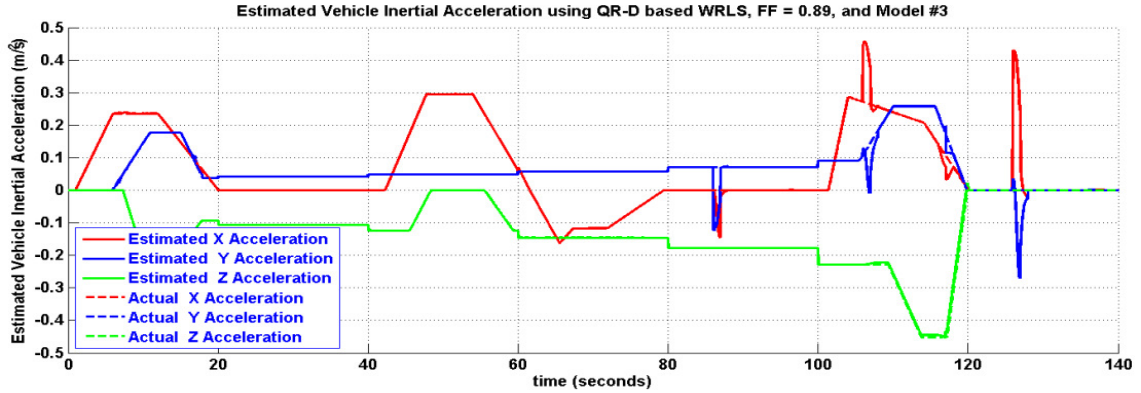


Figure 146: Estimated Inertial acceleration when only angular motion about Z-Axis is present.

8.6 Summary

The RLS algorithms are known to pursue fast convergence even when the eigenvalue spread of the input signal correlation matrix is large. These algorithms have excellent performance when working in time-varying environments. All these advantages come with the cost of an increased computational complexity and some stability problems [109]. Using WRLS is the best method among the available RLS algorithms investigated here for tracking Time-Varying Systems. Although its statistical properties such as consistency in most cases is difficult to find, due to the complex dependency on the time-varying characteristics and on the forgetting factor value [112]. Many efforts were reported in literature to investigate these properties of the RLS with exponential forgetting factor such as [120-123], in which they treat this problem in special cases that may not directly fit to the problem stated in this thesis.

Another thing to keep in mind is the stability of the WRLS estimator when estimating time-varying parameters. The expression used in updating the error covariance matrix in WRLS algorithm is the one that may cause instability [109].

Other alternatives especially when implementing the estimator in finite-precision is QR-Decomposition based RLS, known for short QR-RLS, which stability can be easily proofed [109], so that it was adopted here to build a QR-D based WRLS algorithm.

Another way to enhance the performance of WRLS used here is to introduce a conditional covariance resetting procedure by which the tracking capability of such method is drastically increased [117]. Actually, the WRLS used here was incorporated with this procedure taking the trace of the covariance matrix as the condition upon which the decision to reset the covariance matrix is taken; since it appears to provide the best overall performance [117]. Examples to show how WRLS with covariance resetting can outperform the performance of other methods like Least-Mean Squares are reported in [118]. In [119], a modified RLS algorithm is presented mainly with variable gain, forgetting factor, and reset condition.

Another point of interest is the performance of the WRLS in the finite-precision which can change from that experienced in infinite-precision. Divergence and freezing in the parameter adaptation are examples, which may not be encountered with QR-RLS which performance and stability can be guaranteed [109].

Under the state-space model assumption, there will be a correspondence between the RLS and Kalman Filter that is worthy of investigation [113].

As was concluded by in [114], Least-Squares can be used to determine the model but the Maximum-Likelihood estimation is needed to estimate the parameters accurately, so it is highly recommended to implement MLE as an identification technique rather than using it for correcting the estimates as was done in this thesis.

Finally, it is worth noting that the angular velocity and acceleration used in the identification schemes were obtained from a Body sensor available in the SimMechanics library; and that enabled more focusing on the identification techniques. However, as will be shown in Chapter 9, the filter used to retrieve the angular velocity will affect the estimation results which are considered another motivation to investigate the error propagation within the different stages of the proposed IMU which will be a subject of future work.

CHAPTER 9

COMPLETE PICTURE

In this chapter, the complete picture tackled in this thesis, namely: *how the navigation problem under the conditions of varying center of gravity and unknown varying gravity acceleration can be solved using an identification approach*, is presented. The solution provided herein was based on the usage of linear accelerometers. Since linear accelerometers are affected by the gravitational forces; there is a need to compensate for the contribution of this effect. As was previously shown in equation (132), the accelerometers' measurements contain the contributions of inertial acceleration, gravity effect, and the varying CoG kinematics which makes the problem of providing clean accelerometers measurements a little bit involved. As far as the author is concerned in literature, this kind of problems were partially considered, the focus most of the time was on solving problems containing two out of three contributors among those stated in equation (132), i.e. solving for the position of CoG of air vehicles when the gravity is known, see for example [1-2], or estimating the gravitational acceleration assuming stationary CoG as may be found in [129-130]. Besides that, most of these solutions utilize various components such as accelerometers, gyroscopes, and magnetic sensors integrated with GPS devices, whereas the solution provided in this thesis allows a completely passive INS provided sufficient angular motion is present. This is the first time, as far as the author is aware of, that such a problem is formulated in a way that brings all the parts together in an identification scheme.

9.1 The Proposed IMU Structure

In this section, the various steps taken to achieve the function of the proposed IMU are pointed out with references made to the related parts found within this thesis or to the appropriate external references. Figure 147 shows the proposed IMU which contains parts already implemented and parts to be considered in future versions, such as IACR, estimated mass and inertia of the air vehicle where the current version was adjusted to suite such a future expansion. Moreover, a place for fault detection and correction was also reserved along with preconditioning and pre-filtering stage for the accelerometers' measurements upon which this IMU depends. A look-inside this IMU setup follows in the following figures.

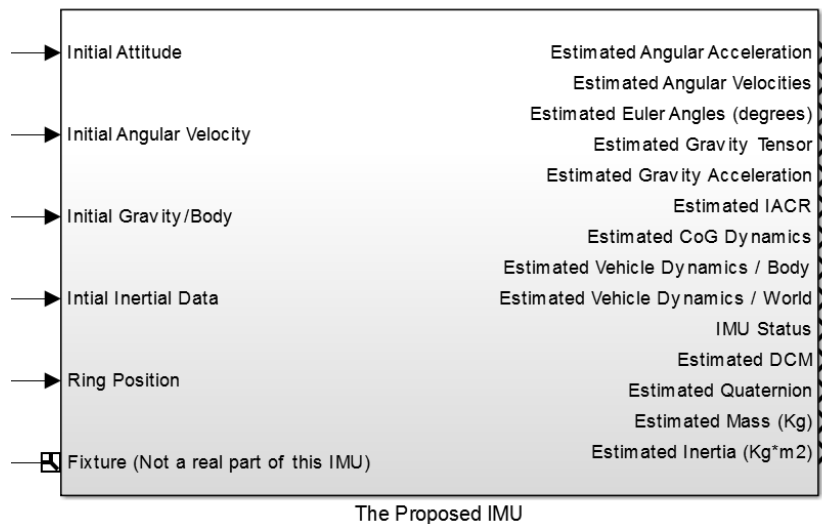


Figure 147: The recent version of the proposed IMU.

Figure 148 shows three blocks representing the actual accelerometers' configuration (Ring) along with two additional blocks - to be implemented in future versions of this IMU- related to measurements preconditioning and pre-filtering. The fault utility was

also equipped with a Fatal Error flag that will give an indication to the autopilot about the current status of IMU whether it is functional, partially functioning, or completely failed which enables the autopilot to decide what to do next.

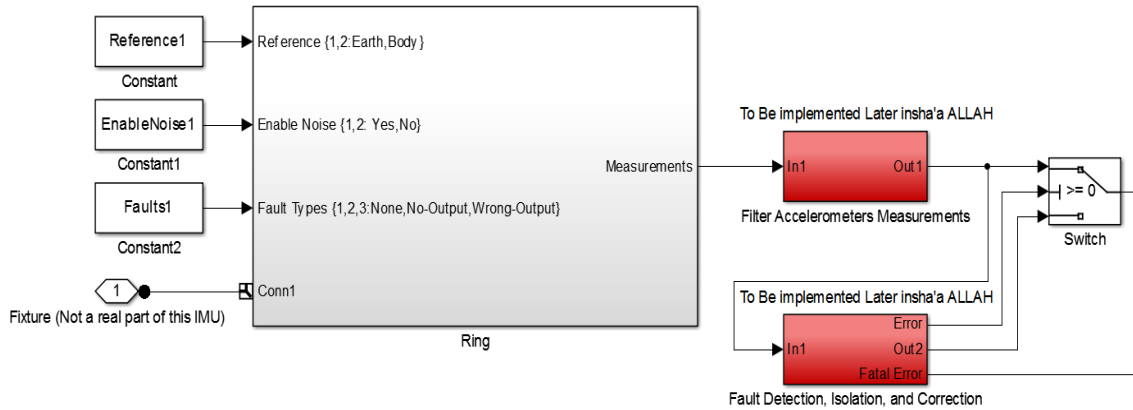


Figure 148: Actual accelerometers' configuration (Ring) along with Suggested units for future work.

Figure 149 shows the inside formulation of the Ring used utilizing the tri-axial accelerometer model previously described in Chapter 5.

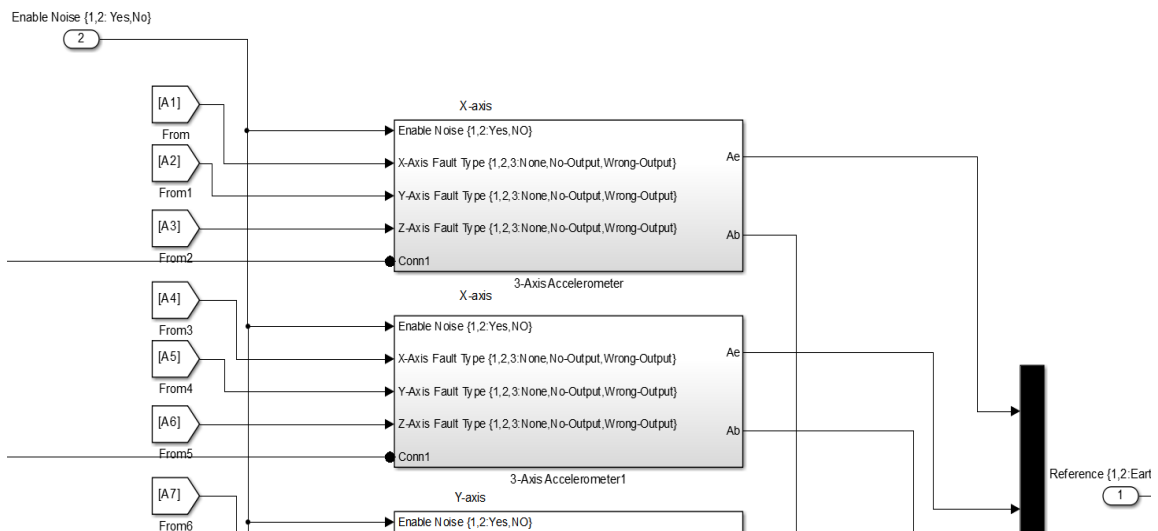


Figure 149: A look inside the Simulated Ring.

In addition, Figure 150 shows the main three stages upon which the remainder of the work done in this thesis relay on. After the angular acceleration is extracted from the accelerometers' measurements, it is numerically integrated to facilitate finding the gravity tensor in acceptable precision [42] or by using a Kalman filter. Then the angular velocity is re-estimated but now by using dedicated filters such as Extended (EKF) and Unscented (UKF) Kalman Filters. The integrator block shown in Figure 150 is used to retrieve the sign of the angular velocity as was shown in Chapter 6.

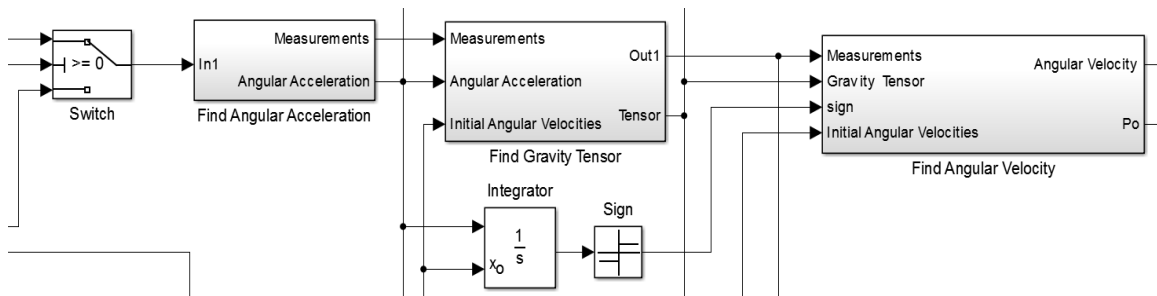


Figure 150: Core units in the proposed IMU.

After the angular velocity is found, the attitude determination can be made easy using the equations available in [123], where both the Quaternion and Euler Angles are made available to enable their usage by other units found in the autopilot configuration. Figure 151 shows the Simulink block that solves the attitude problem along with IMU performance Unit- which to be implemented in future work- responsible of monitoring the performance of every unit within the proposed IMU and to report the IMU status to the autopilot unit. For example, if one of the filters diverges then it is logical to direct the attention of the autopilot that such a sudden change was due to numerical instability rather than an actual sudden change. This simple statement in fact does not reflect the simplicity of this monitoring unit, rather it shows that such an implementation can be

difficult, but it still can justify the existence of such a unit. This will be seen in section 9.3 when hardware implementation problems may cause such performance deterioration.

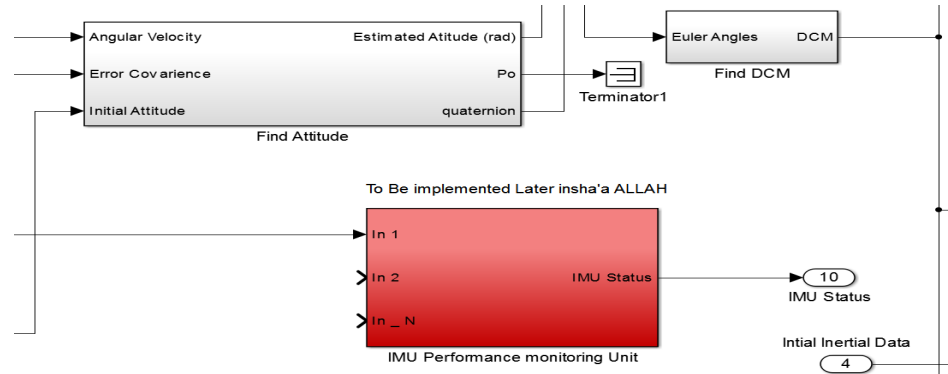


Figure 151: Attitude Finding unit along with IMU Performance Unit suggested for future work.

Next, Figure 152 shows the Simulink blocks used to estimate both the Inertial Data and the Acceleration due to Gravity. Actually, at this stage the superiority of the proposed IMU is revealed; showing the interaction between the various stages within the IMU which makes it possible for alternative signal paths to be taken, such as smoothing and projecting the acceleration before or after the gravity is calculated. Such a choice must be made based on Error Analysis which will reflect how the error is propagated through this IMU as well as discovering the points of weakness to be fixed. Such an analysis is part of the recommended future work.

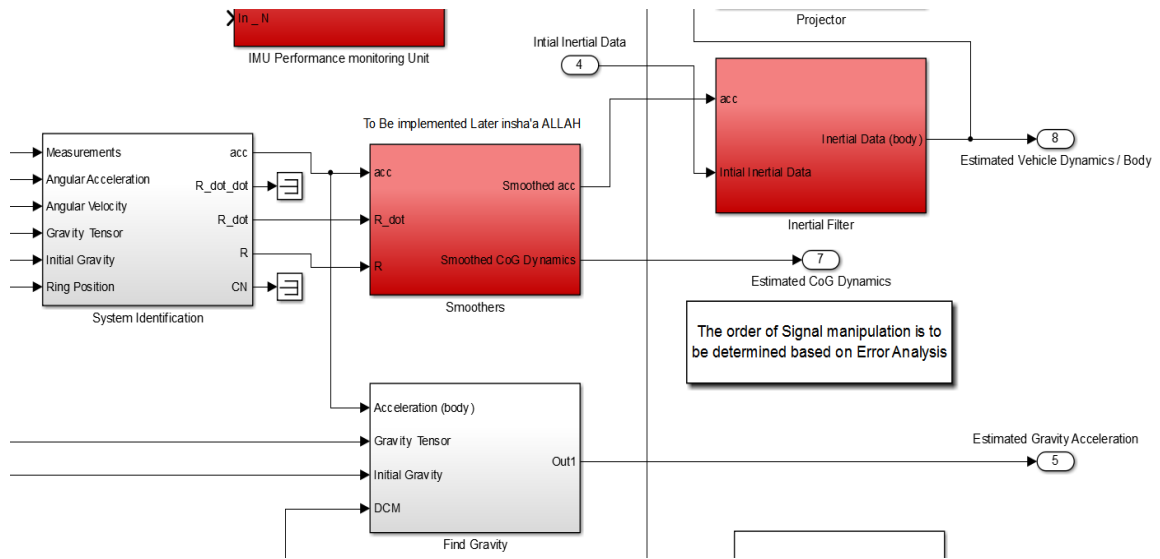


Figure 152: Units used to estimate inertial data and acceleration due to gravity.

The Inertial Filter shown in Figure 152, which is to be implemented in the future, will use the Discrete Wiener Process Acceleration Model (DWPA) as a model to design a suitable filter to retrieve the desired Inertial Data. A good starting point will be found in [124]. Figure 153 shows the blocks reserved for future expansion, namely: finding the Instant Acceleration Center of Rotation (IACR), and the estimated vehicle mass and inertia where the later can make use of equations (24-29) found in Chapter 2.

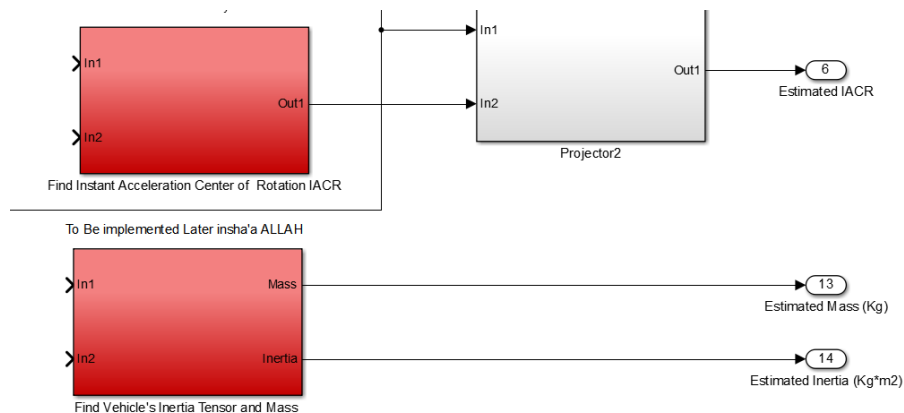


Figure 153: Blocks reserved for future expansion responsible of finding the mass and inertia of the vehicle.

Finally, optimal Smoothers are to be implemented in future work to provide smoothed versions of the estimated parameters that can be used later on in successive units in the autopilot configuration. Figure 154 shows the Simulink block that represents such unit. A good starting point can be found in [81].

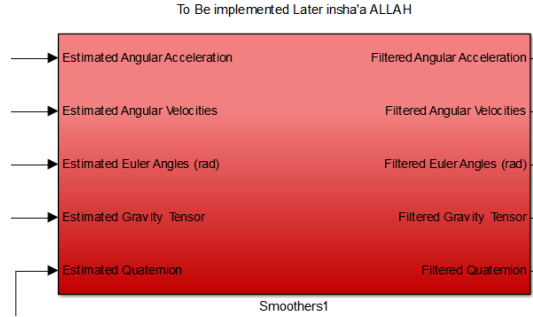


Figure 154: Block reserved for optimal smoothers suggested for future work.

Figure 155 shows the signals flow diagram as found in the proposed IMU.

9.1.1 Identification Model #3 with gravity effect included

Here, the effect of including the acceleration due to gravity in the identification problem is reflected on identification Model #3, and it is given as follows:

$$\begin{aligned}
 h^2 \bar{m}(k) + \frac{h^2}{4} \sum_{i=1}^{k-1} \{ & 3\Gamma^a(i)\bar{S}(i) + (3\Gamma^a(i-1) - 4\Gamma^a(i))\bar{S}(i-1) + (\Gamma^a(i) - 4\Gamma^a(i-1))\bar{S}(i-2) \\
 & + \Gamma^a(i-1)\bar{S}(i-3) \} \\
 = & \left\{ \left(2I - \frac{3h^2}{4}\Gamma^a(k) \right) \bar{S}(k) \right\} - \left\{ \left(5I + \frac{h^2}{4}(3\Gamma^a(k-1) - 4\Gamma^a(k)) \right) \bar{S}(k-1) \right\} \\
 & + \left\{ \left(4I - \frac{h^2}{4}(\Gamma^a(k) - 4\Gamma^a(k-1)) \right) \bar{S}(k-2) \right\} - \left\{ \left(I - \frac{h^2}{4}\Gamma^a(k-1) \right) \bar{S}(k-3) \right\} \\
 & - \left(h^2 \left([\dot{\Omega}](k) + [\Omega \times](k) \right) \right) \bar{R}_G(k) + e(k)
 \end{aligned} \tag{154}$$

And all the parameters are given as before. $e(k)$ is treated as an error that holds in it the contribution of vehicle's inertial velocity as depicted in Figure 155. According to [42], the anomalous gravity can be retrieved by integrating the gravitation gradients measured in the body frame, after transformation to the navigation frame. This transformation can be simply done by pre-and post-multiplying the gravitation gradients by the appropriate DCM.

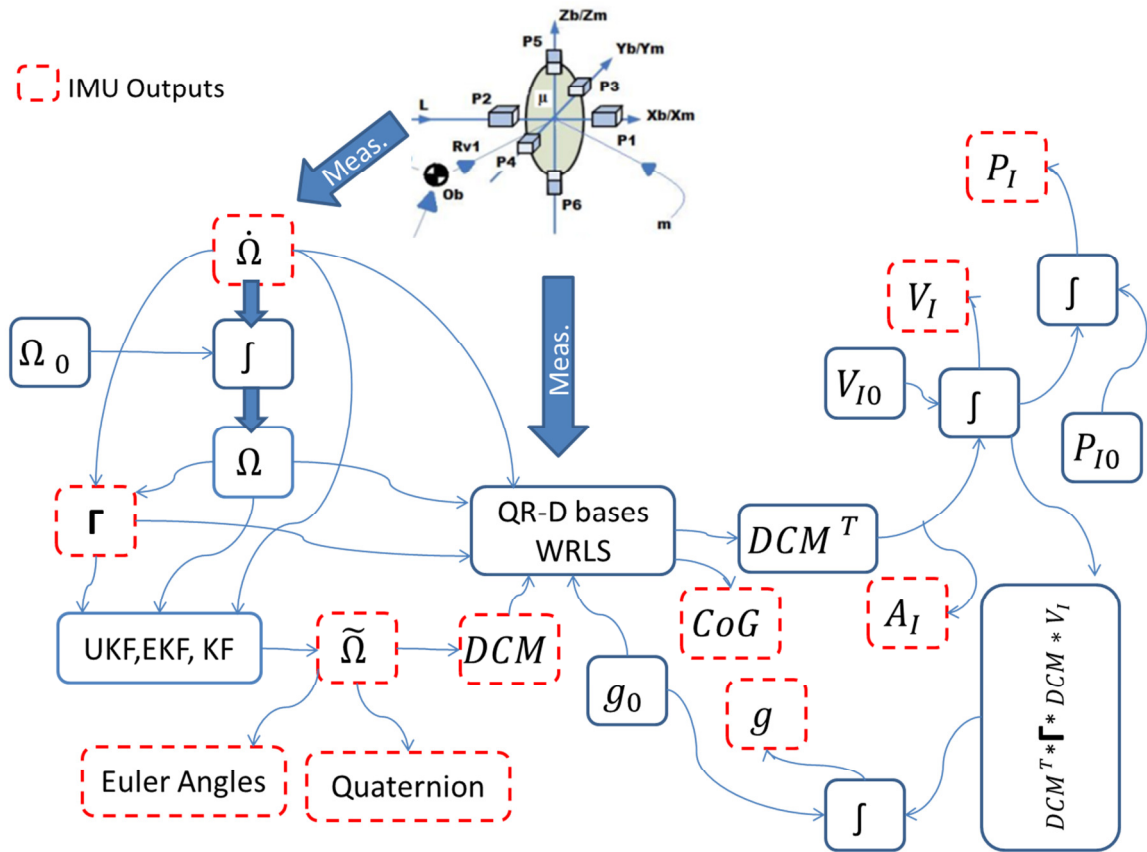


Figure 155: Flow diagram of the proposed IMU showing INS Mechanization procedure.

IMU Outputs

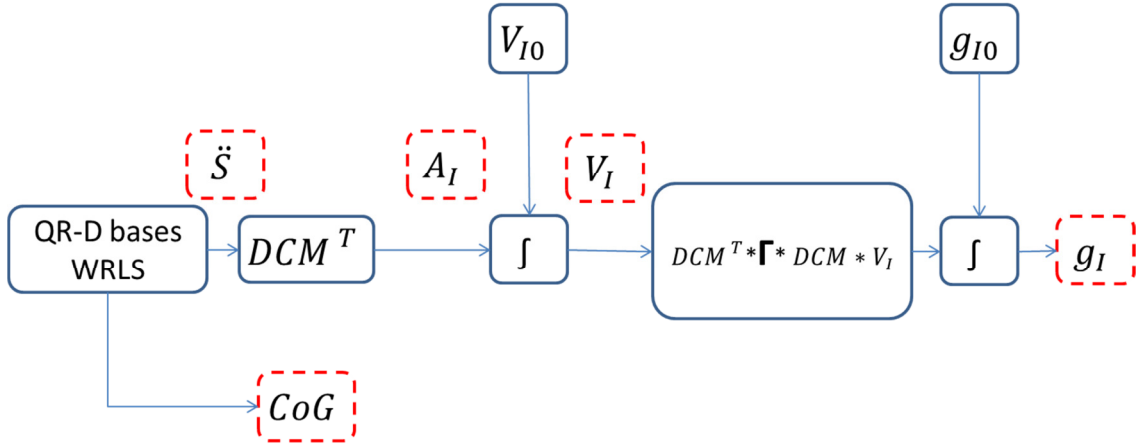


Figure 156: Estimating acceleration due to gravity using the proposed IMU according to [42].

9.1.2 Solving the Attitude Problem

The proposed IMU can be used to retrieve the Attitude, and then the DCM, of the vehicle simply by integrating the non-linear differential equation given by (155) [120]. Although it seems not intimidating, still its solution may suffer from drift- especially if no angular velocity is present - and from a singularity at $\theta = \pm\pi$. The drift will cause a lot of trouble using this approach; since –as can be seen from Figure 155- this approach is highly dependent on the usage of the DCM. To avoid this problem an ideal DCM was used using the Body Sensor previously described. Other solutions for the Attitude problem are available but are beyond the scope of this thesis.

$$\begin{bmatrix} \dot{\phi} \\ \dot{\theta} \\ \dot{\psi} \end{bmatrix} = \begin{bmatrix} 1 & s\phi t\theta & c\phi t\theta \\ 0 & c\phi & s\phi \\ 0 & s\phi/c\theta & c\phi/c\theta \end{bmatrix} \begin{bmatrix} \Omega_x \\ \Omega_y \\ \Omega_z \end{bmatrix} \quad (155)$$

9.2 Simulation Results

In this section, the simulation results of the proposed IMU are shown. These results give a general overview about the IMU performance when operated in ideal situations namely, ideal DCM, and ideal accelerometers measurements. Further investigation of its performance must be conducted to reveal its actual behavior and to provide an insight about the error bounds associated with such operation in real applications with/out a controller action. Figure 157 shows the Simulink model used to facilitate this simulation.

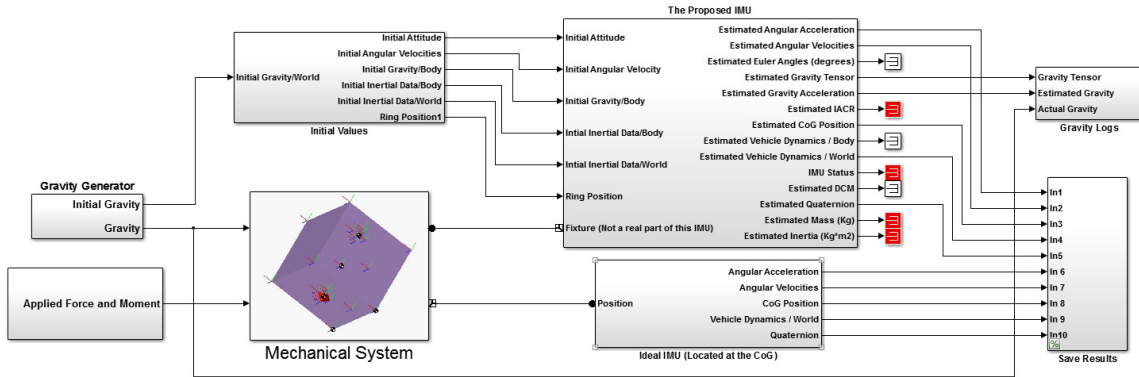


Figure 157: Simulink model used to facilitate simulating the complete IMU.

Since this simulation was based on open loop actuation of a cube in 6-DOF, it was somehow difficult to meet the different requirements of the simulation, namely: maintaining a bounded attitude according to what SimMechanics permits, and providing an adequate “flight” path. As a result, the simulation was split into two parts, one that shows the solution of the navigation problem within 60 seconds to ensure that the attitude is within the allowed limits and another part with extended time duration for 1 hour to show the performance of the proposed IMU in tracking a varying gravity acceleration as may be encountered for long flight missions within which the gravity acceleration may change significantly. It is worth mentioning that this was done because the attitude

information will be lost after 60 seconds within which the CoG position was allowed to change. To summarize, the first part shows how the navigation problem can be solved under varying CoG position and insignificant gravity change, and the second part shows the performance of the proposed IMU in tracking a varying gravity acceleration under insignificant attitude or CoG position changes. Both were simulated using the same setup, hence the claim of this thesis is still valid but there is a need to solve the bounded attitude problem.

Next, the simulation results of solving the navigation problem using UKF, EKF, and a standard KF are shown. In all cases, the QR-D based WRLS and Model #3 -as found in (154) - were used. Different types of filters required different Forgetting Factor, Process, and measurement noise matrices parameters' settings.

9.2.1 Explaining the simulation procedures

In Chapter 7, ideal angular motion- obtained using a Body Sensor - was used to investigate the various identification methods and models in a step to maintain focus on selecting the best among them and the results was a QR-D based WRLS and Model #3. The later was modified as found in (154) to accommodate the gravity effect.

9.2.2 Solving the navigation problem using UKF and QR-D based WRLS

The following figures show the results obtained when solving the navigation problem using the UKF with 1-D and 3-D measurement models.

- UKF with 1-D measurement model
FF = 0.92, $Q = 1e-9 \cdot \text{eye}(3)$, $R = 1e-10 \cdot \text{eye}(3)$

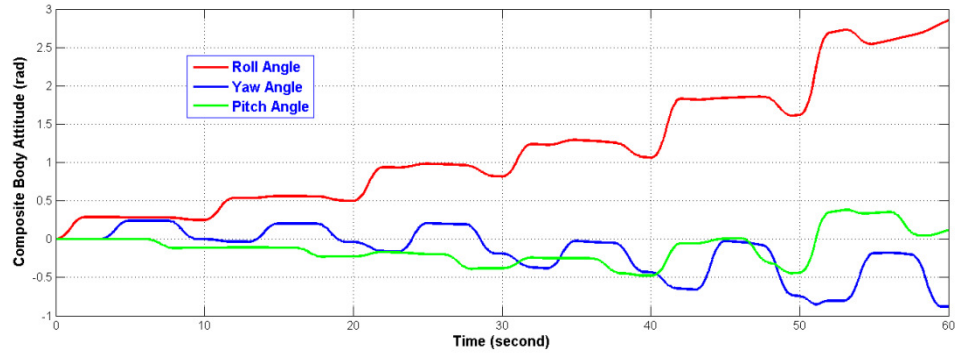


Figure 158: Composite Body Attitude used to check the performance of the proposed IMU.

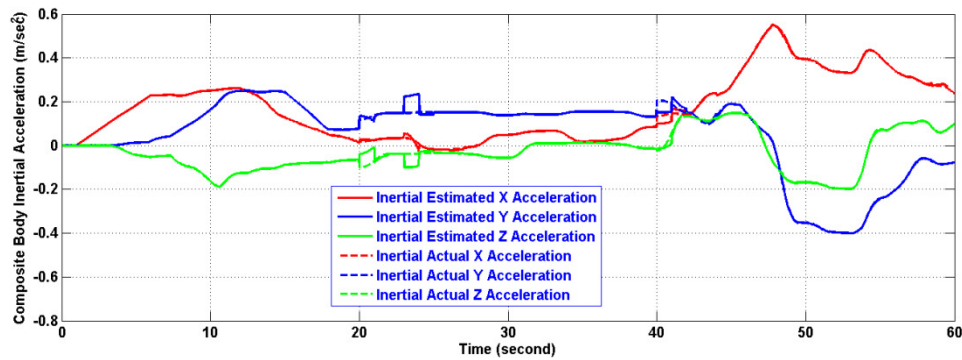


Figure 159: Composite Body Inertial Acceleration, after subtracting the gravity contribution, obtained using the proposed IMU utilizing UKF with 1-D Measurement model.

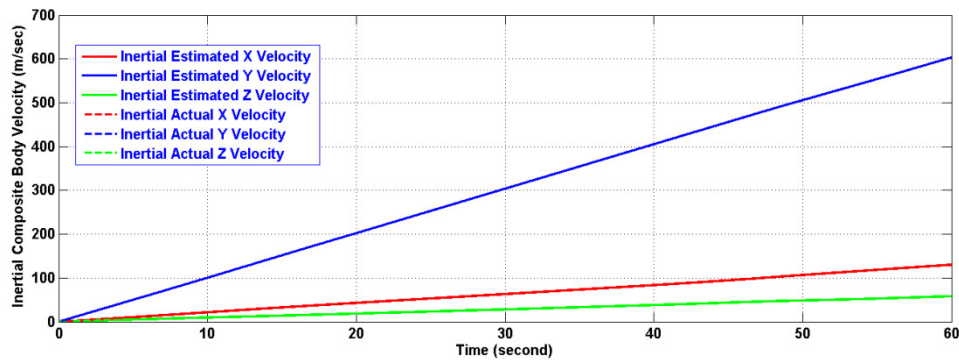


Figure 160: Composite Body Inertial Velocity obtained using the proposed IMU utilizing UKF with 1-D Measurement model.

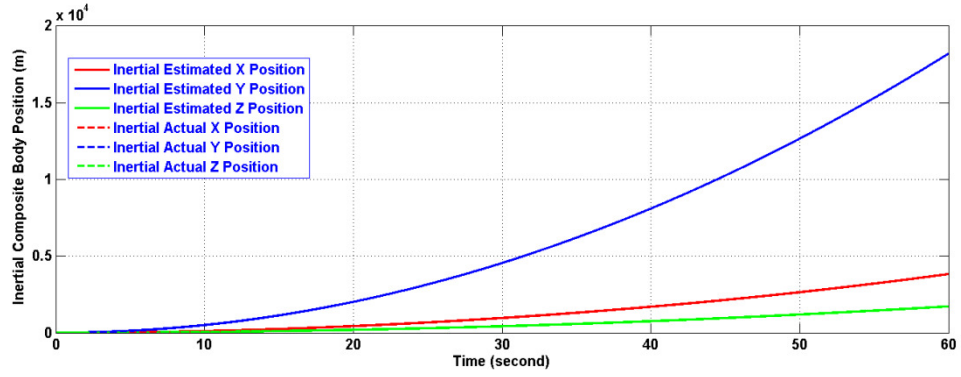


Figure 161: Composite Body Inertial Position obtained using the proposed IMU utilizing UKF with 1-D Measurement model.

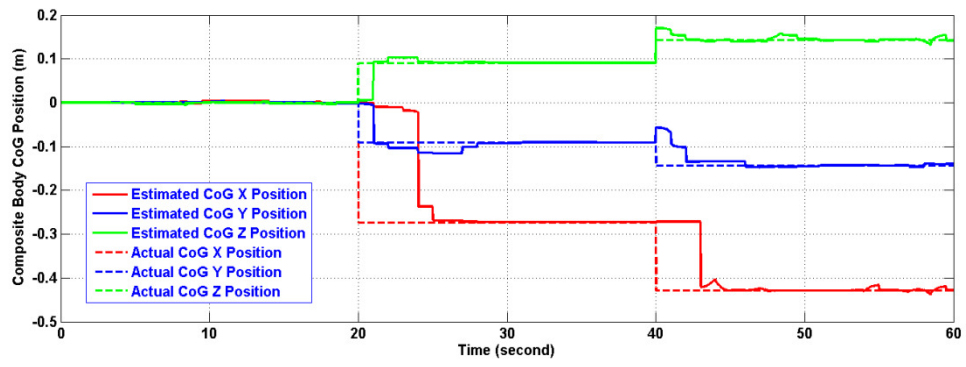


Figure 162: Composite Body position obtained using the proposed IMU utilizing UKF with 1-D Measurement model.

- UKF with 3-D measurement model

$$FF = 0.915, Q = 1e-10 \cdot \text{eye}(3), R = 1e-14 \cdot \text{eye}(3)$$

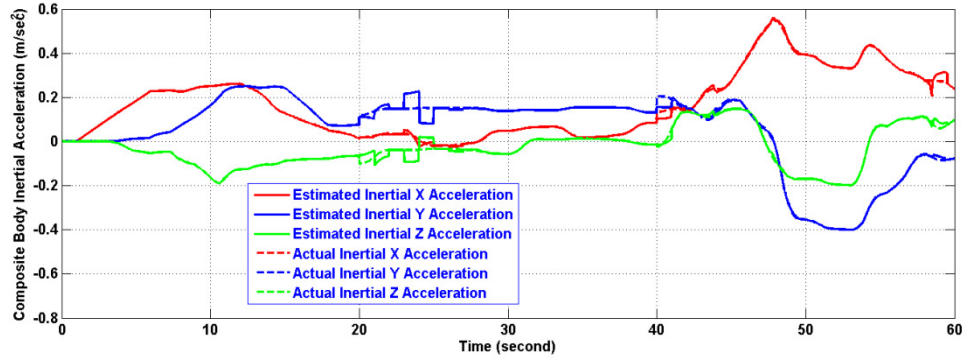


Figure 163: Composite Body Inertial Acceleration, after subtracting the gravity contribution, obtained using the proposed IMU utilizing UKF with 3-D Measurement model.

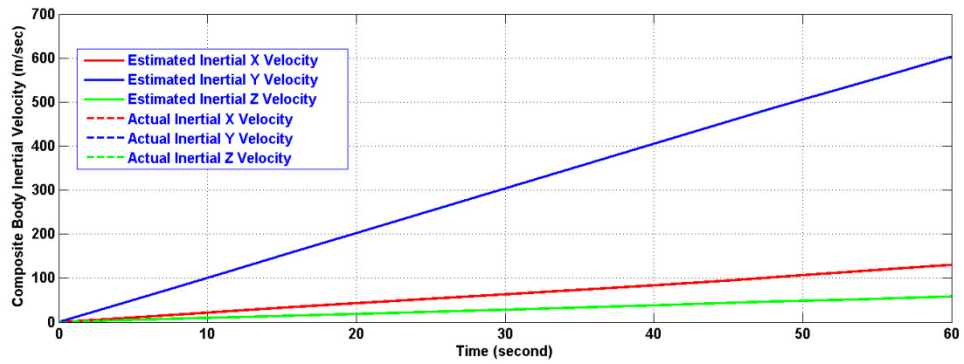


Figure 164: Composite Body Inertial Velocity obtained using the proposed IMU utilizing UKF with 3-D Measurement model.

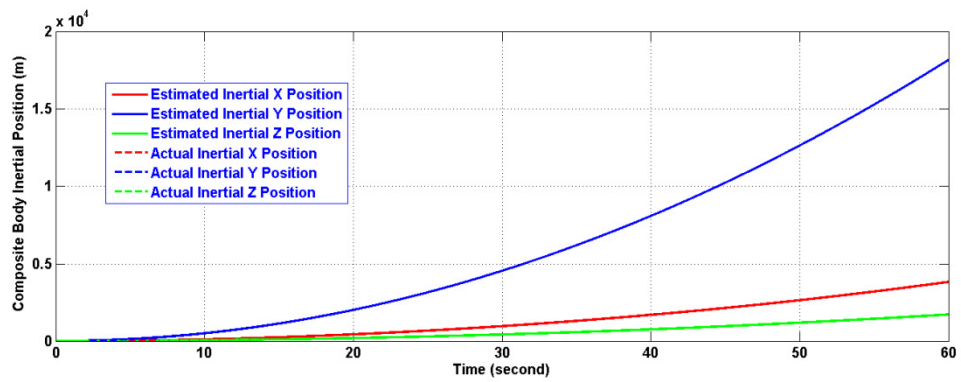


Figure 165: Composite Body Inertial Position obtained using the proposed IMU utilizing UKF with 3-D Measurement model.

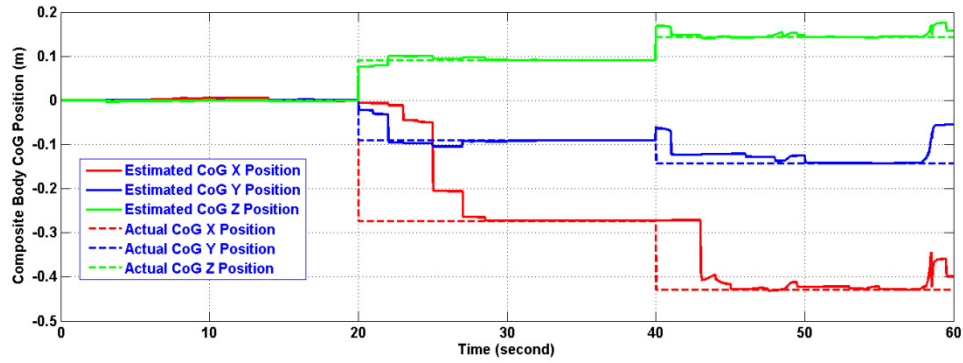


Figure 166: Composite Body position obtained using the proposed IMU utilizing UKF with 3-D Measurement model.

9.2.3 Solving the navigation problem using EKF and QR-D based WRLS

$FF = 0.915$, $Q = 0.01 * \text{eye}(3)$, $R = 0.002 * \text{eye}(3)$

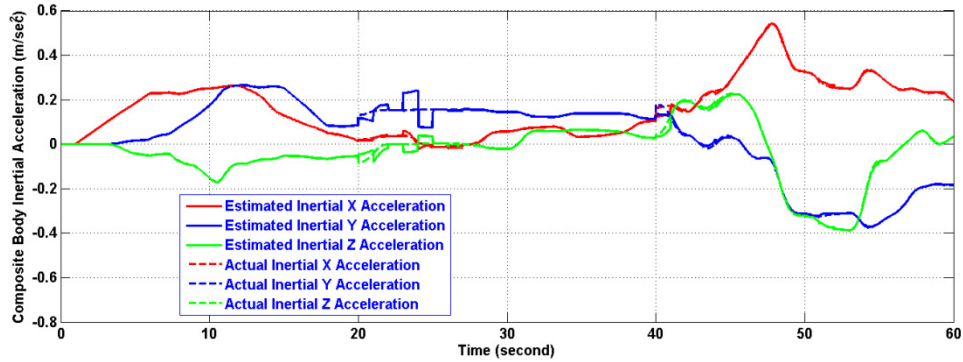


Figure 167: Composite Body Inertial Acceleration, after subtracting the gravity contribution, obtained using the proposed IMU utilizing EKF with 1-D Measurement model.

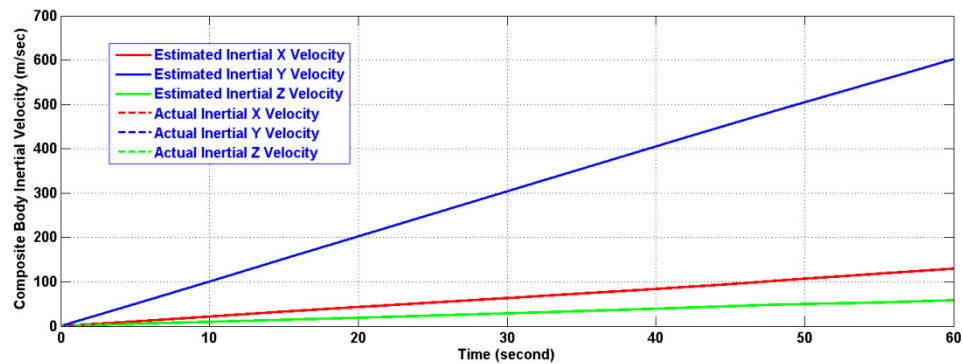


Figure 168: Composite Body Inertial Velocity obtained using the proposed IMU utilizing EKF with 1-D Measurement model.

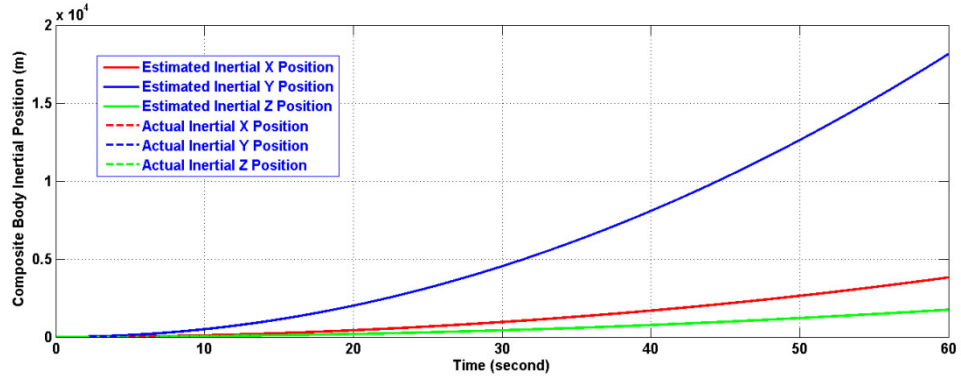


Figure 169: Composite Body Inertial Position obtained using the proposed IMU utilizing EKF with 1-D Measurement model.

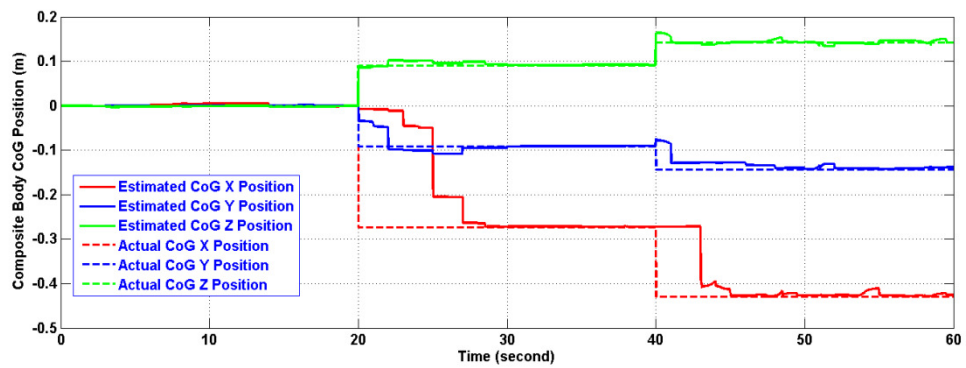


Figure 170: Composite Body position obtained using the proposed IMU utilizing EKF with 1-D Measurement model.

9.2.4 Solving the navigation problem using KF and QR-D based WRLS

$$FF = 0.925, Q = 0.00225 * \text{eye}(3), R = 0.001 * \text{eye}(3)$$

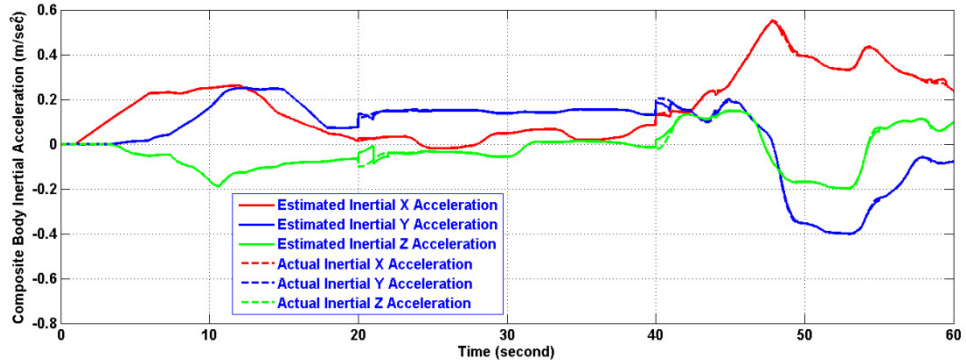


Figure 171: Composite Body Inertial Acceleration, after subtracting the gravity contribution, obtained using the proposed IMU utilizing KF.

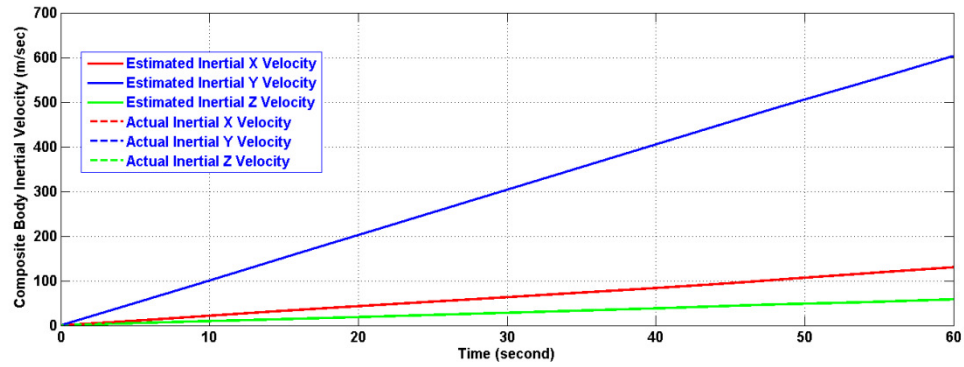


Figure 172: Composite Body Inertial Velocity obtained using the proposed IMU utilizing KF.

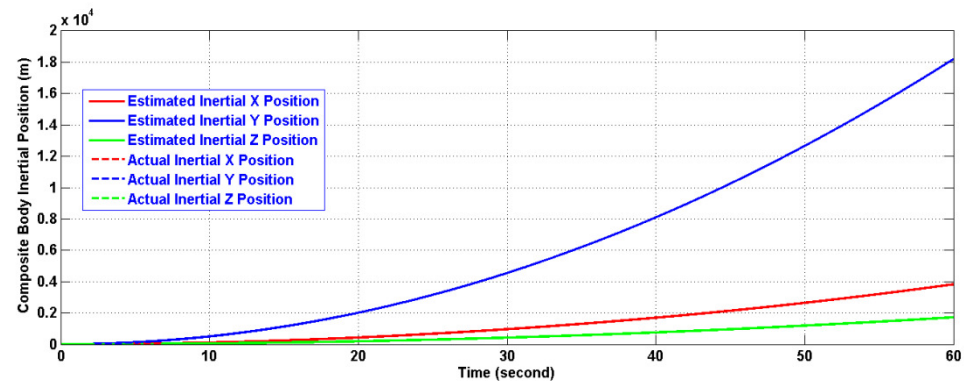


Figure 173: Composite Body Inertial Position obtained using the proposed IMU utilizing KF.

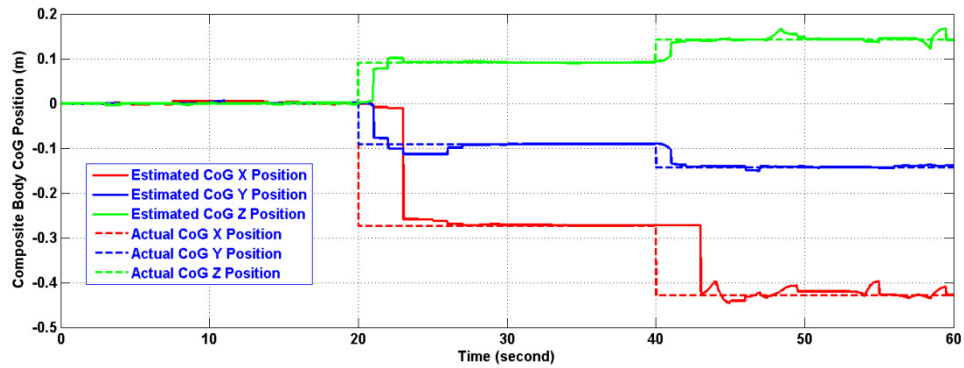


Figure 174: Composite Body position obtained using the proposed IMU utilizing KF.

Next, the gravity estimation using the same setup but with extended time using the UKF with 3-D Measurement model is shown in Figure 175.

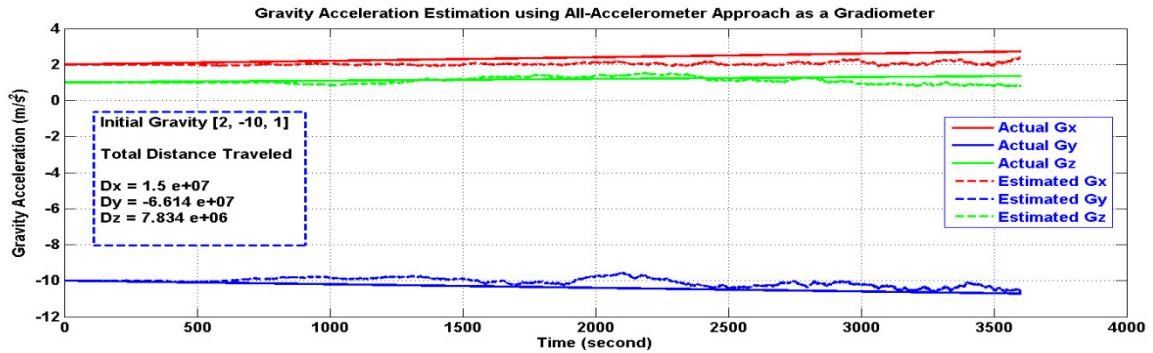


Figure 175: Gravity Estimation using the proposed IMU.

9.3 Hardware Implementation

In this section, some of the aspects related to the hardware implementation of the proposed IMU are presented starting from the linear accelerometers used, till the efficient pieces of hardware to be used, through the best way to implement the algorithms used to fit within a finite-precision devices and controllers. Starting with accelerometers, various types of accelerometers are available and they differ in their properties and performance. Among other important factors to consider when selecting a specific accelerometer, the dynamic range, sensitivity, and the frequency response are very important to consider. It is worth noting that this thesis presents an IMU that can be implemented using different pieces of hardware and software approaches, so it is good to look at it, i.e. the proposed IMU, as an IMU Scheme that can be used with different parts to achieve certain design specifications such as precision and cost.

MEMS accelerometers can provide acceleration measurements with good precision, but may not reach the precision of well-fabricated accelerometers like Cold-Atom interferometry usually used in sophisticated navigation systems. One should keep in mind that the additional cost comes with the increased performance expenses that are governed

by the application. Nevertheless, it is still possible to sacrifice the IMU performance to reduce the cost and this can be made for by moving towards integrated INS rather than being completely a passive INS.

The increased precision needed by the proposed IMU to maintain its complete passive behavior is mainly consumed at the stage where the gravity tensor is estimated. So, in the case where low precision accelerometers are to be used then the available gravity models can be implemented bringing down the complexity of the problem tackled here in this thesis to only finding the inertial acceleration and the kinematics of CoG. In such case, other techniques available in the literature may excel over the proposed IMU scheme especially when used in land-vehicles where the gravity can be known with good precision.

Next, the angular acceleration is determined by utilizing the difference between the corresponding pairs on each axis as was previously shown in Chapter 5. Afterwards, the angular velocity is found by numerically integrating the angular acceleration using one of the available numerical integration techniques; see [125] for example. This step is followed by straight forward algebraic operations to calculate the gravity tensor. It is clear that besides the available accelerometers' precision, the numerical integration method used in finding the angular velocity also plays a significant role in the determination of the gravity tensor.

Now, it is the time to enhance the estimation of the angular velocity by using filters. As was discussed in Chapter 6, the computational power needed by the EKF and the UKF can be comparable although it was preferred to proceed with the UKF based on the 3-D

measurement model; since it provides better estimation as well as reduced sensitivity towards wrong accelerometers' measurements. In [126], a tutorial on how the UKF can be implemented on ARM Cortex-M3 processors (STM32) using Rapid STM32 Blockset in Simulink environment.

One of the important things to consider when implementing these filters on finite-precision devices -aside from the memory allocation problems – is the filter divergence and instability issues. In [81], a number of solutions are provided, namely:

- Increase the Arithmetic precision.
- Consider using Square-Root Filtering.
- Maintain the positive definiteness of the error covariance matrix by using
$$P = (P + P^T)/2 .$$
- Choose appropriate initial value for P; to avoid large changes in its value.
- Consider using Fading-Memory Filters.
- Use fictitious process noise, especially when estimating constants.

At the identification stage and as was stated in the previous chapter, the usage of QR-Decomposition Based RLS method is highly recommended when this method is implemented on finite-precision microprocessor devices.

Finally, finding the inertial velocity and inertial position of the air vehicle is affected by the performance of the filter used, or by the numerical integration method used [58].

In light of the previous discussion, the proposed IMU performance depends on the sampling rate used. So, fast microprocessors with large memory allocation and multiple

threads must be used to reduce the execution time of the algorithms and increase the sampling rate.

The multi-thread architecture can be used wisely to split the different tasks found inside the IMU into sub-tasks. Sub-tasks may be implemented with different updating rates as well. In [66], an FPGA device XC6VLX550T hardware platform accompanied by Xilinx ISE 12.3 software platform were used to parallelize the implementation of a strapdown algorithm on the basis of a fighter data and its computational complexity was analyzed and the results were encouraging to adopt such implementation.

At last, one may find interesting related materials in [85, 128, and 136] which may help in the future work as will be shown in the next chapter.

CHAPTER 10

FUTURE WORK

During the course of this thesis, many problems usually encountered in guidance, navigation, and control of air vehicles started to show relationship to the problem stated here. For example, the usage of gravitational tensor in map matching can be implemented using the solution provided here; since it provides the needed information- thanks to its structure which is built around the same principles as Gradiometer instruments- and this in fact enables the usage of the proposed IMU in designing a potential field within cooperative schemes where agents are interacting nearby each other or in obstacle avoidance and many other applications that depends on the gravitational tensor measurement that are not mentioned here; to avoid lengthy lists. Finding the Instantaneous Acceleration Center of Rotation (IACR) and Instantaneous Velocity Center of Rotation (IVCR) that affect the transient dynamics of air vehicles are other examples, see [122] for more details.

In this chapter, the recommended future work is listed. This list contains the main points found throughout the chapters of this thesis. This list is as follows:

- 1- Build a more sophisticated Simulation Environment in which actual flight routines are possible.

This will enable testing the proposed IMU within actual flight paths rather than applying simple profiles of both forces and moments. A good starting point will be by using this IMU within the simulation example provided in Aerospace Blockset Examples in MATLAB. “The vehicle model includes the aerodynamics, control logic, fault management systems (FDIR), and engine controls. It also includes effects of the environment, such as wind profiles for the landing phase. The entire model simulates approach and landing flight phases using an auto-landing controller. Visualization for this model is done via an interface to FlightGear, an open source flight simulator package”.^[128] Other useful resources can be found in [138-139] respectively.

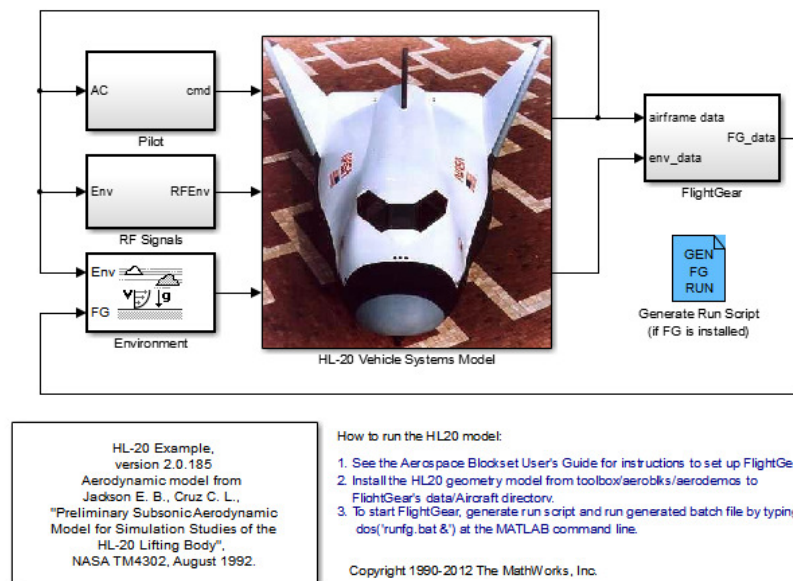


Figure 176: HL20 Example Simulink Model.

- 2- Allow Gradual and abrupt changes in the position of CoG, see [1-2].
- 3- Build an IMU Monitoring Unit that determines the status of the IMU.

- 4- Build Accelerometer's measurements Pre-conditioning and Pre-Filtering Units, see [28-32].
- 5- Build Estimation Smoother to refine the IMU generated estimates, see [81].
- 6- Build Inertial Data Filter, which facilitates retrieving the inertial acceleration, velocity and position of air vehicles, see [127].
- 7- Finding Instant Acceleration Center of Rotation (IACR), see [122].
- 8- Estimating the vehicle mass and inertia see [5-6].
- 9- Analyze the performance of both old and new IMU based on error analysis, see [60-62, 64].
- 10- Include the Earth's rotation into the equations and see how this term can affect the IMU results.

It was shown that the derivation of equations used here relayed on the Flat Earth Model (FEM), which was enough to solve the navigation problem, but it was shown in [95] that this assumption will affect the results obtained when the gravity compensation is included.

- 11- Analyze the performance of the proposed IMU in Centralized Sensing Scheme.
- 12- Consider the System Identification problem into more depth.

As was stated in Chapter 8, the Weighted-Recursive Least-Squares (WRLS) method was unable to handle the problem when it becomes ill-conditioned; so WRLS with varying forgetting factor along with covariance resetting can be considered.

Maximum-Likelihood Estimation may also be a good candidate in addition to the QR-Decomposition-Based RLS Method. Paying more attention to the identification problem may result in better IMU performance.

13- Use frequency domain identification, see [107].

14- Build Adaptive Forgetting Factor QR-D bases WRLS.

15- Make use of RLS and Kalman Filter correspondence to build a state-space estimation model [113].

16- Study the stability of the gravity estimation presented in Chapter 9.

17- Reduce the errors due to uncertainty in initial conditions, see [30].

18- From the error analysis to be done, the effect of the accelerometers separation within the same ring can be investigated and the possibility of having the proposed IMU built in a small chip. This is maybe highly to be possible with MEMS based accelerometers. However, this will not help in compensating for gravity using the procedure proposed here but it still can help in finding the angular velocity and acceleration as a replacement for gyroscopes.

To conclude the work done so far within this thesis, it is evident that the various parts introduced were interacting smoothly. Nevertheless, the listed future work will take this IMU to higher level especially if the system identification problem was dealt with in more detail so that better performance can be obtained out of this IMU.

References

- [1]: X. Yang; Y. Zhong; L. Yang; J. Zhang; G. Shen, "Modeling and attitude control of aircraft with variations in mass and center of gravity," Intelligent Control and Automation (WCICA), 2010 8th World Congress on , vol., no., pp.323,329, 7-9 July 2010.
- [2]: J. Zhang; L. Yang; G. Shen, "Modeling and attitude control of aircraft with center of gravity variations," Aerospace conference, 2009 IEEE, vol., no., pp.1,11, 7-14 March 2009.
- [3]: Aircraft weight and balance handbook, FAA-H-8083-1A, 2007.
- [4]: J. Cummins, A. Bering, D.E. Adams, R. Sterkenburg, "Automated Estimation of an Aircraft's Center of Gravity Using Static and Dynamic Measurements," Proceedings of the IMAC-XXVII, February 9-12, 2009 Orlando, Florida USA.
- [5]: M. Abraham and M. Costello, "In-Flight Estimation of Helicopter Gross Weight and Mass Center Location," Journal of Aircraft, Vol. 46, No. 3, May-June 2009.
- [6]: R. Gowda; P. Mathur; P. Swapnil; T. Ravi; T. C. Rao; N. S. Sundaram; G. V. C. Ragan; K. V. Govinda, "Techniques for Measurement of Center of Gravity & Moment of Inertia and their Importance in Spacecraft Attitude Control," AdMet 2012, Paper No. RA 002.
- [7]: M. F. Almalki and M. Elshafei, "Method and Apparatus for tracking center of gravity of air vehicle," U. S. Patent, US8260477 B2, 4 September 2012.
- [8]: I. Palunko; R. Fierro, "Adaptive Control of a Quadrotor with Dynamic Changes in the Center of Gravity," Preprints of the 18th IFAC World Congress, Milano (Italy), August 28-September 2, 2011.
- [9]: D. H. Titterton and Weston, J. L., "Strapdown Inertial Navigation Technology", 2nd Edition, Progress in Astronautics and Aeronautics, Volume 207, 2004.
- [10]: Guowei Cai, Ben M. Chen, Tong Heng Lee; "Unmanned Rotorcraft Systems", Springer, 2011.
- [11]: http://www.alnasir.com/www/jamie/articles/technology/ins_inertial_navigation_explained.shtml
- [12]: <http://fourier.eng.hmc.edu/e80/inertialnavigation/node4.html>
- [13]: <http://okul.selyam.net/docs/index-14601.html>

- [14]: <http://inertialnavigation.net/strapdown-inertial-navigation-system.htm>
- [15]: <http://fourier.eng.hmc.edu/e80/inertialnavigation/node5.html>
- [16]: Barton J. Bacon, Irene M. Gregory; "General Equations of Motion for a Damaged Asymmetric Aircraft", NASA Langley Research Center, Hampton, VA, 23681.
- [17]: K-W Chiang; TT Duong; J-K Liao; Y-C Lai; C-C Chang; J-M Cai; S-C. Huang, "On-Line Smoothing for an Integrated Navigation System with Low-Cost MEMS Inertial Sensors," *Sensors*, vol. 12, no. 12, pp. 17372-17389, 2012.
- [18]: A. D. Meyer and D. M. Rozelle, "Milli-HRG inertial navigation system," Position Location and Navigation Symposium (PLANS), 2012 IEEE/ION , vol., no., pp.24,29, 23-26 April 2012.
- [19]: M. Barczyk and A.F. Lynch, "Invariant Observer Design for a Helicopter UAV Aided Inertial Navigation System," *IEEE Transactions on Control Systems Technology*, vol. 21, no. 3, pp. 791-806, May 2013.
- [20]: K. Jungmin; P. Jungje; K. Sungshin, "Inertial Navigation System for Omnidirectional AGV with Mecanum Wheel," *Advances in Mechanical Engineering*, vol. 2, no. 1, ISSN 2160-0619, March 2012.
- [21]: S. -B Kim; J. -C Bazin; H. -K Lee; K. -H Choi; S. -Y Park, "Ground vehicle navigation in harsh urban conditions by integrating inertial navigation system, global positioning system, odometer and vision data," *Radar, Sonar & Navigation, IET* , vol. 5, no. 8, pp. 814-823, Oct. 2011.
- [22]: L. R. G. Carrillo; A. E. D. Lopez; R. Lozano; C. Pegard, "Combining Stereo Vision and Inertial Navigation System for a Quad-Rotor UAV," *J Intell Robot System*, vol. 65, pp. 373-387, 2012.
- [23]: J. -H Wang; Y. Gao, "Land Vehicle Dynamics-Aided Inertial Navigation," *IEEE Transactions on Aerospace and Electronic Systems*, vol. 46, no. 4, pp. 1638-1653, Oct. 2010.
- [24]: N. B. Vavilova and Yu. Sazonov, "Calibration of a Ready-Mounted Strapdown Inertial Navigation System on a Low-Accuracy Turntable with One Degree of Freedom," *Moscow University Mechanics Bulletin*, vol. 67, no. 4, pp. 96-98, ISSN 0027-1330, 2012.
- [25]: D. Dube and P. Cardou, "The Calibration of an Array of Accelerometers," *Transaction of the Canadian Society for Mechanical Engineering*, vol. 35, no. 2, 2011.

- [26]: G. Artese and A. Trecroci, "Calibration of a Low Cost MEMS INS Sensor for an Integrated Navigation System," The International Archives of the Photogrammetry, Remote Sensing and Spatial Information Sciences, vol. XXXVII, Part B5, Beijing 2008.
- [27]: S-C Lee and Y-C Huang, "Innovative estimation method with measurement likelihood for all-accelerometer type inertial navigation system," IEEE Transactions on Aerospace and Electronic Systems, vol. 38, no. 1, pp. 339-346, Jan 2002.
- [28]: Q. Fan; W. Li; C. Luo, "Error Analysis and Reduction for Shearer Positioning using the Strapdown Inertial Navigation System," IJCSI International Journal of Computer Science Issues, vol. 9, Issue 5, No 1, September 2012, ISSN (Online): 1694-0814.
- [29]: V. B. Larin; A. A. Tunik, "On Inertial Navigation System Error Correction," International Applied Mechanics, Volume 48, No. 2, March 2012.
- [30]: Chen, T., "Design and Analysis of a Fault-Tolerant Coplanar Gyro-Free Inertial Measurement Unit," Journal of MicroElectroMechanical Systems, Volume 17, No. 1, February 2008.
- [31]: Shi, J.; Miao, L.; Ni, M.; Shen, J., "Optimal robust fault-detection filter for micro-electro-mechanical system-based inertial navigation system/global positioning system," Control Theory & Applications, IET , vol.6, no.2, pp.254,260, January 19 2012.
- [32]: P. A. Akimov; A. I. Matasov, "Processing the Results of SINS Bench Tests by Methods of Nonsmooth Optimization in the Presence of Faults," Gyroscopy and Navigation, vol. 3, no. 2, pp. 91-99, ISSN 2075-1087, 2012.
- [33]: P-C Lin; J-C Lu; C-H Tsai; C-W Ho, "Design and Implementation of a Nine-Axis Inertial Measurement Unit," IEEE/ASME Transactions on Mechatronics, vol. 17, no. 4, pp. 657-668, Aug. 2012.
- [34]: W. Dimin; Z-z Wang, "Strapdown inertial navigation algorithm in geometric algebra," 2011 International Conference on Electrical and Control Engineering (ICECE), vol., no., pp.1842,1845, 16-18 Sept. 2011.
- [35]: K.S. Mostov; A.A. Soloviev; T.-K.J. Koo, "Accelerometer based gyro-free multi-sensor generic inertial device for automotive applications," IEEE Conference on Intelligent Transportation System, 1997. ITSC '97, vol., no., pp. 1047-1052, 9-12 Nov 1997.

- [36]: K. Venkatraman; N. Karthick; J. Naren; B. Amutha, "Sensor-Based Dead Rockening for land vehicle navigation system", International Journal of Recent Trends in Engineering, vol. 2, no. 4, November 2009.
- [37]: J. Zhou; H. Huang; Y. Liu, "Spacecraft center of mass online estimation based on multi-accelerometers," Information Management and Engineering (ICIME), 2010 The 2nd IEEE International Conference on , vol., no., pp.295,298, 16-18 April 2010.
- [38]: C-W Ho and P-C Lin, "Design and implementation of a 12-axis accelerometer suite," IEEE/RSJ International Conference on Intelligent Robots and Systems, 2009. IROS 2009, vol., no., pp.2197-2202, 10-15 Oct. 2009.
- [39]: P-C Lin and C-W Ho, "Design and implementation of a 9-axis inertial measurement unit," IEEE International Conference on Robotics and Automation, 2009. ICRA '09, vol., no., pp.736-741, 12-17 May 2009.
- [40]: K. Parsa; T. A. Lasky; B. Ravani, "Design and Implementation of a Mechatronic, All-Accelerometer Inertial Measurement Unit," IEEE/ASME Transactions on Mechatronics, vol. 12, no. 6, pp. 640-650, Dec. 2007.
- [41]: W-T Ang; P.K. Khosla; C.N. Riviere, "Design of all-accelerometer inertial measurement unit for tremor sensing in hand-held microsurgical instrument," International Conference on Robotics and Automation, 2003. Proceedings. ICRA '03. IEEE, vol. 2, pp.1781-1786 vol.2, 14-19 Sept. 2003.
- [42]: A.H. Zorn, "A merging of system technologies: all-accelerometer inertial navigation and gravity gradiometry," Position Location and Navigation Symposium, 2002 IEEE, pp.66-73, 2002.
- [43]: V. Krishnan, "Measurement of angular velocity and linear acceleration using linear accelerometers," Journal of the Franklin Institute, vol. 280, no. 4, pp. 307-315, ISSN 0016-0032, October 1965.
- [44]: A.J. Padgaonkar, K.W. Krieger, AI. King, "Measurement of Angular Acceleration of a Rigid Body Using Linear Accelerometers," J. Appl. Mech., vol 42, no. 3, pp. 552-556, 1975.
- [45]: A. R. Schuler; A. Grammatikos; K. A. FEGLEY, "Measuring Rotational Motion with Linear Accelerometers," IEEE Transactions on Aerospace and Electronic Systems, vol. AES-3, no. 3, pp. 465-472, May 1967.

- [46]: S. Patrick; K. Lasse; P. Christian; M. Yiannos, "Design, geometry evaluation, and calibration of a gyroscope-free inertial measurement unit," *Sensors and Actuators A: Physical*, vol. 162, no. 2, pp. 379-387, ISSN 0924-4247, August 2010.
- [47]: E. Edwan; S. Knedlik; O. Loffeld, "Constrained Angular Motion Estimation in a Gyro-Free IMU," *IEEE Transactions on Aerospace and Electronic Systems*, vol. 47, no. 1, pp. 596-610, January 2011.
- [48]: C. Tan; S. Park, "Design of Accelerometer-Based Inertial Navigation Systems," *IEEE Transactions on Instrumentation and Measurement*, vol. 54, no. 6, December 2005.
- [49]: ___, "A Comparative Study of All-Accelerometers Starpdowns for UAV INS," Department of Mechanical Engineering & Centre for Intelligent Machines McGill University, NATO, 1 May 2005.
- [50]: C. Songyin and G. Lei, "Multi-objective robust initial alignment algorithm for Inertial Navigation System with multiple disturbances," *Aerospace Science and Technology*, vol. 21, no. 1, pp. 1-6, ISSN 1270-9638, September 2012
- [51]: W. Xinlong, "Fast alignment and calibration algorithms for inertial navigation system," *Aerospace Science and Technology*, vol. 13, no. 4-5, pp. 204-209, ISSN 1270-9638, June-July 2009.
- [52]: A. Jamshaid; M. Rasheeq Ullah; M. Baig, "Initial orientation of inertial navigation system realized through nonlinear modeling and filtering," *Measurement*, vol. 44, no. 5, pp. 793-801, ISSN 0263-2241, June 2011.
- [53]: L. Chang; B. Hu; A. Li; F. Qin, "Strapdown inertial navigation system alignment based on marginalised unscented kalman filter," *Science, Measurement & Technology, IET*, vol. 7, no. 2, March 2013.
- [54]: Q. Li; Y. Ben; Z. Zhu; J. Yang, "A Ground Fine Alignment of Strapdown INS under a Vibrating Base," *The Journal of Navigation*, vol. 66, pp. 49-63, 2013.
- [55]: K. K. Veremeenko; V. M. Savel'ev, "In-Flight Alignment of a Strapdown Inertial Navigation system of an Unmanned Aerial Vehicle," *Journal of Computer and Systems Sciences International*, vol. 52, no. 1, pp. 106-116, ISSN 1064-2307, 2013.
- [56]: X. Wang; G. Shen, "A Fast and Accurate Initial Alignment Method for Starpdwn Inertial Navigation System on stationary base," *Journal of Control Theory and Applications*, vol. 2, pp. 145-149, 2005.

- [57]: J.G. Lee; C.G. Park; H.W. Park, "Multiposition alignment of strapdown inertial navigation system," IEEE Transactions on Aerospace and Electronic Systems, vol. 29, no. 4, pp. 1323-1328, Oct 1993.
- [58]: Y.K. Thong; M.S. Woolfson; J.A. Crowe; B.R. Hayes-Gill; D.A. Jones, "Numerical double integration of acceleration measurements in noise," Measurement, vol. 36, no. 1, pp. 73-92, ISSN 0263-2241, July 2004.
- [59]: A. M. NIA; R. Mirzajani; M. Esfalani, "Subtractive Composite Simpson Method for low cost Inertial Navigation Systems," Journal of Circuits, Systems, and Computers, vol. 20, no. 4, pp. 667-680, 2011.
- [60]: I. Miller and M. Campbell, "Sensitivity Analysis of a Tightly-Coupled GPS/INS System for Autonomous Navigation," IEEE Transactions on Aerospace and Electronic Systems, vol. 48, no. 2, pp. 1115-1135, April 2012.
- [61]: M. Jafari and J. Roshanian, "Optimal Redundant Sensor Configuration for Accuracy and Reliability Increasing in Space Inertial Navigation Systems," The Journal of Navigation, vol. 66, pp. 199-208, 2013.
- [62]: P. Sungsu; T. Chin-Woo; P. Joohyuk, "A scheme for improving the performance of a gyroscope-free inertial measurement unit," Sensors and Actuators A: Physical, vol. 121, no. 2, pp. 410-420, ISSN 0924-4247, 30 June 2005.
- [63]: W. Zhang; M. Ghogho; B. Yuan, "Mathematical Model and Matlab Simulation of Strapdown Inertial Navigation System," Hindawi Publishing Corporation, Modeling and Simulation in Engineering, vol. 2012, Article ID 264537, 25 pages.
- [64]: A. A. Odintsov, "Testing Strapdown Inertial Navigation Systems on a Test Bench," Gyroscopy and Navigation, vol. 1, no. 4, pp. 239-245, ISSN 2075-1087, 2010.
- [65]: D. J. Allerton; H. Jia, "Distributed data fusion algorithms for Inertial Network Systems," IET Radar Sonar Navigation, vol. 2, no. 1, pp. 51-62, ISSN 1751-8784, 2008.
- [66]: Z-T Li; T-J Wu; C-L Lin; L-H. Ma, "Field Programmable Gate Array Based Parallel Strapdown Algorithm Design for Strapdown Inertial Navigation Systems," Sensors, vol. 11, no. 8, pp. 7993-8017, 2011.
- [67]: O. J. Woodman, "An Introduction to Inertial Navigation," Computer Laboratory, University of Cambridge, Tech. Rep. 696, August 2007.
- [68]: J. H. Glover, "Aircraft In-Flight Center of Gravity Measuring System," U. S. Patent, 4545019, 1 October 1985.

- [69]: M. Orgun and S. J. Flannigan, "Method and Apparatus for real time estimation of aircraft center of gravity," U. S. Patent, 5034896, 23 July 1991.
- [70]: C. R. McClary, "Fault Tolerant Inertial reference system," U. S. Patent, 5719764, 17 February 1998.
- [71] N. Lovren; J.K. Pieper, "A strapdown inertial navigation system for the flat-Earth model," IEEE Transactions on Aerospace and Electronic Systems, vol. 33, no. 1, pp. 214-224, Jan. 1997.
- [72]: G. Feng; W. Wu; J. Wang, "Observability Analysis of a Matrix Kalman Filter-Based Navigation System Using Visual/Inertial/Magnetic Sensors," Sensors, vol. 12, pp. 8877-8894, 2012.
- [73]: X. Chen; J. Yu; X. Zhu, "Theoretical Analysis and application of Kalman filters for ultra-tight global position system/inertial navigation system integration," Transactions of the Institute of Measurement and Control, vol. 34, no. 5, pp. 648-662, 2011.
- [74]: Y-l HAO; M-h Chen; L-j Li; B. Xu, "Comparison of robust H_{∞} filter and Kalman filter for initial alignment of inertial navigation system," J. Marine. Sci. Appli. Vol. 7, pp. 116-121, 2008.
- [75]: S. Zhi; G. Jacques; J. K. Michael; N. Aboelmagd, "Low cost two dimension navigation using an augmented Kalman filter/Fast Orthogonal Search module for the integration of reduced inertial sensor system and Global Positioning System," Transportation Research Part C: Emerging Technologies, vol. 19, no. 6, pp. 1111-1132, ISSN 0968-090X, December 2011.
- [76]: A. Jamshaid and U. Muhammad, "A consistent and robust Kalman filter design for in-motion alignment of inertial navigation system," Measurement, vol. 42, no. 4, pp. 577-582, ISSN 0263-2241, May 2009.
- [77]: A. Kluga; V. Bistrows, "Adaptive Extended Kalman Filter for Aided Inertial Navigation System," Electronics and Electrical Engineering, vol. 6, no. 122, ISSN 1392-1215, 2012.
- [78]: H. K. Kwang; J-G Lee; C-G Park, "Adaptive Two-Stage Extended Kalman Filter for a Fault-Tolerant INS-GPS Loosely Coupled System," IEEE Transactions on Aerospace and Electronic Systems, vol. 45, no. 1, pp. 125-137, Jan. 2009.
- [79]: P. Zarchan and H. Musoff, "Fundamentals of Kalman Filtering: A practical approach," 3rd Edition, Progress in Astronautics and Aeronautics, Volume 232, 2009.

- [80]: ____; “Course 8 – An Introduction to the Kalman Filter”, SIGGRAPH 2001, Los Angeles, CA, August 12-17, 2001.
- [81]: Dan Simon; “Optimal State Estimation: Kalman, H_∞ , and Nonlinear Approaches”, WILEY-INTERSCIENCE, 2006.
- [82]: Steven C. Chapra, Raymond P. Canale; “Numerical Methods for Engineers”, 4th Edition, Mc Graw Hill, 2002.
- [83]: B.D.O. Anderson, J.B. Moore; “Optimal Filtering”, Minola, NY, Dover Publications, Inc. Chapter 3, 1995.
- [84]: Paul John Huxel; “Navigation Algorithms and Observability Analysis for Formation Flying Missions”, PhD Dissertation, THE UNIVERSITY OF TEXAS AT AUSTIN, May, 2006.
- [85]: Vibhor L. Bageshwar, Demoz Gebre-Egziabher, William L. Garrard, Tryphon T. Georgiou; “A Stochastic Observability Test for Discrete-Time Kalman Filters”, University of Minnesota, Minneapolis, MN 55454.
- [86]: Horn, Roger A.; Johnson, Charles R.; “Matrix Analysis”, Cambridge University Press, ISBN 978-0-521-38632-6, 1990.
- [87]: Jaw-Kuen Shiau and I-Chiang Wang; “Unscented Kalman Filtering for Attitude Determination Using MEMS Sensors”, Journal of Applied Science and Engineering, Vol. 16, No. 2, pages 165-176, 2013.
- [88]: Simon J. Julier, Jeffery K. Uhlmann; “Unscented Filtering and Nonlinear Estimation”, PROCEEDINGS OF THE IEEE, Vol. 92, No. 3, March, 2004.
- [89]: A. UmaMageswari, J. Joseph Ignatious, R. Vinodha; “A Comparative Study of Kalman Filter, Extended Kalman Filter And Unscented Kalman Filter For Harmonic Analysis Of The Non-Stationary Signals”, International Journal of Scientific & Engineering research, Vol. 3, Issue 7, July, 2012.
- [90]: T. Fiorenzani, C. Manes, G. Oriolo, P. Peliti; “A Comparative Study of Unscented Kalman Filter and Extended Kalman Filter for Position/Attitude Estimation in Unmanned Aerial Vehicles”, Istituto Di Analisi Dei Sistemi Ed Informatica, 2008.
- [91]: C. A. Murphy; “The Air-FTG airborne gravity gradiometer system”, in Abstracts from the ASEG-PESA Airborne Gravity Workshop: Geoscience Australia Record, pages 7-14, 2004.

- [92]: Troy C. Welker, Meir Pachter, Richard E. Huffman; "Gravity Gradiometer Integrated Inertial Navigation", 2013 European Control Conference (ECC), Zürich, Switzerland, July 17-19, 2013.
- [93]: Troy C. Welker, Richard E. Huffman, Meir Pachter; "Use of Gravity Gradiometer in Precision Inertial Navigation Systems", AIAA guidance, Navigation, and Control Conference, Portland, Oregon, 08-11 August, 2011.
- [94]: Christopher Jekeli; "Precision Free-Inertial Navigation with Gravity Compensation by an Onboard Gradiometer", Journal of guidance, Control, and Dynamics, Vol. 29, No. 3, May-June, 2006.
- [95]: Y. M. WANG; "The Gradiometer-Gravimeter Equation in Various Coordinate Systems", Bull. Géod. 61, pages 125-144, 1987.
- [96]: Lin Zhao, Fengming Liu, Haijing Yuan; "The Design and Analyse for Accelerometer-based Gravity Gradiometer ", Proceedings of the 2009 IEEE, International Conference on Mechatronics and Automation, Changchun, China, August 9-12, 2009.
- [97]: T. Tijing, "A platformless inertial navigation system based on a canonical gravitational gradiometer," Journal of Applied Mathematics and Mechanics, vol. 62, no. 5, pp. 819-822, ISSN 0021-8928, 1998.
- [98]: A. S. Devyatisil'nyi, "Model of a Correctable Inertial Navigation System Capable of Determining the Earth's Gravitational Field Strength," Technical Physics, vol. 57, no. 1, pp. 141-144, ISSN 1063-7842, 2012.
- [99]: A. S. Devyatisil'nyi and K. A. Chislov, "Three-Component Position Correctable Astro-Inertial Navigation System with a Function for Determining Gravitational Field Strength," Measurement Techniques, vol. 55, no. 2, may 2012.
- [100]: A. S. Devyatisil'nyi and K. A. Chislov, "Model of Onboard Vector Gravi-Inertial Navigation System," Measurement Techniques, vol. 55, no. 11, February 2013.
- [101]: A. S. Devyatisil'nyi, "model of a Vector Gravimetry Based on a Correctable Two-Component Inertial Navigation System," Technical Physics, vol. 57, no. 12, pp. 1730-1732, ISSN 1063-7842, 2012.
- [102]: R. Hongliang and P. Kazanzides, "Investigation of Attitude Tracking Using an Integrated Inertial and Magnetic Navigation System for Hand-Held Surgical Instruments," IEEE/ASME Transactions on Mechatronics, vol. 17, no. 2, pp. 210-217, April 2012.

- [103]: Justin A. Richeson; "Gravity Gradiometer Aided Inertial Navigation within Non-GNSS Environments", PhD Dissertation, University of Maryland, College Park, 2008.
- [104]: C. Grubin; "Accuracy Improvement in a Gravity Gradiometer-Aided Cruise Inertial Navigator Subjected to Deflections of the Vertical", AIAA Guidance and Control Conference, Boston, MA, August 20-22, 1975.
- [105]: W. G. Heller, S. K. Jordan; "Error Analysis of Two New Gradiometer-Aided Inertial Navigation Systems", AIAA Journal of Spacecraft and Rockets, Vol. 13, No. 6, pages 340-347, 1976.
- [106]: Philippe Cardou; "Computing the Rigid-Body Acceleration Field from Nine Accelerometer Measurements," Advances in Soft Computing, vol. 83, pages 325-339, 2010.
- [107]: Naren K. Gupta, and Kenneth W. Liff; "Identification of Unsteady Aerodynamics and Aerolastic Integro-Differential Systems", NASA Technical Memorandum 86749, August, 1985.
- [108]: In Jae Myung; "Tutorial on maximum likelihood estimation", Journal of Mathematical Psychology, Vol. 47, pages 90-100, 2003.
- [109]: Paulo S. Diniz, "Adaptive Filtering: Algorithms and Practical Implementation", 3rd Edition, Kluwer Academic Publishers, 2008.
- [110]: Yunmin Zhu, X. Rong Li; "Recursive Least Squares With Linear Constraints", Communications in Information and Systems, Vol. 7, No. 3, pages 287-312, 2007.
- [111]: Kenya Muakami, Dale E. Seborg; "Constrained parameter estimation with applications to blending operations", Journal of Process Control, Vol. 10, pages 195-202, 2000.
- [112]: Bengt Lindoff, "On Parameter Estimation and Control of Time-Varying Stochastic Systems", Thesis, Department of Mathematical Statistics, Lund University, Sweden, 1997.
- [113]: Ta-Hsin Li, "On Exponentially Weighted Recursive Least Squares for Estimating Time-Varying Parameters", Department of Mathematical Sciences, IBM T.J. Watson Research Center, Yorktown Heights, NY 10598-0218, December 9, 2003.
- [114]: Marco C. Campi, "Exponentially Weighted Least Squares Identification of Time-Varying Systems with White Disturbances", IEEE TRANSACTION ON SIGNAL PROCESSING, Vol. 42, No. 11, November 1994.

- [115]: S. Bittanti, P. Bolzern, M. Campi, and E. Coletti; “Deterministic Convergence Analysis of RLS Estimators with Different Forgetting Factors”, Proceedings of the 24th Conference on Decision and Control, Austin, Texas, December 1988.
- [116]: B. Lindoff, and J. Holst; “Convergence Analysis of the RLS Identification Algorithm with Exponential Forgetting in Stationary ARX-Structures”, INTERNATIONAL JOURNAL OF ADAPTIVE CONTROL AND SIGNAL PROCESSING, Int. J. Adapt. Control Signal Process. Vol. 13, pages 1-22, 1999.
- [117]: M.T. Tham, and S.N. Mansoori; “COVARIANCE RESETTING IN RECURSIVE LEAST SQUARES ESTIMATION”, International Conference on Control, pages 128-133, April 13, 1988.
- [118]: Geoffrey W.K. Colman, and Jeffery W. Wells; “On the Use of RLS with Covariance Reset in Tracking Scenarios with Discontinuities”, Canadian Conference on Electrical and Computer Engineering CCECE '06, pages 693-696, May 2006.
- [119]: XUE Yuncan, and QIAN Jixin; “Modified Recursive Least Squares Algorithm with Variable Parameters and Resetting for Time-Varying System”, Chinese J. Chem. Eng., Vol. 10, No. 3, pages 298-303, 2002.
- [120]: Esmat Bekir; “Introduction to modern Navigation Systems”, World Scientific, 2007.
- [121]: Der-Ming Ma, Jaw-Kuen Shiau, I-Chiang Wang and Yu-Heng Lin; “Attitude Determination Using a MEMS-Based Flight Information Measurement Unit”, Sensors, vol. 12, pages 1-23, 2012.
- [122]: Jin Yan, Jesse B. Hoagg, Richard E. Hindman, and Dennis S. Bernstein; “Longitudinal Aircraft Dynamics and the Instantaneous Acceleration Center of Rotation: The case of the vanishing zeros”, November 7, 2010.
- [123]: Peter H. Zipfel; “Modeling and Simulation of Aerospace Vehicle Dynamics”, AIAA Educational Series, 2000.
- [124]: Yaakov Bar-Shalom, X. Rong Li, Thiagalingam Kirubarajan; “Estimation with Applications to Tracking and Navigation”, WILEY-INTERSCIENCE, 2001.
- [125]: Jose J. Rosales, Ismael Colomina; “A Flexible Approach for the Numerical Solution of the INS Mechanization Equations”, Institute of Geomatics, Generalitat de Catalunya & Universitat Politecnica de Catalunya, Castelldefels, Spain.

- [126]: Rapid STM32 Team; “Developing a Tilt Sensor System Using Rapid STM32 Blockset (Part 1 Design and Simulation)”, Application Note 1A, August, 2nd, 2009.
- [127]: Robert M. Rogers, “Applied Mathematics in Integrated Navigation Systems”, 3rd Edition, AIAA Education Series, 2007.
- [128]: ___; “NASA HL-20 with FlightGear Interface”, Aerospace Blockset Examples, MATLAB documentation files.
- [129]: Ashish Tewari; “Advanced Control of Aircraft, Spacecraft and Rockets”, WILEY, Aerospace Series, 2011.
- [130]: Ashish Tewari; “Atmospheric and Space Flight Dynamics: Modeling and Simulation with MATLAB and Simulink”, Birkhäuser, 2007.
- [131]: <https://earth.esa.int>
- [132]: The European GOCE Gravity Consortium,” GOCE Standards,” Doc. No.: GO-TN-HPF-GS-0111, Issue: 3, Revision: 2, Date: 23 / 06 / 2010
- [133]: Alberto Bigazzi, Björn Frommknecht, Marco Meloni, Loretta Mizzi,” GOCE Data and Formats”.
- [134]: Claudia Stummer,”Analyse der Gradiometergleichungen der GOCE Satellitenmission zur Schwerefeldbestimmung”, Diplomarbeit, in German, July 2006

Vitae

Name : YAZAN MOHAMMAD SULIMAN AL-RAWASHDEH

Nationality : JORDANIAN

Date of Birth : 5/21/1983

Email : yazanmrawashdeh@gmail.com

Address : Amman-Jordan

Academic Background : B.Sc. in Mechatronics Engineering – University of Jordan
GPA 3.34 / 4.00

Professional Experience

- September 2006 – April 2008:
Engineer, University of Jordan, Amman-Jordan
Mechatronics Labs Supervisor, Experiments Designer.
- April 2008 – August 2009:
Institute of Applied Technology IAT, Al Ain-UAE
Engineering Labs Teacher.
- August 2009-August 2010:
Teaching Assistant, University of Jordan, Amman-Jordan

Mechatronics Engineering Department.

- October 2010-February 2011:

Engineer, Integrated Control and Electrical Systems (ICES)

Amman-Jordan

Part-time employee.

- February 2011-September 2012:

CNC Machine Maintenance, Amman-Jordan, Self-owned
Business.

Symposiums

Symposium on Industrial System and Control 2014, King
Fahd University of Petroleum and Minerals, Dhahran-
Kingdom of Saudi Arabia, 6-7th May 2014

- 3D Virtualization in Industrial Automation
Education.
- Estimating the Center of Gravity position of Air
vehicles under varying gravity forces using All-
accelerometers

Scholarships

Ministry of Higher Education in Kingdom of Saudi Arabia,
King Fahd University of Petroleum and Minerals KFUPM,
September 2012.

